CRANFIELD UNIVERSITY

CHARLENE GREENWOOD

PHYSICOCHEMICAL MODIFICATIONS TO BONE MINERAL

DEPARTMENT OF ENGINEERING AND APPLIED SCIENCE

PhD Thesis

Academic Year: 2013 -2014

Supervisors: Professor Keith Rogers & Dr Sophie Beckett

February 2014

CRANFIELD UNIVERSITY

DEPARTMENT OF ENGINEERING AND APPLIED SCIENCE

PhD Thesis

Academic Year 2013-2014

CHARLENE GREENWOOD

PHYSICOCHEMICAL MODIFICATIONS TO BONE MINERAL

Supervisors: Prof. Keith Rogers & Dr. Sophie Beckett

February, 2014

This thesis is submitted in partial fulfilment of the requirements for the degree of PhD

ABSTRACT

Bone is a complex composite material consisting of three main components: a mineral phase structurally similar to calcium hydroxyapatite (HAp), an organic matrix containing collagenous and non-collagenous proteins and, water. The complexity of bone has led to an abundance of literature across a wide range of disciplines, which have endeavoured to provide a greater understanding of this material. In particular, heated bone studies are prevalent in biomedicine where heat treatment is often used to sterilise bone material required for xeno– and allo- grafts, in forensic science where species differentiation of unknown heated bone specimens would prove invaluable and in archaeology, where heated bone material often provides information about the cooking and funeral practices of our ancestors. Unfortunately, many of these studies are largely observational and some of the processes and mechanisms associated with heated bone are largely assumed and in some instances ambiguous.

Over 1000 biological and synthetic HAp specimens were utilised during this research to investigate the fundamental processes and mechanisms associated with unheated and heated bone. In particular, three controversial areas of bone research were considered: - *in vivo* HAp crystal size control, the relationship between the organic and mineral components of bone during heat treatment and the confounding effects of cooling on bone mineral during heat treatment. This was achieved by considering the chemical composition of unheated biological and synthetic HAp specimens, and heated bone specimens from various species including human.

The results of this thesis demonstrate that an intrinsic rather than extrinsic source may be responsible for *in vivo* biological HAp crystal size control, a concept which has not previously be considered. The results have also shown bone mineral crystallisation during heat treatment is promoted by the organic matrix and, cooling has an impact on both crystallisation and thermal decomposition of HAp during heat treatment. This research has also questioned the use of current X-ray diffraction (XRD) refinement techniques with nanocrystalline materials such as bone, to determine crystalline size and strain. Further interpretation of the results questioned whether heated bone data is comparable between research groups, whether it was possible to create a time and

temperature predictive model for heated bone and whether human bone is statistically different from other bone types when dynamically heated. Due to the fundamental nature of this research, it is expected the results will have an impact across a wide range of disciplines including biomedicine, forensic science and archaeology.

Keywords: calcium hydroxyapatite, crystallisation kinetics, dynamic heat treatment, heated bone, X-ray diffraction (XRD).

To Dad,

Thank you for always believing in me, I wouldn't be where I am today without you.

I hope I forever make you proud.

Love and miss you more than words can express.

ACKNOWLEDGEMENTS

Many, many thanks are given to those who have supported me through my years as a PhD student. My supervisors, Professor Keith Rogers and Dr. Sophie Beckett are thanked for their supervision, guidance and patience. Thank you for selecting me for the role and for your continued belief in me. Most of all thank you for being there for me when I needed it the most, without your support I certainly wouldn't be sat here today typing these acknowledgements.

Cranfield University is thanked for funding this project and providing me with the opportunity to carry out this work. I'd like to express my gratitude to the staff at Cranfield, whose expertise was always available when I needed it. The banter provided by the staff at Cranfield (in particular Alistair Doig) during coffee break would never fail to lift my mood and put a smile on my face. Adrian Mustey is specially thanked for his help with anything practical (including checking my car for faults) and for being a good friend. The staff at Cranfield's Barrington Library are acknowledged for their cheery attitude and chats (especially Iain McKay) every time I went in to pick up a book or inter-library loan. Many thanks are also given to Dr Tim Comyn, Leeds University, UK for enabling use of the Hot Stage X-ray Diffraction equipment and for his advice throughout the dynamically heated bone project.

The work could not have progressed without donations of bone samples. The North London Tissue Bank is thanked for providing human bone specimens (via Dr Peter Zioupos). Special thanks are extended to the families who kindly donated this tissue. Gratitude is expressed to The Animal Veterinary and Health Laboratories Agency (AVHLA) and Mick Kirby who provided porcine and red deer antler specimens. Local abattoirs are thanked for their contribution of bovine specimens. The provision of rostrum bone material was gratefully received (via Dr Peter Zioupos) from Dr. A. Casinos of the Department of Biology, University of Barcelona, Spain, and Dr Vivian de Buffrénil of the Muséum National d'Histoire Naturelle, Paris.

Throughout my PhD I have been lucky enough to attend various conferences and summer schools. The Bone Research Society (BRS) are thanked for awarding me a

grant to attend their Young Investigator workshop, Sheffield in July 2011 - their advice on CV writing came in handy when applying for my post-doctoral position. Thanks are given to the International School on Biological Crystallisation who awarded a bursary, allowing me to attend the School of Crystallisation conference, Granada, Spain in May 2012 – I made some amazing friends and witnessed Flamenco dancing in an incredible restaurant in the mountains, something I will never forget. Diamond Light Source, Oxford are thanked for awarding me a grant which enabled me to attend their summer school in September, 2012 – the knowledge and experience I gained has proven invaluable, not to mention the friends I made. In addition, I would like to acknowledge all the organisations who allowed me to present my work at their conferences.

Finally, but not at all least I would like to express my immense gratitude to my friends and family. For all my friends who have supported me through the bad times as well as the good, thank you. I cannot count the amount of times I needed that chat, hug or drink. To one of my special friends, Charlie Enright, you've never failed to be there for me and that means a lot. (Thank you for not replacing 'the' with some obscene word whilst proof reading this thesis). John Rock and Leigh Fenton are also thanked for giving up their time to proof read this thesis.

For their unquestionable love and support throughout my education, my family are thanked. A huge thank you is required for my Mum and Dad who have never failed to provide me with emotional and financial support, guidance and an ear to listen when things didn't go to plan. I wouldn't be where I am without you both. My little brother, Arran (who at the time of writing this is 24 years old and a college teacher, but will always be my baby bro), is thanked for being there for me when I needed it the most, you seem to have adopted the older brother role in the last few months. However, 'my sister just sticks bone in a furnace to see what happens' when describing what I do is less appreciated. My partner, Reece is thanked for his love and support and for putting up with me for the last two years, it can't have been easy!

TABLE OF CONTENTS

LIST OF FIGURES

LIST OF TABLES

LIST OF ABBREVIATIONS

α - TCP	alpha-tri-calcium phosphate , α - $Ca_3(PO_4)_2$
β - TCP	beta - tri-calcium phosphate, β - $Ca_3(PO_4)_2$
BSP	Bone sialoprotein
A - type HAp	A- type carbonated HAp: $Ca_{10}(PO_4)_6CO_3$
AB - type HAp	AB- type carbonated HAp: $Ca_{10-x}[(PO_4)_{6-2x}(CO_3)_{2x}](CO_3)$
B - type HAp	B - type carbonated HAp: $Ca_{10-x}[(PO_4)_{6-2x}(CO_3)_{2x}](OH)_2$
C	Carbon
Ca	Calcium
Ca: P	Calcium to Phosphorous ratio
CaO	Calcium oxide
Cd	Cadmium
CI	Crystallinity Index
CIE	International Commission on Illumination
CL	Coherence length
Cl	Chloride
CL_Y	Citrate Lyase
CO_3	Carbonate
D-LDH	D-lactate dehydrogenase
DNA	Deoxyribonucleic acid
DSC	Differential scanning calorimetry
F	Fluorine
FTIR	Fourier transform infrared spectroscopy
FWHM	Full width - half maximum
H	Hydrogen
HAp	Calcium HAp, stoichiometric form: $Ca_{10}(PO_4)_6(OH)_2$
HCL	Hydrochloric acid
HPO_4	Acid phosphate / Phosphoric acid
HWHH	Half width - half height
ICDD	International Centre for Diffraction Data

IR	Infra-red
IRF	Instrument resolution factor
K	Potassium
KBr	Potassium bromide
KJMA	Kolmogorov-Johnson-Mehl-Avrami
LA-ICP-MS	Laser ablation-inductively coupled –mass spectrometry
L-MDH	L-Malate dehydrogenase
MBM	Meat and bone meal
Mg	Magnesium
MgO	Magnesium Oxide
Na	Sodium
NADH	Glycylglycine nicotinamide adenine dinucleotide
NMR	Nuclear magnetic resonance
O	Oxygen
OAP	Calcium oxyapatite, $Ca_{10}(PO_4)_6O$
OH	Hydroxide
P	Phosphorous
Pb	Lead
PO_4	Phosphate
PVP	Polyvinylpyrollidone
RD Antler	Red deer antler
SCE	Specular component excluded
SF	Splitting factor
sHAp	Synthetically produced HAp
SPV	Asymmetrical pseudo-voigt
Sr	Strontium
TEM	Transmission electron microscopy
TTCP	Tetra-calcium phosphate, $Ca_4(PO_2)_2(O)$
UC	Urinary calculi
UV-Vis	Ultraviolet-Visible spectroscopy
XRD	X-ray diffraction
Zn	Zinc

Chapter 1: INTRODUCTION

Bone is a complex composite material consisting of three main components: a mineral phase structurally similar to calcium hydroxyapatite (HAp), an organic matrix containing collagenous and non-collagenous proteins and, water. The complexity of bone has led to an abundance of literature which has endeavoured to determine the general composition and structure of bone. This has in some instances proven extremely difficult due to the apatite mineral phase. Due to its misleading similarity to other materials, 'apatite' was named from the Greek word, *apatē* which translates as deceit. This is particularly fitting for biologically formed apatites such as that in bone, teeth and urinary calculi, in which the chemical composition is not fixed due to constant ion migration.

In recent years, a limited number of researchers have used this to their advantage and have investigated differences in the chemical composition and structure of several biological and synthetic HAp specimens. For example, physicochemical information obtained from bone of several different species, with the aim to differentiate between human and non-human specimens has recently been reported (Beckett *et al*., 2011, Piga *et al*., 2013), although the success of this is debated (discussed further in section 1.2.3). This research area not only investigated the chemical state of unheated bone, but also considered the physicochemical behaviour of bone when heated to different temperatures. Research in this area has the potential to have a significant impact in forensic science and archaeology. The fundamental processes and mechanisms associated with the physicochemical modifications (crystallisation and thermal decomposition) to bone during heat treatment however have not been fully considered.

The study of heated bone is not limited to the field of forensic science and is also prevalent in biomedical (Murugan *et al*., 2003, Volkmer *et al*., 2009, Lau *et al*., 2013) and archaeological (Koon *et al*., 2003, Pijoan *et al*., 2007, Piga *et al*., 2010) studies. These studies have provided indications of physicochemical changes (crystallisation and thermal decomposition) to bone during heat treatment (Rogers & Daniels, 2002, Schiegel *et al*., 2003). There are many conflicting views associated with the fundamental mechanisms and processes of these physicochemical modifications. For

example, it has been proposed that the organic matrix has a ‘shielding effect’ on the mineral during heat treatment of bone (section 4.3). Researchers have suggested that mineral crystallisation (growth of HAp crystals during heat treatment) cannot occur until the organic has been completely removed. Further, the confounding effects of cooling have not previously been considered, and therefore these studies cannot strictly provide a complete model of the physicochemical modifications associated with heated bone.

The fundamental processes and mechanisms associated with unheated bone including HAp nucleation, mineralisation (section 2.2.3) and *in vivo* HAp crystal growth (chapter 3) are also conflicting and not fully understood. HAp crystallite size and the organic content of unheated bone for instance have been reported to differ according to species. This has led many researchers to question the control mechanism of HAp crystallite growth during bone formation. Currently, there appears to be three schools of thought associated with this area of research. Firstly, a mechanical restriction provided from collagen fibrils has been reported. The second school of thought suggests macromolecules, such as proteins and citrate, bind to the HAp surface, consequently limiting crystal growth. Arguably this form of extrinsic control is currently the most conventional within the literature. The third and less explicit suggestion is an intrinsic form of control; associated with incorporation of certain ions, lattice disorder and crystal dissolution. These areas of research are discussed further in chapter 3. *In vivo* HAp crystal size control is an area of research which needs to be understood in order to develop a complete model of the physicochemical modifications to bone during heat treatment.

Certain research areas associated with unheated and heated bone are also controversial and are not fully understood. Consequently, the mechanisms associated with both unheated and heated bone are often assumed and ambiguous (elaborated in subsequent chapters). It is proposed that this is possibly due to the observational nature employed by many studies, as well as the complexity associated with bone as a material. For example, during heat treatment it is assumed the organic matrix restricts bone mineral crystallisation (Roberts, 2002, Trueman, 2004, Wang, 2010), discussed further in section 4.3. This is largely due to the observation that the complete combustion of the

organic matrix occurs prior to the crystallisation of the mineral component. However, the complete combustion of the organic has been shown to occur by 500 ^{o}C (Lozano *et al*., 2003), whilst the crystallisation of hydroxyapatite crystals begins at approximately 600 ^{o}C (Rogers & Daniels, 2002, Beckett *et al*., 2011). If the organic matrix provided this apparent 'protective barrier' (Etok *et al*., 2007), then one would expect mineral crystallisation to occur at approximately 500 ^{o}C. Furthermore, due to the nanocrystalline nature of bone mineral, refinement of X-ray diffraction data can be extremely complex, which can often lead to ambiguous results. A more in-depth consideration of the current issues and controversies within bone research, which arguably leave a major gap in knowledge within bone research, is provided in subsequent chapters (1-5) of this thesis.

The overall aim of this thesis was to provide a new insight into the fundamental processes and mechanisms associated with unheated and heated bone. This was achieved by focusing on three main areas of debate: *in vivo* HAp crystallite size control (chapter 3), the relationship between the organic and mineral components of bone during heat treatment and the confounding effects of cooling on the crystallisation and thermal decomposition of HAp after heat treatment (chapter 4). Further analysis was applied to consider solutions to current problems within bone research. This included developing a model to accurately estimate the temperature and time period at which bone specimens had been heated to (chapter 4) as well as species differentiation (discussed further in section 1.2.3). The effects of heating and cooling rates on the physicochemical changes to bone mineral during heat treatments were also investigated, which previous studies have overlooked. The novel approaches employed for this work challenged some of the current ideologies in bone research as well as moving forward this research area. Due to the fundamental nature of this research, it is proposed that the work presented in this thesis will be beneficial across a wide range of disciplines including biomedical research, forensic science and archaeology.

1.1 Thesis Outline

This thesis presents the results of an investigation employed to provide a new insight into the fundamental processes and mechanisms associated with unheated and heated biological HAp. Application of the research and rationale for carrying out this work is considered in chapter 1. A variety of analytical techniques were adopted including X-ray diffraction (XRD), Fourier transform infra-red spectroscopy (FTIR), differential scanning calorimetry (DSC), laser ablation inductively coupled plasma – mass spectrometry (LA-ICP-MS) and colourimetry. The fundamental principles and the rationale for using these techniques are introduced in chapter 5.

The general structure and composition of bone is outlined in chapter 2, whilst a more in-depth consideration of primary *in vivo* HAp crystallite size control mechanisms and response of bone to heat treatment are provided in chapters 3 and 4 respectively. Summary of the literature and the aims and objectives associated with the work presented in this thesis, are detailed in chapter 6. Results of this study are presented in chapter 8, from size control mechanisms of *in vivo* HAp crystals, through to the growth of HAp crystals during heat treatment and finally to thermal decomposition of HAp crystals at high temperatures. The results are discussed in chapter 9 within the context of general characteristics of unheated HAp specimens and heated bone specimens. A novel approach employed to determine crystallisation kinetics of bone mineral is discussed, whilst the confounding effects of cooling (discussed further in chapter 4) are considered for the first time. Furthermore, the results are discussed in terms of applications of the research to current issues. The research is summarised in chapter 10 along with recommendations for future work and consideration of how this research has contributed to scientific knowledge.

1.2 Application of Research

1.2.1 Biomedical Applications

The thermal behaviour of bone is of great importance within biomaterials and orthopaedics. As discussed in chapter 4, bone mineral microstructure is particularly sensitive to temperature, which can alter the mechanical, ion storage and osteoconductive function of bone (Rogers & Daniels, 2002). High temperature processing of bone material is frequently used for medical, biomaterial and orthopaedic applications. Medical applications, such as allo- and xeno- graft replacements, frequently use high temperature processing of bone material to produce HAp bioceramics (Murugan *et al.*, 2003, Yan *et al.*, 2008, Lau *et al.*, 2013). High temperature treatment of bone is also used for scaffold development in biomaterial research (Ivankovic *et al.*, 2009, Emadia *et al.*, 2010). Methods often utilised in orthopaedic surgery result in significant temperature increases in bone. During drilling temperatures may reach 300 ^{o}C, causing osteonecrosis (Hillery, 1999) whilst thermal denaturing of tissues by lasers, can result in temperatures of up to 800 ^{o}C (Pratisto *et al.*, 1996, Yilbas *et al.*, 1996). Furthermore, radiofrequency ablation has recently been used to treat single bone metastases, which can also thermally influence bone (Volkmer *et al.*, 2009). Understanding the fundamental processes and mechanisms associated with physicochemical changes to bone mineral due to the application of heat will provide a new insight into these particular areas of research and applications, as well as help future development of these biomedical methods.

1.2.2 Archaeological Applications

Archaeological bone is often found during excavations. Among archaeological remains, bone specimens and objects made from bone material have been reported which Reiche and Chadefaux (2009) argue can largely contribute to the understanding of ancient

societies. In many instances, specimens which show indications of being subjected to some form of heat treatment have been discovered (Bennett, 1999, Pijoan *et al.*, 2007, Yravedra & Uzquiano, 2013). This has resulted in an increasing number of studies which have concentrated on the effect of heat treatment on bone in order to contextualise the conditions of a burning event (Schiegl *et al.*, 2003). These studies have allowed cooking (Koon *et al.*, 2003) and funeral practices (Grupe & Hummel, 1991, Piga *et al.*, 2010) of our ancestors to be further understood as well as providing information on cannibalism (Fernández-Jalvo *et al.*, 1999, Cáceres *et al.*, 2007). Unfortunately, this area of research is often limited as burnt bone is frequently rejected as suitable material for isotope analysis due to changes to both the organic and mineral components of bone during heat treatment (Munro *et al.*, 2007 & 2008, Schurr *et al.*, 2011). A new insight into the physicochemical modifications to bone during heat treatment could potentially allow a more formative determination of the burning event. With this in mind, the ability to identify how long an archaeological bone specimen may have been subjected to heat treatment for and at what temperature could prove invaluable.

Currently anthropologists and archaeologists use techniques including visual inspection (Devlin & Herrmann, 2008), bone colour (Shipman, 1984), fracturing of bone due to fire temperature (Herrmann & Bennett, 1999), macroscopic modifications to bone (Solari *et al.*, 2013) and the presence of soft tissues (Ubelaker, 2009) to characterise burning events in terms of temperature and period of heating. However, these techniques can often be complicated and ambiguous (Thompson, 2005). By adopting a fundamental approach to investigate the physicochemical changes to bone during heat treatment, it may be possible to provide a new insight into how to accurately estimate both the temperature and period of time (dwell period) a bone specimen has been heated. This is not currently available and in many instances the temperature at which bone has been heated is determined without consideration for the dwell period. The need for a time/ temperature model for heated bone is prevalent in archaeological and forensic science literature, in which contextualising the burning event may aid in determining certain practices of our ancestors as well as complementing other forensic evidence.

1.2.3 Forensic Science Applications

In an attempt to prevent identification of a victim, or disguise the cause of death of a victim and/or to destroy relevant forensic evidence such as blood, semen and saliva, fire is often used (Correia & Beattie, 2002, Abrams, 2008). Due to the threat of being 'caught in the act', accelerants are frequently used by criminals. The use of accelerants does not significantly increase the temperature of a fire in comparison to non-accelerated fires in the same surrounding, as often erroneously reported, but increases the rate at which the fire reaches maximum temperature (Stauffer *et al.*, 2007). The ability to calculate the temperature and the period of time a bone specimen has been heated, could potentially allow a burning event to be contextualised. For example, bone specimens heated in the presence of an accelerant may show indications of being burnt at a faster rate than bone specimens burnt without the use of an accelerant. Thus, the amount of time the bone has been heated to at maximum temperature would be significantly longer if accelerants are used. Contextualising a burning event will not only be invaluable in establishing criminal intent (with the use of an accelerant for example) but may also be used to confirm or refute witness statements and alibis.

Further, forensic cases and mass disaster events such as bush fires, terrorist attacks, earthquakes and transport accidents (such as aircraft, train and car), often leave forensic practitioners the difficult task of identifying human skeletal remains. This task has proven much more difficult with regards to burnt human remains (Berketa, 2013). In most instances, physical evidence such as visual identification, documents, tattoos and clothing is destroyed, leaving forensic experts dependent upon DNA, fingerprint and dental analysis (Cattaneo *et al.*, 1999, Prahlow 2010). Unfortunately, analysis of this type is not always possible. Fingerprints are unattainable from severely burnt victims due to the destruction of soft tissue (Schwark *et al.*, 2011) whilst dental analysis is dependent on the presence of the cranium and sufficient ante-mortem dental records (Pretty, 2007). Consequently, DNA typing is often used as the primary diagnostic tool for identification of mass disaster victims (Olaisen *et al.*, 1997, Brenner and Weir, 2003, Meyer, 2003).

In extreme temperatures, DNA is often extracted from robust material such as bone or teeth, due to the absence of hair, nails, soft tissue. However, when subjected to extreme temperatures, bone DNA is denatured (Von Wurmb-Schwark *et al.* 2004, Senn & Weems, 2013). Recent research has suggested the probability of obtaining a nuclear DNA profile from bone decreases as the temperature of the burning event exceeds 200 ^{o}C (Fredericks, 2011, Fredericks *et al*., 2012). Due to such compromised samples, unsuccessful DNA typing of bone subjected to heat treatment is common (Rainio *et al.*, 2001, Nelson & Melton, 2007, Schwark *et al.*, 2011). This was highlighted by the lack of success in identifying victims of the Australian bushfires in 2009, where temperatures were thought to exceed 1000 ^{o}C (Turney, 2010). Furthermore, severely burnt bone material is highly susceptible to contamination with external DNA (Schwark *et al.*, 2011). Unsuccessful or 'mixed' DNA profiles consume valuable resources. In addition, remains may be visually assessed as being unsuitable for DNA analysis due to the severity of charring, and consequently may not be tested. Heinrich *et al.* (2009) found a correlation between the severity of charring/bone colour and obtaining a successful DNA profile. In charred bones (black), DNA was usually highly degraded and in some instances no nuclear DNA remained, leaving only mitochondrial DNA. Burnt bones of blue/ grey colour lead to sporadic successful profiling, whilst it was almost impossible to obtain a DNA profile from burnt bone specimens which were white in colour (*ibid*). Understanding the physicochemical changes to bone mineral could potentially provide a new insight into this area of research, and may aid future studies into DNA extraction from heated bone. Potentially, investigation of the physicochemical changes to bone prior to DNA extraction may provide a cheap, reliable method to determine whether material should be rejected or accepted for DNA analysis.

The problem of identifying human bone from other species was addressed by Beckett *et al.* (2011). This research discovered heated bone can be differentiated according to species through the observation of several chemical characteristics of bone mineral using X-ray diffraction (XRD). Crucially, human bone was found to be significantly different to a wide range of other species. Subsequent research within this area is conflicting (Piga *et al.*, 2013). Differences in the opinion of Beckett *et al.* (2011) and Piga *et al*. (2013) may be due to the material employed for this research. Beckett *et al*. (2011) utilised fresh, unheated contemporary bone specimens for their research whilst

Piga *et al*.(2013) utilised both contemporary and archaeological (up to 900,000 years old) specimens. Previous studies have shown that diagenetic processes can alter both the organic and mineral microstructure of bone due to microbiological attack (Hedges, 2002). Physicochemical differences between human bone and other species was possibly not observed by Piga *et al*. (2013), due to confounding differences between the initial state of fresh, defleshed bone and dry, archaeological bone. This was not considered by the authors.

Analytical solutions to identify human bone could prove invaluable for legal cases. This was highlighted as recently as 2013 during the trial of Mark Bridger, who was found guilty of the abduction and murder of five year old April Jones, and consequently sentenced to life imprisonment (Judiciary England and Wales, 2013). Small fragments of burnt bone were found within the fireplace at Bridger's home, however due to the compromised nature of the material, DNA profiling was unsuccessful. Consequently, anthropologists were required to determine whether these bone specimens were of human origin or not. Regrettably, their expert opinions were conflicting (BBC News, 2013). This case highlights the need for further research into the physicochemical modifications to bone during heat treatment in order to determine whether species differentiation is possible using XRD. Further research within this area is also required in order to provide a more fundamental understanding of the physicochemical differences between human bone and other species, as reported by Beckett *et al.* (2011).

Chapter 2: GENERAL BONE STRUCTURE[1] AND COMPOSITION

Bone, which is a living organ, is not a solid entity but is made from a hierarchy of structures (Rho *et al.*, 1998) (Figure 2.1). The various structures enable bone to perform a wide range of functions such as structural support, protection and storage of healing cells, and mineral ion homeostasis (*ibid*). This chapter will detail the structure[1] and composition of bone from the macro- to nano-structure.

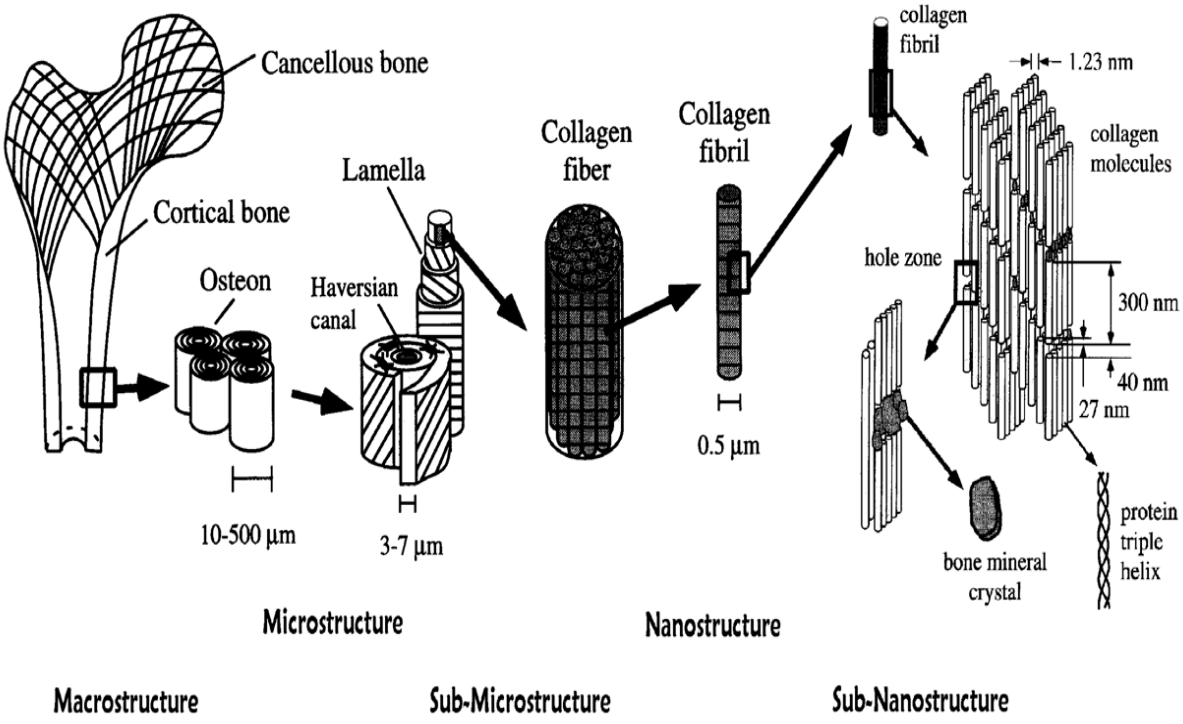

Figure 2.1 The hierarchal structure of bone from the macro- to nano-structure (Source Rho *et al.*, 1998)

[1] In bone chemistry, structure is used to define architectural and morphological properties of bone whilst crystallographic structure is often employed by crystallographers to describe the atomic arrangement of a material. In this chapter, both these terms are employed. In section 2.1, structure is employed to describe the physical architectural properties of bone whilst in section 2.2 this term is employed to define the crystallographic structure of HAp i.e. the atomic arrangement of HAp crystals.

2.1 General Bone Structure

2.1.1 Bone Macrostructure

Mammalian adult bone exists in two distinct forms, trabecular and cortical (Figure 2.2). The composition of trabecular and cortical bone is similar; however their architectural structure differs due to the arrangement of the mineral and organic components at the macro level (Currey, 2002).

Trabecular bone also known as cancellous bone is very porous and lightweight and has a ‘honeycomb’ appearance (Currey, 2002). This is a result of the rapid mineralisation process during which roughly spherical centres of calcium phosphate crystals randomly impregnate the collagen and surrounding substrate (Wojnar, 2010). As these mineralisation centres spread, they adjoin and frequently leave ‘mineral – free’ spaces (Currey, 2002). Consequently, trabecular bone is very porous although highly mineralised. Trabecular bone is most commonly found under protuberances where tendons attach, in the vertebral bodies, in the ends of long bones, in short bones, and sandwiched within flat bones (Parker, 2007).

In comparison, cortical bone, also known as compact bone (Figure 2.2), is denser, as it is formed at a much slower rate, and is more precisely arranged than trabecular bone (Currey, 2002). In cortical bone, collagen fibrils and calcium phosphate crystals are arranged into sheets of differing thickness (Currey, 2002). As a result, the final degree of mineralisation of cortical bone is considerably less than trabecular bone. Cortical bone is found in the walls of bone shafts and on external bone surfaces (Currey, 2002).

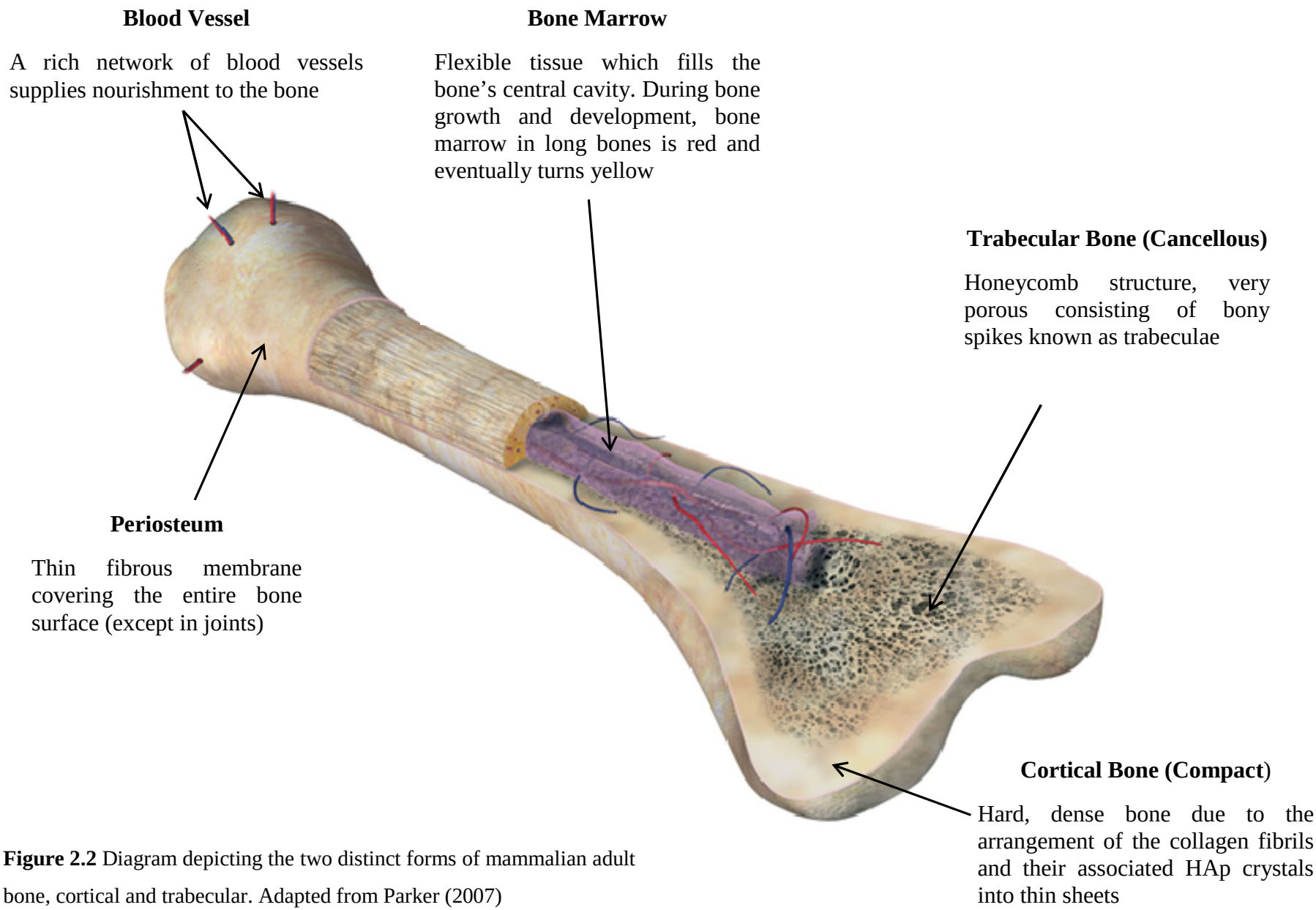

Figure 2.2 Diagram depicting the two distinct forms of mammalian adult bone, cortical and trabecular. Adapted from Parker (2007)

2.1.2 Microstructure of Bone

Trabecular and cortical bone are very different at the micro level. Cortical bone is constructed of organised osteons known as Haversian systems (Martin & Burr, 1989) (Figure 2.3). Osteons are rod-like cells which during bone development are packed tightly in a circular formation. The central (Haversian) canal of the osteons contains blood vessels and nerves, and is surrounded by concentric layers of tissue termed lamellae (Parker, 2007). The blood vessels provide nutrients to the bone and remove waste products from the cells. In between the layers of lamellae, there are cavities known as lacunae that contain osteocyte cells (Bonucci, 2000). In contrast, trabecular bone does not contain true Harversian systems and instead consists of an irregular lattice of thin columns of bone termed trabeculae (Parker, 2007).

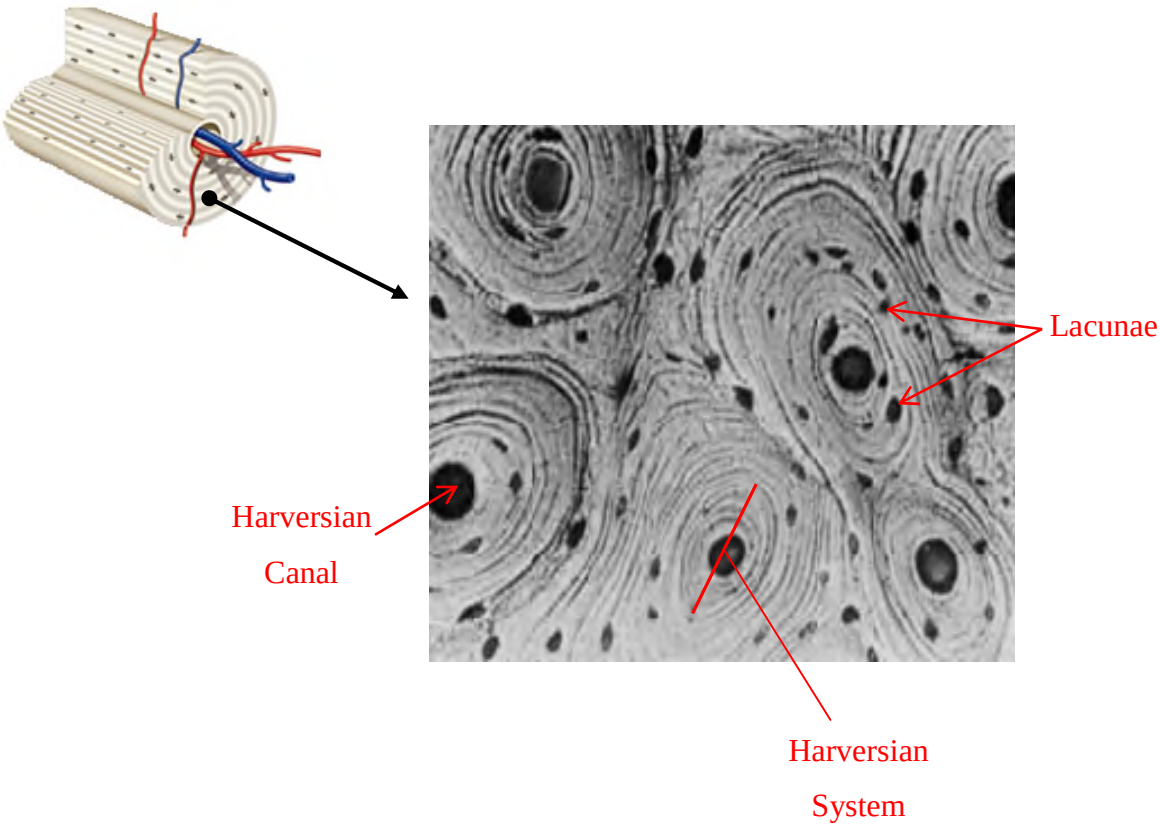

Figure 2.3 Microscopic view of osteons within cortical bone (Adapted from Parker, 2007)

2.1.3 Bone Nanostructure

At the molecular level there is little difference between the composition of trabecular and cortical bone. Bone is a nano composite material consisting of an organic matrix (20 – 30 wt. % for human bone) (section 2.2.1), which is impregnated by the mineral component (70 – 80 wt. % for human bone) (section 2.2.2) during bone formation and growth (Currey, 2002). The organic matrix is formed mainly from Type I collagen (90 wt. %) whilst the mineral component has been found to resemble nano calcium hydroxyapatite (HAp) (Olszta, 2007). In addition to these components, bone consists of other constituents such as water, non-collagenous proteins, blood vessels and living cells (Currey, 2002). HAp and collagen form the basic building blocks of bone and are arranged to form a hierarchy of structures from the macro- to nano-scale (Rho *et al.*, 1998) (Figure 2.1). As this thesis is concerned with observing the physicochemical changes to bone at the molecular level, HAp and collagen will be discussed in further detail.

2.2 Bone Composition

2.2.1 Organic Matrix: Collagen

Collagen is a fibrous protein found in all multi-cellular animals. The primary feature of a typical collagen molecule is its triple-stranded helical structure, in which three collagen polypeptide chains, termed α-chains, are wound around one another creating a 'rope like' structure (Woodhead – Galloway, 1980). Collagen is rich in both proline and glycine, which are essential amino acids required for the formation of the triple-stranded helix. The ring structure of proline stabilises the helical confirmation in each α-chain, whilst glycine, the smallest amino acid, is spaced at every third residue throughout the central region of the α-chain (*ibid*). The position of glycine allows the three helical α-chains to pack tightly together to form the final collagen superhelix. Type I collagen is

known as fibrillar collagen and once secreted into extracellular space, the collagen molecules assemble into higher-order polymers called collagen fibrils (Viguet-Carrin *et al.*, 2006). These are thin structures (10 – 300nm in diameter) and are many hundreds of micrometres long in mature tissues. In bone, Type I collagen is mineralised with calcium HAp crystals.

2.2.2 Mineral Matrix: Calcium Hydroxyapatite

Calcium hydroxyapatite (HAp), the crystallographic structural reference for bone, is a mineral which occurs naturally within the environment. Its most common occurrence is within the human body and has been identified as the main mineral phase of bone, teeth and urinary calculi (Elliot, 1973, Brown and Chow, 1976, Smith *et al.*, 1983, Olszta *et al.*, 2007). In recent years, there has been extensive research into synthetically producing this naturally occurring mineral for use as bone repair materials, forming the basis of bioactive ceramic research (Chang *et al.*, 1999, Ślósarczyk *et al.*, 2000, Combes & Rey, 2010). In this thesis, calcium hydroxyapatite is shortened to HAp. Biological and synthetic HAp specimens are differentiated throughout.

Stoichiometric HAp is a crystalline mineral which consists of phosphate (PO_4^{3-}), calcium (Ca^{2+}) and hydroxyl (OH^-) ions (Kay *et al.*, 1964, Elliot, 1973, Rey *et al.*, 2009). The general unit formula for calcium HAp is $Ca_5(PO_4)_3(OH)$, however this is often written has $Ca_{10}(PO_4)_6(OH)_2$ to highlight that there are two formula units in the crystallographic unit cell (Elliott, 1973). As shown in Figure 2.4, the crystal lattice of calcium HAp is dominated by phosphate ions which are stacked in a closely packed arrangement. The tetrahedral sites for the six phosphate ions are each in 4 fold coordination with the oxygen ions (Gross *et al.*, 2002). Interstices (holes) are observed between phosphate ions. The arrangement of some of these interstices creates channels through the structure, known as phosphate interstices. Two crystallographically different Ca^{2+} atoms exist in HAp (Elliott *et al.*, 2002). Six of the calcium ions are arranged in such a way that they form a calcium 'channel site' along the c-axis (referred to as the c-axis channel site or anion channel). These are known as Ca^{2+} (II) ions and are

found within interstices that are not within the phosphate channel sites (Beckett, 2009). The other four calcium ions, known as Ca^{2+} (I) ions, are found within the phosphate interstices. Hydroxyl ions (OH^-) are located within the c-axis channel site (partially formed by the Ca^{2+} (II) ions).

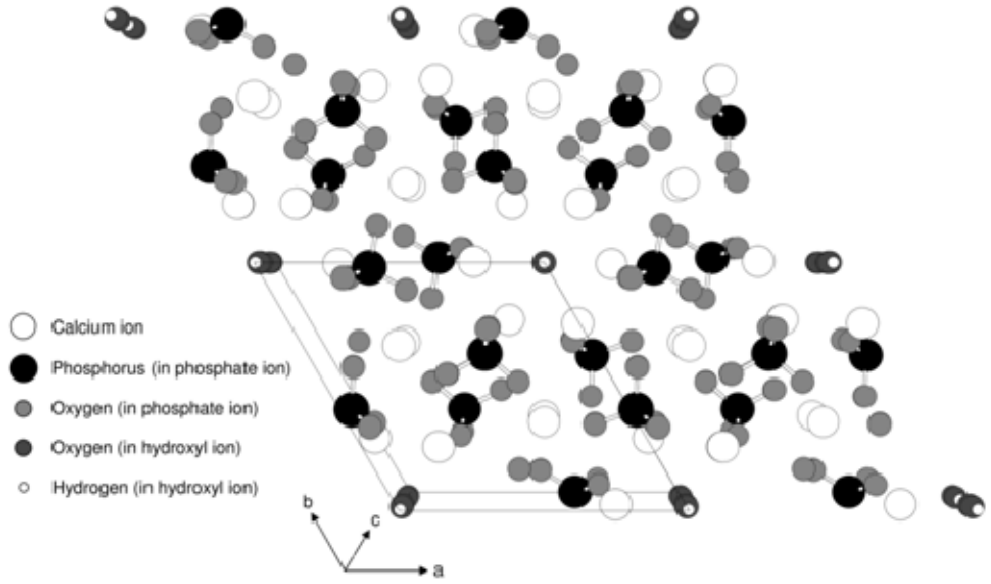

Figure 2.4 Crystal lattice structure of stoichiometric HAp. The crystal lattice is viewed down the 'c' axis and shows two unit cells along each axis: 'a', 'b' and 'c' (Beckett, 2009). Atoms not drawn to scale for clarity.

As mentioned, calcium HAp is considered only as a reference for bone mineral as the composition of biological hydroxyapatites are not fixed (Elliott *et al.*, 2002). Biologically formed HAp found in bone is particularly accommodating to chemical substitutions due to ion site vacancies provided by channel sites (discussed in the previous section), which enables ion exchange. Ion exchange is aided by two main attributes of the HAp crystals. Firstly, due to their nano size, biological HAp crystals have a large surface area to volume ratio, which aids ion migration (Palmer *et al.*, 2008). Secondly, HAp crystals are thought to be surrounded by a hydrated surface layer which contains, in varying concentrations, a wide variety of mineral ions and charged groups of proteins (Neuman & Weikel, 1955, Rey *et al*., 2007), as shown in Figure 2.5.

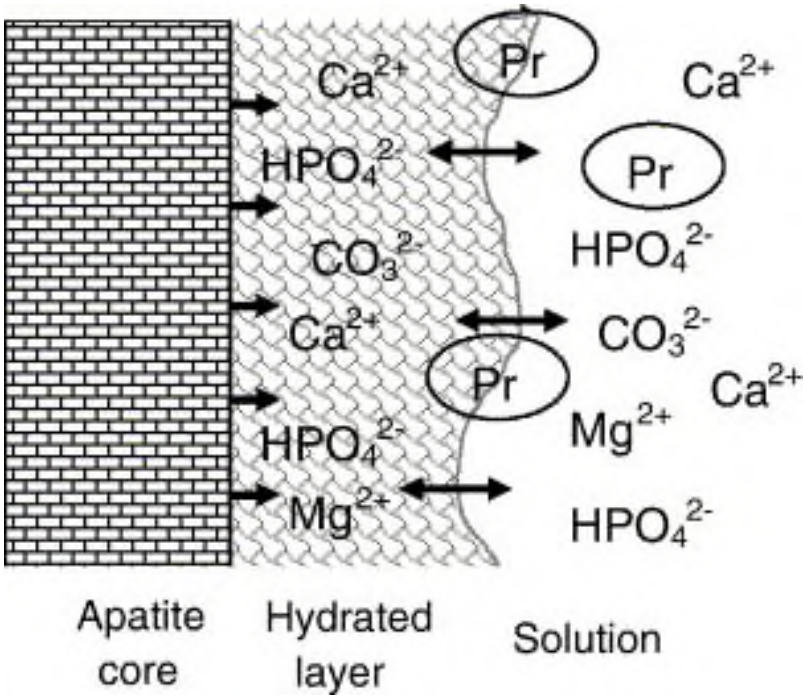

Figure 2.5 Diagrammatical representation of the solid: solution interface of HAp crystals, divided into four sub groups; the HAp crystal lattice (interior), the crystal surface, the hydrated layer which surrounds the crystal and the bulk solution (Rey *et al.*, 2007). It is important to note that this hydration layer is not a universally accepted view of all mineral surfaces, and is in fact debated within bone mineral research.

Fundamentally, biological HAp differs from stoichiometric calcium HAp due to its deficiency in calcium and hydroxyl ions (Rey *et al.*, 1995, Loong *et al.*, 2000, Cho *et al.*, 2003, Pasteris, 2004). In addition to this, due to constant ion migration, biological HAp contains a variety of ions including carbonate, sodium, magnesium, potassium, fluoride and chloride (Elliot *et al.*, 2002, Shea & Miller, 2005, Rey *et al.*, 2009). Ions are incorporated through ion substitutions, ion site vacancies and interstitial ions (Neuman & Weikel, 1955). It is important to note that any chemical exchanges must fulfil an overall neutral charge balance, which occurs through exchange of other ions (Wopenka & Pasteris, 2005). Studies have suggested incorporation of some extraneous ions (ions not associated with stoichiometric HAp), in particular carbonate can cause crystallographic structural disorder and lattice strain within bone mineral (Bigi *et al.*,

1995, Li *et al*., 2007, O'Donnell *et al*., 2008, Yao *et al*., 2009, Delgado-López, 2012, Ghadimi *et al*., 2013). This concept is discussed further in chapter 3. Strain in HAp crystals arises from ionic substitutions and vacancies which distorts the regular unit cell pattern, thus decreasing the long range order of a crystallite. A detailed account of strain is provided by Wopenka & Pasteris, (2005). Structural disorder and lattice strain is discussed further in chapter 3.

As early as 1965, LeGeros recognised that biological HAp specimens contain a substantial amount of carbonate and later stated carbonate 'is the chief foreign ion in biological apatites' (LeGeros *et al.*, 1971). Bone and dentin for example contains between 5 -6 wt. % carbonate, whilst enamel contains between 2 – 4 wt. %. (LeGeros, 1981, Koch *et al.*, 1997, Pasteris *et al.*, 2004, Shi *et al.*, 2005, Reyes-Gasga *et al.*, 2012). Early studies established carbonate ions can occupy two non-equivalent sites within the calcium HAp lattice (Emerson & Fisher, 1962, Elliott, 1962, Baxter *et al.*, 1966, LeGeros *et al.*, 1969), now commonly referred to as A or B type carbonate substitution (Rey *et al.*, 1989, Feki *et al.*, 1991). 'A' and 'B' type carbonate was first introduced in 1938 by McConnell, a geologist who studied the release of carbonate during hydrochloric acid (HCl) dissolution of apatites (Wopenka & Pasteris, 2005). McConnell observed two distinct optical properties when different apatites were treated with HCl, which he termed A and B type. McConnell did not propose the exact location of the carbonate ion within the apatite lattice. Due to several subsequent studies, it is now commonly accepted carbonate ions which occupy the tetrahedral site due to substitution with phosphate ions, is 'B-type carbonate substitution' (Rey *et al.*, 1989, Rey *et al.*, 1991, Astala & Stott, 2005, Danilchenko *et al.*, 2005). Carbonate ions which are substituted for hydroxyl ions found in the 'c' axis channel site are commonly referred to as 'A – type carbonate' (*ibid*). Carbonate substitution alters the atomic structure and general structure formula of HAp as shown in equation 2.1 (Wopenka & Pasteris, 2005).

A type	$Ca_{10}(PO_4)_6CO_3$	
B type	$Ca_{10-x}[(PO_4)_{6-2x}(CO_3)_{2x}](OH)_2$	
A/B type	$Ca_{10-x}[(PO_4)_{6-2x}(CO_3)_{2x}]\ (CO_3)$	**(2.1)**

It is generally accepted that carbonate preferentially substitutes for phosphate ions (B-type substitution) in bone (Landi *et al.*, 2003), whereas the occurrence of A-type carbonate is disputed (Elliott, 2002 as cited in Wopenka & Pasteris, 2005). This is possibly due to the knowledge that A-type carbonated HAp is synthesised at temperatures exceeding 800 ^{o}C, whereas B-type carbonated HAp can be precipitated from solution at much lower temperatures (< 100 ^{o}C) (Rey *et al.*, 1989, Penel *et al.*, 1998, Gibson & Bonfield, 2002, Landi *et al.*, 2003, Frank-Kamenetskaya *et al.*, 2011). Many studies have shown that biological HAp specimens are typically B-type carbonated apatites which contain a small amount of A-type carbonate (Rey *et al.*, 1989, Rey *et al.*, 1991, Miller *et al.*, 2001). Based on results from synthetically produced HAp studies, carbonate substitutions are known to cause physical and chemical changes to the properties of calcium HAp. Changes to lattice parameters, dissolution, lattice strain, crystal morphology, overall crystallite size and thermal decomposition mechanisms have been documented (LeGeros *et al.*, 1967, Baig *et al.*, 1999, Shi *et al.*, 2005, Pasteris *et al.*, 2007). Due to their structural differences, these changes will differ depending on the type of carbonate substitution. For example, A - type substitution, where the larger planer CO_3 group is substituted for a smaller linear OH group, causes an expansion in the '*a*' axial lattice parameter length and a contraction in the '*c*' axial length, as shown in Figure 2.6. B - type substitution, where the smaller planar CO_3 group is substituted for a larger tetrahedral PO_4 group, has the opposite effect (LeGeros, 1969, Nelson & Featherstone, 1981). In addition to A- and B - type carbonate, many spectroscopic studies have also reported the presence of carbonate ions on the crystallite surface, often termed labile carbonate (Rey *et al.*, 1989, Paschalis *et al.*, 1996, Boskey *et al.*, 1998, Camacho *et al.*, 1999, Miller *et al.*, 2001)

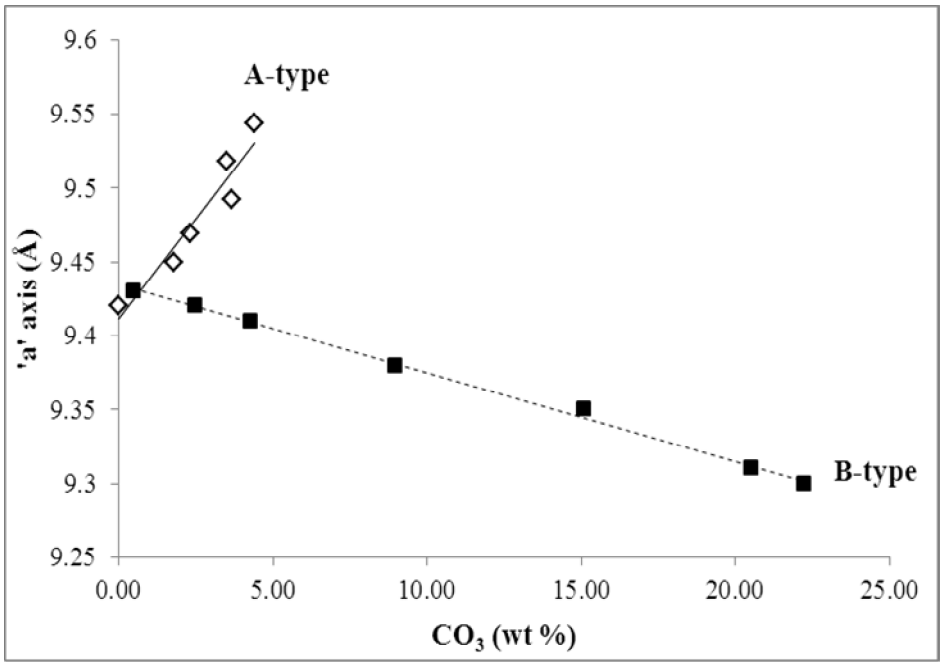

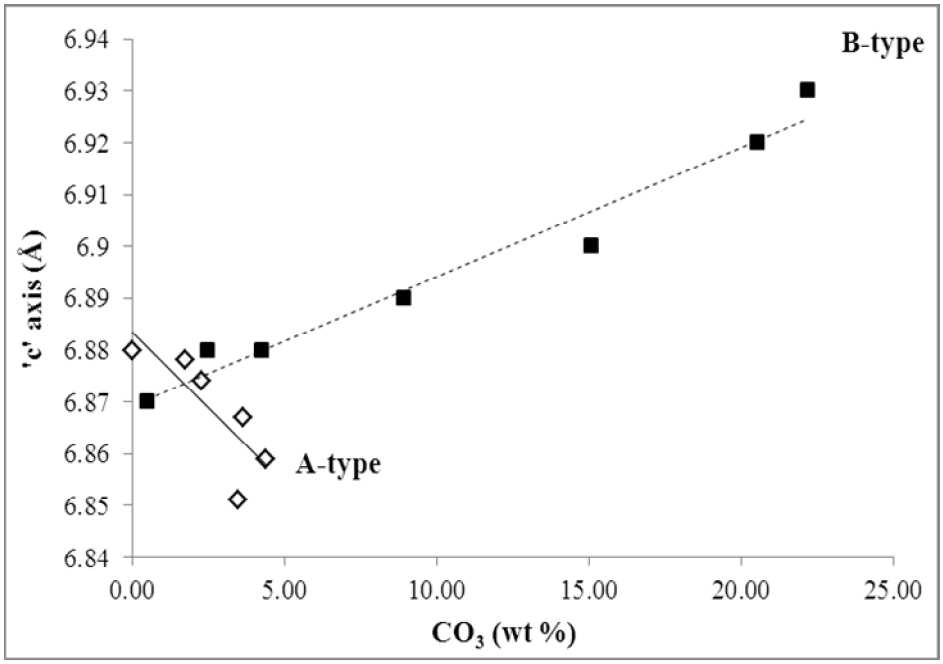

Figure 2.6 Lattice parameters of synthetic A and B type carbonated calcium HAp plotted against amount of carbonate (wt. %). Graphs constructed from lattice parameters values taken from LeGeros *et al.* (1969). For completeness, lattice parameter and wt. % carbonate values are tabulated in appendix A. Errors were not reported by LeGeros.

Information on the crystallographic structure of both biological and synthetic HAp has been extensively studied using X-ray diffraction (XRD) (Bonar *et al.*, 1983, Handschin & Stern, 1992, Rogers & Daniels, 2002, Boskey, 2003, Hiller *et al.*, 2003, Landi *et al.*, 2003, Lin *et al.*, 2004). Stoichiometric calcium HAp has characteristic atomic (1.67, 10 atoms of Ca per unit cell/ 6 atoms of P per unit cell) and weight (2.16, 39.9 $gmol^{-1}$ of Ca/ 18.5 $gmol^{-1}$ of P) ratios of calcium to phosphorus (Young, 1975). Although there is an agreement on the atomic and weight ratio of calcium to phosphorus for stoichiometric HAp, the unit cell space group and consequently the unit cell dimensions (lattice parameters) are not clear (Calderin *et al.*, 2003). Two kinds of crystallographic structure have been reported for synthetic HAp. The structure observed is dependent on the preparation techniques employed and is influenced by stoichiometry, temperature and pressure (*ibid*). Consequently, the general crystallographic structure of synthetic and biologically formed calcium HAp is reported as hexagonal with a $P6_3/m$ space group, with lattice parameters of a= b = 9.432 Å, c = 6.881 Å, and $\gamma = 120^{o}$ (Posner *et al.*, 1958) or monoclinic with a $P2_1/b$ space group with lattice parameters of a = 9.421 Å, $b = 2a$, c = 6.881 Å, and $\gamma = 120^{o}$(Elliot *et al.*, 1973, Haverty *et al.*, 2005).

Space groups are described in terms of symmetry and the monoclinic structure assumes ordering in the orientation of the hydroxyl ions (Calderin *et al.*, 2003, Ma & Liu, 2009). As discussed, biologically formed HAp does not have a fixed chemical composition due to constant ion migration, which is known to induce disorder and lattice strain in the crystals (Wopenka & Pasteris, 2005). This includes disorder in the hydroxyl ion channels (Elliott, 1969). Symmetry associated with the hexagonal space group accommodates for strain and disorder caused by ion site vacancies, ion substitutions and interstitial ions, whereas the monoclinic form is destabilised by ionic substitutions (Elliott *et al.*, 2002). Consequently, many researchers employ the hexagonal space group configuration when dealing with HAp, especially biologically formed HAp (Rogers & Daniels, 2002, Panda *et al.*, 2003, Reyes-Gasga *et al.*, 2012).

2.2.3 Bone Mineralisation

The precise formation mechanism for the nucleation and growth of bone HAp crystals, termed mineralisation, is heavily debated. One theory which seems to dominate the literature is the formation of HAp from a precursor in the form of an amorphous calcium phosphate phase (Johnsson & Nancollas, 1992, Weiner, 2006, Beniash *et al.*, 2009). In 1970, Eanes and Posner suggested a two stage process for the formation of HAp. In the first stage, it was suggested dissolution of non-crystalline calcium phosphate leads to the formation of colloidal HAp particles by a diffusion controlled dendritic mechanism. During this rapid process, the average crystallite size remains constant until complete depletion of the non-crystalline precursor. In the second stage, the HAp crystals continue to grow by a process of consolidation, which occurs at the expense of smaller crystallites resulting in a reduced number of total crystals but a greater proportion of larger crystals. This process is commonly known as Ostwald ripening and relies on the principle that the equilibrium dissolution of crystals decreases with increasing crystallite size (Eanes & Posner, 1970).

Other theories propose that rather than the dissolution of a precursor mineral phase, highly phosphorylated, acidic, non-collagenous proteins act as nucleators of HAp. Osteocalcin, osteopontin, osteonectin and bone sialoprotein (BSP), the major phosphorylated proteins of mammalian bone are often identified as having a primary role in the initiation of mineralisation (Nagata *et al.*, 1991, Hunter & Goldberg, 1993, Roach, 1994, Ganss *et al.*, 1999, George & Veis, 2008). These calcium and phosphate binding proteins are thought to regulate the ordered deposition of the mineral matrix by controlling the amount and size of the HAp crystallites formed during mineralisation. Evidence for the role of these proteins in the nucleation of HAp is conflicting. Research carried out by Hunter & Goldberg (1993) for example reported that BSP may have a role in the nucleation of HAp whilst no accumulation of calcium and phosphate occurred in the presence of osteopontin. Conversely, a model simulation study questioned the role of BSP, stating that a stable nucleating template for the formation of orientated HAp was not possible in the presence of this protein (Yang *et al.*, 2010). The authors suggest the BSP nucleating motif is more likely to nucleate an amorphous

calcium phosphate cluster, which ultimately converts to HAp. Interestingly, rather than having a nucleating role during the formation and growth of HAp, a number of researchers have suggested proteins can inhibit the nucleation and growth of the crystals (Romberg *et al.*, 1986, Boskey *et al.*, 2002). The role of proteins in *in vivo* HAp crystal size control is considered further in chapter 3.

Although the exact nucleation mechanisms of bone mineral are not fully understood, there is a general consensus that bone HAp crystals are intimately and specifically associated with collagen fibrils (Marino & Becker, 1967, Lowestam, 1989 cited in Tampieri *et al.*, 2002, Wang *et al.*, 2012). This relationship is possibly best described by the Landis model (Landis *et al.*, 1996), which is based on ex situ observations of mineralising turkey tendon using high voltage transmission electron microscopy (TEM) and tomographic reconstruction imaging. The Landis model is widely accepted by many academics (Figure 2.7).

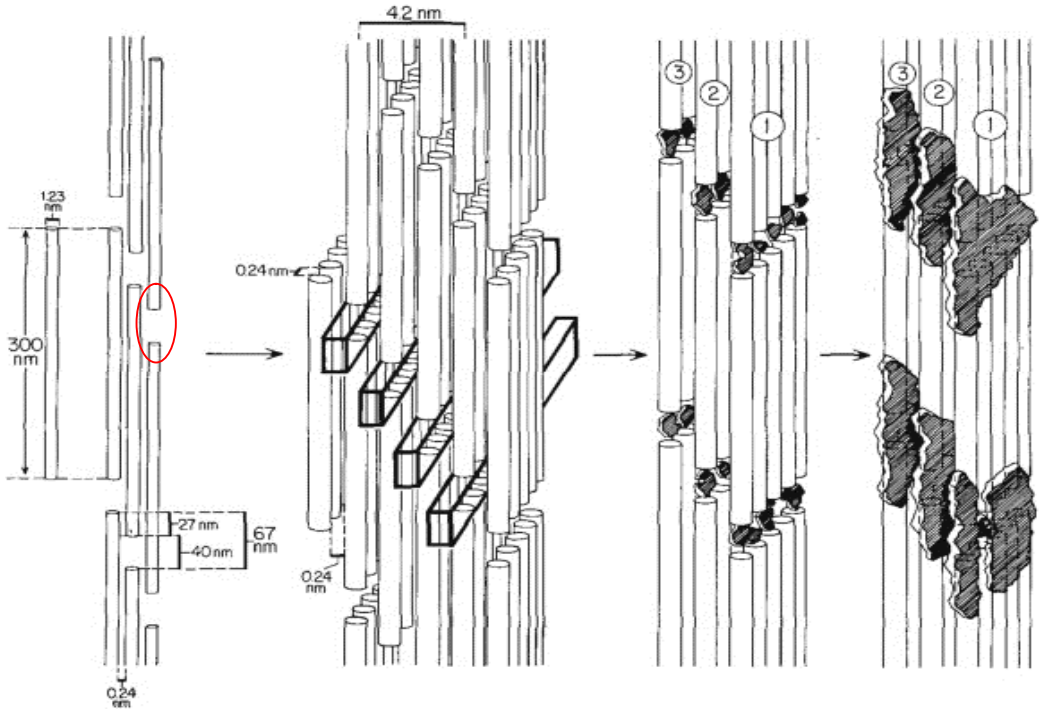

Figure 2.7 Schematic of the Landis model. The cylindrical rods illustrate collagen units which assemble into fibrils, leaving periodic ~40 nm gap regions (circled in red). HAp crystals are deposited into the gap regions, which then grow and expand forming sheets of poorly crystalline HAp between the collagen fibres.

The model suggests calcium HAp crystals preferentially form within the discrete spaces between the collagen fibrils, often referred to as the gap or hole regions. During mineralisation, HAp crystals impregnate the gap regions (~ 40 nm in height) and the mineral matrix continues to grow and expand forming sheets of poorly crystalline HAp between the collagen fibres. The plate-like mineral crystals are thought to grow with a specific crystalline orientation with the c - axes of the crystals roughly parallel to the long axes of the collagen fibrils (Currey 2002). This mineralisation process is thought to limit the primary growth of the mineral crystals, forcing the crystals to be discrete and discontinuous (Landis *et al.*, 1996).

2.3 Concluding Remarks

This chapter has deconstructed bone from the macro through to the nano-structure. This has demonstrated that bone is a complex composite material which consists of two main components, a mineral matrix and an organic phase, which are intimately associated with one another. Both of these phases were considered individually with calcium HAp identified as the structural reference for bone mineral whilst Type I collagen was identified as the primary component of the organic matrix. The chemical composition of bone mineral and the non-stoichiometric nature of biologically formed HAp (due to constant ionic exchanges) were discussed. Although the nucleation and growth mechanisms of bone mineral are debated, the location and orientation of the mineral crystals in relation to the organic matrix is understood through the Landis model. The role of proteins in *in vivo* HAp crystallite size control was briefly considered. For several years, the fundamental control mechanism of HAp crystallite size has been investigated with studies suggesting a variety of mechanical, extrinsic and intrinsic sources of control. This is discussed further in chapter 3.

Chapter 3: *IN VIVO* SIZE CONTROL OF HYDROXYAPATITE CRYSTALS

Hydroxyapatite crystallite sizes differ in a variety of biological systems including teeth, bone and urinary calculi (Kim *et al.*, 1995, Koch *et al.*, 1997, Currey, 1999, Pasteris *et al.*, 2004, Greenwood *et al.*, 2013, Reyes-Gasga *et al.*, 2012). Consequently, there have been various studies which have investigated the fundamental control mechanisms associated with biological and synthetic *in vivo* HAp crystal growth (Romberg *et al.*, 1986, Mann *et al.*, 1989, Moore *et al.*, 1991). Mechanical restrictions (collagen), extrinsic sources (proteins, citrate) and intrinsic sources (ionic substitutions, lattice strain, and crystal dissolution) have previously been individually considered as the regulatory mechanism of *in vivo* HAp crystal growth. Studies which have synthesised HAp in the presence of these molecules and ions have demonstrated that crystal growth is inhibited when compared to control samples. The remainder of this chapter provides a review of the current literature investigating control mechanisms of HAp crystal growth. Mechanical and extrinsic sources of control are considered before intrinsic sources of control.

3.1 Mechanical Restriction: Collagen

Due to the intimate association between HAp and collagen during bone formation (discussed in section 2.2.3), it has been suggested the organic matrix may limit the primary growth of HAp crystals (Boskey, 2003, Nudelman *et al.*, 2010, Wang *et al.*, 2012). Although studies which have suggested this mechanical restriction are largely observational; the research seems feasible when considering the mineral to organic ratio. Many biological HAp specimens, including bone from different species, enamel and dentin differ according to mineral and organic content (Figure 3.1) (Curry, 1999, Zioupos, *et al.*, 2005). Further, systems with a greater proportion of organic matrix tend to have smaller HAp crystals and vice versa (Rogers & Zioupos, 1999, Currey, 1999, Greenwood *et al.*, 2013)

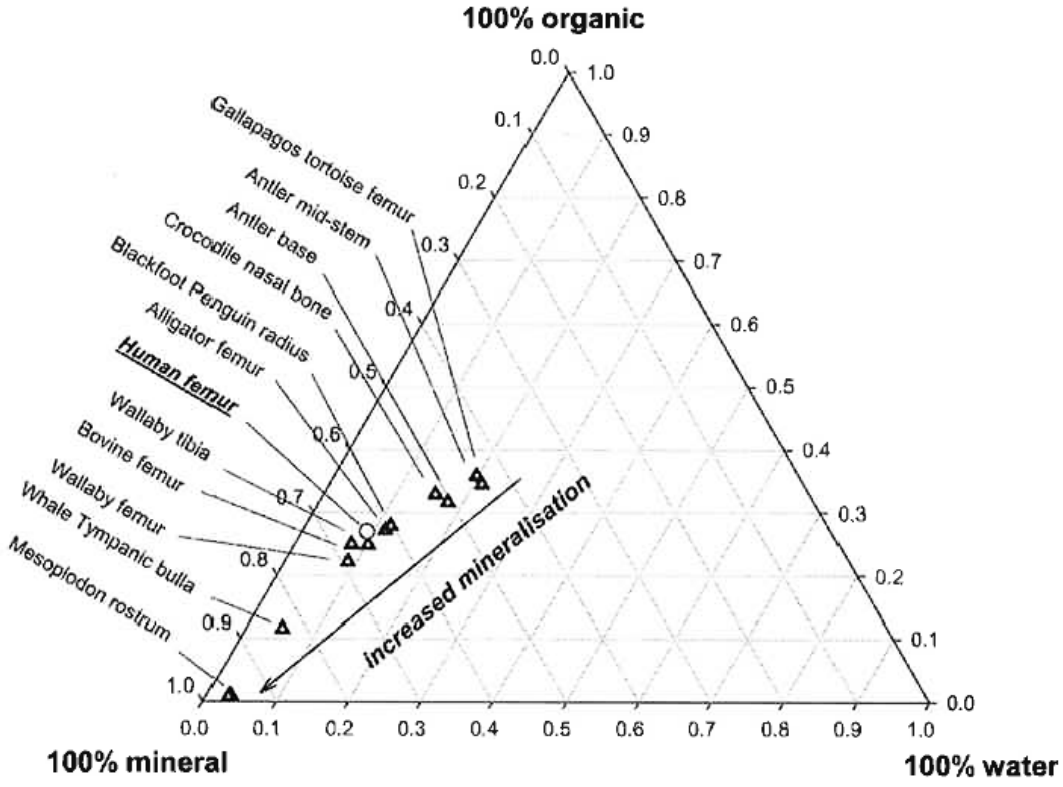

Figure 3.1 Tertiary diagram depicting the relationship and variation between the organic, mineral and water content (as a percentage) of bone obtained from several different species (Zioupos *et al.*, 2005).

3.2 Extrinsic Control: Proteins and Citrate

Amino acids (Chen *et al.*, 2012) and biological macromolecules such as carboxylate-rich proteins have also been reported to inhibit calcium phosphate crystal growth (George *et al.*, 1996, Gericke *et al.*, 2005). This research suggests surface absorption of proteins blocks potential growth sites. Other studies have suggested smaller citrate molecules ($C_6H_8O_7$) rather than proteins play a critical role in the mechanism of *in vivo* HAp crystal size control. This is due to the large number of carboxylates available for calcium binding provided by citrate in comparison to protein molecules.

Several studies have demonstrated smaller HAp crystal size are observed when synthesised in the presence of citrate in comparison to control samples (López –Macipe,

1998, Martins *et al.*, 2008). The regulatory role of citrate in unheated bone was perhaps not fully understood until the study by Hu and colleagues in 2010. This study for the first time quantified the amount of citrate present in avian, bovine and fish bone using advanced solid-state nuclear magnetic resonance (NMR) spectroscopy and distance measurements. The study suggested molecular control over the growth of HAp crystals. It was proposed ionised carboxyl groups of citrate bind to Ca^{2+} ions at the HAp crystal surface, at distances of 0.3 to 0.45 nm (Figure 3.2).

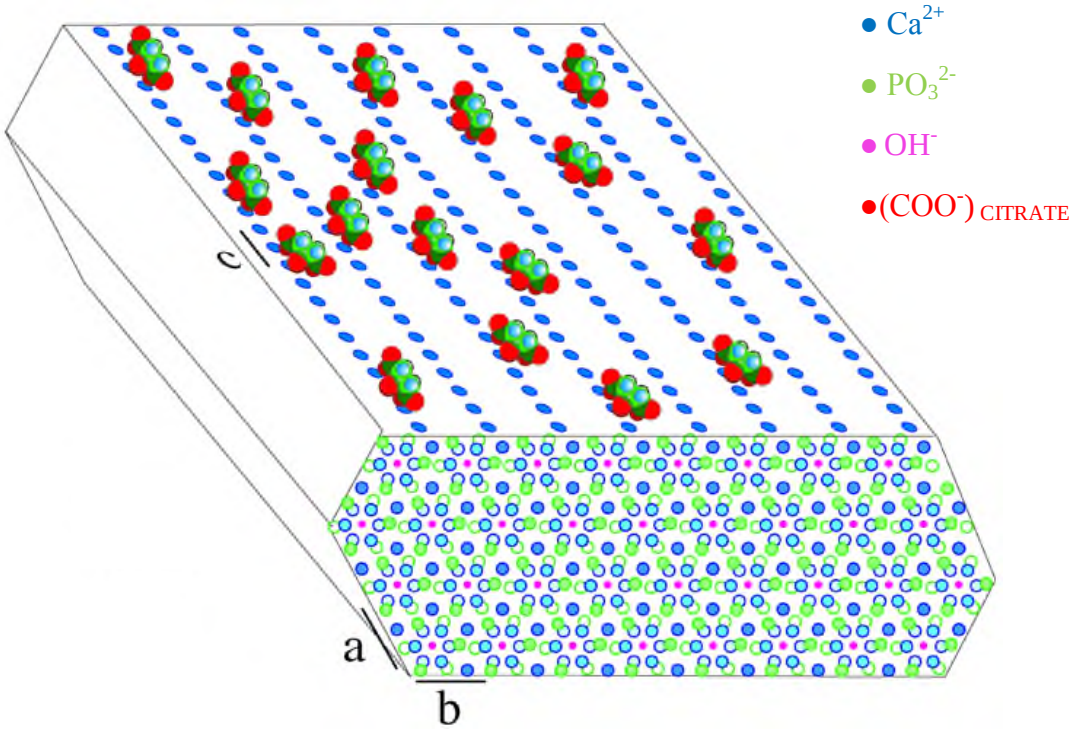

Figure 3.2 Schematic diagram of citrate bound to the apatite surface through interaction with hydroxyapatite calcium ions. Taken from Hu *et al.* (2010)

P

being incorporated into the crystal lattice. This is due to the relatively large size of citrate molecules in comparison to lattice ions, such as phosphate or hydroxide (López – Macipe, 1998, Rhee & Tanaka, 1999, Hempel *et al.*, 2004, Martins et al., 2008, Hu *et al.*, 2011). Once a citrate molecule occupies the HAp surface area, the growth of the

crystal in that crystallographic direction is inhibited (Xie and Nancollas, 2010, Hu *et al.*, 2011). It has also been proposed a negatively charged surface area is generated by surface-bound citrate molecules, which repels negatively charged phosphate ions and consequently limits further crystal growth (Martins *et al.*, 2008, Hu *et al.*, 2011) Thus, many studies have concluded that citrate restricts *in vivo* HAp crystal growth (Martins *et al.*, 2008, Hu *et al.*, 2011 & 2012). In the study by Hu *et al.* (2010), citrate was removed from unheated bone specimens using hot dilute acid treatment and replaced with ^{13}C labelled citrate in order to enhance the NMR signature. Unfortunately, the authors make little reference to the confounding effect of acid on the mineral microstructure (discussed in section 4.3) and the influence this could possibly have on the binding sites of the citrate molecules.

Van der Houwen *et al.* (2003) also reported that the presence of citrate during synthesis of HAp resulted in a lower crystallite size; however this phenomenon was related to imperfection of the crystal lattice rather than binding of the citrate to HAp crystal surfaces. The authors suggest interaction of citrate molecules with newly formed calcium phosphate nuclei can lead to incorporation of carboxyl ions into the OH^- and/ or PO_4^{3-} / phosphoric acid (HPO_4^{2-}) vacancies in the HAp crystal structure. Further, the author suggests substitution of carboxyl ions is likely to result in a greater lattice disorder and allow inclusion of impurities such as chloride (Cl^-) and sodium (Na^+) (*ibid*). The authors state highly disordered HAp structures may lead to a reduction in HAp crystal size but do not expand on this hypothesis further.

3.3 Intrinsic Control

3.3.1 Ion Substitutions

Studies which have incorporated extraneous ions into the lattice of synthetic HAp have also suggested that highly disordered structures may inhibit *in vivo* crystal growth. For

example, Li *et al.* (2007) demonstrated synthesis of HAp in the presence of strontium induced incorporation of phosphoric acid (HPO_4^{2-}) and a greater quantity of carbonate (CO_3^{2-}) in comparison to a control. This occurred when 15% of strontium was substituted for calcium. The authors suggest the partial substitution of strontium for calcium resulted in a larger lattice strain, which consequently allowed incorporation of more carbonate ions into the lattice structure. It is likely that this introduces further disorder into the system. The authors suggest this may cause a decrease in crystallite size but do not expand on this concept. Similar observations were also reported by O'Donnell *et al.* (2008), although when over 25% of strontium was substituted into the HAp lattice, the crystallite size increased. It is proposed that the observed increase in crystallite size with increasing percentages of strontium (>25%), is associated with how this additional ions are incorporated into the lattice structure. Substitution for certain ions or into lattice vacancies may reduce lattice strain thus leading to an increase in crystallite size. Other studies have shown incorporation of low concentrations of lead (Pb^{2+}) can also limit HAp crystal size (Mavropoulos *et al.*, 2002, Ghadimi *et al.*, 2013). Control of *in vivo* HAp crystal growth due to the incorporation of certain ions including (Mg^{2+}) and zinc (Zn^{2+}) is disputed, with studies suggesting crystal growth is inhibited due to lattice disorder (Bigi *et al.*, 1993, Fuierer *et al.*, 1994, Bigi *et al.*, 1995, Kanzaki et al., 2000). In contrast investigations by Cuisinier *et al.* (1995) and Mayer *et al.* (2000) reported a reduction in crystal defects, which the authors argue results in a decrease in structural disorder and larger crystallite sizes.

An abundance of studies have also investigated the influence of fluorine (F^-) on the chemical properties of HAp, in particular within tooth enamel. The dissolution of fluorapatite has been extensively studied within dental literature. The studies are consistent and suggest the presence of high concentrations of fluorine incorporated into the HAp lattice through substitution with OH^-, results in larger mean crystallite sizes and lower lattice strain in comparison to a control (Rodríguez-Lorenzo *et al.*, 2003). The large OH- ions occupy the centre of the calcium (II) triangle, which displaces the oxygen atoms approximately 0.3Å from the calcium plane (Kay *et al.*, 1964). As F^- ions are much smaller than OH^- ions, this substitution results in a reduction in the volume of the unit cell, the lattice becomes denser, and a decrease in dissolution due to the

electrostatic bond between fluoride and the adjacent ions (Aoba, 1997). Thus, substitution of fluoride into the HAp lattice structure decreases lattice strain.

In bone, as discussed in section 2.2.2, ion substitution between carbonate and hydroxide and/ or phosphate is prevalent, with carbonate constituting between 5 - 6 wt. % of bone. Over the years, carbonate substitution has received an overwhelming amount of attention, due to the dissolution rates associated with carbonated HAp. Various studies from a wide range of disciplines have synthesised HAp in the presence of varying concentrations of carbonate to observe changes to crystallite size and morphology and dissolution rates (LeGeros *et al.*, 1967, Baig *et al.*, 1999, Shi *et al.*, 2005, Pasteris *et al.*, 2007). The research is consistent, suggesting incorporation of carbonate results in decreased crystal size, changes to crystal morphology and an increase in dissolution (Yao *et al.*, 2009, Delgado-López, 2012). Some authors suggest this is due to lattice disorder and strain (Featherstone & Nelson, 1980); however this has not been developed further for biological HAp.

Lattice disorder and strain as well as crystallite size have previously been linked to dissolution rates of carbonated apatites (Baig *et al.*, 1996, Pan and Darvell, 2010). As early as 1945 Greenwald reported an increase in the dissolution of calcium phosphates in the presence of carbonate, which has been confirmed by subsequent studies (Baig *et al.*, 1996, Tang *et al.*, 2003, Shellis *et al.*, 1999, Tang *et al.*, 2004, Yao & LeGeros, 2010). These studies suggest HAp dissolution may be influenced by crystal size. Smaller crystallites, as observed for carbonated HAp, exhibit larger chemical reaction surface areas which lead to a greater dissolution rate. This is compared to fluorapatite in which larger crystal sizes are observed and the dissolution rate is reduced (Yao and LeGeros, 2010). Earlier research however disputed the role of crystallite size in the dissolution of apatites and instead reported that lattice strain (disorder) was the dominant factor controlling HAp crystal dissolution (Baig *et al.*, 1999).

Although dissolution and lattice strain of carbonated HAp has been correlated with HAp crystallite size, a direct *in vivo* HAp crystallite size control mechanism within biological systems has not previously been reported. However, the literature implicitly implies that ionic substitutions may induce lattice strain and increase HAp dissolution, which consequently limits *in vivo* HAp crystallite size. Thus, it appears both lattice strain and

HAp dissolution play a fundamental role in *in vivo* HAp crystallite size control. Further consideration of this concept is provided in the next section.

3.3.2 Dissolution and Lattice strain

The dissolution of HAp crystals are governed by a number of factors which can be considered from two aspects: the environmental conditions and the properties of the material (Zhang *et al.*, 2003). As the properties of biological apatites are variable and complex, many studies have concentrated on controlling the environmental factors during the nucleation and growth of synthetic HAp crystals. The type, concentration, pH, ionic strength and degree of saturation of buffered and unbuffered solutions have been investigated. As the environmental factors influence the properties of HAp crystals, many studies have suggested dissolution characteristics can be deduced from chemical composition, crystallinity, density and crystallite size of biological and synthetic HAp.

The properties and therefore the dissolution of HAp crystals are thought to be controlled by surface processes as well as by ionic substitutions from the hydrated surface layer of HAp crystals into the crystal lattice structure (Zhang *et al.*, 2003). During the nucleation of biological HAp, incorporation of foreign ions into the lattice structure results in an increase or decrease in dissolution, depending on the ionic substitution (Boanini *et al.*, 2010). For example, an increase in dissolution is caused by carbonate substitution (LeGeros & Tung, 1983). Carbonate ions have a planar triangular configuration, which do not fit perfectly into either PO_4 (a pyramidal arrangement) or OH^- sites. This gives rise to strain in the local atomic arrangement within the lattice. During the incorporation of carbonate, other hetero-ionic substitutions or vacancy formations are required in order to accommodate the created charge imbalance (Wopenka & Pasteris, 2005), which depending on the ionic substitution, may increase lattice strain. Conversely, substitution of F^- for OH^- ions decreases lattice strain and dissolution (LeGeros & Tung, 1983). With increased dissolution, it is proposed crystal growth rate is inhibited due to continuous, rapid dissolution of the material. Thus, it seems plausible that the primary

control mechanisms for *in vivo* HAp crystallite growth, is associated with ion substitutions which may induce strain (depending on the substitution) and increase crystal dissolution, which results in smaller crystallite sizes. Further, smaller crystals have a larger surface to area ratio, which is thought to accelerate dissolution. A summary of the proposed links between ionic substitution, lattice strain, dissolution and *in vivo* crystallite size are provided in Figure 3.3.

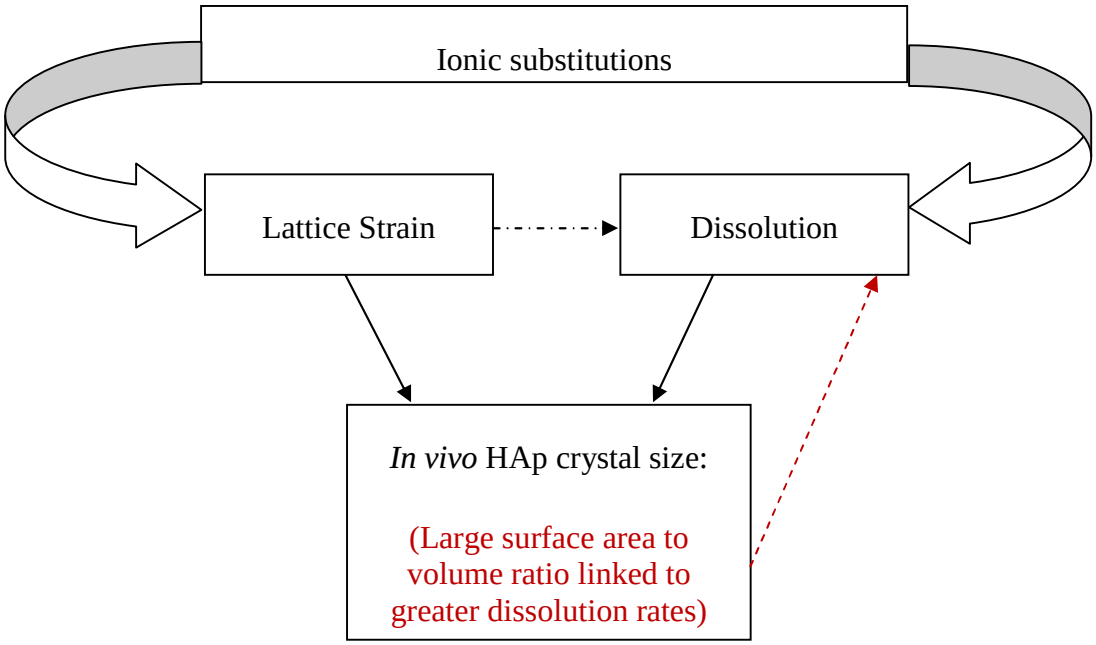

Figure 3.3 Diagram highlighting the proposed links between ionic substitutions, lattice strain, HAp dissolution and *in vivo* crystallite size. Ionic substitutions are thought to influence lattice strain and HAp dissolution. Both these parameters are indirectly linked and have been shown to influence *in vivo* HAp crystallite size. The larger surface area to volume ratio of small HAp crystals is thought to accelerate dissolution.

3.4 Concluding Remarks

In summary, three very distinct schools of thought with regards to *in vivo* HAp crystallite size control have evolved. The first suggests a mechanical restriction in the form of collagen. During formation, HAp crystals are deposited into gap regions in between collagen fibrils, which is thought to limit the primary growth of HAp crystals. The second suggests an extrinsic control mechanism that assumes carboxylate groups of organic macromolecules (proteins, citrate) bind to Ca^{2+} ions at the HAp crystal surface. This creates a negatively charged surface which limits HAp crystal growth. The third and less implicit, suggests an intrinsic control. Ionic substitutions, HAp dissolution and lattice disorder have all been reported to have an influence on *in vivo* HAp crystallite size. However, these forms of intrinsic control have not previously been explicitly linked to *in vivo* HAp crystal size control within biological systems. Incorporation of impurities, in particular carbonate ions (at the levels found in bone mineral), increases lattice disorder which consequently leads to a decrease in crystallite size. Arguably, this is highlighted by comparing crystallite size and percentage carbonate of enamel (~30 nm, 2 - 4%) and dentin (~20 nm, 5- 6%) (LeGeros, 1981, Koch *et al.*, 1997, Pasteris *et al.*, 2004, Shi *et al.*, 2005, Reyes-Gasga *et al.*, 2013). Further, due to a decrease in crystallite size, studies have proposed the large chemical surface area of small crystals accelerates dissolution. Research has also suggested dissolution rate of HAp is correlated to lattice strain. Interestingly, Van Der Houwen *et al.* (2003) indirectly correlates the two very different intrinsic and extrinsic hypotheses. The authors agree that the presence of citrate (extrinsic source of control) during synthesis of HAp causes a decrease in crystal size. However, they suggest that rather than bind to the HAp surface, the citrate molecules interact with newly formed calcium phosphate, which leads to incorporation of carbonate ions and an increase in lattice disorder (intrinsic source of control).

Interestingly, after consideration of the literature it is proposed dissolution of HAp crystals is indirectly governed by lattice strain. Incorporation of extraneous ions into the crystal lattice causes an increase or decrease in lattice strain, depending on the substitution. Lattice strain, which is not only dependent on incorporation of extraneous

ions but also lattice vacancies, increases dissolution. It is therefore proposed that an increase in dissolution leads to smaller crystals, as growth is retarded due to rapid dissolution of the material. With this mind, it seems plausible that lattice strain could be an intrinsic source of biological *in vivo* HAp crystallite size control, a concept which has not previously been explicitly developed. Quantification of biological HAp lattice strain is however extremely difficult due to broad, overlapping peaks associated with the nanocrystalline nature of this material, as discussed in section 5.1.3.

It is clear that the causal mechanisms that control crystallite size within HAp biological systems are not well defined. Arguably, this is due to the fact that the majority of studies report *in vivo* HAp crystallite size control of synthetic specimens. Unfortunately, there have been few studies which have investigated *in vivo* crystallite size control of biological HAp specimens. This thesis will go on to address these controversial issues.

Chapter 4: HEAT TREATMENT AND BONE

The response of bone and synthetic HAp to heat treatment is well documented across a wide range of disciplines including forensics, archaeology and biomedicine (Murugan *et al.*, 2003, Schiegl *et al.*, 2003, Pijoan *et al.*, 2007, Beckett *et al.*, 2011, Lau *et al.*, 2013, Piga *et al.*, 2013, Yravedra & Uzquiano, 2013). As a consequence, a wide range of studies have reported colour changes and mass loss as well as physicochemical changes to bone during heat treatment. In most instances, these studies utilise fresh, defleshed animal bone, although archaeological bone has also been considered. Unfortunately, research to date is largely observational. As a consequence, the fundamental processes and mechanisms associated with physicochemical modifications to bone mineral during heat treatment have not been fully appreciated. In particular, the fundamental relationship between the organic and mineral components of bone during heat treatment is often assumed and ambiguous. Further, the majority of studies have employed a static heating approach, where the bone is heated to temperature, dwelled and allowed to cool prior to analysis.

This approach cannot strictly provide a complete model of the physicochemical modifications to bone, as the confounding effects of cooling are not fully known. Previous studies may not have not considered the effects of cooling due to the difficulties and/ or limitations of dynamically analysing the changes to bone during cooling. For example, many analytical techniques commonly used to analyse bone cannot be adapted to facilitate a heat stage capable of reaching high temperatures (> 600 ^{o}C). For those analytical techniques which can be adapted, such as powder X-ray diffraction kits, very few research institutes have employed this dynamic protocol. Consequently, the availability for dynamic analysis during the heat treatment of bone is limited. Dynamic heat treatment of synthetic HAp has however been previously reported. These studies concentrate mainly on the thermal decomposition products during cooling and report that the various thermal decomposition products of HAp are not thermally stable during cooling (discussed further in section 4.2.2).

This chapter will provide a detailed account of the behaviour of bone and synthetic HAp during heat treatment, with attention paid to the crystallisation and thermal

decomposition of HAp. The implications of the intimate relationship between the mineral and organic components of bone during heating are considered separately.

4.1 General Observations

4.1.1 Colour and Mass Loss

During heating, bone undergoes a number of colour changes (Figure 4.1). A loss in mass is also observed, as well as shrinkage, warping and cracking of the bone (Shipman *et al.*, 1984). This has previously been associated with the physicochemical processes which occur during heat treatment (Shipman *et al.*, 1984, Thompson, 2004, Munro *et al.*, 2007, Devlin & Herrman, 2008, Ubelaker, 2009, Waterhouse, 2013). At temperatures < 200^{o}C, the colour of bone has been reported to remain the same (cream/ yellow) as unheated bone, whilst a small mass loss is observed within this temperature range. This has been associated with loss of surface absorbed water. A constant mass loss and darkening of bone to a brown/black colouration when heated between approximately 200 – 500^{o}C, occurs due to the loss of lattice incorporated water (by 400 ^{o}C), combustion of the organic matrix and carbonisation of the mineral (denoted by the release of CO_2 and H_2O). A subsequent colour change to light blue/ grey at temperatures 500 – 700 ^{o}C; signifies the removal of structural carbonates and the complete combustion of the organic matrix. At temperatures > 700^{o}C, a colour change to white is indicative of mineral calcination.

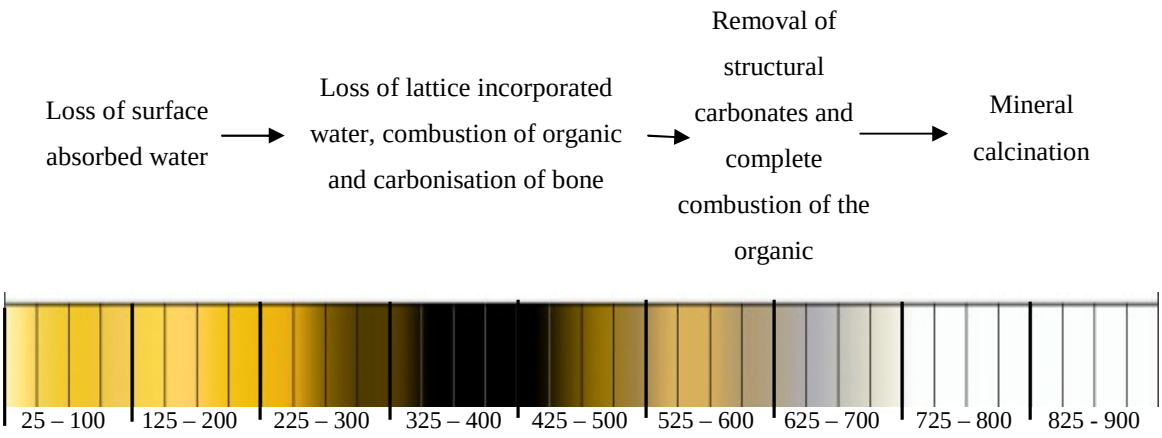

Figure 4.1 Colour index for burnt bone which is superscripted with the physicochemical processes which have previously been associated with certain colour changes/ temperatures

Colour typing of burnt bone has to date been carried out using Munsell colour charts. This has allowed anthropologists to estimate the temperature to which a bone specimen has been heated to, reportedly within an error of ± 50°C (Shipman *et al.*, 1984, Grévin, 1998). The period of time the bone has been heated is often not considered. Research has also shown many physical and taphonomic factors can affect the colour change of heated bone, including insulation by soft tissue, proximity of the bone to the flame, sun exposure and alteration during burial including diagenesis and discolouration due to soil environment (Shahack-Gross *et al.*, 1997, Symes *et al.*, 2008 Ubelaker, 2009). Although there are several confounding influences, Munro *et al.* (2007) argue colour typing remains one of the main methods for recognition of burnt bone. This has led to the use of spectroscopic techniques such as colourimeters and spectrophotometers (Devlin & Hermann, 2008, Walker *et al.*, 2005, Fredericks 2011). These techniques numerically represent colour which not only improves accuracy but allows for quantitative analysis. Spectrophotometers can provide more accurate quantification, however colourimeters are preferred as there is very little associated sample preparation and the equipment can be used in the field.

Within this thesis, colour of heated bone was quantified using a colourimeter and the values employed to develop a predictive time/ temperature model (sections 8.8.2 & 9.8.2). Mass loss values were recorded and are reported in section 8.5.1.

4.2 Physicochemical Modifications

4.2.1 Crystallisation

Through the use of crystallographic and microscopic techniques, changes to the mineral microstructure of bone and teeth during heat treatment are well documented (Holden *et al.*, 1995. Hiller *et al.*, 2003, Reyes-Gasga *et al.*, 2008, Piga *et al.*, 2009, Rogers *et al.*, 2010, Squires *et al.*, 2011, Pramanik *et al.*, 2012, Castillo *et al.*, 2013). At temperatures exceeding 600 ^{o}C, studies have reported a rapid change in the mineral microstructure of bone. Studies have suggested this is due to an increase in HAp crystallite size and microstructural order (Haberko *et al.*, 2006, Beckett *et al.*, 2011). With continued heating, the mineral microstructure of bone transforms from a highly anisotropic strained material to a material with significantly larger equi-dimensional crystals with little microstrain (Rogers & Daniels, 2002). For this thesis, the growth of HAp crystals will be referred to as '*crystallisation'*. The point at which crystallisation is first observed is referred to as the *'onset of crystallisation'*. This should not be confused with *recrystallisation* often used by metallurgists, where a new set of crystal grains (with less defects) replace deformed crystals grains during heat treatment. The new crystals nucleate and grow until the original grains have been entirely consumed. This eliminates almost all of the dislocations and defects (Rios *et al.*, 2005). Crystallisation of HAp crystals during heat treatment does not involve formation of new crystals. Instead, larger crystals form at the expense of smaller crystallites (Figure 4.2).

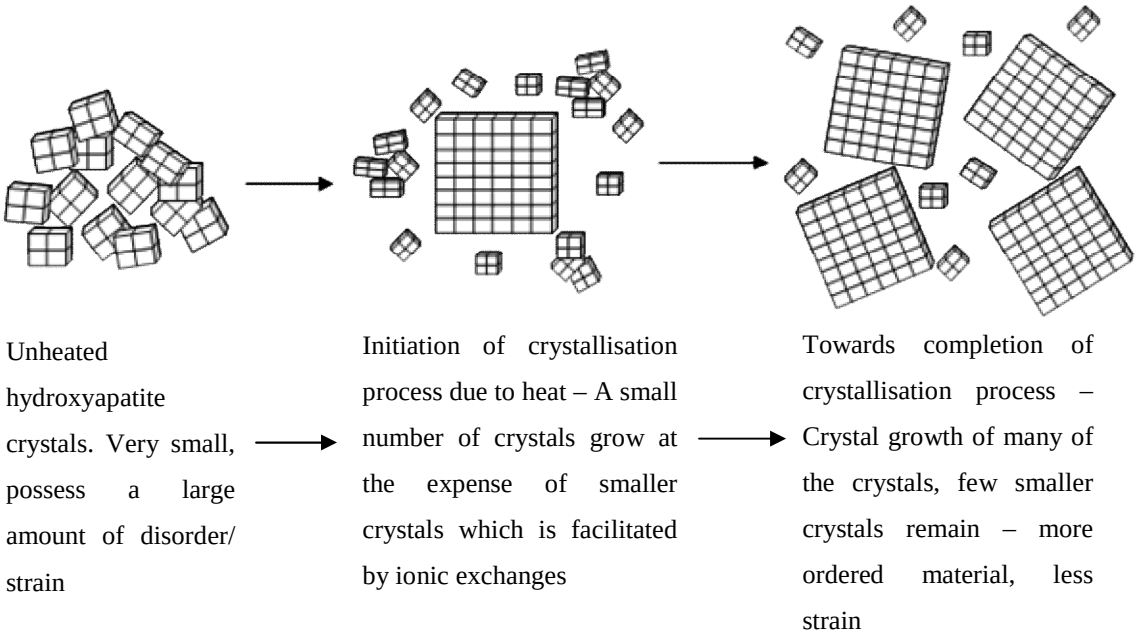

Figure 4.2 Diagram illustrating the crystallisation process.

During crystallisation of bone mineral, HAp lattice parameters tend towards stoichiometric values (a = b = 9.4225 and c= 6.8850 Å) (Haberko *et al.*, 2006), as the HAp crystals become larger, more ordered and less strained. This is primarily caused by ion loss (Rogers & Daniels, 2002). As the incorporation of carbonate influences lattice parameter values (section 2.2.2), the loss of carbonate ions during heat treatment (section 4.1.1) must have a substantial effect on lattice parameters (Wang *et al*., 2010). Consequently, during heat treatment, an expansion or contraction of the lattice parameters is observed dependent on the loss of A – or B- type carbonate and the axial length being considered (Assuming the opposite effect occurs when carbonate is lost from the lattice rather than incorporated) (Table 4.1).

A- Type Carbonate		B- Type Carbonate	
'a' axis	'c' axis	'a' axis	'c' axis
⇩	⇧	⇧	⇩

Table 4.1 The effect (expansion, ↑ or contraction, ↓) on the 'a' and 'c' axial lengths, if A – or B – type carbonate is lost during heat treatment of biological HAp

A limited number of studies have suggested a three stage carbonate loss process during thermal decomposition of HAp in enamel (Holcomb & Young, 1980, Dowker & Elliott, 1983, Shi *et al.*, 2005). According to Shi *et al.*(2005), the amount of B –type carbonate and total carbonate content decreases during heat treatment, whereas the amount of A-type carbonate firstly decreases when heated up to 300 ^{o}C, then increases from 300 – 700 ^{o}C before decreasing again (Shi *et al.*, 2005). It is proposed the increase in A-type carbonate is due to 'trapping' of B-type carbonate ions expelled during heat treatment. (i.e. carbonate ions lost from B type sites (PO_4^{3-} vacancies) are incorporated into the A-type site (OH^- vacancies)). Assuming this model is correct and considering only A – type carbonate, a contraction and expansion in the 'a' and 'c' axial lengths would be observed between 25 -300 ^{o}C. An increase in A-type carbonate between 300 -700 ^{o}C would cause an expansion in the 'a' axial length and a contraction in the 'c' axis. At temperatures > 700 ^{o}C, a contraction and expansion in the 'a' and 'c' axial lengths would be observed due to the loss of the recently incorporated 'A' type carbonate ions (Table 4.2).

	‘a’ axis	‘c’ axis
25 – 300 ^{o}C	⇩	⇧
300 – 700 ^{o}C	⇧	⇩
700 – 900 ^{o}C	⇩	⇧

Table 4.2 The effect (expansion ↑ or contraction ↓) on the ‘a’ and ‘c’ axial lengths, assuming during heat treatment carbonate ions lost from the B type sites (PO_4^{3-} vacancies) are incorporated into the A type site (OH^- vacancies) (Adapted from Shi *et al.*, 2005).

4.2.2 Thermal Decomposition

The thermal decomposition (a process were the mineral component of bone begins to break down and form other calcium phosphate phases) of biologically formed and synthetically produced HAp has been reported to occur at temperatures exceeding 600 ^{o}C (Laio *et al.*, 1999, Ravaglioli 1996, Ooi *et al.*, 2007, Beckett *et al.*, 2011). This process is signified by the presence of additional crystalline mineral phases. Calcium oxide (CaO) (biological HAp only), tetra-calcium phosphate (TTCP), alpha-tri-calcium phosphate (α-TCP) and beta-tri-calcium phosphate (β-TCP) are frequently reported as thermal decomposition products of biological and synthetic HAp (Brown and Chow, 1976, Locardi *et al.*, 1993, Mayer *et al.*, 1997, Barralet, 2002, Dorozhkin *et al.*, 2002, Haberko *et al.*, 2006). Magnesium oxide (MgO) has also been detected in heated bone specimens (Mkukuma *et al.*, 2004, Beckett *et al.*, 2011), although it is less frequently reported than the aforementioned mineral phases.

Thermal decomposition of HAp into CaO (for biologically formed HAp), TTCP and TCP is thought to occur through a stepwise process (Figure 4.3). The initial stage involves the removal of the OH^- groups from the HAp lattice (Bett *et al.*, 1967, Brown

and Chow, 1976, Liao *et al.*, 1999). This is thought to result in the formation of calcium oxyapatite (OAP), which has been reported to act as a precursor to the development of the decomposition phases (Brown and Chow, 1976, Gross *et al.*, 1998). In addition to the removal of OH^- groups, carbon dioxide is also released from the HAp lattice as a result of the decomposition of carbonate ions (Barinov *et al.*, 2006, Haberko *et al.*, 2006). To date, the mechanism for formation of MgO has not been validated as this mineral phase is not often detected. Beckett (2009) proposed the formation of MgO may be due to the presence of a greater amount of magnesium than can be accommodated within HAp, β - TCP and TTCP crystal lattices. During heating, the capability of the crystal lattices to accommodate the Mg ions is reduced due to competitive substitution of both sodium and potassium ions (*ibid*). However, Beckett (2009) only investigated the thermal decomposition of bone heated to two temperatures, 600 ^oC and 1400 ^oC.

The thermal decomposition products of biologically formed and synthetically produced HAp have been reported at different temperatures. The presence of CaO has been observed for bone when heated at ~ 700 ^oC, whilst TTCP and β - TCP are observed at 1200 ^oC for biologically and synthetically produced HAp. β - TCP has been reported to undergo a further transformation to α - TCP between 1300 - 1450 ^oC in biologically and synthetically produced HAp (Ando *et al.*, 1958, Wang *et al.*, 2009). At temperatures exceeding 1400 ^oC, only small quantities of HAp are observed due to almost complete transformation into the various decomposition products (*ibid*). The presence of MgO was reported in bone specimens heated to 1400 ^oC (Beckett *et al.*, 2011). By approximately 1600 ^oC, melting of the calcium phosphate mineral phases occurs.

Synthetic HAp studies have shown TTCP, α - TCP and β - TCP are not thermally stable, and during cooling these mineral phases are thought to reconstruct into OAP, which is gradually rehydrated and reconstituted into HAp, again by a stepwise process (Figure 4.3) (Liao *et al.*, 1999, Lin *et al.*, 2004, Wang *et al.*, 2009). Unfortunately, the cooling effects on thermal decomposition of HAp have to a certain extent been overlooked, especially for biologically formed HAp. Thus, the thermal stability of CaO and MgO is largely unknown, although these mineral phases are detected in specimens which have been slowly cooled (Mkukuma *et al.*, 2004, Beckett *et al.*, 2011).

HEATING

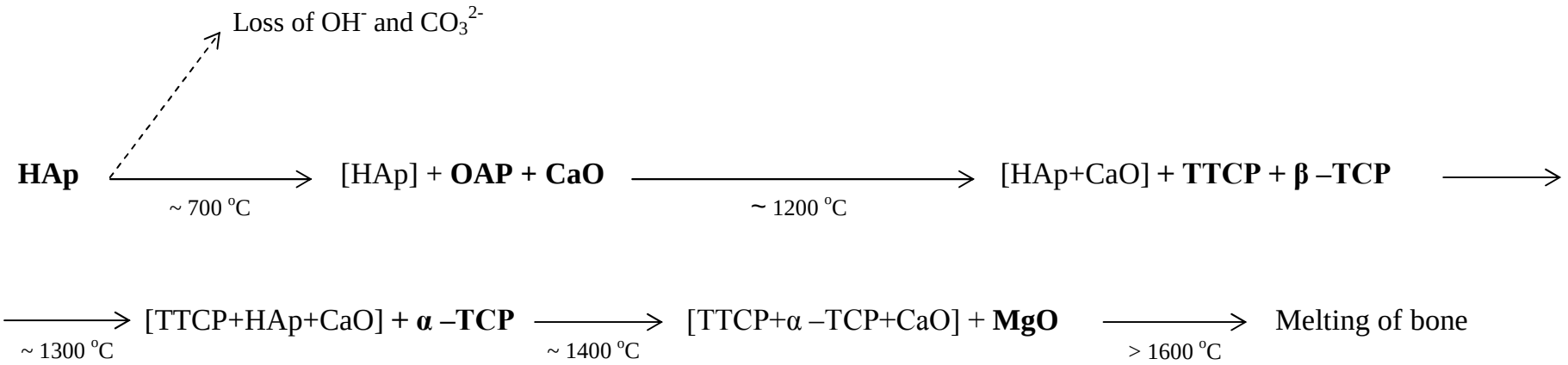

COOLING

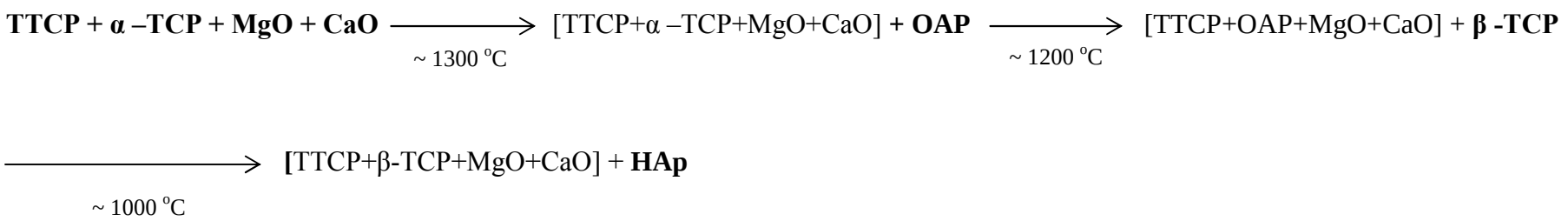

Figure 4.3 A combined step-by step diagram depicting the expected thermal decomposition pathway for biological HAp during heating and the reconstitution of HAp during cooling, based on biological and synthetic Hap studies. Square brackets [ ], indicate the mineral phases were formed in the previous step. The temperatures at which these mineral phases have previously been reported for biological and synthetic HAp are included.

Studies have also suggested the thermal decomposition of HAp is dependent on the original lattice chemistry. A study carried out by Mkukuma et al. (2004), which investigated the role of the organic matrix on thermal decomposition of HAp, found Ca: P molar ratios (which gives an indication of relative calcium content) have a substantial effect on the thermal decomposition products observed. This dynamic study reported the presence of β-TCP when red deer antler (which had a Ca/ P molar ratio of 1.53) was heated at high temperatures, whilst for whale tympanic bulla (which had a Ca/ P molar ratio of 1.69), calcium oxide was observed. These results are supported by similar research which observed thermal decomposition of synthesised carbonated HAp (Barralet, 2002).

Thermal decomposition of HAp is also dependent on ionic chemistry. For instance, the stability of HAp is influenced by hydroxyl and acid phosphate content. Incorporation of these ions into the crystal lattice is thought to increase the thermal stability of HAp. Mayer *et al*. (1997) suggested in the absence of carbonate, synthetic HAp transforms to β - TCP at lower temperatures (~700 ^{o}C), whilst the presence of magnesium is thought to favour the formation of β - TCP, TTCP, MgO and CaO. Magnesium is also thought to stabilise these thermal decomposition products during heat treatment. It has also been proposed that magnesium promotes the transformation of α - TCP to β - TCP during slow cooling (Beckett, 2009). Elemental analysis of several bone specimens collected from different species suggested β - TCP formation is favoured in the presence of potassium ions; strontium stabilises MgO decomposition, and fluorine ions promote formation of TTCP (ibid). Many studies have also shown that substitution of fluorine for hydroxyl ions stabilises Hap, as discussed in chapter 3.

4.3 Bone Mineral / Organic Relationship during Heat Treatment

Due to the intimate relationship between the mineral and organic components of bone as described by the Landis model (section 2.2.3); several studies have proposed the organic matrix restricts bone mineral crystallisation during heat treatment (Roberts, 2002, Trueman, 2004, Wang, 2010). During heating, the organic matrix is thought to

have a ‘thermal shielding’ effect on bone mineral. Degradation and decomposition of the restrictive collagen fibrils releases the nanocrystalline mineral surfaces and encourages sintering at higher temperatures (Walsh, 1994, Person *et al.*, 1996). For instance, a thermal analysis study carried out by Etok *et al.* (2007) found that the crystallisation of biological HAp occurred almost immediately after the combustion of the organic. Thus, Etok *et al.* (2007) reported that HAp crystal growth does not occur until the protective organic ‘barrier’ has been removed. However, a thermal analysis study by Lozano *et al.* (2003) reported the complete combustion of the organic occurs by approximately 500 ^{o}C, whilst XRD studies have revealed the onset of crystallisation of bone mineral occurs at approximately 600 ^{o}C (Rogers and Daniels, 2002, Beckett *et al.*, 2011, Greenwood *et al.*, 2013).

Unfortunately, these studies are largely observational and very little in-depth work has been carried out in order to confirm these hypotheses. There has however been an attempt in recent years to observe the thermal effects on bone mineral once the organic matrix has been removed. These studies have produced ‘anorganic’ bone material using a wide range of chemical methods, including submersion in sodium hypochlorite solution (Wright & Schwarcz, 1996, Haberko *et al.*, 2006), hot dilute acid solution (Hu *et al.* 2010), subcritical water and alkaline hydrolysis methods (Barakat *et al.*, 2009). However, these studies fail to consider the possible concomitant modification to the mineral microstructure. Rey *et al.* (2009) for example criticised work carried out by Mahamid *et al.* (2008), who in order to investigate the mineral structure only, removed the organic matrix from fins of zebrafish using sodium hypochlorite. Rey *et al. (*2009) suggests the use of sodium hypochlorite can cause precipitation of an amorphous calcium phosphate solid phase and consequently highlighted their reservations with regards to Mahamid *et al* (2008) study. Several studies have also reported that aqueous solutions such as inorganic solvents and even pure water can considerably alter the mineral microstructure of bone (Kim *et al.*, 1995, Karampas *et al.*, 2012, Liu *et al.*, 2013). Dissolution of HAp crystals and loss of carbonate and acid phosphate ions from the HAp lattice, due to the removal of the organic matrix using various chemical extraction methods, have been reported (*ibid*).

4.4 Concluding Remarks

In general, during heat treatment of bone, five main processes occur. Firstly, the evolution of surface bound (~200 ^{o}C) and lattice incorporated water occurs by 400 ^{o}C. At temperatures up to 500 ^{o}C, the denaturing and combustion of the organic matrix is observed. Between 600 and 700 ^{o}C, a rapid change in the mineral microstructure (due to the onset of crystallisation) has been reported. After the onset of crystallisation, continued growth of the HAp crystals is observed (crystallisation). At temperatures exceeding 700 ^{o}C, additional phases are observed due to thermal decomposition of HAp. Melting of bone mineral occurs at temperatures above 1600 ^{o}C.

The general observations associated with heated bone include a change in colour, shrinkage, warping and cracking, and a decrease in mass. The physicochemical modifications to bone during heat treatment are documented by crystal growth, ionic exchange and the presence of additional mineral phases due to thermal decomposition of HAp. Studies have suggested these physicochemical modifications are in some way influenced by the intimate relationship between the mineral and organic matrices in bone. By investigating the fundamental processes and mechanisms of these physicochemical changes this thesis has provided a new insight into the role of the mineral and organic relationship during heat treatment.

Chapter 5: INTRODUCTION TO ANALYTICAL TECHNIQUES

In order to understand the fundamental processes and mechanisms associated with unheated and heated bone, a wide variety of analytical techniques were employed. These were X-ray diffraction (XRD), Fourier transform infra-red spectroscopy (FTIR), ultraviolet-visible spectroscopy (UV-VIS), colourimetry, laser ablation-inductively coupled – mass spectroscopy (LA-ICP-MS) and differential scanning calorimetry (DSC). This chapter provides a brief overview of each technique and outlines the current use of these techniques within bone research. The use of these techniques within this thesis is considered along with the limitations associated with data collection and analysis.

5.1 X-ray Diffraction (XRD)

'Every crystalline substance gives a pattern; the same substance always gives the same pattern; and in a mixture of substances each produces its pattern independently of the others' Hull (1919)

For several years, X-ray diffraction (XRD) has played a substantial role in understanding the fundamental crystallographic structure of biological and synthetic apatites (Trautz, 1955, Bonar, 1983, Handschin & Stern, 1995, Peters *et al.*, 2000, Rogers & Daniels, 2002, Tadano & Gin, 2011). XRD is a non-destructive analytical technique which can be used to reveal structural, physical and chemical information of an unknown crystalline material. This is based on the premise that for any given crystal, planes of atoms exist in a number of different orientations, each with its own interplanar spacing, termed d-spacing. The orientation and interplanar spacings of these planes are defined by three integers h, k, ℓ; termed Miller indices and the way in which these crystallographic planes intersect the unit cell are used to define directions and distances in the crystal (Culity, 1978). It is the investigation of these d-spacings which can aid in

the identification of an unknown material. XRD is the primary tool used for this study. A summary of the information which can be obtained from XRD analysis is provided in Figure 5.1.

Figure 5.1 Flow diagram depicting information which can be obtained from XRD data

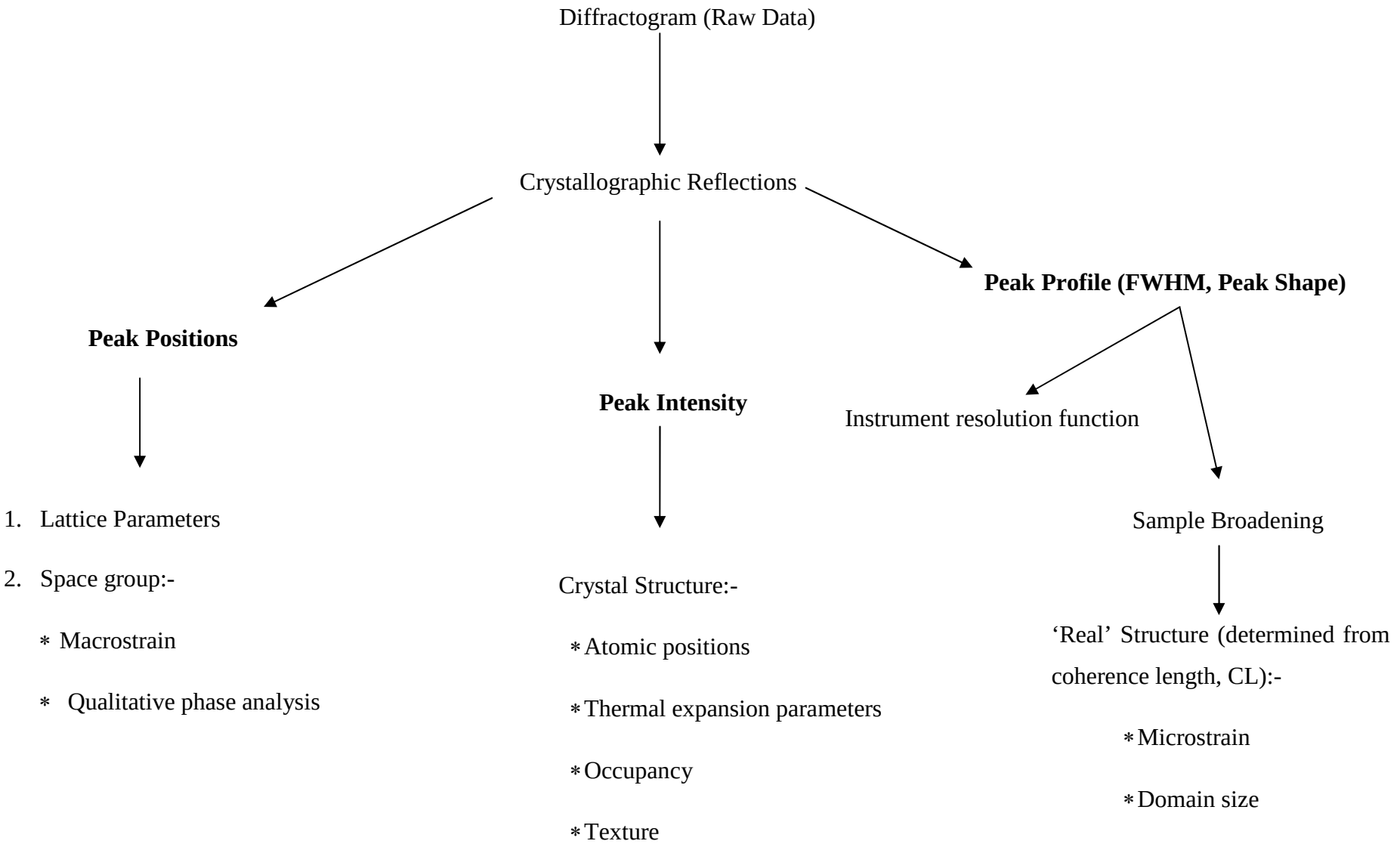

5.1.1 Basics of Crystals and their Structures

In order to understand the use of diffraction, the fundamental principles of crystals and their structures must be considered. Crystals are solids which possess a long range order and are defined by the orderly periodic arrangement of atoms (Tilley, 2006). The arrangement of atoms at one point in a crystal is identical (accepting localised defects which can arise during crystal growth), to that of a corresponding point in any other remote part of the crystal (Rousseau, 1999). The smallest repeating arrangement of atoms within a crystal is termed the unit cell. Materials which possess these characteristics are considered to be crystalline and produce distinct diffractive signals (Wahab, 2009). Conversely, amorphous materials, such as glass, are substances with no regular interior arrangement of atoms. Most inorganic minerals are considered crystalline materials, including calcium HAp. Therefore, XRD can be used to analyse bone and is particularly useful for observing physicochemical changes to bone mineral.

5.1.2 Theoretical Considerations of Diffraction

When an X-ray beam hits an atom, the electrons around the atom begin to oscillate with the same frequency as the incoming beam (Jackson & Jackson, 2008). In most instances, the combining waves are out of phase and no resultant energy leaves the sample. This is known as destructive interference. In very few directions the periodic array of atoms scatters the radiation coherently, producing waves which are in-phase and leave the sample at specific angles, θ. This is termed constructive interference (Jenkins and Snyder, 1996). Constructive interference is most comprehensively understood using Braggs Law (Figure 5.2, equation 5.1).

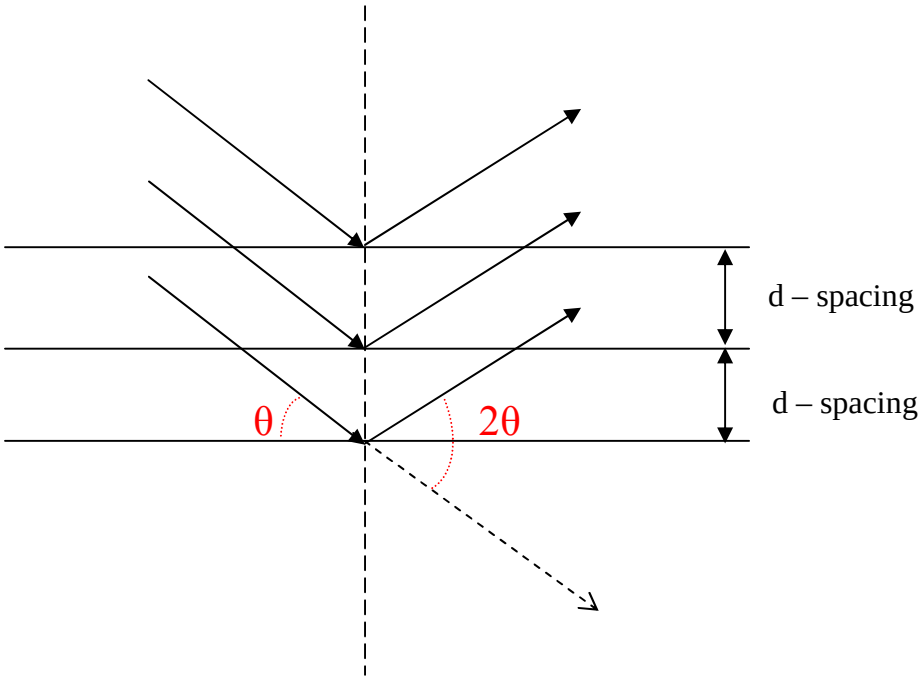

Figure 5.2 Diagrammatical representation of Braggs Law, which describes the reflection of X-rays from planes rather than electrons (Adapted from Jenkins and Synder, 1996)

$$\lambda = 2d_{hkl} \sin\theta \qquad \textbf{(5.1)}$$

Bragg's equation, where the variable, d is the perpendicular distance between atomic layers in a crystal (termed d-spacing), λ is the wavelength of the incident X-ray beam and θ is the angle between the X-ray beam and the atomic plane.

This simplistic model must be satisfied for diffraction to occur (Culity, 1978). According to Bragg's equation, the angles at which the X-rays are diffracted are determined by the wavelength of the incident X-rays and inter-planar spacing between the atomic layers (d-spacing) (Dinnebier & Billinge, 2008). Interplanar spacing differ

for crystalline materials with different compositions and lattice structures. The angle at which X-rays are diffracted, are represented as peak positions in diffractograms whilst peak intensity is determined by atomic arrangement in the diffracting plane.

In addition to Bragg's equation, to determine the composition and lattice structure of a material using XRD, the structure factor which describes the total scattering intensity from a unit cell, must also be considered (Jenkins & Synder, 1996). The structure factor groups atoms within the unit cell into planar elements, and the diffraction intensities from each of those planar elements are summed to calculate the total diffraction intensity from each d_{hkl} plane, as shown in equation 5.2:

$$F_{hkl} = \sum_{j=1}^{m} f_j \exp[2\pi i(hk_j + ky_j + lz_j] \quad \textbf{(5.2)}$$

, where $F_{(hkl)}$ is the structure factor for the hkl reflection of the unit cell, *f* refers to the atomic scattering factor for each of the atomic planes, m is the number of j atoms, h, k and l are the scattering vectors and x, y, and z refer to the fractional coordinates of the atoms within the unit cell.

Consequently, the structure factor is dependent on the atomic arrangement in a material, and provides information on the types of atoms present and their location within the unit cell. The structure factor is used to calculate the intensity of a peak as shown in equation 5.3:

$$K_{hkl} = \frac{M_{hkl}}{V^2} |F_{hkl}|^2 \left(\frac{1 + \cos^2(2\theta)\cos^2(2\theta_m)}{\sin^2\theta \cos\theta} \right)_{hkl} \quad \textbf{(5.3)}$$

, where K_{hkl} is the constant for each diffraction reflection *hkl* from the crystal structure, M_{hkl} is the multiplicity for reflection *hkl*, V is the volume of the unit cell F_{hkl} is the structure factor and $2\theta_m$ is the diffraction angle of the monochromator.

5.1.3 XRD and analysis of bone

Conventionally, powder X-ray diffraction (pXRD) is used for the analysis of bone. Powdering a crystalline material increases the number of randomly orientated crystallites, which increases the number of lattice plane orientations which interact with the incident X-ray beam at any one time. In single crystal X-ray diffraction, the sample would need to be rotated to ensure each lattice plane is investigated, unless white radiation (Laue method) is used (Warren, 1941). Powder XRD analysis is carried out using an X-ray powder diffractometer, which consists of an X-ray source, a specimen stage and an X-ray detector (Figure 5.3).

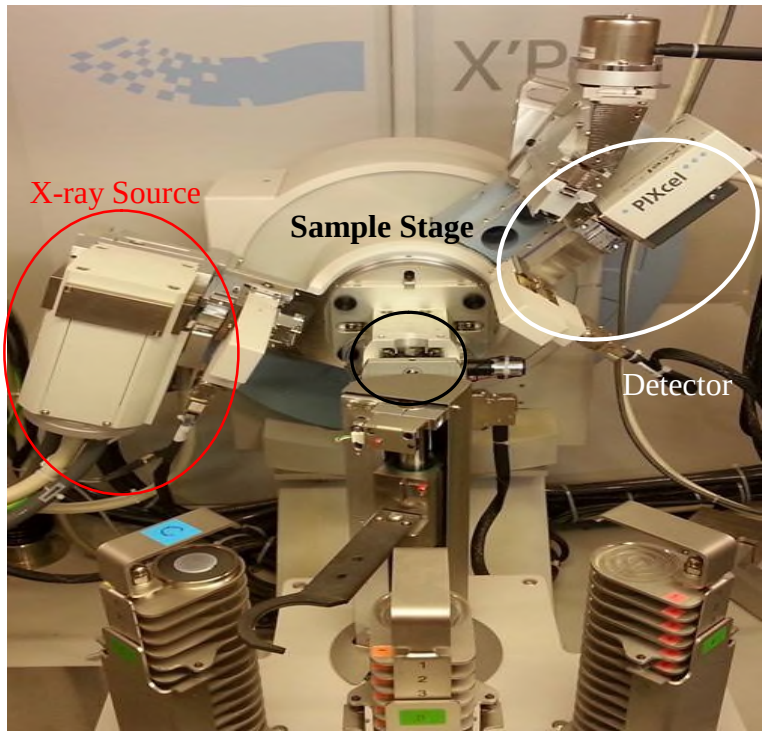

Figure 5.3 Photograph of the PANalytical X'pert powder diffractometer employed for this research. The X-ray source, sample stage and X-ray detector are highlighted.

The collection of X-ray diffraction data is relatively simple; however analysis of the raw data can be problematic for nanocrystalline materials such as bone mineral. For several years, accurate calculation of HAp crystallite size and strain has been particularly difficult. Arguably this is due to direction dependence peak broadening (i.e. crystallite size and strain contributions to peak broadening in XRD data differs depending on the crystallographic reflection which is being considered).

In pXRD, full pattern fitting and diffraction line broadening analysis techniques are often used to calculate crystallite size for a variety of materials including biological HAp (Handschin & Stern, 1995, Rogers & Daniels, 2002). Peak broadening observed for biological HAp is not only caused by the nanocrystalline dimensions but also by lattice imperfections (i.e. strain) (Danilchenko *et al.*, 2002). Further, some studies have shown that lattice strain is the dominant factor contributing to peak broadening for biological HAp. Due to the difficulty of separating crystallite size and strain for biological HAp, diffraction broadening methods such as the Scherrer equation is often used (Venkateswarlu *et al.*, 2010). As shown in equation 5.4.

$$CL = \frac{k\lambda}{(\beta - \beta_{IRF})\cos\theta} \qquad \textbf{(5.4)}$$

The Scherrer equation is used to calculate coherence length, which encompasses both crystallite size and strain, where k corresponds to the shape factor (0.9), λ is the wavelength used (1.54 Å), β is the full width half maximum (FWHM) or integral breath of the diffraction peak for the sample, β_{IRF} is the full width half maximum or integral breath of the diffraction peak for a standard with no sample broadening and θ is the angle of diffraction. If the Scherrer equation is calculated using FWHM, the volume weighted average size is provided whereas if the integral breadth is used, the area weighted average size is calculated.

Some authors employ ‘coherence length’ calculated from the Scherrer equation to report crystallite size and strain, whilst others ignore lattice strain contribution and the

Scherrer equation is used to incorrectly report absolute crystallite values (Bloebaum *et al.*, 1997, Gashti *et al.*, 2014). Attempts to refine diffraction data further to account for size and strain broadening contributions have varied in success for nanocrystalline HAp such as bone mineral.

Full pattern fitting methods such as Rietveld refinement, are routinely employed for size and strain determination of a wide range of materials including bone mineral (Lutterotti & Scardi, 1990, Handschin & Stern, 1995, Meneghini *et al.*, 2003, Zhao *et al.*, 2014). The Rietveld method was originally developed to refine crystal structures from neutron powder diffraction data but was soon applied to X-ray powder diffraction data (Jenkins & Snyder, 1996). Rietveld refinement differs to other methods as rather than using integrated intensities from a powder diffraction pattern in a single-crystal-like manner, the entire information content of a powder diffraction pattern is refined by means of a nonlinear least-squares minimisation (Von Dreele, 2008). This method relies on refining user-selected parameters to minimise the difference between the observed data (experimental data) and calculated data (a model based on the hypothesised crystal structure and instrumental parameters) (Tilley, 2006). This is summarised in equation 5.5:

$$M = \sum_{i}^{n-1} w(Y_0 - Y_C)^2 \qquad \textbf{(5.5)}$$

, where the squared sum of all differences between the step scan intensities in the diffraction pattern of observed (Y_o) and calculated (Y_c) is subjected to minimisation (Von Dreele, 2008). ‘w’ represents the weight and is derived from the variance in the observed data (Y_o). *i* is a running index (0, …., n-1) which represents the angular position in the diffraction data according to equation 5.6:

$$2\theta_i = 2\theta_{start} + i\Delta 2\theta \qquad \textbf{(5.6)}$$

, with the starting angle defined as $2\theta_{start}$ and the angular step width as $\Delta 2\theta$. Calculation of Y_c (the diffraction profile intensity), is shown in equation 5.7:

$$Y_C = K\left|F_{hkl}\right|^2 H(\Delta T_h) \qquad \textbf{(5.7)}$$

, where K is the product of various correction factors and scaling factors to the reflection intensities, $|F_{hkl}|^2$, which may be dependent on the diffraction geometry and/ or individual reflections. $H(\Delta T_h)$ relates to the value of the profile function for the location of the profile point relative to the position of the Bragg reflection, *hkl*.

As previously mentioned, Rietveld refinement involves modelling the entire powder diffraction pattern. Every point in the refinement pattern contributes to the determination of each variable value. This makes Rietveld refinement a powerful method which can provide simultaneous information on crystal structure and geometry from peak intensities, $|F_{hkl}|^2$, crystallographic lattice and symmetry as well as instrument contributions, from peak positions, *hkl* and microstructural parameters and instrument profile from peak shape, $H(\Delta T_h)$ (McCusker *et al.*, 1999). Each one of these parameters has contributions from both the sample and the instrument and should be considered separately in a sequential manner during the refinement.

A number of software packages can be used for Rietveld refinement and almost all of these programs use a Caglioti profile function (or similar fixed functions), which refine the diffraction data according to the full width half maximum (FWHM) of the peaks (McCusker *et al.*, 1999), as shown in equation 5.8.

$$FWHM^2 = U\tan^2\theta + V\tan\theta + W \qquad \textbf{(5.8)}$$

, where U, V and W are coefficients associated with fitting FWHM data plotted against θ.

This analytical expression assumes equal size and strain contribution to peak broadening in all crystallographic directions and is frequently used to calculate the instrumental resolution function (IRF) (Gozzo *et al.*, 2006). Size and strain broadening contributions observed for nanocrystalline HAp crystals are, however, direction dependent (Rogers and Daniels, 2002). Consequently, the average size and strain values provided from Rietveld refinement of nano HAp are largely inaccurate, as fixed functions do not account for direction dependence peak broadening (McCusker *et al.*, 1999). Attempts have been made to model direction dependence broadening using full pattern refinements; however these tend to be phenomenological models (Stephens, 1999). These refinements fit the data very well; however they cannot provide direct quantification of crystallite size and strain (Leineweber and Mittemeijer, 2003).

Due to the fundamental limitations associated with the implementation of fixed profile functions during Rietveld refinement, many researchers have employed less direct line broadening methods to analyse nanocrystalline materials. The line broadening approach, which includes Warren – Averbach, Williamson – Hall and single line analysis, considers peaks individually. Crucially, size and strain contribution is specific for each Bragg peak and therefore each crystallographic direction. The Warren-Averbach method employs a deconvolution Fourier transform approach, also known as the Stokes method (Turunen *et al.*, 1983, Marinkovic *et al.*, 2001). Although a robust method which is often applied in the field of metals, alloys, ceramics and polymer materials (Turunen *et al.*, 1983, Lutterotti & Scardi, 1990), use of the Warren- Averbach method for nanocrystalline material is limited (Baig *et al.*, 1996). This method not only requires high quality data and assumes a Gaussian strain distribution, but is also limited by overlapping, poorly resolved and weak intensity peaks (*ibid*), features that cannot be avoided when analysing nanocrystalline material such as biological HAp.

Consequently, the Williamson-Hall method is preferred for biological and synthetic nanocrystalline HAp (Rogers *et al.*, 2010, Eshtiagh-Hosseini *et al.*, 2007, Venkateswarlu *et al.*, 2010). The Williamson-Hall method relies on the principle that size broadening and strain broadening differ with respect to the Bragg angle, θ. Size broadening varies according to $1/\cos\theta$, as shown by the Scherrer equation (equation 5.4)

whilst strain broadening varies as a function tanθ (Biju *et al.*, 2008), as shown in equation 5.9:

$$\varepsilon = \frac{\beta_{hkl}}{4\tan\theta} \tag{5.9}$$

, where ε corresponds to strain, β_{hkl} is full width half maximum (FWHM) or integral breadth of the diffraction peak for the sample (corrected for instrument broadening) and θ is the angle of diffraction.

Assuming both crystallite size and strain are contributing to line broadening and are independent of each other, the observed peak broadening is the linear sum of these equations, which can be rearranged to give equation 5.10:

$$\beta_{hkl}\cos\theta = \frac{k\lambda}{D} + 4\varepsilon\sin\theta \tag{5.10}$$

, where β_{hkl} is full width half maximum (FWHM) or integral breath of the diffraction peak for the sample, k corresponds to the shape factor (0.9), λ is the wavelength used (1.54 Å), D is crystallite size and ε corresponds to strain.

A Williamson-Hall plot is then constructed as a linear plot of βcosθ versus sinθ which is used to calculate the size and strain contribution from the y-intercept and gradient respectively. Williamson – Hall analysis is particularly useful as it can be used to quantitatively assess the crystallite size and strain direction dependent nature of biological HAp. However, this technique is not without limitations. Due to broad and overlapping diffraction peaks observed for nano-sized HAp crystallites, the fitting errors associated with the full width half maximum (or integral breadth); limit the use of this technique for quantitative calculation of crystallite size and strain.

A less conventional diffraction line broadening method for bone material is single line analysis, where size and strain are calculated from convolution of the integral breadths of Lorentzian and Gaussian peak functions respectively (Langford, 1992). The main advantage of this refinement is that direction dependent crystallite size and strain can be calculated from a single peak (De Keijser *et al.*, 1982) (in contrast, at least two reflections in the same crystallographic direction are required for both Williamson Hall and Warren - Averbach analysis).

Following the analysis of Langford (1992), crystallite size is calculated (once the instrument resolution factor has been accounted for) using equation 5.11:

$$\beta_L^* = \frac{1}{D} \qquad \textbf{(5.11)}$$

, where β_L* is the Lorentzian integral breadth (in reciprocal units) and D is crystallite size, whilst strain effects are calculated using equation 5.12:

$$\beta_G^* = \frac{\varepsilon d}{2} \qquad \textbf{(5.12)}$$

, where β_G* is the Gaussian integral breadth (in reciprocal units) and ε is crystallite strain.

Lorentzian and Gaussian integral peak breadths are calculated from the integral breadth of the peak according to equations 5.13 and 5.14:

$$\beta_G = \beta_{\exp}(y^2).[1 - erf(y)] \tag{5.13}$$

$$\beta_L = y(\pi^2).\beta_G \tag{5.14}$$

, where β is the total integral breadth of the observed peak and erf is the error function. Co-efficient 'y' is defined by equation 5.15:

$$y = \frac{EA - ((C\phi - EA)^2 - 4(D\phi - EB)(\phi - E))^{\frac{1}{2}}}{2(D\phi - EB)} \tag{5.15}$$

, where A = 0.9039645, B = 0.7699548, C = 1.364216, D = 1.136195 and E = 0.9394372. Co-efficient 'Φ' is defined by equation 5.16:

$$\phi = \frac{FWHM}{\beta} \tag{5.16}$$

, where β is the total integral breadth of the observed peak and FWHM is the full width half maximum of the peak.

β_G and $\beta_{L,}$ which are expressed in angular units (2θ) are transformed and expressed in reciprocal units (β_G^* and β_L^*), using equation 5.17.:

$$\beta_x^* = \beta_x . \cos\left(\frac{\theta}{\lambda}\right) \qquad \textbf{(5.17)}$$

, where β_x^* is the integral breadth in reciprocal units, β_x is the integral breadth in angular units, (x corresponds to either the Lorentzian or Gaussian component), θ corresponds to the angle of the peak and λ is the radiation wavelength.

Single line analysis is limited in that it cannot be applied if peaks are distinctly asymmetric. Further, Φ must lie within the Lorentzian and Gaussian limits, $0.6366 \leq \Phi \leq 0.9394$. (Langford, 1992)

Interestingly, in 2003, Leineweber and Mittemeijer demonstrated that direction dependence strain broadening contributions may be attributed to compositional variations in the material. This approach, which has not previously been applied to HAp data, investigated peak broadening contributions due to compositional variations in iron nitride (FeN). The method is modelled on materials where peak broadening is considered to be a product of strain only; size contributions are assumed to be negligible.

Direction dependent strain broadening of FeN was demonstrated by plotting structural broadening value (calculated using equation 5.18, discussed in the next paragraph) against $\tan\theta_{0,hkl}$ as a function of the angle between the crystallographic directions and <00ℓ>. Leineweber and Mittemeijer explained and reported that the largest broadening occurs in the (hk0) planes (Figure 5.4).

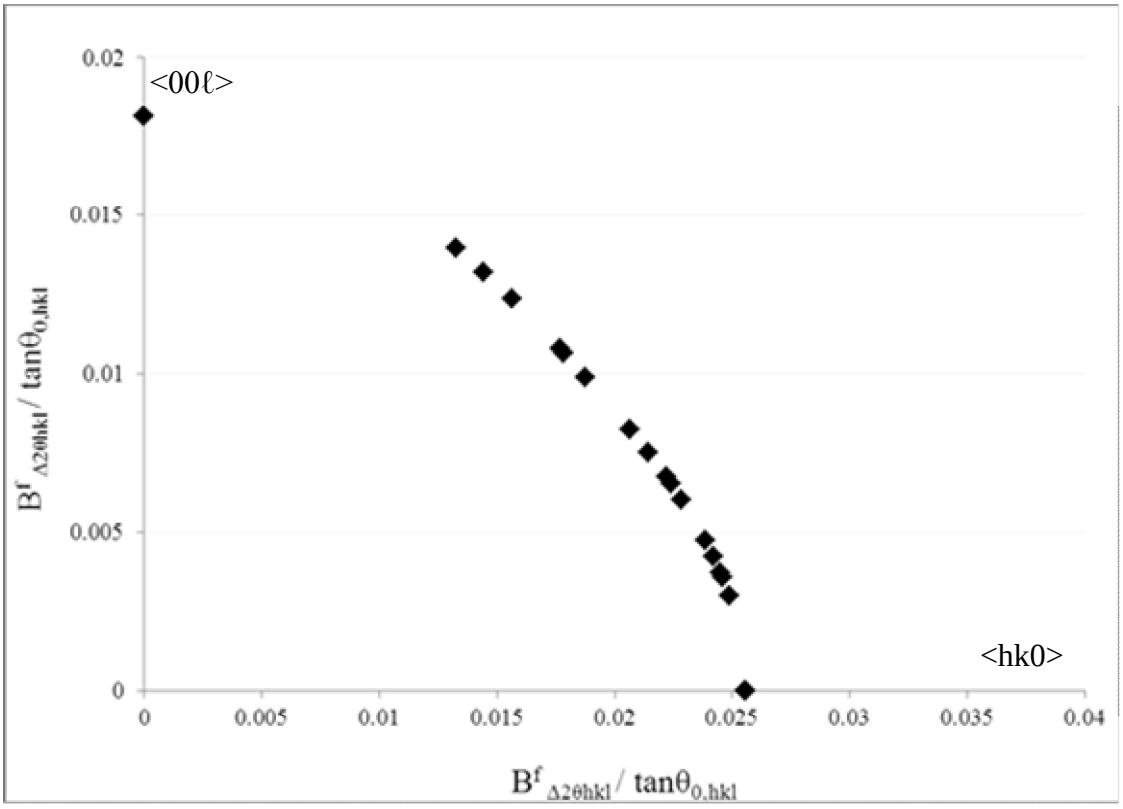

Figure 5.4 Illustration of direction dependence strain-like broadening of ε-$FeN_{0.433}$

Using equation 5.18, which applied symmetry restrictions of hexagonal crystal, Leineweber and Mittemeijer obtain fitting values of $B_\xi d\alpha_{11}/d\xi$ = 0.000966 $Å^{-2}$ and B_ξ $d\alpha_{33}/d\xi$: = 0.000173 $Å^{-2}$ for FeN. These values correspond to the extent of strain dependence broadening in the (hk0) and (00ℓ) planes respectively. The ratio of these fitting parameters (which provides an indication of the extent of direction dependence between (hk0) and (00ℓ) planes), was calculated as 0.180.

$$B^f{}_{strain} = \left(\frac{180^o}{\pi}\right)\tan\theta_{0,hkl}\cdot\left|\frac{\left[B_\xi.\frac{d\alpha_1}{d\xi}\right].(h^2+k^2+hk)+\left[B_\xi.\frac{d\alpha_3}{d\xi}\right].\ell^2}{\alpha_1.(h^2+k^2+hk)+\alpha_3.\ell^2}\right| \qquad \textbf{(5.18)}$$

, where (B^{f}_{strain}) is structural broadening caused by strain contributions only, *h, k, l* and α are coefficients associated with the symmetry restrictions of the hexagonal crystal system, ξ is the composition in each coherently diffracting crystallite, $B_{\xi,}$ is the FWHM of the probability density function of the composition and $d\alpha_1/d\xi$ and $d\alpha_3/d\xi$ relate to the extent of strain direction dependence broadening in the hk0 and 00ℓ planes, respectively.

The authors then demonstrate that $d\alpha_1/d\xi$ and $d\alpha_3/d\xi$ can be calculated from known composition dependence of the lattice parameters for the material obeying Vegards law, where α_1 is the reciprocal of the 'a' axis lattice parameters squared (a*.a*) and α_3 is the reciprocal of the 'c' axis lattice parameters squared (c*.c*). For FeN_y, the known composition dependence values where, 'a' axis = 0.3843y + 2.5828 and 'c' axis = 0.3834y + 4.2470, between $0.33 < y < 0.44$. This gave values of $d\alpha_1/d\xi$ = -0.0493Å and $d\alpha_3/d\xi$ = -0.0089 Å for y_0 = 0.433 (the known composition variation for FeN). The ratio $d\alpha_3/d\xi$ to $d\alpha_1/d\xi$ was calculated as 0.181, which is comparable to the value obtained from the ratio of the fitting parameters, B_ξ $d\alpha_3/d\xi$: $B\xi d\alpha 1/d\xi$ (0.180). Thus, this suggests that the compositional variations considered using Vegards law, are solely responsible for peak broadening. For bone mineral, it may be possible to use this model to observe and quantify direction dependence broadening caused by compositional variations due to carbonate substitutions. This would involve calculating the extent of direction dependence broadening from the coefficients corresponding to data fitted to the lattice parameters of increasing concentrations of carbonate (Figure 2.6, section 2.2.2). Ultimately Leineweber and Mittemeijer analysis leads to quantification of the compositional direction dependence of a material. In this case, FeN_y was quantified as $FeN_{0.433\pm0.008}$.

To conclude, X-ray diffraction is essential within bone research due to its sensitivity to the structural and compositional changes to bone mineral during heat treatment. In this thesis, information on coherence length, changes to lattice parameters and additional mineral phases were obtained using X-ray diffraction. This provided an insight into *in vivo* crystallite size control and crystallisation and thermal decomposition processes during heat treatment. Analysis of XRD data obtained from bone to calculate parameters such as crystallite size and strain can be extremely complex due to direction

dependence peak broadening. As described, the main limitation of Rietveld refinement of XRD data obtained from bone; is the use of fixed profile functions such as the Caglioti function. Refining data using such functions does not take into account direction dependence peak broadening. Williamson Hall analysis and single line analysis do not employ a full profile refinement method, which allows crystallite size and strain peak broadening contributions to be considered as a function of crystallographic direction. Leineweber and Mittemeijer (2003) reported that direction dependence broadening was a function of compositional variations in the material. If this model can be applied to bone, it may be possible to observe and quantify compositional variations in bone due to carbonate substitutions. These refinement techniques and models were applied to bone mineral data and investigated for this thesis (sections 8.3 and 9.3).

5.2 Spectroscopic Analysis

Spectroscopic analytical techniques are used to investigate the interaction of electromagnetic radiation with matter (Smith, 2003). When a sample is irradiated, typically using radiation in the ultra-violet, infra – red and visible regions of the spectrum, a certain proportion of the electromagnetic radiation (radial intensity) is absorbed (Figure 5.5).

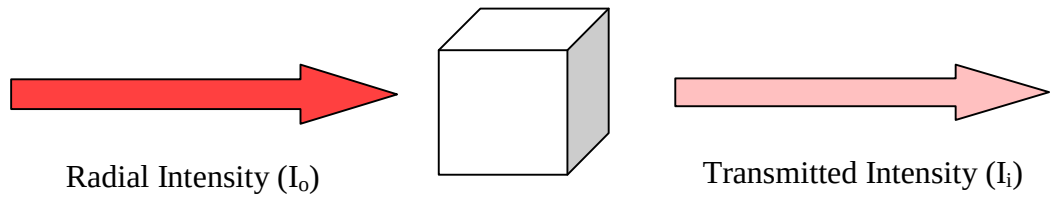

Figure 5.5 Diagram depicting the radial and transmitted intensities in equation 5.19.

Radiation which is not absorbed is known as transmitted intensity (I_i) and is measured using a detector and recorded as 'transmittance'. As shown in equation 5.19:

$$T = \frac{I_i}{I_0} \tag{5.19}$$

, where transmittance (T) is the ratio of transmitted intensity (I_i) to the radial intensity (I_o). Transmittance can be translated to absorbance using equation 5.20:

$$A = -\log T \tag{5.20}$$

For this research, three spectroscopic techniques were used: Fourier transform infra-red spectroscopy (FTIR), ultraviolet – visible spectroscopy (UV-Vis) and colourimetric analysis. The mechanism of absorption of energy differs for the infrared region in comparison to the ultraviolent and visible regions; however the fundamental idea is the same: different materials absorb different amounts of energy. These techniques will be considered in more depth in subsequent sections.

5.2.1 Infra – red Spectroscopy (IR)

Infra-red (IR) spectroscopy relies on the notion that covalent bonds with permanent electrical dipoles have particular frequencies of vibration within the infra-red region (Dyer, 1965, Atkins & Jones, 2005, Atkins & Paula, 2005). These frequencies are known as resonant frequencies. When a beam of infrared light is passed through a sample, some of the energy is absorbed by vibrating chemical bonds. The frequency of the absorbed energy is equal to the resonant energy of the vibrating bond. The

absorption of energy differs for each bond. Consequently, IR techniques are used to measure the absorbed energy which is characteristic of a particular bond. This allows the molecular structure of a compound to be determined. Each peak in the IR spectrum corresponds to the absorbance of a given vibrating bond.

It is worth noting that for a vibration to be detected in the IR region, a change in the dipole moment of the bond must occur. Bonds with the largest change in dipole moment during vibration correspond to the most intense absorption peaks. For several years, Fourier Transform infra-red spectroscopy (FTIR) has been the preferred method of infrared spectroscopy. In FTIR, data is collected and converted from an interference pattern to a spectrum using a Fourier Transform spectrometer, which has been shown to enhance sensitivity (Smith, 2011). FTIR consists of an infrared radiation beam course, an interferometer, a Fourier Transform spectrometer, an IR detector and a sample stage (Figure 5.6). The data collected is represented on a spectrum where the x-axis represents infrared radiation frequencies (wavenumber, cm^{-1}) and the y-axis represents the absorbance of infrared radiation at each frequency.

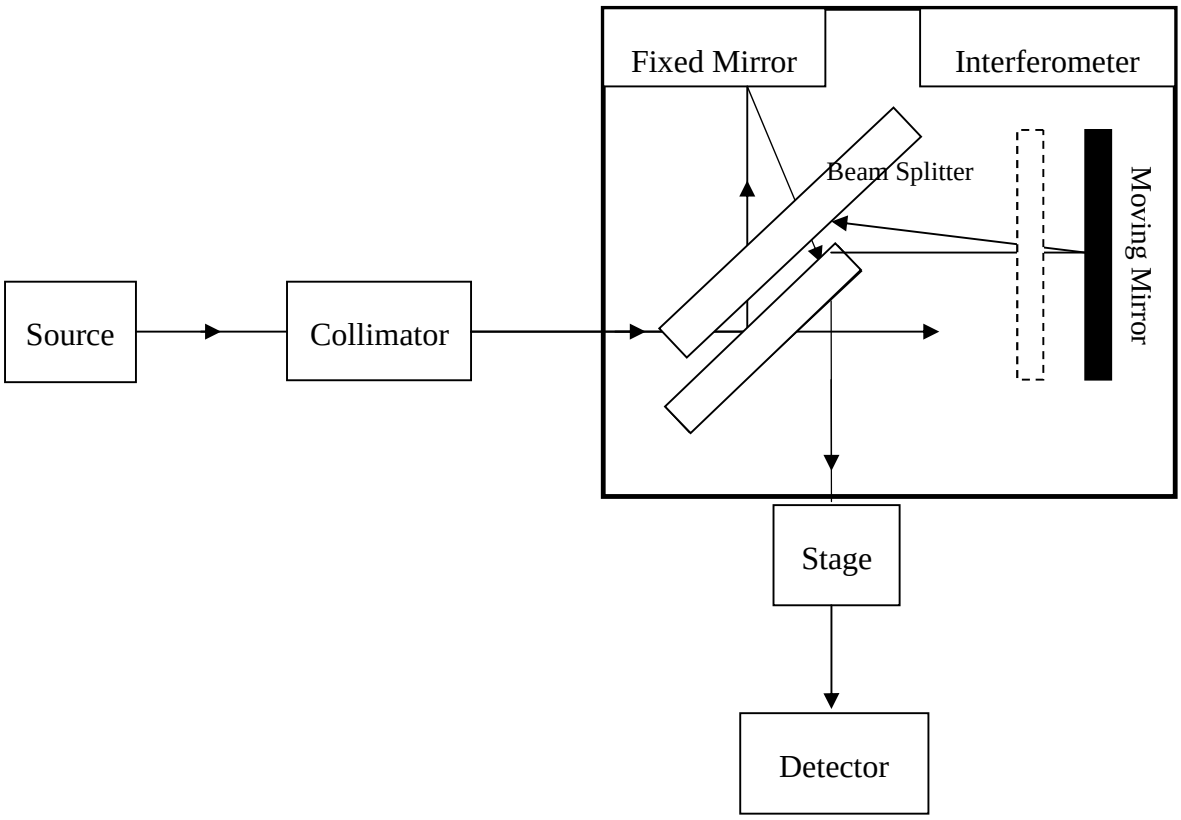

Figure 5.6 Infra-red spectrophotometer

FTIR has over the years been used extensively to analyse synthetic and biological HAp including bone, as this highly sensitive technique offers the user the potential to simultaneously compare both organic and mineral components of specimens (Rey *et al.*, 1989, Rey *et al.*, 1990, Paschalis *et al.*, 1997, Bohic *et al.*, 1998, Carden & Morris, 2000, Boskey, 2005, Chaumat *et al.*, 2012, Heredia *et al.*, 2013).This is limited with other analytical techniques. The complex pattern of vibrations relating to both the organic and inorganic components of bone is shown in Figure 5.7.

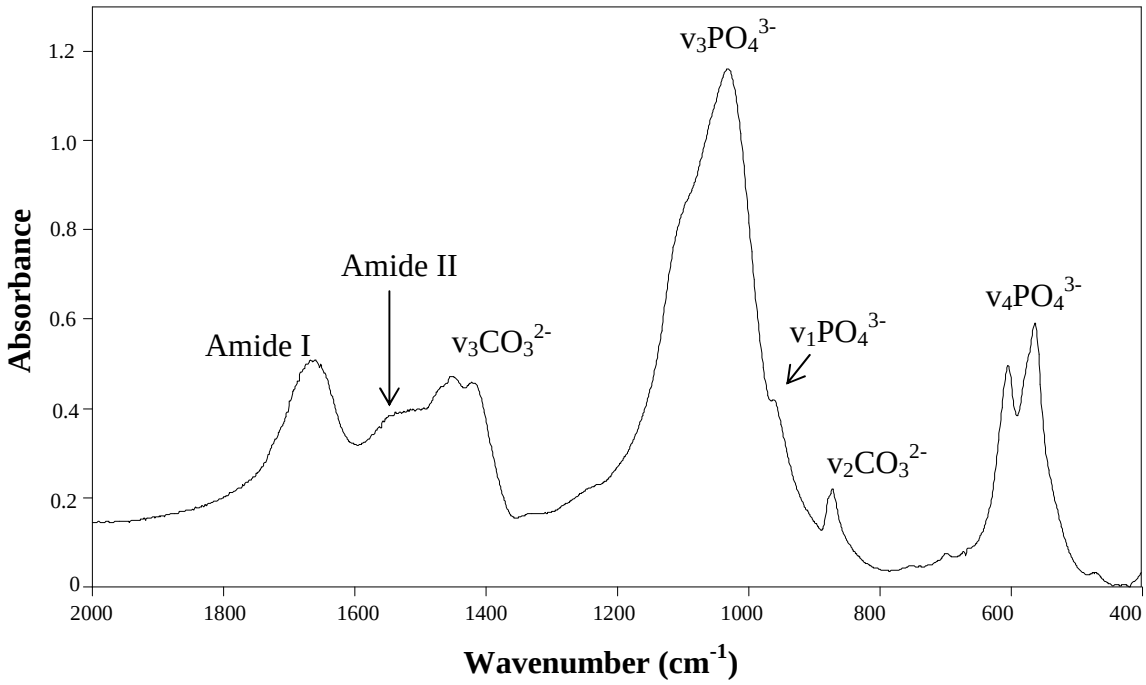

Figure 5.7 FTIR spectra of unheated bovine bone

As shown in Figure 5.7, the organic component of bone is represented by amide bands I and II in the absorbance region 1800 – 1500 cm^{-1}. These vibrational modes represent the C=O and C-N bonds that derive from collagen polypeptides. The phosphate vibrational modes, which correspond to the mineral component of bone, are observed within the regions 1200 – 900 cm^{-1} ($v_1v_3PO_4^{3-}$) and 565 – 605 cm^{-1} ($v_4PO_4^{3-}$). Peaks in regions 900 – 850 cm^{-1} ($v_2CO_3^{2-}$) and 1500 – 1350 cm^{-1} ($v_3CO_3^{2-}$) indicate the presence of carbonate.

Previous studies have exploited FTIR to document various parameters associated with the composition and crystallinity of unheated and heated bone. Degree of bone mineralisation (also termed mineral to organic ratio), relative amount of carbonate and mineral crystallinity (in the short range order of the phosphate ions), have previously been calculated from FTIR spectra of bone (Rey *et al.*, 1991, Pienkowski *et al.*, 1997, Miller *et al.*, 2001, Surovell & Stiner, 2001, Bazin *et al.*, 2009, Thompson *et al.*, 2012, Turunen *et al.*, 2013, Pestle *et al.*, 2014). Calculation of these parameters is considered in Table 5.1.

Parameter	**Calculation** (where A relates to integrated area)	**References**
Degree of bone mineralisation (Mineral to organic ratio)	$v_1v_3PO_4^{3-}$ / Amide I **A(900 – 1200cm^{-1}) / A (1600 – 1800 cm^{-1})**	Paschalis *et al.*, 1997 Pienkowski *et al.*, 1997
Relative amount of carbonate (Carbonate to phosphate ratio)	$v_2CO_3^{2-}$ / $v_3PO_4^{3-}$ **A(840 – 890cm^{-1}) / A (900 – 1200 cm^{-1})**	Pienkowski *et al.*, 1997 Bohic *et al.*, 1998
Mineral crystallinity (referred to as crystallinity index, CI)	See Figure 5.8, where A+C/B (the splitting factor) corresponds to:- **605 cm^{-1} + 565 cm^{-1} / 595 cm^{-1}** (Each numerical value represents the absorbance at the given wavelength i.e. .the height of the peak.)	Weiner & Bar-Yosef, 1990 Thompson *et al.*, 2012

Table 5.1 Summary of the parameters often obtained from FTIR spectra of bone. Calculations of these parameters are included along with literature references.

Degree of mineralisation and relative amount of carbonate are calculated from the ratio of integrated peak areas of phosphate, amide I and carbonate peaks (Table 5.1). Mineral crystallinity is calculated from peak intensity values and measures the degree of separation of two asymmetric bending phosphate ($\nu_4PO_4^{3-}$) bands at 565 cm^{-1} and 605 cm^{-1} (Figure 5.8). This calculation is often termed the splitting factor (SF) and large values indicate a high crystallinity (Thompson *et al.*, 2012).

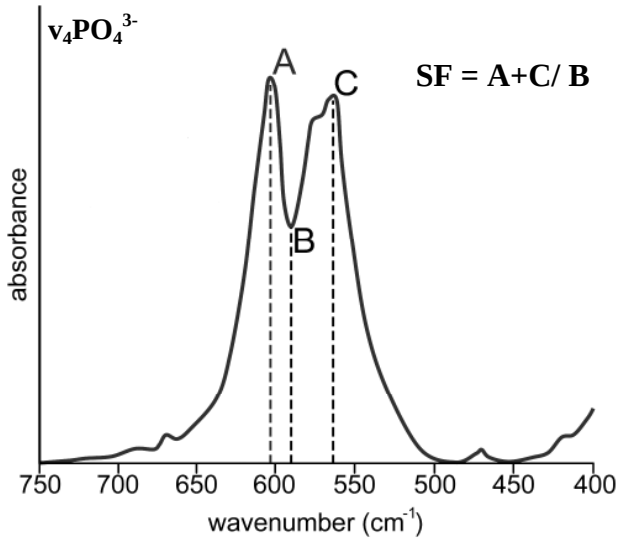

Figure 5.8 Diagram representing calculation of the splitting factor (SF) from the phosphate vibrational mode at 565 – 605 cm^{-1} ($\nu_4PO_4^{3-}$).

As can be appreciated from Figure 5.7, FTIR spectra collected from bone can be extremely complex due to the overlapping peaks associated with both the organic and mineral matrices. Many researchers have tried to overcome this problem using a technique known as Fourier self-deconvolution (Rey *et al.*, 1990, Paschalis *et al.*, 2001, Muyonga *et al.*, 2004, Kaflak *et al.*, 2011, Spevak *et al.*, 2013, Brangule *et al.*, 2014). Using this technique, peak broadening may be reduced without distorting the spectrum, which increases the resolution of the overlapping spectral features (Giffiths and Pariente, 1986, Tooke, 1988, Mantsch *et al.*, 1988). This approach was first applied to infrared spectroscopy by Kauppinen *et al.* (1981), who found peak widths at half height can be reduced without significantly distorting the spectrum.

In order to understand the basic principles of this Fourier self-deconvolution, the infrared absorbance band at a given wavelength, $A_{v,}$ needs to be considered as shown in equation 5.21:

$$A_v = A_0 \frac{y^2}{[y^2 + (v - v_0)]^2} \tag{5.21}$$

, where A_v corresponds to the infrared absorbance band at a given wavelength, A_0 is the maximum absorbance of the peak, ν_0 is the wavenumber of the peak and γ is the half-width at half-height (HWHH) of the peak.

By taking the cosine Fourier transform of equation 5.21, equation 5.22 is derived:

$$F(x) = \int_0^\infty A_v \cos(2\pi vx)dv = 0.5A_0\gamma \cos(2\pi vx)\exp(-2\pi vx) \tag{5.22}$$

, where x is the spatial frequency and has the units of 'reciprocal wavenumbers' or centimetres

The exponential decay term, exp(-2πvx), is determined by γ, thus the wider the peak, the more rapidly the Fourier transform decays. By decreasing the rate of decay of the exponential term, the peak width is reduced. In theory, this can be achieved by multiplying F(x) by an exponentially increasing function. Fourier self-deconvolution is performed by multiplying F (x) by exp(2πγ' x), which yields a new function, as shown in equation 5.23:

$$F'(x) = F(x)\exp(2\pi\gamma' x) = 0.5A_0\gamma \cos(2\pi vx)\exp[-2\pi(\gamma - \gamma')x] \tag{5.23}$$

By performing the reverse Fourier transform on F'(x), a new peak, A'ν, which is narrower than Aν and has the shape of the Fourier transform, exp(2πγ'x), is obtained. The HWHH of each peak is reduced to (γ - γ').

For this research, FTIR was used to quantify differences in the organic and carbonate content between unheated and heated biological and synthetic HAp specimens. FTIR was also used to investigate the presence of A - type carbonate, which is currently disputed by some researchers. This is discussed further in section 7.2.2.2.

5.2.2 Ultraviolet –Visible Spectroscopy (UV-Vis)

Ultraviolet-visible spectroscopy (UV-Vis) relies on the premise that electrons from ions, molecules and atoms are located in orbitals capable of holding up to two electrons (Dyer, 1965, Clark *et al.*, 1993, Langford *et al.*, 2005, Jackson & Jackson, 2008, Chen *et al.*, 2013). Absorbance of electromagnetic radiation in the ultra violet to visible region causes a promotion of an electron from the ground state (the current orbital) to a higher energy status (an orbital which is either unoccupied or partially occupied). These promotions, termed electronic transitions, require a certain amount of energy which is proportional to the wavelength absorbed. Again, the energy transmitted is detected and the absorbance (and therefore the amount of energy required to cause electronic transition) can be calculated as a function of wavelength. UV-Vis spectroscopy consists of a radiation source, an optical spectrometer, a detector and a sample stage. The data collected is represented on a spectrum where the x-axis represents wavenumber (cm^{-1}) and the y-axis represents the intensity of the transmitted or absorbed radiation.

In comparison to infra-red spectroscopy, spectra obtained from UV-Vis spectroscopy provide limited information about the structure of the molecule. However, it is a powerful technique when used to calculate solution concentrations. With increasing concentration, an increase in absorbance is observed and can be quantified according to Beer Lamberts Law, shown in equation 5.24:

$$A = \varepsilon \ell c$$

(5.24)

, where A is absorbance, ε relates to the molar absorption coefficient, ℓ is the length of the light path (cm) and c is the molar concentration

In this thesis, UV-VIS spectroscopy was used for the first time to calculate the concentration of citrate extracted from various biological HAp specimens (section 7.2.2.6). The amount of citrate in bone has previously been quantified using nuclear magnetic resonance (NMR) (Hu *et al*., 2010), however the sample preparation method employed could potentially be flawed as discussed in chapter 3. Further, the amount of citrate in other biological HAp specimens has not previously been considered.

5.2.3 Colourimetric Analysis

As discussed in section 4.1.1, bone undergoes a wide range of colour changes during heat treatment, which has been associated with the loss of surface bound and lattice incorporated water, combustion of the organic matrix, loss of carbonate from the mineral matrix and mineral calcination (thermal decomposition). The colour of bone is commonly used by anthropologists to estimate the temperature at which a bone specimen had been heated using the standardised Munsell chart. Unfortunately this method is largely subjective and can be influenced by the eyesight of the individual, fading of the standard Munsell chart and inconsistencies in the light source. To avoid any potential errors, colourimetric analysis will be employed in this research to accurately determine the colour of bone specimens heated at various temperatures for a variety of time periods. Colourimetric analysis refers to the process of quantifying and numerically describing human colour perception (Malacara, 2002, Ohta & Robertson, 2006, Konica Minolta, 2014). For this research, a colourimeter was used following the protocol outlined in section 7.2.2.4.

Colourimetric measurements are based on human colour perception (Stockman, 2003, Konica Minolta, 2014). The sample is illuminated with white light and dependent on the colour of the sample, some of the light is absorbed whilst a proportion of the light is reflected (termed spectral reflectance). In humans, the reflected light is perceived by the cones in the eye and processed by the brain. In contrast, colourimeters use optical systems and sensors.

To quantify colour data, colourimetry instruments depend upon colour scales. For this thesis, the CIE (International Commission on Illumination) L*a*b colour scale, which is widely used in a variety of industries, was employed. This three dimensional scale uses a linear colour space which correlates to the human perception of colour according to the opponent colours theory (Schanda, 2007, Konica Minolta, 2014). According to this theory, responses from the red, green and blue cones found within the human eye are re-coded into black-white, red-green and yellow-blue once the signals reach the brain. The CIE L*a*b colour scale simulates the colour of a sample according to the linear colour space as shown in Figure 5.9.

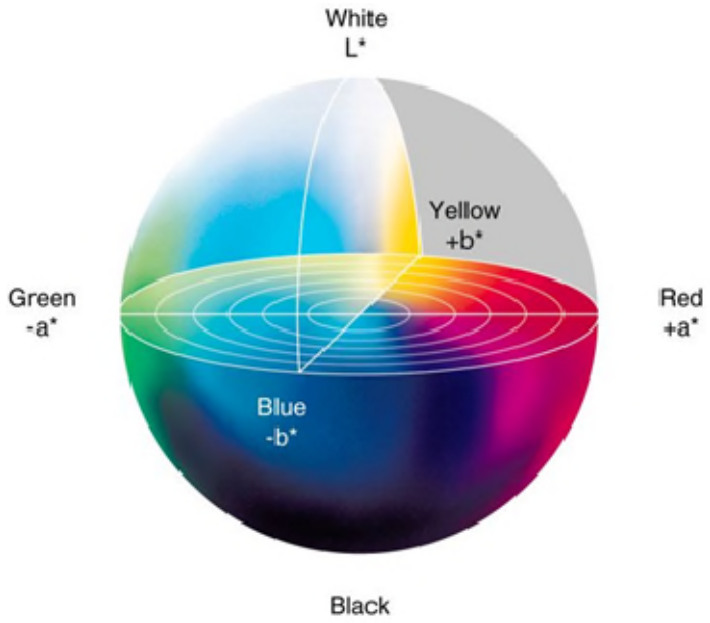

Figure 5.9 3-D representation of colour using L*a*b* colour scale

The ‘lightness’ of a sample is quantified by the L* axis, which has a scale of 0 (black) to 100 (white), the a* axis quantifies the sample between green (negative values) and red (positive values) and the b*axis describes the blue (negative values) or yellow (positive samples) colouration of the sample (Konica Minolta, 2014). For both a* and b* axis, a value of 0 corresponds to a neutral result

5.3 Laser Ablation-Inductively Coupled Plasma – Mass Spectroscopy (LA-ICP-MS)

Atomic spectroscopic techniques (such as inductively coupled plasma-mass spectroscopy, ICP-MS) are used to determine the presence of certain elements in a sample and utilise the phenomenon that gaseous atoms absorb electromagnetic radiation in the ultraviolet-visible range across a wide wavelength region of 0.002 to 0.005 nm (Becker & Dietze, 1998, Gross, 2004, Resano *et al.*, 2010). This allows the concentration of a large number of elements to be determined, even in complex mixtures. Atomic spectrometry in the form of laser ablation – inductively coupled plasma – mass spectrometry (LA-ICP-MS) has in recent years become the preferred elemental analysis technique for complex matrices such as bone (Prohaska *et al.*, 2002, Kang *et al.*, 2004, Castro *et al.*, 2010, Kowal-Linka *et al.*, 2014).

During LA-ICP-MS analysis, a solid sample is laser ablated to generate fine particles. These particles are then transported to the ICP instrument where the chemical compounds contained in the fine particles are decomposed into their atomic constituents using inductively coupled argon plasma. The gaseous atoms are then ionised with a low fraction of multiple charged ions. The now positively charged ions are extracted into the mass spectrometer via an interface. The ions are separated according to their mass to charge ratio using a mass analyser and detected by a photomultiplier.

The use of laser ablation coupled to ICP-MS offers robust, rapid analysis without compromising on resolution. Further, and possibly the major advantage of LA-ICP-MS is minimum sample preparation. Analysis is performed on solid specimens unlike conventional ICP-MS which requires solution digestion prior to sampling. For this research, LA-ICP-MS was used to quantify trace amounts of lead (Pb), strontium (Sr),

zinc (Zn), iron (Fe), potassium (K) and magnesium (Mg) in unheated bone specimens collected from various species. Evaluating the elemental composition of unheated bone may aid in providing a new insight into the processes associated with the physicochemical modifications to bone during heat treatment, in particular the thermal decomposition process.

5.4 Differential Scanning Calorimetry (DSC)

Differential scanning calorimetry (DSC) analysis has become a powerful technique for determining the thermodynamic properties of many biological systems including bone (Sturtevant, 1987, Cooper & Johnson, 1994, Miles *et al.*, 1995, Nielsen-Marsh *et al.*, 2000, Lozano *et al.*, 2003, Garbett *et al.*, 2014). It is used to monitor exothermic and endothermic reactions associated with chemical changes and phase transitions within materials during heat treatment (Watson *et al.*, 1964, Laye, 2002, Höhne, 2003, Dunn, 2003, Gill *et al.*, 2010). This simple yet very effective technique involves simultaneously heating (and cooling) a specimen and reference sample (usually an empty DSC pan) under identical conditions (Figure 5.10).

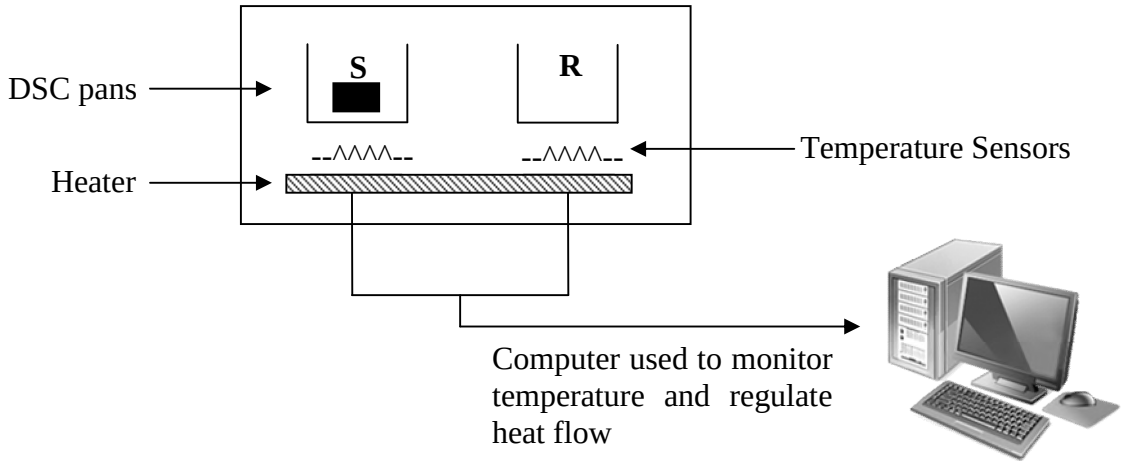

Figure 5.10 Diagram representing a DSC sample chamber adapted from Dunn (2003). In this example, a single heater is described, however in a power-compensated DSC; individual heaters are used (Zucca *et al.*, 2002).

During heating, DSC measures the difference in the heat flow rate to the specimen and the reference sample, which is recorded as a function of temperature or time. Any physicochemical changes to the specimen which causes an increase in the temperature, is recorded as an exothermic peak on the DSC curve. Conversely, a chemical change to the specimen which requires more energy (increase in absorption of heat), results in an endothermic peak.

DSC data is plotted as a function of heat flow (in watts per gram, Wg^{-1}) against temperature. Peaks within a DSC plot represent the rate of the energy absorption by the specimen, relative to that of the reference sample. Information such as the temperature at which a chemical process occurs and the peak temperature associated with maximum reaction rate can be obtained from DSC curves. Further, the total enthalpy change (in Jg^{-1}) for any chemical process resulting from an exothermic or endothermic reaction can be calculated from the integral area of a DSC peak using equation 5.25:

$$\Delta H = \int \frac{1}{R} \frac{dQ}{dt} dT \qquad \textbf{(5.25)}$$

, where ΔH corresponds to total enthalpy change, R is the heating rate employed for the experiment, dQ/dt is the net rate of heat absorbed or released by the sample and dT is the temperature (Ohodnicki , 2008).

For this research, DSC was used to investigate any exothermic or endothermic reactions occurring during heat treatment for a variety of bone specimens. Based on previous work, it may be possible to observe and quantify the loss of surface and lattice bound water, collagen combustion and/ or the physicochemical changes to the mineral component using DSC (Nielsen-Marsh *et al.*, 2000, Lozano *et al.*, 2003, Etok *et al.*, 2007).

5.5 Concluding Remarks

A wide range of analytical techniques were utilised for this research. Some of these techniques are routinely used to analyse bone (XRD and FTIR), whilst others are not as conventional within bone literature (LA-ICP-MS, UV-Vis, colourimetry). It is proposed that using these techniques will provide a new insight into the fundamental processes and mechanisms associated with unheated and heated bone.

The primary technique utilised was XRD, which is a non-destructive technique used to provide information on crystalline structures. The use of XRD to investigate changes to the mineral microstructure of unheated and heated is well documented in the literature. Although a powerful technique, XRD analysis of bone is not without limitations. Due to direction dependence broadening and nanocrystalline nature of biologically formed HAp crystals, diffraction data can be difficult to appropriately parameterise. FTIR, a complementary technique to XRD, is used to investigate the molecular structure of a sample. The advantage of FTIR is that both the mineral and organic components of bone can be investigated simultaneously. For instance, the carbonate content, associated with the mineral matrix and relative amount of collagen can both be quantified using FTIR, as outlined in section 7.2.2.2. The main limitation of FTIR is the complexity of the raw data. Due to overlapping absorbance bands associated with both the mineral and organic components of bone, the analysis of FTIR spectra can prove difficult. Consequently, Fourier self-deconvolution is often used to resolve the issue of overlapping peaks.

As discussed in section 4.1.1, bone undergoes a number of colour changes during heating, which have been associated with the combustion of the organic matrix and chemical changes to the mineral. Using colourimetry, these colour changes where quantified and the values used to develop a time and temperature predictive model for heated bone (section 8.8.2). LA-ICP-MS is a highly sensitive elemental technique, used in this research to investigate the elemental differences between different bone types (different speices). For the first time, UV-Vis was used to quantify the amount of citrate in a variety of biological HAp specimens, in order to investigate the hypothesis that this molecule provides an extrinsic source of control on *in vivo* HAp crystallite size (chapter

3). DSC was used to quantify any exothermic or endothermic reactions occurring during heat treatment of bone.

Chapter 6: SUMMARY OF LITERATURE, AIMS & OBJECTIVES

6.1 Summary of Literature

Bone is a highly complex composite material which receives a large amount of attention across a wide range of disciplines. Although the general structure and composition of bone is largely understood, discrepancies at the nano-level are highlighted in the literature. For instance, nucleation and *in vivo* growth of biological HAp crystals is heavily disputed (section 2.2.3). Once nucleated, *in vivo* growth of HAp crystals are limited to various degrees, resulting in a range of biological apatites exhibiting crystals of different sizes. Over the years, various mechanical, extrinsic and intrinsic sources of control have been proposed for this *in vivo* HAp crystallite size control (chapter 3). Current literature appears to favour extrinsic control mechanisms, with citrate currently deemed to play a crucial role in *in vivo* HAp crystal size control. Intrinsic sources of control due to ion substitutions, lattice strain and dissolution have also been implicitly suggested. Controversies within unheated bone studies are possibly due to the complexity of bone as a material. As discussed in section 5.1.3, unheated bone can be difficult to parameterise (in particular for crystallite size and strain) due to its nanocrystalline, direction dependent nature. Further, the composite nature of bone can complicate data analysis (section 5.2.1).

Heated bone studies are prevalent, however the fundamental processes and mechanisms associated with physicochemical modifications to bone mineral during heat treatment are not fully understood. Arguably, studies within this area are largely observational and in some instances ambiguous. For instance, many studies do not take into account confounding effects of cooling on the HAp structure. There are currently various debates within heated bone research including whether it is possible to differentiate burnt bone according to species using XRD (section 1.2.3) as well as the role of the organic matrix during heat treatment (section 4.3).

6.2 Aims and Objectives

The overall aim of this thesis was to investigate the fundamental processes and mechanisms associated with physicochemical modifications (crystallisation and thermal decomposition) to bone mineral during heat treatment. In particular, the role of the organic matrix during heat treatment was considered. This was achieved through investigation of the physicochemical changes to bone specimens which varied in organic content and consequently in crystallite size. A wide range of temperatures and time periods were investigated. The confounding effects of cooling were also investigated; this is a fundamental area of research which has not previously been considered.

In order to provide a new insight into the fundamental processes and mechanisms associated with physicochemical changes to bone mineral during heat treatment, it was necessary to appreciate the mineral microstructure of HAp prior to heat treatment. This included investigation of current refinement methods used to parameterise XRD data in terms of crystallite size and strain. These methods have not previously been critically assessed for biological HAp. As aforementioned, biological HAp specimens which differed according to *in vivo* crystallite size and strain, were utilised for this research. It was therefore essential to understand *in vivo* HAp crystallite size control, an area of research which is currently conflicting. The individual thesis objectives are as follows:-

1. Investigate current refinement methods used to obtain crystallite size and strain values from XRD data of unheated biological HAp specimens (section 5.1.3).
2. Investigate the source of *in vivo* crystallite size control in unheated biological HAp specimens. Literature suggests various mechanical, extrinsic and intrinsic sources, with current studies suggesting citrate plays a primary role (chapter 3).

3. Provide a new insight into the fundamental processes and mechanisms associated with crystallisation and thermal decomposition of bone mineral during heat treatment. The role of the organic matrix during these physicochemical changes will be examined (chapter 4). The influence of cooling on the physicochemical changes to bone mineral will be investigated using dynamic heat treatment. I.e. Data is collected during heat treatment, negating the influence of cooling.

4. Apply the research to current issues within bone research to:-

    - Determine whether work from different research groups can be compared depending on heating and cooling regimens employed.

    - Develop a method to calculate both the temperature and time of an unknown burnt bone specimen. Current techniques are limited as they only predict temperature (chapter 4).

    - Validate whether burnt bone can be differentiated according to species using XRD. This is currently debated between research groups (chapter 1).

A summary of the key areas of research investigated in this thesis in order to meet the aims and objectives is provided in Figure 6.1. The results (chapter 8) and discussion (chapter 9) will follow the order proposed in Figure 6.1. An extension of Figure 6.1, which summarises the key findings of this research, is provided at the end of chapter 9 in Figures 9.1 and 9.2.

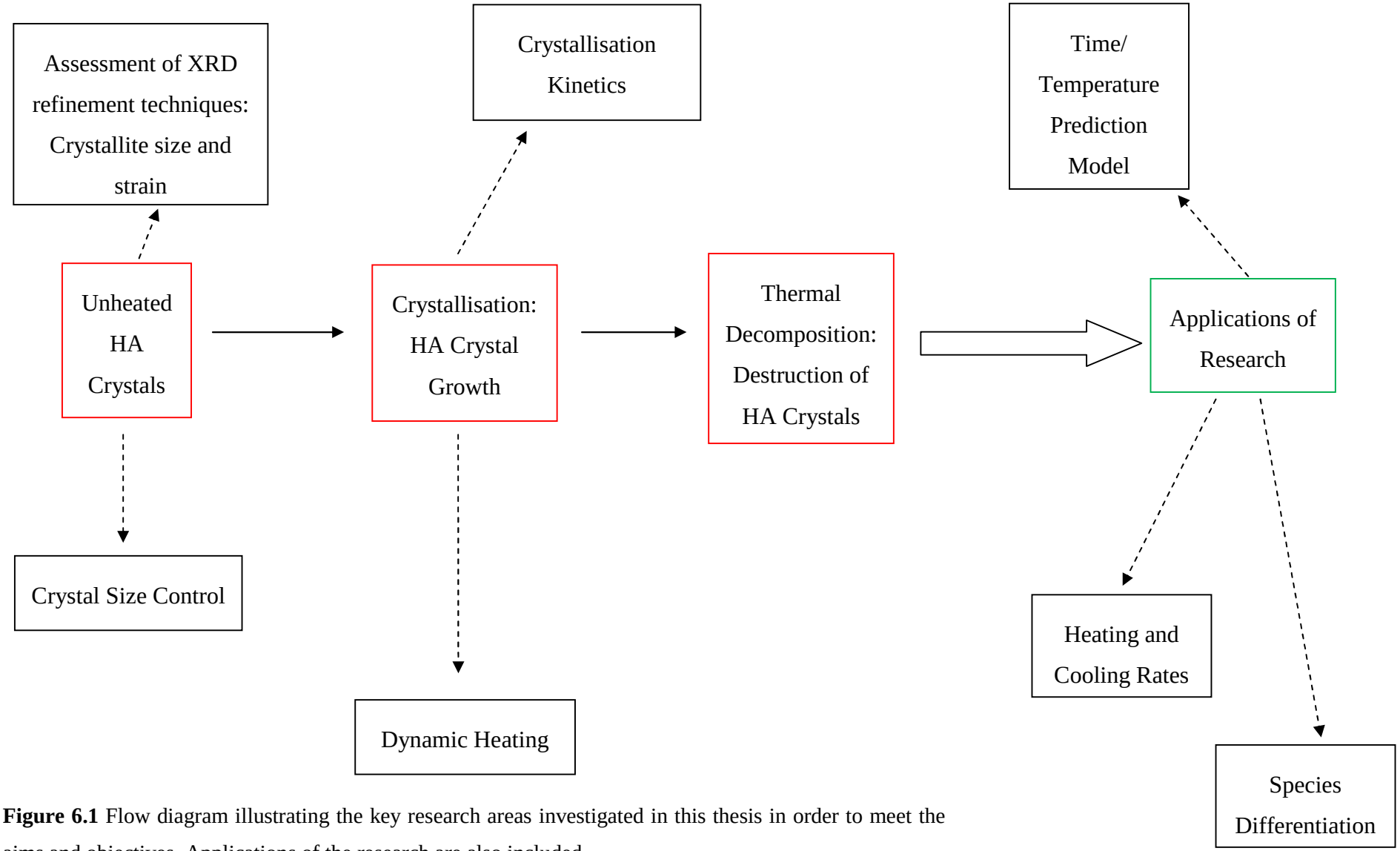

Figure 6.1 Flow diagram illustrating the key research areas investigated in this thesis in order to meet the aims and objectives. Applications of the research are also included

Chapter 7: MATERIALS AND METHODS

This chapter outlines the materials utilised for this study and the methods employed. The main aim of this research was to provide a new insight into several fundamental processes associated with unheated and heated bone. This was achieved by considering a range of HAp specimens, including bone from various species, urinary calculi and synthetic HAp. Three repeats for each specimen were obtained and each analysed using the analytical techniques outlined in section 7.2.2. The source and biographical information of these specimens are provided below in section 7.1. Section 7.2 outlines the methods employed for this research and initially details general sample preparation techniques, which includes details on different heating and cooling regimens. The individual protocols associated with each analytical technique are then described. The analytical techniques employed were used to characterise HAp specimens as well identify and quantify physicochemical modifications to bone mineral during heat treatment. Each technique provides different, and in some instances, complementary data.

7.1 Materials

7.1.1 Bone Types

Porcine, bovine, their anorganic analogues and human bone, rostrum (defined as the beak, upper jaw or 'snout') from a *Mesoplodon densirostris* whale and red deer antler specimens were utilised throughout this research. *Mesoplodon densirostris* whale rostrum specimens are termed 'rostrum' for the remainder of this thesis whilst red deer antler specimens are referred to as 'antler'. Details regarding the source and biographical information for these specimens are provided in Table 7.1. All specimens were obtained and stored at approximately -20 ^{o}C immediately after death, from animals

and donors with no known diseases. All specimens were defleshed prior to use within this research, detailed in section 7.2.1.1.

Bone Type	Source	Age	Sex	Received from
Bovine	Femoral Shaft	~ 2.5 yrs. and ~ 3 yrs.	Male	Local Abattoir
Porcine	Femoral Shaft	~ 1 yr. and ~ 2 yrs.	Female	Animal Health and Veterinary Laboratories Agency (AHVLA)
Human	Femoral Shaft	55 yrs.	Male	London Tissue Bank
Rostrum (*Mesoplodon densirostris)*	NA	Unknown	Unknown	Department of Biology, University of Barcelona, Spain,
Red Deer Antler	NA	Unknown	Male	Animal Health and Veterinary Laboratories Agency (AHVLA)

Table 7.1 Details of which bone was utilised, the age and sex of the individual / animal the bone was collected from and the organisation which supplied the material.

Animal bone specimens were utilised for this research due to the limited availability of human bone tissue. For porcine, bovine and human bone, the specimens were obtained from the femoral shaft as this bone type provides a large number of samples, is more likely to be found within a forensic context as it is more robust than smaller bone types after heat treatment and/ or smaller bone types are more likely to be removed from a

scene by scavengers. To reduce the number of variables associated with different bone types, maximise the breadth of research and to allow for inter-species comparisons, one bone type (the femoral shaft) was utilised. All soft tissue was removed from the bone specimens to ensure the behaviour of bone during heat treatment was investigated, without being affected by an external factor such as soft tissue. Archaeological bone specimens were not utilised as the initial chemistry of the bone (both the organic and mineral components) may have been altered due to diagenetic processes (Rogers *et al*., 2010).

'Anorganic' bone material (essentially collagen free bone) was produced and utilised throughout this research. The method for this is outlined in section 7.2.1.1, whilst the results are presented in section 8.1. 'Anorganic' bone material was utilised in this research to investigate the intimate relationship between the mineral and organic matrices in bone. By comparing the thermal behaviours of anorganic material to those of untreated bone specimens (essentially organic material), the role of the organic matrix during crystallisation and thermal decomposition could be evaluated. With regards to this rationale, by investigating the thermal behaviours of both rostrum and red deer antler specimens, which differ significantly in their mineral to organic content, this intimate relationship could be investigated further. Current literature suggests the organic matrix has a 'shielding' effect on bone mineral during heat treatment as discussed in section 4.3.

7.1.2 Urinary Calculi Specimens

Urinary calculi from six individual canines and one feline were utilised in this research, details of which are outlined in Table 7.2. The specimens were prepared for analysis as outlined in section 7.2.1. The main mineral phase of these specimens resembled calcium HAp as outlined in section 8.2.2. Urinary calculi specimens were utilised in this research to investigate *in vivo* HAp crystallite size control. As discussed in chapter 3, various extrinsic and intrinsic forms of control have been suggested for *in vivo* HAp crystallite size control in bone. However, *in vivo* crystallite size control of HAp crystals

formed in different chemical environments has not previously been reported. Considering urinary calculi as well as bone specimens allowed investigation into whether current reported forms of control can be applied to other biologically formed hydroxyapatites. Potentially, this could refute or validate the current schools of thought with regards to *in vivo* HAp crystallite size control. Animal rather than human urinary calculi were utilised due to availability and were deemed suitable for investigating the fundamental mechanism associated with *in vivo* HAp crystallite size control.

Urinary Calculi Specimen	**Species**	**Breed**	**Sex**	**Age**
A	Canine	Shih Tzu	Female	7 yrs.
B	Canine	Bichon Frise	Female	11 yrs.
C	Feline	Unknown	Male	Unknown
D	Canine	West Highland Terrier	Male	Unknown
E	Canine	Greyhound	Male	2 yrs.
F	Canine	Cairn Terrier	Female	10 yrs.
G	Canine	Yorkshire Terrier	Female	4 yrs.

Table 7.2 Details of the species, breed, sex and age of the animal from which the urinary calculi specimens were collected.

7.1.3 Synthesis of Calcium Hydroxyapatite

Nanocrystalline hydroxyapatite (sHAp1) was prepared by a wet chemical precipitation method through slow addition of aqueous calcium nitrate tetrahydrate [$Ca(NO_3)_2.4H_2O$] into a di-ammonium hydrogen orthophosphate [$(NH_4)2HPO_4$] solution. This reaction is expressed in equation 7.1:

$$10Ca(NO_3)_2.4H_2O + 6(NH_4)_2HPO_4 + 8NH_4OH \rightarrow Ca_{10}(PO_4)_6(OH)_2 + 20NH_4NO_3 + 6H_2O \quad \textbf{(7.1)}$$

0.5M solutions of $Ca(NO_3)_2.4H_2O$ and $(NH_4)2HPO_4$ were prepared by adding 5.91g and 3.30g respectively to 50ml of distilled water. $Ca(NO_3)_2.4H_2O$ solution was slowly added to 30 ml of $(NH_4)2HPO_4$ solution at a rate of 1.5 mL min^{-1} under continuous agitation. This ensured a Ca: P ratio of ~ 1.67. During synthesis, the pH of the mixture was kept constant at 10.4 by drop wise addition of 2% ammonium solution (NH_4OH).

The solution was allowed to mature as a precipitate, for 50 hours at room temperature under constant agitation. The resultant precipitate was washed with distilled water four times to remove ammonia. After each wash, the precipitate was centrifuged at a speed of 10,000 rpm for 5 minutes. Once washed, the precipitate was dried at 37 ^oC for 12 h. The precipitate was powdered following the procedure discussed in section 7.2.1 and characterised as calcium HAp using XRD and FTIR as outlined in section 8.2.3. Three individual batches were produced to ensure reproducibility.

In addition to synthetic HAp specimen, sHAp1, two further synthetic HAp specimens (sHAp2 and sHAp3) were utilised throughout this research. All three synthetic HAp specimens differed in crystallinity (section 8.2.3). sHAp2 and sHAp3 were supplied from Dr Kyriaki Skartsila at the Natural History Museum, London, and were thought to be synthesised in the same way as described above. However, as the crystallinity varied for sHAp2 and sHAp3 it is anticipated an additional step was included in the synthesis. Unfortunately, this information was not available for inclusion in this thesis.

7.1.4 Concluding Remarks

A range of biological and synthetic HAp specimens have been employed in order to provide a complete model of the processes associated with unheated and heated bone. These specimens were used in this research to investigate the use of current XRD refinement techniques (used to determine crystallite size and strain) for nanocrystalline HAp data and to provide information on *in vivo* HAp crystallite size control, HAp crystallite growth during heat treatment (crystallisation) and thermal decomposition of HAp. Thus, several individual experiments were carried out to investigate these four fields of research. A summary of which specimens were used within each experiment is provided in

Table 7.3.

Research Topic	Specimens Utilised	No. of Specimens (inc. repeats)
Producing ‘Anorganic’ Bone Material	Bone: Bovine and Porcine	247
Material Characterisation	All specimens	51
Assessment of XRD refinement techniques: Crystallite size and strain	All specimens	33
In vivo HAp crystallite size control	Bone: Rostrum, bovine, porcine, red deer antler	12
	Urinary Calculi: All specimens except UC_E	33
	Synthetic HAp: All specimens	9
Statically Heated Bone	Bone: Bovine, porcine, ‘anorganic’ bone material, rostrum, red deer antler	582
Dynamically Heated Bone	Bone: Rostrum, human, porcine, bovine, red deer antler	15
Heating and Cooling Rates	Bone: All specimens except anorganic	56
Time/ Temperature Model	Statically heated bone data (except anorganic material)	
Species differentiation	Dynamically heated bone data	

Table 7.3 Summary of which specimens (bone, urinary calculi and synthetic HAp) were used within each experiment

The specimens utilised in this research were chosen to provide a fundamental understanding of the physicochemical changes to bone mineral during heat treatment. Animal proxies were selected due to the limited availability of human bone tissue as well as the ethical implications of using human tissue to investigate a fundamental area of research. Both rostrum and red deer antler were selected to provide 'extremes' specimens in relation to mineral and organic content. This allowed the mineral to organic relationship during heat treatment to be considered through the widest natural range. Although the specimens were carefully selected in order to fulfil the aims and objectives of this research, there were some confounding effects to keep in mind for ultimate application of the results. For example, all specimens were defleshed prior to heat treatment to remove any confounding effects the soft tissue may have had. Arguably, such 'ideal' specimens cannot be applied to 'real life' forensic cases, where most bone specimens would have been heated in the presence of soft tissue. To use fleshed bone specimens in this research would have provided a very complex variable which may have obscured the fundamental physicochemical changes to bone mineral during heat treatment. Furthermore, as human specimens were not utilised throughout this research for reasons discussed earlier, this research cannot strictly be applied to forensic cases immediately. Further work would be required as discussed in section 10.3.

The research presented here used 'fresh' bone. Thus some caution should be adopted when translating the results to archaeological burnt bone that may be affected by diagenetic processes. Again, the confounding effects of diagenesis would have provided another variable to an already complex system. In order to understand the changes to bone mineral at certain temperatures, the specimens were heated within a controlled setting at the desired temperature. Although this enabled a fundamental study it is highly unlikely a burning event associated with a forensic case would take place in a controlled environment, with many external factors influencing the rate and temperature of a fire.

This research has provided a fundamental understanding of the physicochemical changes to bone during heat treatment which will be beneficial in future bone mineral studies. It is essential to understand the fundamentals prior to introducing other variables such as fleshed or archaeological bone specimens. As this is a fundamental study there is wide scope to extend the research, discussed further in section 10.3.

7.2 Methods

The methods employed for this research individually allowed investigation of the mechanisms associated with *in vivo* HAp crystallite size control of unheated HAp specimens, and the crystallisation and thermal decomposition processes associated with heated bone. Removal of citrate from biologically formed HAp specimens for example, provided a new insight into *in vivo* HAp crystal size control, whilst dynamic heat treatment allowed the confounding effects of cooling on the physicochemical changes to bone mineral to be considered, as well as providing an *in situ* view of the chemical processes.

The specimens identified in the previous section were characterised using XRD and FTIR, whilst physicochemical processes associated with heated bone were identified and quantified using XRD, FTIR, DSC and colourimetric analysis. LA-ICP-MS was used to quantify the elemental compositional of unheated bone specimens, for comparison to the thermal decomposition products observed in heated bone specimens. Results obtained from UV-VIS, XRD and FTIR analysis were used to investigate *in vivo* crystallite size control. Parameters obtained from XRD, FTIR and colourimetric analyses were employed to develop a time and temperature predictive model. The remainder of this section outlines the general sample preparation before providing the methods associated with each analytical technique employed. A summary of how each analytical technique was used in this research as well as any limitations identified, is provided at the end of this chapter in Table 7.7.

7.2.1 General Sample Preparation

7.2.1.1 Bone Preparation

All bone specimens were defleshed using a scalpel. Care was taken to remove all residual soft tissue. Once cleaned, bone specimens were cut into roughly equal sized segments (Figure 7.1) using a Draper (B5355A) 14" band saw and allowed to thaw at room temperature. The samples were cut when frozen to prevent friction between the bone and band saw, limiting any heating effects. All specimens were then weighed to ensure continuity in mass. This also allowed assessment of mass loss due to heating.

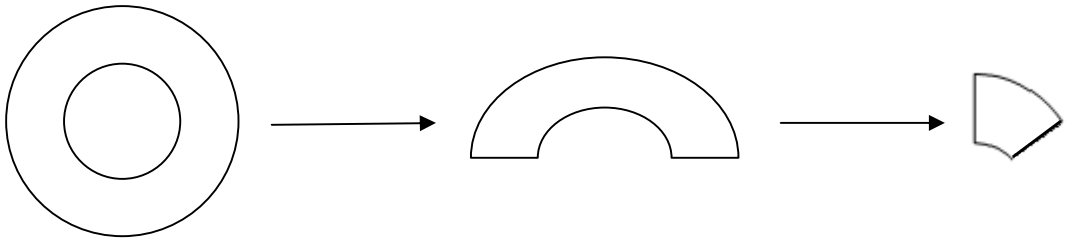

Figure 7.1 Diagram depicting how the bone specimens were cut (~ 1 x 1 x 1 cm).

7.2.1.2 Powdering Specimens

Prior to analytical analysis, all bone specimens were powdered using a Retsch mixer mill (mm 2000). Zirconium oxide milling baskets and balls were used in this process as they are deemed the most durable and efficient media for milling robust materials such as bone. The specimens were milled for one minute and allowed to stand for approximately one minute before milling was continued. This limited the potential of the specimen 'over heating' during milling, which could potentially cause changes to the mineral microstructure. Once powdered, the specimens were sieved through a

stainless steel mesh of 106 µm to produce a homogenous fine powder sample. Due to the integrity of unheated bone, these specimens were cut into smaller segments prior to powdering. This aided the milling process and reduced the number of milling cycles required. This was deemed suitable to eliminate the potential effects of 'over – milling' on the mineral microstructure.

The same protocol was followed for urinary calculi and synthetic HAp specimens except a pestle and mortar was used to powder the specimens rather than a milling device. These specimens were not as robust as bone, which allowed for manual powdering. When appropriate (when the integrity of the material allowed), manual milling was employed, as this protocol was deemed more advantageous due to quicker sample preparation times. Although two different protocols were employed to powder the bone and urinary calculi specimens, both protocols resulted in a homogenous fine powder with particles of approximately 106 µm. Further, extreme care was taken to ensure the specimens were not 'over-milled'.

7.2.1.3 Statically Heated Bone

Within this thesis, static heating refers to the process in which a specimen is heated (at temperature) and allowed to cool prior to analysis. Static heated bone specimens were placed into the middle of a Carbolite 1600 furnace within individual alumina crucibles. A thermocouple was used to monitor temperature throughout heat treatment. Static heating was utilised to investigate both crystallisation kinetics of bone mineral and the effect of heating and cooling on crystallisation and thermal decomposition of bone mineral. Specimens used to investigate the crystallisation kinetics of bone mineral were placed into the furnace at temperature, heated for a predetermined period of time (dwell period), before being removed at temperature and cooled in air. Bone specimens heated in this way are referred to as 'quenched' specimens. Table 7.4 outlines the dwell periods and temperatures investigated for statically heated bone. Rostrum and red deer antler specimens were also heated at 700 ^{o}C for 5 and 10 minutes and 4 hours using the same regimen as described above, in order to investigate the role of the organic during static heating.

	Temperature (^{o}C)								
	500	**550**	**575**	**600**	**650**	**700**	**750**	**800**	**1000**
Time									
1 m									B
5 m									B
10 m									
20 m									
30 m									
1 hr									
2 hr									
4 hr									
6 hr									
24 hr			B						
48 hr	B	B	B						
72 hr									
96 hr	B								

Table 7.4 Temperature and dwell periods bovine, porcine and their anorganic bone specimens were subjected to in order to investigate the physicochemical changes to statically heated bone. The cells which contain the letter 'B' indicate that only bovine bone was heated at this time / temperature.

The effect of heating and cooling on crystallisation and thermal decomposition of bone mineral, were investigated by programming the furnace to heat and cool at rates of 2, 10 and 25 ^{o}C. Heating rates were investigated by placing bovine bone specimens into the furnace (at room temperature), ramping to the dwell temperature and dwelling for a certain time period before removing and quenching in air. These are referred to as 'heated' specimens in sections 8.8.1 and 9.8.1. Conversely, cooling rates were investigated by placing bovine bone specimens into the furnace at temperature, dwelling and then cooling within the furnace at a certain ramp rate. These are referred to as 'cooled' specimens in sections 8.8.1 and 9.8.1.

To investigate the effect of cooling on the thermal decomposition of bone mineral, bovine, porcine, rostrum, red deer antler and human specimens were heated at 1200 ^{o}C

and 1400 ^{o}C, with a dwell period of two hours. The effect of slow cooling was observed by allowing specimens to cool in the furnace to room temperature immediately after the dwell period, whilst 'fast' cooling was investigated by removing bone specimens immediately after the dwell period (quenched in air).

7.2.1.4 Dynamically Heated Bone

Within this thesis, dynamic heating refers to the process of obtaining data during heat treatment. In this instance, X-ray diffraction was utilised, which provided *in situ* investigation of the physicochemical changes to bone mineral. Approximately 0.5 g of unheated powdered bone from human, bovine, porcine, red deer antler, rostrum and anorganic (bovine) specimens were individually packed into alumina heat stage holders and loaded into an Anton Paar HTK-1200 high temperature X-ray diffraction chamber (section 7.2.1.2 describes the method employed for powdering bone specimens whilst section 7.2.2.1 details the instrumental set up for XRD analysis). A temperature range from 25 – 900 ^{o}C was investigated with diffraction data collected at 25, 100, 200, 350, 400, 450, 500, 550 and 580 ^{o}C and then at every 10 ^{o}C, up to and including the final temperature of 900 ^{o}C. Smaller increments were measured from 580 ^{o}C due to the nature of the crystallisation process. Based on previous work this was expected to occur from approximately 600 ^{o}C, over a short temperature range (Beckett *et al.*, 2011, Greenwood *et al.*, 2012,). A ramp rate of 10 ^{o}C min^{-1} was employed. Data collection time at each selected temperature was 10 minutes. This was considered a good compromise between the quality of data and the period of time the specimen was heated at each temperature point. The same regimen was employed during the cooling period. Dynamic heat treatment of the specimens was conducted at Leeds University, UK.

7.2.2 Analytical Techniques

A wide range of analytical techniques were employed for this research. This section describes instrumental set up, sample preparation and data analysis for each analytical technique. A summary of the information obtained from each technique for use within this research is provided at the end of this chapter in Table 7.7. The errors associated with quantification of the data obtained from these techniques where calculated from the standard deviation of three repeats. For each sample (unheated and heated), three repeats were obtained. Each repeat was analysed and in most instances, the standard deviation of the values calculated for each of the three repeats was used to report error.

7.2.2.1 X-ray Diffraction (XRD) Analysis

All powdered samples (with the exception of those which were dynamically heated as detailed in section 7.2.1.4) were individually back loaded into a XRD specimen holder. A microscope slide was used to flatten and compact the powder into the holder, creating a smooth, even surface, essential for XRD analysis. X-ray diffraction analysis for statically and dynamically heated bone specimens was carried out using a PANalytical X'Pert PRO Multi-Purpose Diffractometer with Cu Kα radiation. A PIXcel strip detector was used to collect data as stepped scans across an angular range of 15 – 80 2θ(^{o}) (5.90 – 1.20 Å d-spacing). The count time at each step was equivalent to five seconds. Two further stepped scans were also carried out (except for those samples which were dynamically heated) under the same conditions but across an angular range of 23 – 27 2θ (^{o}) (3.86 – 3.30 Å d-spacing) and 50 - 55 2θ(^{o}) (1.82 – 1.67 Å d-spacing). These were collected to provide greater data quality for the (002) and (004) reflections respectively. Bruker Topas software (Version 4.1, 2008) was used to carry out profile fitting of each diffraction profile and the structural parameters of the crystal lattice which included lattice parameters, coherence lengths and phase analysis, were calculated.

Coherence lengths were calculated to examine any changes to structural order (size and strain) of HAp crystals. Three different crystallographic directions, <00ℓ>, <0k0> and <hk0> were chosen to investigate the non-isotropic growth of HAp crystals. Asymmetrical split pseudo-voigt (SPV) peaks were fitted to the 002, 004, 030 and 210 diffraction maxima (deemed a good compromise between intensity, overlapping and differing lattice direction) for all diffraction data. SPV peaks are an approximation to a Voigt function which is a combination of Gaussian and Lorentzian peaks (Langford, 1992). Once the peaks were fitted and refined, the peak fitting data was used to calculate the full width half maximum (FWHM). The FWHM values, were used to calculate the relative coherence lengths (CL) in the <00ℓ>, <210> and <030> crystallographic directions using the Scherrer equation (equation 5.3, section 5.1.3). Before calculating coherence length, XRD data was corrected for instrument broadening. A silicon standard (NB1640), which was measured weekly, was used to calculate the instrument resolution factor (IRF) using the peak fitting method described above. The Caglioti equation (equation 5.8) was used to calculate the IRF (section 5.1.3). To investigate bone mineral crystallisation kinetics, coherence length data was fitted to Arrhenius and Kolmogorov-Johnson-Mehl-Avrami (KJMA) equations (section 8.6).

Phase analysis was carried out to identify and quantify HAp thermal decomposition products, present due to high temperature heating. Initially, the mineral phases present within each specimen were identified by comparing the diffractograms with the International Centre for Diffraction Data (ICDD) Powder Diffraction File (version PDF-2, 2004), using Crystallographica Search-Match software (version 2.1.1.1 1996 – 2004). Reference diffraction data of identified mineral phases (provided from ICDD) were fitted and refined to each specimen diffractogram. This provided quantification of each mineral phase in the form of weight percentage (wt. %). Lattice parameters were examined in order to observe chemical modification due to ionic exchanges. To obtain lattice parameter values, whole pattern fitting refinement of diffraction profiles was employed. Sample displacement was also refined and lattice parameter data corrected accordingly.

Rietveld refinement, Williamson-hall plots and single line analysis (section 5.1.3) were investigated for use with nanocrystalline materials such as bone. Crystallite size and strain were individually calculated using the equations outlined in section 5.1.3. For Williamson-hall plots, 002 and 004 reflections were analysed as a compromise between intensity and overlapping peaks. Due to the unreliability associated with fitting the 004 reflection (highlighted in section 8.3.2 and discussed in section 9.3), the peak corresponding to the 002 reflection was employed for single line analysis. The data collected for single line analysis was not corrected for instrument broadening, as the IRF values were negligible compared to the FWHM values.

Direction dependence size and strain broadening contributions due to compositional variations was investigated by employing and extending the model described by Leineweber and Mittemeijer (2003) (Section 5.1.3). This approach, which has not previously been applied to HAp data, investigates peak broadening contributions due to compositional variations in the material. However, the method is modelled on materials where peak broadening is considered to be a product of strain only. For this research, Leineweber and Mittemeijer's model was extended by modifying equation 5.18 (section 5.1.3) to allow for size broadening contributions. This is reported in section 8.3.4.

7.2.2.2 Fourier Transform Infrared Spectroscopy (FTIR) Analysis

Approximately 0.002g of powdered sample and 0.3g of dried powdered (<106 μm sieved) potassium bromide (KBr) was mixed thoroughly and pressed into a pellet using a pressure of 10 tonnes for ~ 20 seconds. Three pellets were made per specimen to investigate reproducibility. KBr was used as a supporting medium in this analysis as it has a large spectral range and excellent transmission (250 nm – 26 μm). FTIR spectra were collected using a Perkin Elmer Spectrum 100 and analysis carried out using PerkinElmer Spectrum software. A scan resolution of 4 cm^{-1} and 16 scans was employed for data collection, within a range of 550 – 2000 cm^{-1} (Figure 7.2).

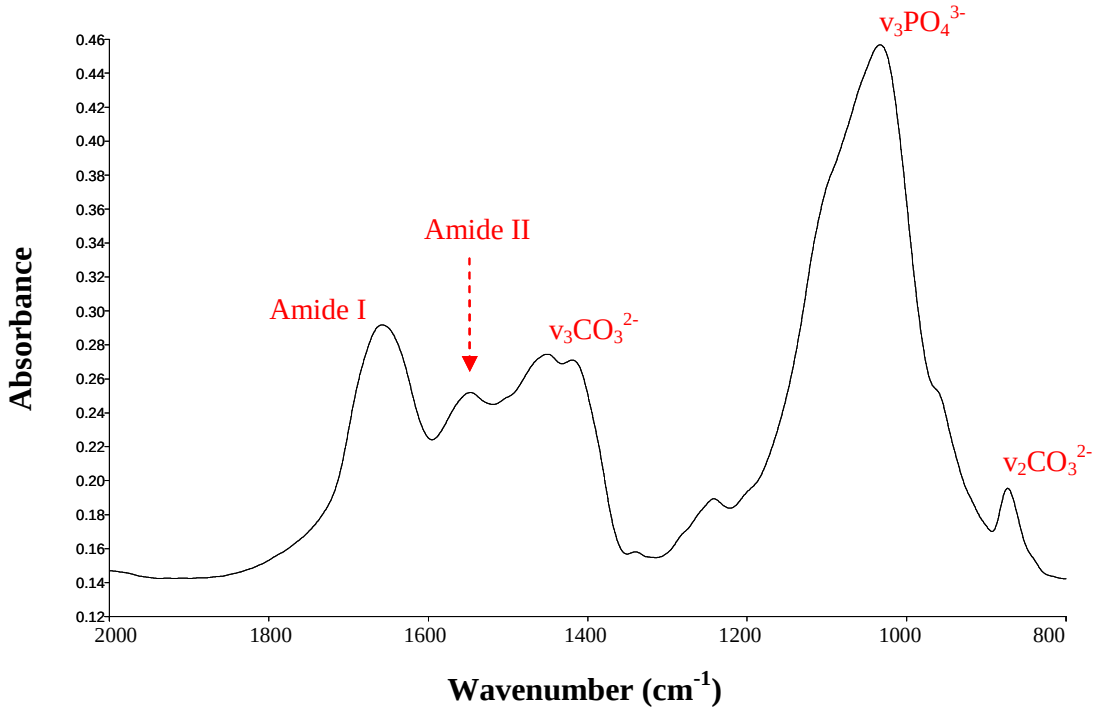

Figure 7.2 FTIR spectra of unheated porcine bone. Amide I, amide II, phosphate and carbonate bands are highlighted. The areas of these bands were used to assess the organic and carbonate content, as discussed in section 5.2.1.

FTIR analysis was employed to provide semi-quantitative data on organic and carbonate content. The organic matrix was assessed through measuring the area of the amide I (1750 - 1600 cm^{-1}) and (1200 – 900 cm^{-1}) phosphate bands (Figure 7.2). The ratios of these values were used has an indication of the amount of organic matrix present within the specimen. This is conventional measurement within bone research as discussed in section 5.2.1.

Prior to assessing carbonate content within biological and synthetic HAp specimens, carbonated HAp standards (purchased from Clarkson Chromatography Products Inc.) were analysed. These contained varying amounts of A-, B- or a mixture of A- and B-type carbonate. As there is conflicting research regarding the presence of A type carbonate (discussed in section 2.2.2), this allowed clarification of the presence of both A and B type carbonate and their associated absorbance bands, prior to analysis of biological and synthetic HAp specimens. Doublet bands observed at 1545 and

1450 cm^{-1} (asymmetric stretching vibration, v_3) and a singlet band at 880 cm^{-1} (out-of-plane bending vibration, v_2) were assigned to A type carbonate. Absorbance bands observed at 1455, 1410 and 875 cm^{-1} were assigned to B type carbonate (Figure 7.3).

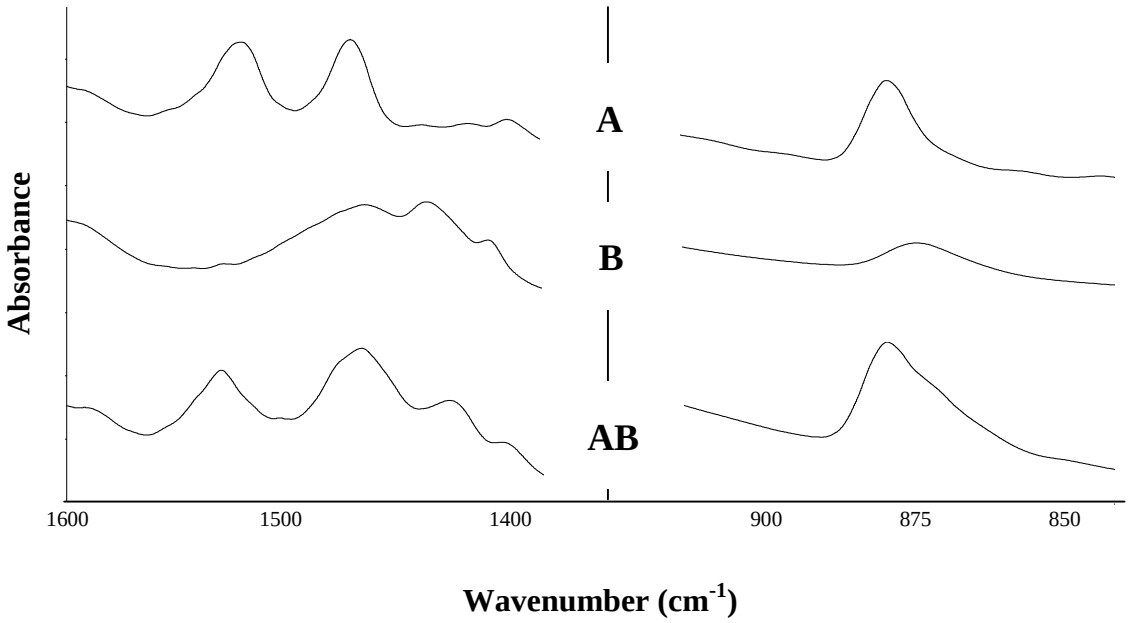

Figure 7.3 Spectra of A-type, B-type and AB – type carbonated synthetic HAp specimens. The spectrums highlight the overlapping nature of carbonate absorbance bands. In bone, the stretching absorbance for amide II would be observed between 1600 – 1500 cm^{-1}.

For bone, the amide II stretching absorbance is observed within the same absorbance as the main peaks for A and B type carbonate (1600 – 1400 cm^{-1}). Consequently, the bands at 880 and 875 cm^{-1} were used to investigate carbonate content. Due to the overlapping nature of the bands within this region (Figure 7.3), FTIR spectra for each specimen were Fourier self-deconvoluted after baseline correcting (section 5.2.1). This separated A and B type carbonate bands as well as the labile carbonate peak (860 cm^{-1}), as shown in Figure 7.4 .

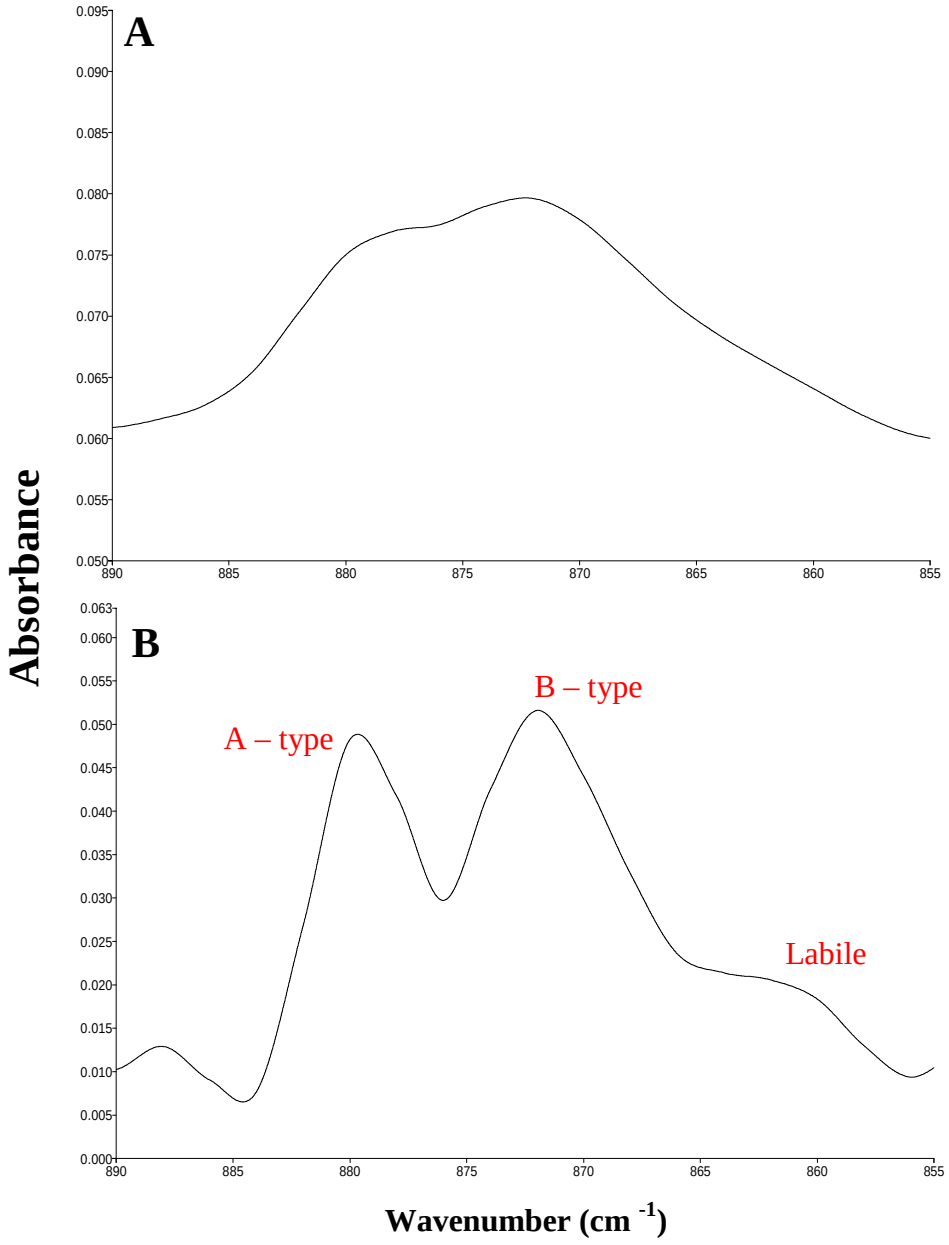

Figure 7.4 FTIR spectra of red deer antler in the range 880 – 855 cm^{-1}. **A** is the raw spectra whereas **B** has been deconvoluted. Both spectra have been baseline corrected.

This allowed accurate measurement of A and B type carbonate whilst ensuring the exclusion of the labile carbonate. Carbonate was investigated with regards to *in vivo* HAp crystallite size control. Thus, lattice incorporated carbonate was solely investigated. Carbonate content was assessed through measurement of A and B type

carbonate peak areas (in the range 880 – 855 cm^{-1}). These values were then used along with phosphate ($v_3PO_4^{3-}$) peak area values to calculate carbonate to phosphate ratios. This semi quantitative measurement is a conventional calculation within bone research and is described in section 5.2.1.

7.2.2.3 Differential Scanning Calorimetry (DSC) Analysis

Approximately 2 mg of powdered unheated bovine, porcine, rostrum, red deer antler and anorganic bovine bone were individually sealed in aluminium pans. A small hole was pierced into the pan cover to allow the release of any combustion gases during heating. Using a Mettler Toledo M3 DSC, bone specimens were heated from 25 ^oC to 600 ^oC at a rate of 10 $^oC\ min^{-1}$. An air flow pump was fitted to the instrument to ensure oxidisation of specimens throughout analysis. Analysis of DSC spectra was carried out using Mettler Toledo Star-e Software. The data was baseline corrected before using the software to calculate integrated peak areas. From the integrated area values, the software was used to calculate the amount of specific energy required to produce each peak, as described in section 5.4.

7.2.2.4 Colourimetric Analysis

For colourimetric analysis, powdered heated bone specimens were placed into individual 50 ml glass sample bottles, ensuring the powder completely covered the bottom of the bottle. The individual glass bottles were placed over the aperture of the Konica Minolta Spectrophotometer cm-700D/600d colourimeter and a total of 10 measurements were taken per sample in specular component excluded mode (SCE). SCE, which excludes all specular light from the measurement, was chosen due to the reflective nature of the glass bottle surface. This ensured a true representation of colour was obtained, rather than a perceived colour due to specular reflectance. Numerical values of ‘L’, ‘a’ and ‘b’ (section 5.2.3) were recorded as well as the gloss value.

7.2.2.5 Laser Ablation-Inductively Coupled Plasma – Mass Spectrometry (LA-ICP-MS) Analysis

Prior to LA-ICP-MS analysis, approximately 1g of powdered bone sample was pressed into a pellet using a pressure of 10 tonnes for approximately 10 seconds. The pellets where mounted on a 10 cm by 10 cm perspex plastic square using double-sided sticky tape. The direct solid laser ablation sampling system (Q switched Nd: YAG 213 nm laser ablation system, New Wave Research) coupled with a quadrupole ICP-MS (Thermo Electron Corporation XSERIES 2, operating in standard mode, Xt cone) was employed to perform 50 second scan-mode analyses (crater of 80 μm) on the surface of the bone pellets.

A pre-ablation time of approximately 15 seconds was selected in order to reduce any contaminations or alterations which may have been present on the outer surface of the pellets. To monitor instrumental drift, reduce background interference and to improve instrument sensitivity, after every six measurements, two synthetic certificated reference glasses (NIST 610-612) were analysed. Certificated bone meal (NIST 1486) and bone ash (NIST 1400) powders were used as reference material for this analysis. Elemental quantification was carried out through PlasmaLab software prior to LA-ICP-MS signals being automatically background and instrument drift corrected. A total of 53 different elements were selected for analysis

7.2.2.6 Extraction and UV-VIS Quantification of Citrate from Biological Hydroxyapatites

A commercially available citric acid assay kit was purchased from Megazyme Ltd, to determine the amount of citrate present within bone and urinary calculi specimens. The reagent solutions and suspensions which were supplied in the assay kit and the preparation required for these solutions are outlined in Table 7.5.

Reagent Solutions / Suspensions	Preparation Required
Buffer Solution (pH 7.5) plus sodium azide (0.02%) as a preservative.	-
Glycylglycine Nicotinamide Adenine Dinucleotide (NADH) and Polyvinylpyrollidone (PVP) Tablets	Dissolve in 16 mL of distilled water.
L-Malate dehydrogenase (L-MDH) and D-lactate dehydrogenase (D-LDH) solution	-
Citrate lyase lyophilisate (CLy) solution	Dissolve in 0.55 mL of distilled water
Citric acid standard solution (5 mL, 0.20 mg/mL)	-

Table 7.5 Reagent solutions and suspensions supplied in the citric assay kit along with any additional preparation which was required prior to UV-VIS analysis. A dash (-) indicates no additional preparation was required.

It was necessary to remove citric acid from bone and urinary calculi specimens prior to assay testing using the following protocol. 10 ml of 1M perchloric acid was added to 0.5g of representative powdered specimen and homogenised. Whilst the solution was continuously mixed using a magnetic stirrer, the pH was adjusted to 8 by slow addition of approximately 1 ml of 8M potassium hydroxide. The solution was then transferred into a 50 ml centrifuge tube and filled with distilled water. The centrifuge tubes were stored on ice for approximately 20 minutes to precipitate potassium perchlorate and to allow for fat separation. The resultant solution was then centrifuged at 13,000 g for 10

minutes using a Mistal 1000 Centrifuge. The clarified supernatant was removed for use with the assay kit.

A Varian Cary 50 UV-VIS Spectrophotometer was used to measure and record the absorbance difference at 340 nm for all specimens following the protocol described below in Table 7.6.

Pipette into 2 separate cuvettes	**Blank**	**Sample**
Distilled Water	2.00 ml	1.80 ml
Sample*	-	0.4 ml
Solution 1: Buffer Solution	0.50 ml	0.50 ml
Solution 2: NADH / PVP	0.20 ml	0.20 ml
Suspension 3: L-MDH / D-LDH	0.02 ml	0.02 ml
A1: Mix, read the absorbance of the solutions after approximately 4 minutes and the reaction is started by addition of:-		
Solution 4: Citrate Lyase (CLy)	0.02 ml	0.02 ml
A2: Mix, read the absorbance of the solutions at the end of the reaction (approximately 5 minutes)		

Table 7.6 The procedure followed for UV-VIS analysis of citric acid extracted from bone type using the citrate assay kit. (*refers to the supernatant obtained during the extraction of citrate).

The citric acid standard supplied in the assay kit was also analysed following the protocol outlined in Table 7.6, to assess the accuracy of the UV-VIS equipment. A background was taken against air (without the cuvette in the light path) and the baseline was corrected for all spectra. A plastic cuvette with a 1cm light path was utilised for this analysis. The concentration and amount of citric acid present within the supernatant of each specimen were calculated using equations 7.2 and 7.3 respectively:

$$c_{citric\ acid} = \frac{VM}{\varepsilon dv} * \Delta A_{citric\ acid} \quad \textbf{(7.2)}$$

, where c = concentration of citric acid (g L^{-1}), V = final Volume (ml), M = molecular weight of citric acid (g mol^{-1}), ε = 6300 L mol^{-1} cm^{-1} (the extinction coefficient of NADH at 340 nm), d = 1cm, the light path of the cuvette, v = sample volume (ml) and $\Delta A = (A_1 - A_2)_{sample} - (A_1 - A_2)_{blank}$.

$$a_{citric\ acid} = \frac{c_{citric\ acid}}{w_{specimen}} \quad \textbf{(7.3)}$$

, where a = amount of citric acid (g/100 g), c = concentration of citric acid (g L^{-1}) and w = weight of the specimen prior to the removal of citric acid (g L^{-1}).

In order to understand the aforementioned protocol, the chemical reactions of the solutions and suspensions which occur when added to a specimen, should be considered. The principle is as follows (Megazyme, 2013):-

Oxaloacetate and acetate are produced from citrate by addition of citrate lyase, equation 7.4:

$$\text{Citrate} \xrightarrow{\textit{Citrate Lyase}} \text{Oxaloacetate + Acetate} \quad \textbf{(7.4)}$$

The oxaloacetate product is then converted to L-malate and NAD+ in the presence of NADA and L-malate dehydrogenase (L-MDH), equation 7.5:

$$\text{Oxaloacetate} + \text{NADH} + H^{+} \xrightarrow{\textit{L-MDH}} \text{L-malate} + NAD^{+} \quad \textbf{(7.5)}$$

If oxaloacetate decarboxylase is present within a specimen, a proportion of the oxaloacetate product is converted to pyruvate. D-lactate dehydrogenase (D-LDH) is employed to efficiently convert any pyruvate into D-lactate and NAD+, to ensure citric acid is measured quantitatively, equation 7.6:

$$\text{Pyruvate+ NADH} + H^{+} \xrightarrow{\textit{D-LDH}} \text{D-lactate} + NAD^{+} \quad \textbf{(7.6)}$$

The amount of NAD+ formed in the above pathway is stoichiometric with the amount of citric acid. The consumption of NADH is measured by a decrease in the absorbance at 340 nm.

7.2.3 Concluding Remarks

To investigate the potential role of citrate in *in vivo* crystallite size control, UV-VIS was employed. Changes to mineral microstructure of heated bone specimen, in terms of crystallite size, strain and ionic exchanges was determined using XRD, whilst changes to the molecular structure associated with the mineral (carbonate) and the organic content (collagen) was monitored using FTIR. DSC was employed to calculate the potential energy provided from physicochemical changes to bone during heat treatment, whilst colourimetric analysis was used to quantify colour changes in bone during heat treatment. LA-ICP-MS was employed to provide trace elemental analysis of unheated

bone. A summary which outlines what each technique measures, the information acquired from these techniques for this research and the limitations associated with each technique can be found in Table 7.7.

Analytical Technique	Measures	Used in this research	Limitations
XRD	Changes to the crystal lattice structure	**To investigate the mineral microstructure** ∗ HAp crystal size ∗ Lattice parameters ∗ Quantification of mineral phases	Due to the nanocrystalline nature of biological HAp, broad, overlapping diffraction peaks are observed. This can make analysis difficult (section 5.1.3)
FTIR	The molecular structure of materials	**To investigate both the organic and mineral** ∗ Quantify the organic matrix (Amide: phosphate ratio) ∗ Identify and quantify A and B type carbonate (Carbonate: phosphate ratio)	Analysis of FTIR spectra can be extremely complex due to the overlapping peaks associated with both the organic and mineral matrices in bone
UV – Vis	Quantitative determination of an analyte	∗ Quantification of citrate in unheated biologically formed HAp specimens	Prior extraction of citrate from biological HAp is time and labour intensive
Colourimetry	Quantification of colour	∗ Quantify the colour changes during heat treatment	Utilises a single band of wavelength, therefore not as sensitive to changes as a spectrophotometer
LA-ICP-MS	Elemental analysis of materials	∗ Quantify the elements present in unheated bone specimens	Surface analysis only
DSC	Energy changes during thermal treatment of materials	∗ Quantify any energy changes during heat treatment of bone specimens	Very small amounts required for analysis, therefore may not be representative of entire sample

Table 7.7 Summary of the techniques used in this research

Chapter 8: RESULTS

This chapter presents the results of this thesis. (All raw data can be found on the disc attached to the back cover of this thesis). Investigation into control mechanisms associated with *in vivo* HAp crystal growth is followed by processes associated with crystal growth during heat treatment and then the 'destruction' of HAp crystals due to thermal decomposition at high temperatures. The data is then applied to current issues within bone mineral research.

Initially, the results relating to the investigation into the production of 'anorganic' bone material are presented. This is followed by material characterisation of all the specimens according to coherence length (XRD) and where applicable, the organic content (FTIR). Material characterisation of this nature was essential for this research as it provided fundamental information required for subsequent experimental work. The use and reliability of current X-ray diffraction refinement techniques with nanocrystalline HAp is then considered. The refinement techniques are used to calculate crystallite size and strain. The results associated with the control mechanisms of *in vivo* HAp crystallite size are then presented. Citrate, carbonate and organic content, as well as lattice strain are individually considered with regards to coherence length or crystallite size.

The results associated with heated bone specimens are then detailed. Statically heated bone is considered first. The general response to static heat treatment in terms of mass loss and colour are presented along with general observational changes to XRD, FTIR and DSC data. The results associated with bone crystallisation kinetics, obtained from novel applications of the coherence length data to the Arrhenius and Kolmogorov-Johnson-Mehl-Avrami (KJMA) equations, are presented. Further work investigating the role of the organic matrix during static heating is detailed. Dynamically heated bone is then considered. Initially the results detail the general observational changes to the XRD data. Quantification of dynamic data is presented in terms of coherence length, observed in order to investigate the crystallisation process. Lattice parameters were calculated in order to provide information on any chemical changes due to ionic exchanges. Results associated with the quantification of additional mineral phases due to thermal decomposition of HAp are then detailed.

The last section of this chapter covers further interpretation of the results. The results are applied to current issues within heated bone research. The effect of different heating and cooling rates on crystallisation and thermal decomposition of statically heated bone are presented. Data associated with statically heated bone is then applied to develop a time/ temperature predictive model. Dynamically heated XRD data is statistically analysed to investigate the premise of species differentiation.

8.1 Investigation into the production of an 'Anorganic' Bone Analogue using Heat Treatment

Comparison of the thermal behaviours of bone specimens (containing an organic matrix) to those of anorganic bone material was required to provide a new insight into the role of collagen during heat treatment. Production of anorganic bone material was considered carefully. Chemical methods, although reported to be very effective were deemed unsuitable for this study due to the possibility of concomitant modification to the bone mineral (section 4.3). In particular, aqueous substances including water have been shown to cause changes to coherence length and/or carbonate content. Consequently, heat treatment was employed for the removal of the organic.

Diffractograms for unheated bovine bone and bovine bone specimens heated to 100, 200, 300 and 400 ^{o}C are consistent with broad, overlapping diffraction peaks (Figure 8.1). A change in the diffraction peaks is observed for bone specimens heated to 500 and 600 ^{o}C. A decrease in peak broadening is observed for these specimens, which is highlighted by the main HAp peak at ~ 30 - 35 2θ (^{o}).

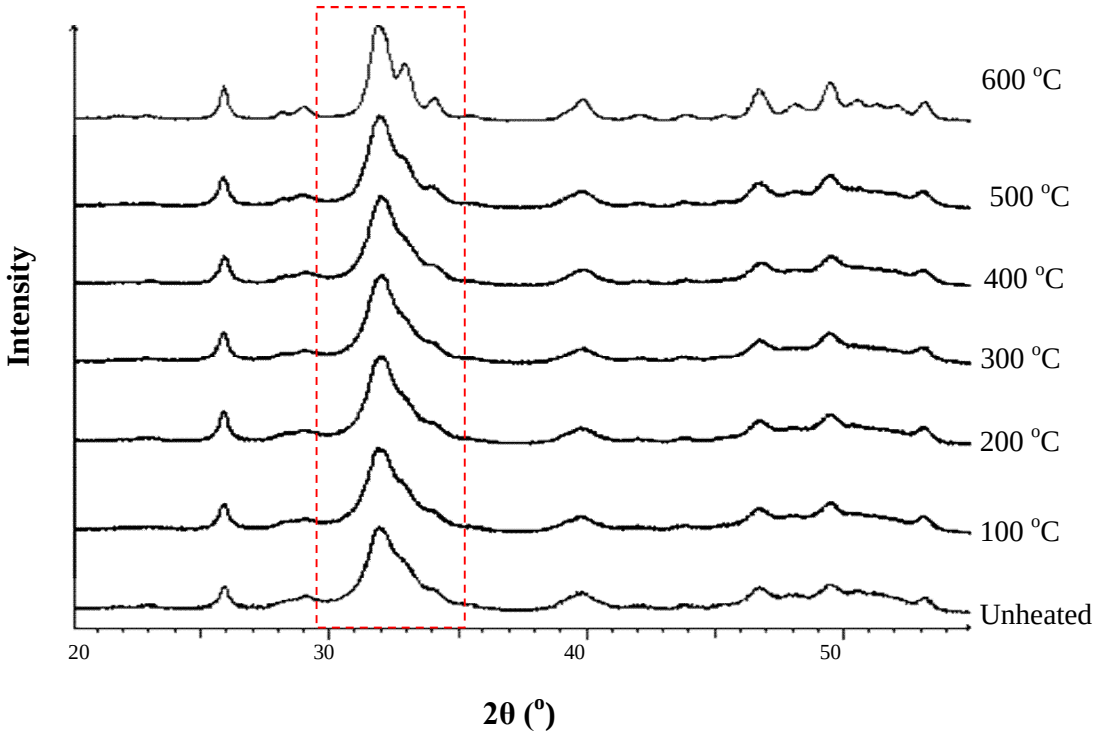

Figure 8.1 X-ray diffractograms of unheated bovine bone and bovine bone heated for 2 hours at 100, 200, 300, 400, 500 and 600 °C. A decrease in peak broadening with increased temperature is highlighted between 30 –35 2θ (°) (boxed), which signifies a change in the mineral microstructure.

FTIR analysis was carried out to assess the loss of the organic matrix during heat treatment. The amide I (1600 – 1750 cm^{-1}) and amide II (1600 – 1550 cm^{-1}) bands, which represent the vibrational modes of bonds that derive from collagen polypeptides, are prominent in the spectra of unheated bone and bone heated at 100 and 200 °C (Figure 8.2). With increasing temperature, the amide bands become less intense. In the spectra of the bone specimens heated to 400, 500 and 600 °C the amide bands are no longer present. The phosphate absorbance bands (1200 – 900 cm^{-1}) remain constant for all specimens except those heated to 500 and 600 °C, when the absorbance bands become more resolved at these temperatures.

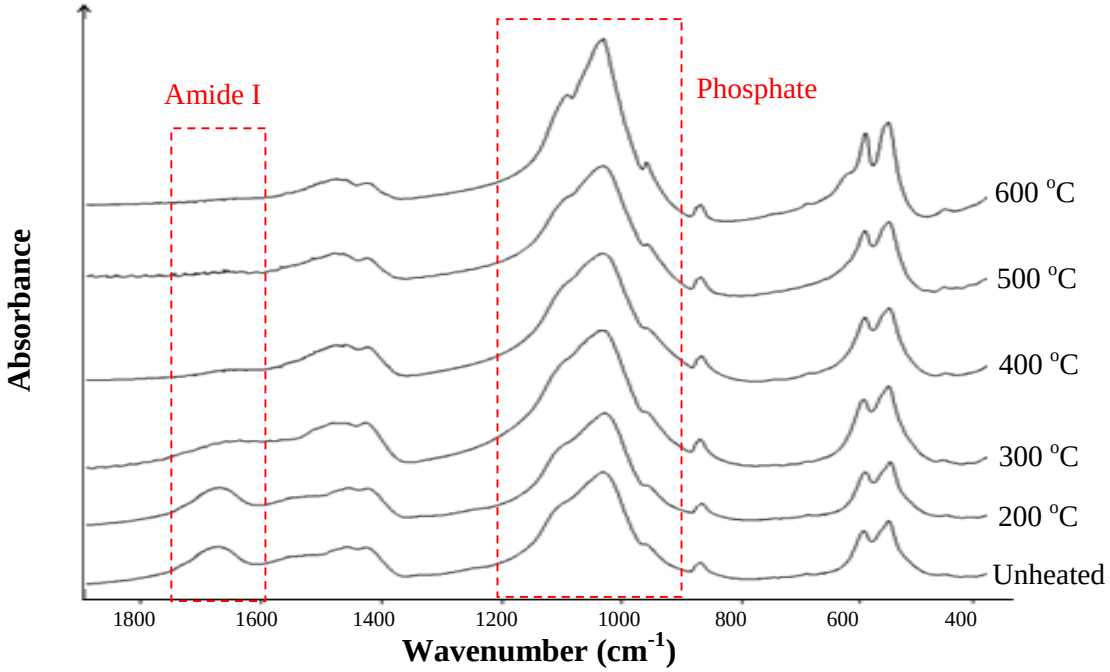

Figure 8.2 FTIR spectra of unheated bovine bone and bovine bone heated for 2 hours at, 200, 300, 400, 500 and 600 °C. The absorbance bands associated with amide I and phosphate are highlighted. For clarity, amide II, which is in close proximity to the amide I absorbance band, is not highlighted in this figure. (Figure 7.2, section 7.2.2.2)

Quantification of coherence length (XRD) and amide I to phosphate ratio (FTIR) is provided in Table 8.1. The coherence length was similar for unheated bone and bone specimens heated to 100, 200, 300 and 400 °C. A slight increase in coherence length was observed for bone heated to 500 and 600 °C, particularly in the hk0 reflections. A gradual decrease in the amide I: phosphate ratio was observed with increasing temperature.

	Coherence length (nm)			Amide I: Phosphate
	<00ℓ>	<0k0>	<hk0>	
Temperature (^{o}C)				
Unheated	26 ± 3	9 ± 2	12 ± 3	0.25 ± 0.02
100	24 ± 2	10 ± 2	12 ± 1	0.21 ± 0.03
200	25 ± 1	9 ± 1	12 ± 1	0.18 ± 0.02
300	24 ± 2	9 ± 1	12 ± 1	0.11 ± 0.02
400	23 ± 1	10 ± 2	11 ± 1	0.04 ± 0.01
500	23 ± 2	13 ± 1	11 ± 1	0.02 ± 0.02
600	26 ± 1	16 ± 1	14 ± 1	0.01 ± 0.01

Table 8.1 Coherence lengths (calculated in three different crystallographic directions) and the amide I to phosphate ratio for unheated bovine bone and bovine specimens heated for 100, 200, 300, 400, 500 and 600 ^{o}C for 2 hours. Errors calculated from the standard deviation of three repeats.

8.2 Determination of Hydroxyapatite Coherence Length and Organic Content: XRD and FTIR analysis

All specimens were characterised according to coherence length (in different crystallographic directions) using XRD as described in section 7.2.2.1. The organic to mineral content was also calculated for unheated bone and urinary calculi specimens using FTIR (as described in section 7.2.2.2). In general, the coherence lengths for all specimens were larger in the <00ℓ> direction in comparison to the <0k0> and <hk0> directions. The remainder of this section will consider each group of specimens (bone types, urinary calculi and synthetic HAp) individually.

8.2.1 Bone types

All unheated bone specimens utilised in this research resembled calcium HAp. No additional mineral phases were detected. The diffraction peaks for rostrum were narrower than the other bone types, highlighted by the main HAp peaks between 30 – 35 2θ (^{o}) (Figure 8.3). The diffractograms for bovine, porcine, human and red deer antler specimens were similar, with broad, overlapping peaks.

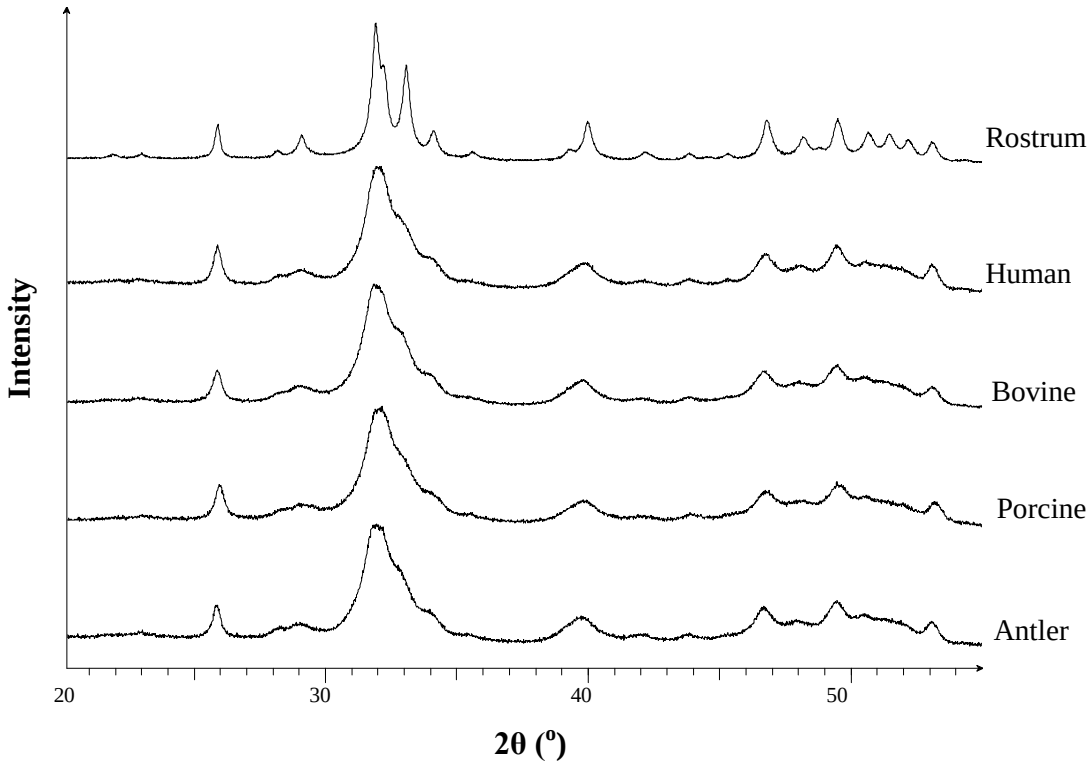

Figure 8.3 X-ray diffractograms of the five bone types. The difference between the rostrum specimen and the other bone types is highlighted by the main HAp peaks between 30 –35 2θ (^{o}).

FTIR data differed between bone types (Figure 8.4). The phosphate band (1200 – 900 cm^{-1}) was sharper and more resolved for rostrum, whilst the intensity of the amide I band (1750 – 1600 cm^{-1}) was less intense in comparison to the other bone types. The spectra for bovine, porcine and human were similar. The intensity of the amide I peak was greater for the red deer antler in comparison to the other bone types.

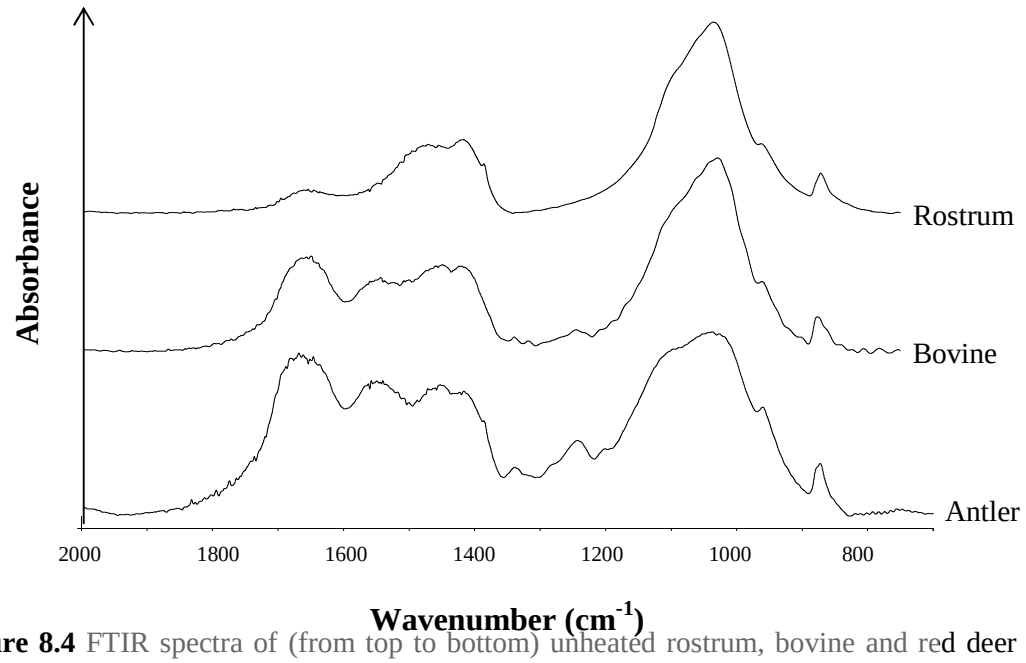

Figure 8.4 FTIR spectra of (from top to bottom) unheated rostrum, bovine and red deer antler specimens.

Quantification of the XRD and FTIR data revealed rostrum exhibited the largest coherence length in all crystallographic directions and the lowest amide I to phosphate ratio (Table 8.2). In comparison, red deer antler exhibited the largest amide I to phosphate ratio. The coherence lengths and amide I to phosphate ratios for bovine, porcine and human specimens were similar at approximately 25 nm and 0.3 respectively. The anorganic analogues of porcine and bovine exhibited coherence lengths, which were within errors, the same as their organic counterparts, however the amide I to phosphate ratio was much lower for the anorganic specimens.

Unheated Bone Types	Coherence Length (nm)			Amide I : Phosphate
	<00ℓ>	<0k0>	<hk0>	
Rostrum	57 ± 2	33 ± 1	32 ± 1	0.11 ± 0.02
Bovine	26 ± 1	9 ± 2	12 ± 3	0.25 ± 0.02
Porcine	25 ± 1	10 ± 3	10 ± 2	0.33 ± 0.01
Human	26 ± 1	9 ± 2	8 ± 3	0.30 ± 0.01
Red Deer Antler	30 ± 3	10 ± 3	10 ± 3	0.50 ± 0.05
Anorganic Bovine	26 ± 1	9 ± 2	12 ± 2	0.08 ± 0.01
Anorganic Porcine	24 ± 1	9 ± 2	12 ± 2	0.07 ± 0.01

Table 8.2 Coherence lengths (calculated in three different crystallographic directions) and amide I to phosphate ratios for all bone types including bovine and porcine anorganic material. Errors calculated from the standard deviation of three repeats.

8.2.2 Urinary Calculi Specimens

All urinary calculi specimens resembled calcium HAp. Additional mineral phases were observed in specimens B and F (Figure 8.5). A small quantity of monetite was observed in specimen B whilst β - TCP was observed in specimen F. The diffraction peaks associated with these additional mineral phases did not overlap the HAp peaks corresponding to the crystallographic directions investigated in this research.

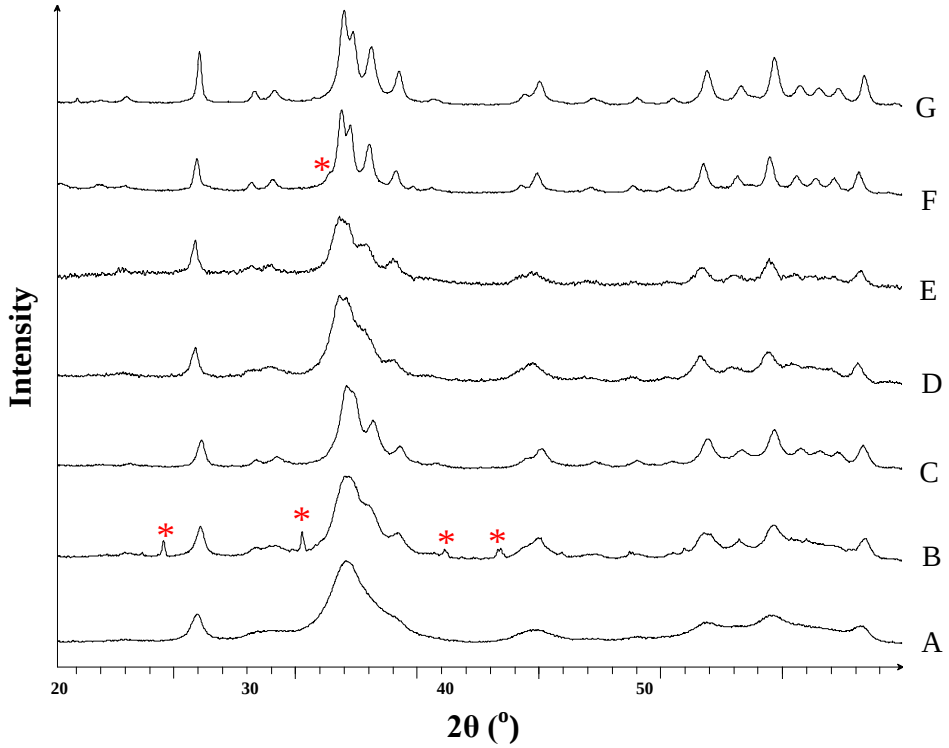

Figure 8.5 X-ray diffractograms (in order of crystallinity) of urinary calculi specimens A-G. Additional peaks in the diffractograms for urinary calculi B and F, which correspond to **B:** monetite and **F:** β –TCP are denoted with *.

Quantification of the XRD data revealed a wide range of coherence lengths for the urinary calculi specimens as shown in Table 8.3. Amide I to phosphate values calculated for urinary calculi specimens A, D and E differed. The amide I to phosphate ratios are not reported for specimens B, C, F and G due to insufficient amount of material required for FTIR analysis.

Urinary Calculi	**Coherence Length (nm)**			**Amide I : Phosphate**
	<00ℓ>	**<0k0>**	**<hk0>**	
A	19 ± 1	11 ± 3	8 ± 4	0.13 ± 0.03
B	27± 1	15 ± 4	11 ± 2	
C	31 ± 1	18 ± 3	17 ± 4	
D	32 ± 3	9 ± 2	11 ± 4	0.11 ± 0.02
E	46 ± 4	19 ± 5	23 ± 6	0.25 ± 0.02
F	50 ± 1	30 ± 1	34 ± 2	
G	77 ± 1	27 ± 1	28 ± 1	

Table 8.3 Coherence lengths (calculated for <00ℓ>, <0k0> and <hk0> reflections) for urinary calculi specimens. Amide I: phosphate ratio values are not reported for specimens B, C, F and G due to insufficient material required for FTIR analysis. Errors calculated from the standard deviation of three repeats.

8.2.3 Synthetic HAp Specimens

Synthetic HAp specimens (sHAp1, sHAp2 and sHAp3) resembled calcium HAp. No additional mineral phases were detected. Sharp, narrow peaks were observed in the diffractogram of specimen sHAp3 whilst broad, overlapping peaks were observed for sHAp1 (Figure 8.6). Peaks associated with sHAp2 were slightly narrower than the peaks observed for sHAp1. The diffractogram of sHAp1 is comparable to unheated bovine bone where broad, overlapping peaks are also observed.

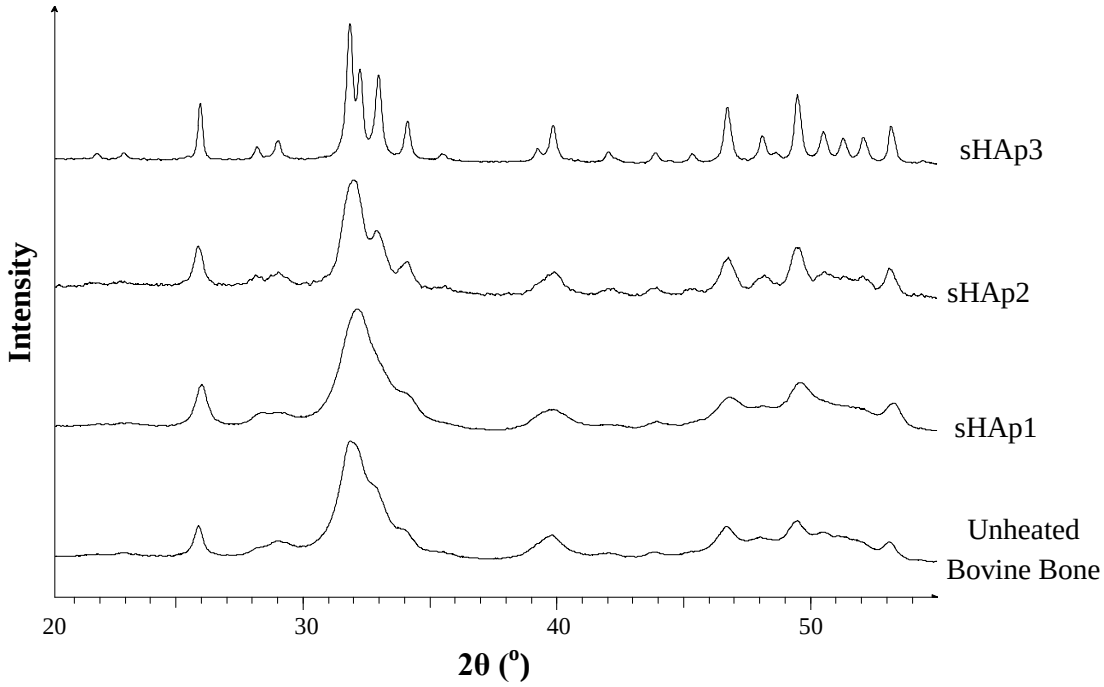

Figure 8.6 X-ray diffractograms (in order of crystallinity) of the three synthetic HAp specimens. The diffractogram of unheated bovine bone has been included for comparison.

Quantification of the data revealed the coherence lengths for these specimens differed as shown in Table 8.4, with the calculated values demonstrating the series; sHAp3 > sHAp2 > sHAp1.

Synthetic HAp	**Coherence Length (nm)**		
	<00ℓ>	**<0k0>**	**<hk0>**
sHAp1	18 ± 1	8 ± 2	11 ± 5
sHAp2	27 ± 1	16 ± 5	11 ± 3
sHAp3	77 ± 3	46 ± 2	48 ± 3

Table 8.4 Coherence lengths (calculated in three different crystallographic directions) for the synthetic HAp specimens. Errors calculated from the standard deviation of three repeats.

8.3 Calculation of Crystallite Size and Strain

The difficulty of obtaining accurate independent values for crystallite size and strain for nano HAp due to overlapping diffraction peaks and crystallographic direction dependence broadening was discussed in section 5.1.3. This section will firstly consider the implementation and use of Rietveld refinement for nanocrystalline materials such as bone mineral. The Williamson-Hall method for crystallite size and strain will then be considered followed by Langford's method of single line size / strain determination. The limitations of these three refinement techniques will be highlighted. Leineweber & Mittemeijer's crystallographic direction dependence broadening due to compositional variations is then explored and enhanced to include crystallite size broadening. This novel approach has not previously been reported for bone.

8.3.1 Rietveld Refinement

As discussed in section 5.1.3, the use of Rietveld refinement is limited within bone mineral research as the Caglioti profile function (or other similar fixed functions) is inadequate for crystallographic direction dependence broadening. Rietveld refinement of bovine bone is shown in Figure 8.7. The blue profile is the raw data whilst the Rietveld refinement profile is in red. As can be seen in Figure 8.7, the refinement profile is not a good fit to the raw data profile, which is particularly evident at the 002 peak (~28.5 2θ (^{o})).

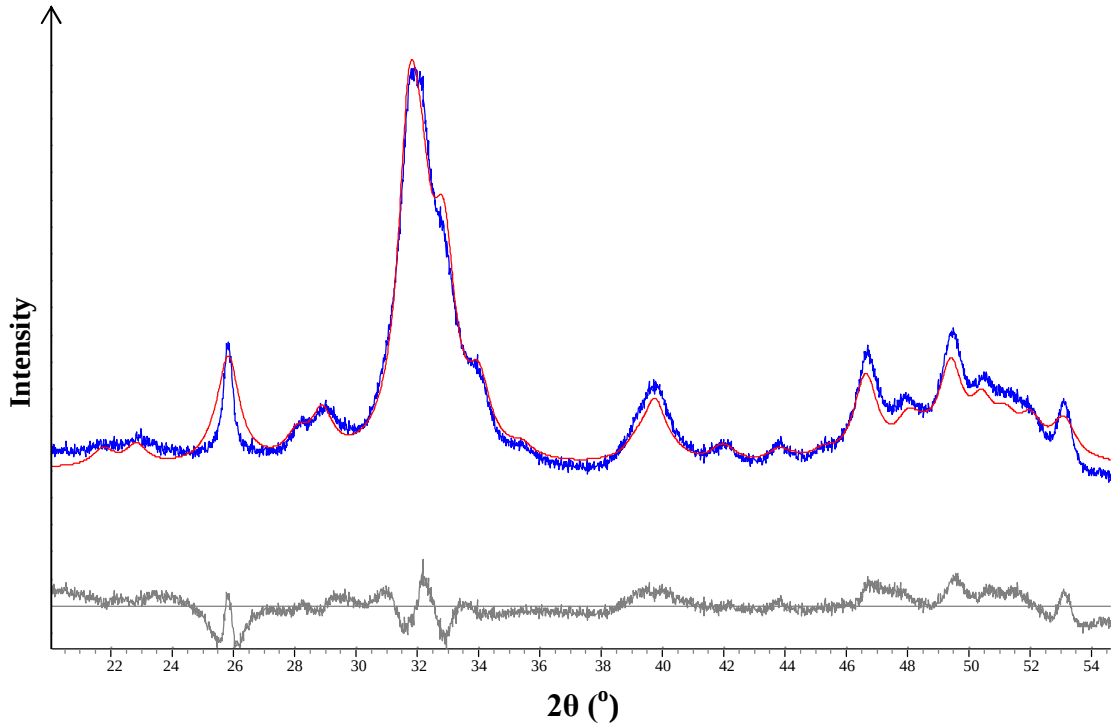

Figure 8.7 Rietveld refinement (Full pattern profile fit) of XRD data obtained from unheated bovine bone

As shown in Figures 8.8 and 8.9, the extent of broadening has a strong dependence upon the crystallographic direction observed. In general, hk0 reflections exhibit the greatest extent of broadening whilst the narrowest diffraction peaks were observed for 00ℓ reflections, for both red deer antler (Figure 8.8) and rostrum (Figure 8.9) bone mineral. This relationship was also observed in synthetically produced HAp specimens (Figure 8.10). The difference in the extent of broadening between these two reflections is more evident in the red deer antler data (Figure 8.8).

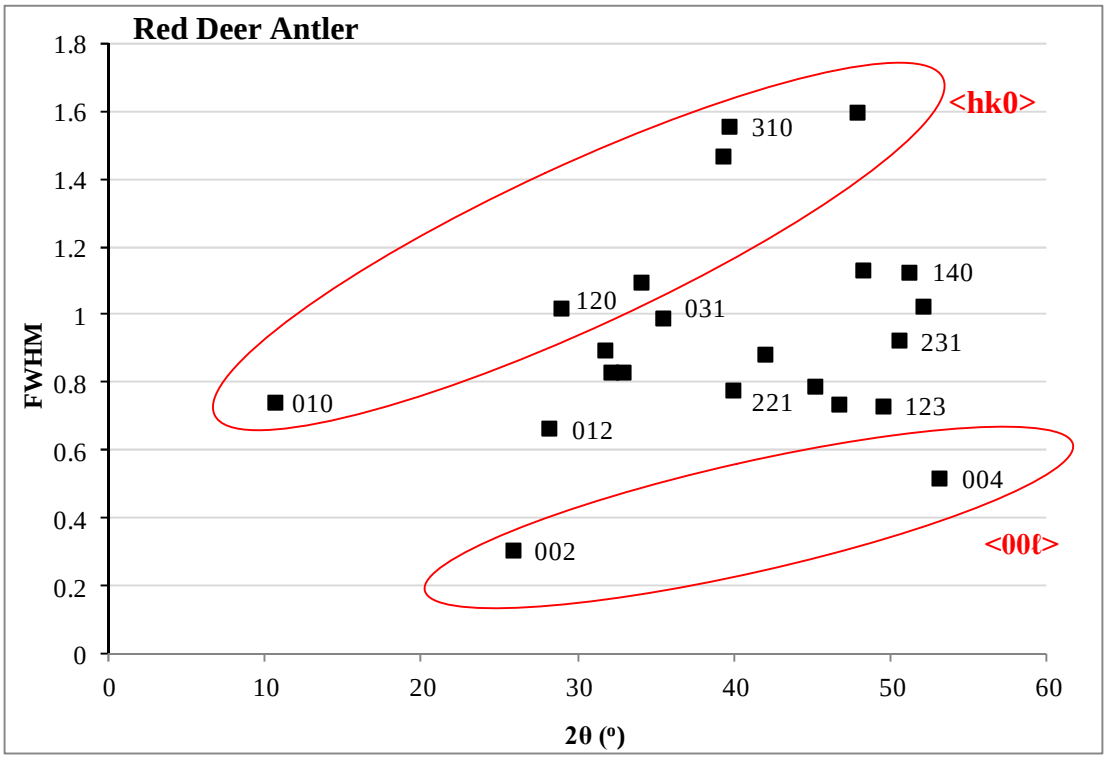

Figure 8.8 FWHM data for the diffraction peaks observed for red deer antler plotted against 2θ (º). This highlights crystallographic direction peak broadening dependence. For clarity, errors have not been included.

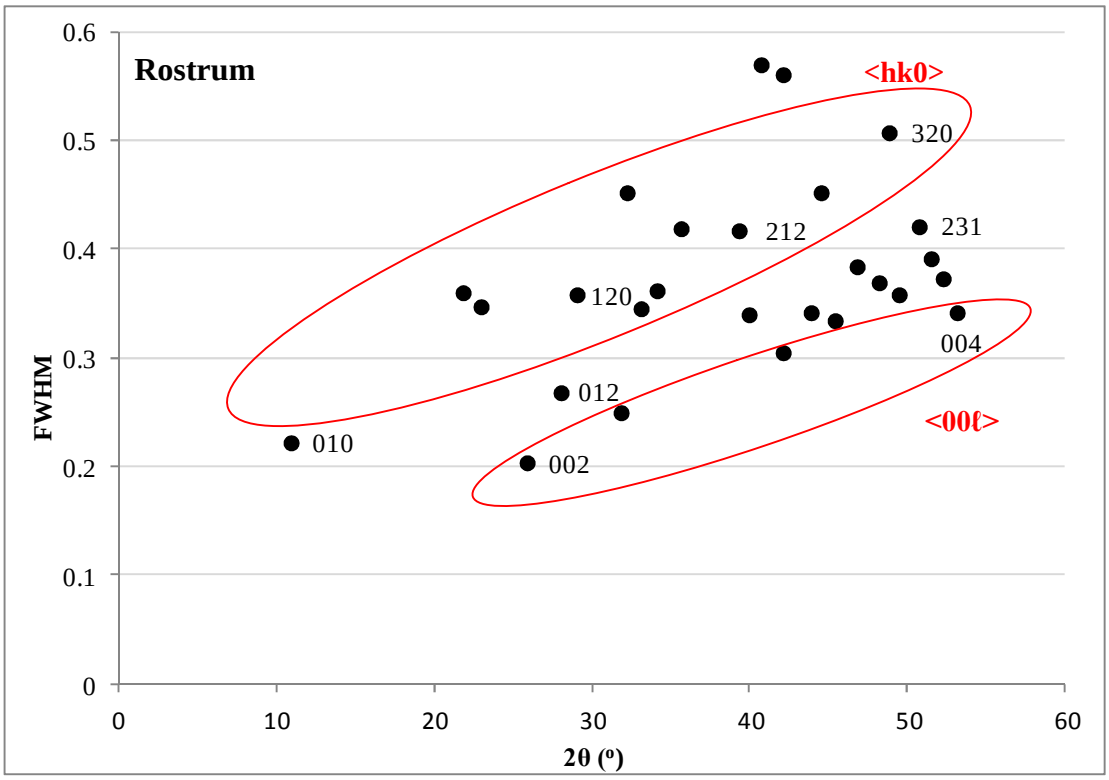

Figure 8.9 FWHM data for the diffraction peaks observed for red deer antler plotted against 2θ (º). This highlights crystallographic direction peak broadening dependence. For clarity, errors have not been included.

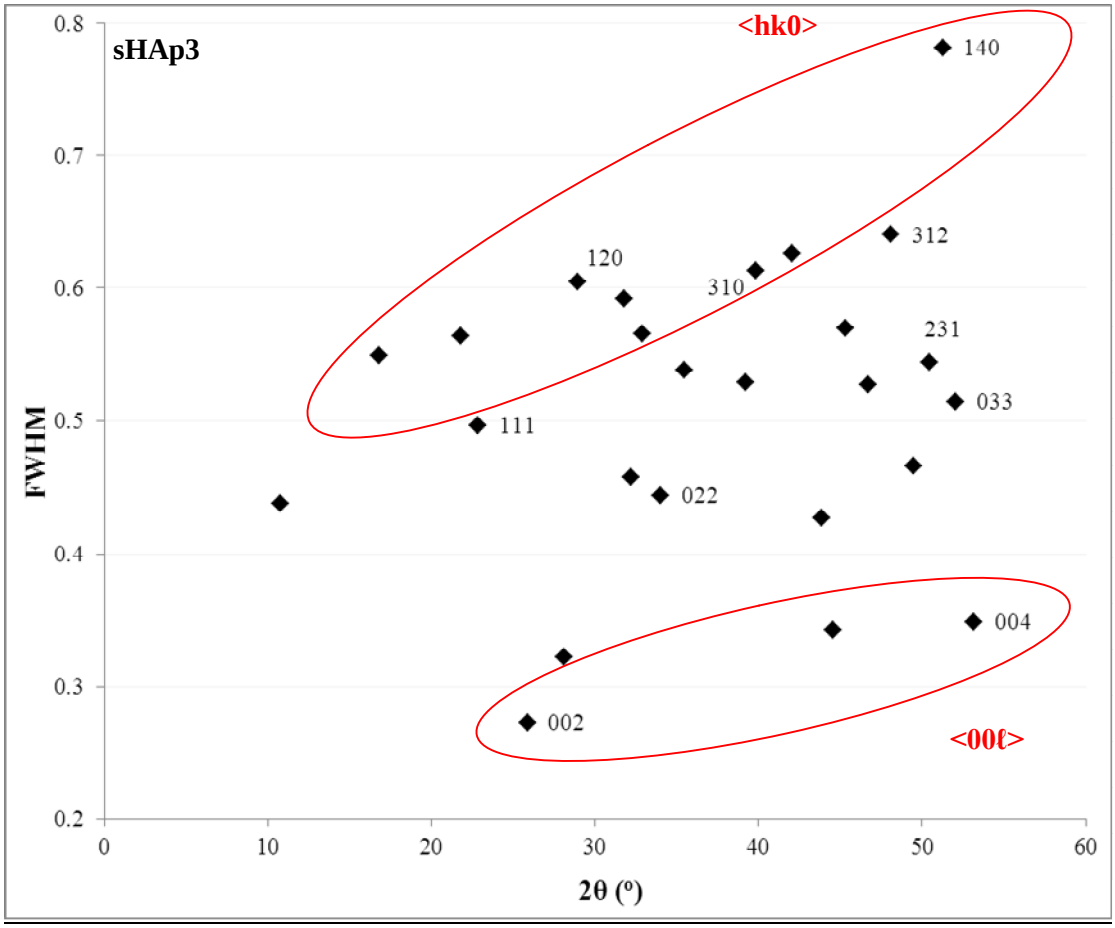

Figure 8.10 FWHM data calculated from the diffraction peaks observed for synthetic HAp (sHAp3) plotted against 2θ (°). This highlights crystallographic direction peak broadening dependence. For clarity, errors have not been included.

As shown in Figure 8.11, changes to the FWHM (i.e. peak broadening) are related to the angle between the <00ℓ> and other crystallographic directions. As highlighted in Figure 8.11, there is spread in the broadening associated with the peaks in the <hk0> crystallographic direction. This relationship was observed for synthetic HAp and bone mineral.

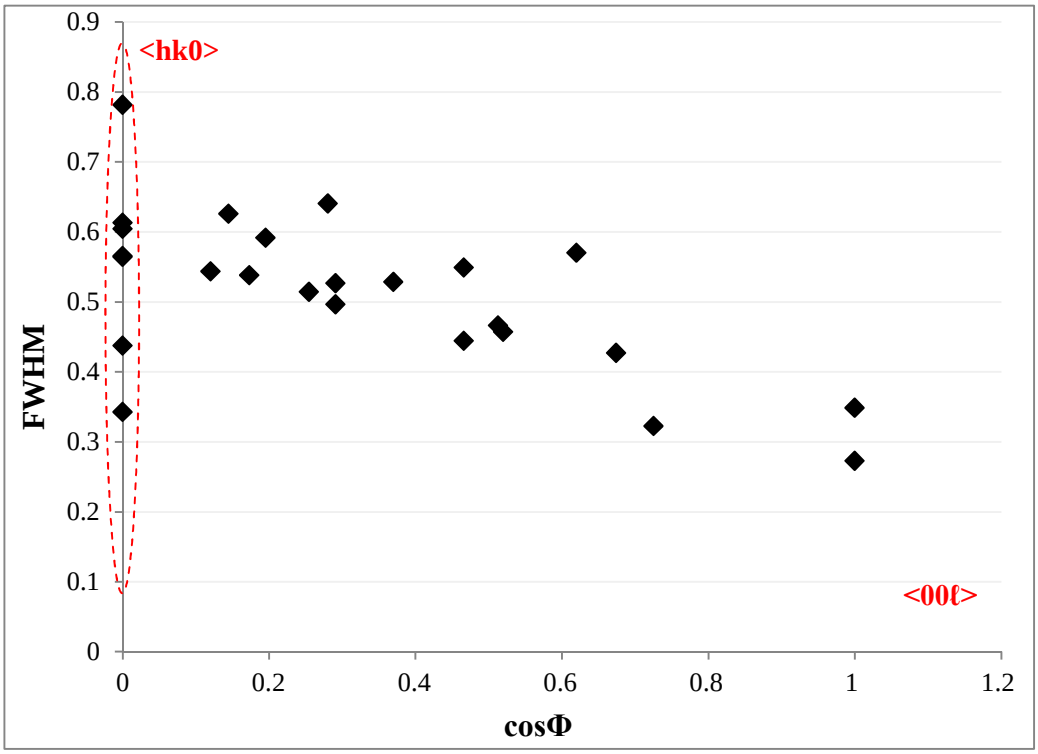

Figure 8.11 FWHM data from the diffraction peaks observed for synthetic HAp (sHAp3) plotted against the angle (cos Φ) between <00ℓ> and the other directions 2θ (°). For clarity, errors have not been included.

8.3.2 Williamson - Hall Size/ Strain Determination

Williamson-Hall plots (section 5.1.3) were constructed using FWHM data collected from peaks corresponding to the 00ℓ reflection. Data from hk0 reflections were found to be unreliable due to the spread in broadening in these crystallographic directions (Figure 8.11). This is discussed further in section 9.3. Crystallite size and strain values for the bone types, urinary calculi specimens A, D and E and synthetic HAp specimens calculated from Williamson Hall plots and equations 5.4 and 5.9 (section 5.1.3) are presented in Table 8.5.

Specimen	Size (nm)	Strain
Rostrum	64 ± 4	0.007 ± 0.004
Bovine	32 ± 1	0.005 ± 0.001
Porcine	30 ± 1	0.004 ± 0.001
Human	35 ± 3	0.003 ± 0.001
Red Deer Antler	35 ± 6	0.005 ± 0.009
UC_A	25 ± 1	0.008 ± 0.001
UC_D	37 ± 1	0.003 ± 0.001
UC_E	57 ± 4	0.009 ± 0.007
sHAp1	20 ± 2	0.004 ± 0.002
sHAp2	29 ± 1	0.002 ± 0.001
sHAp3	84 ± 4	0.002 ± 0.001

Table 8.5 Crystallite size and strain values for bone, urinary calculi and synthetic HAp specimens calculated using Williamson Hall analysis. Errors calculated from the standard deviation of three repeats.

Taking into account the bone types first, rostrum exhibited the largest crystallite size in comparison to the other bone types. Red deer antler, bovine, porcine and human bone was found to exhibit similar crystallite sizes. With regards to the urinary calculi specimens, the crystallite size values followed the series, E > D > A and for the synthetic HAp specimens, sHAp3 > sHAp2 > sHAp1. Due to the errors associated

with the strain values, it was difficult to determine whether a trend existed between the specimens. This issue was investigated and the same data was analysed several times. It was found that changing the 2θ range and the number of peaks fitted in close proximity during analysis had a significant effect on the FWHM data obtained from the 004 peak. The 002 FWHM data remained, within errors, consistent. Consequently, the gradient of the Williamson hall plots are significantly affected. This directly affects the strain component but not necessarily the size component (Figures 8.12 & 8.13). This is discussed further in section 9.3.2.

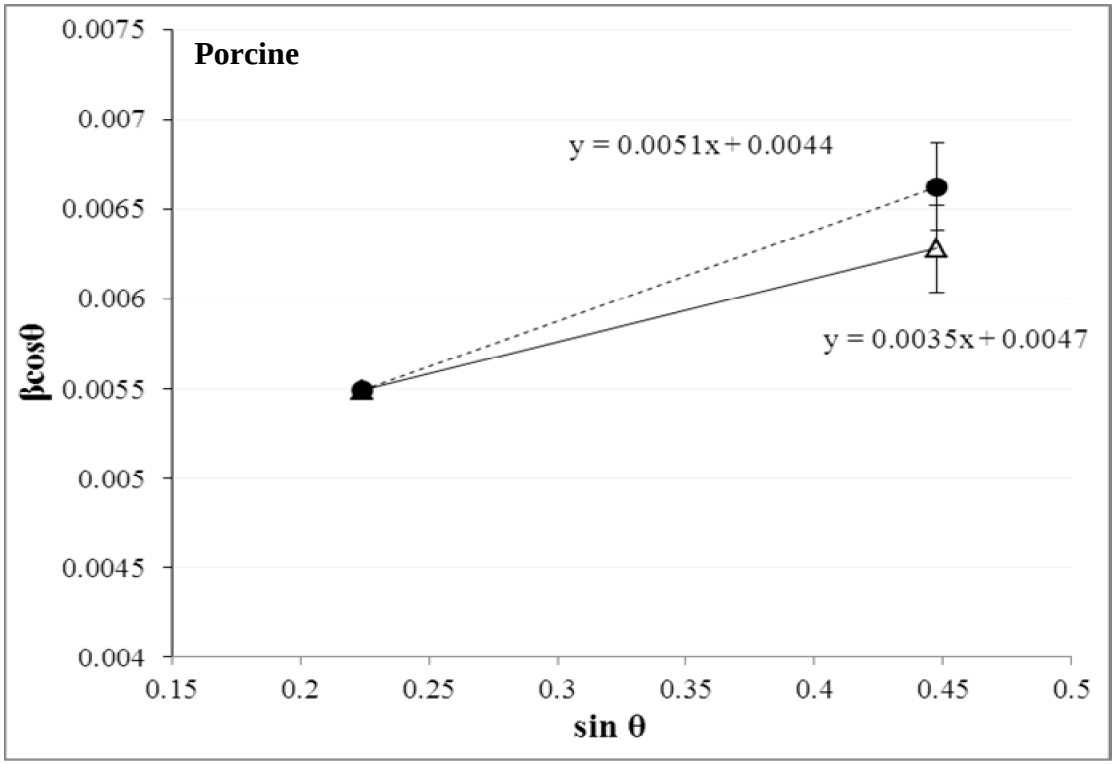

Figure 8.12 Williamson Hall plot (00ℓ reflection) for unheated porcine bone. The two plots (obtained from repeat analysis of the same data) highlight the fitting errors associated with the 004 reflection.

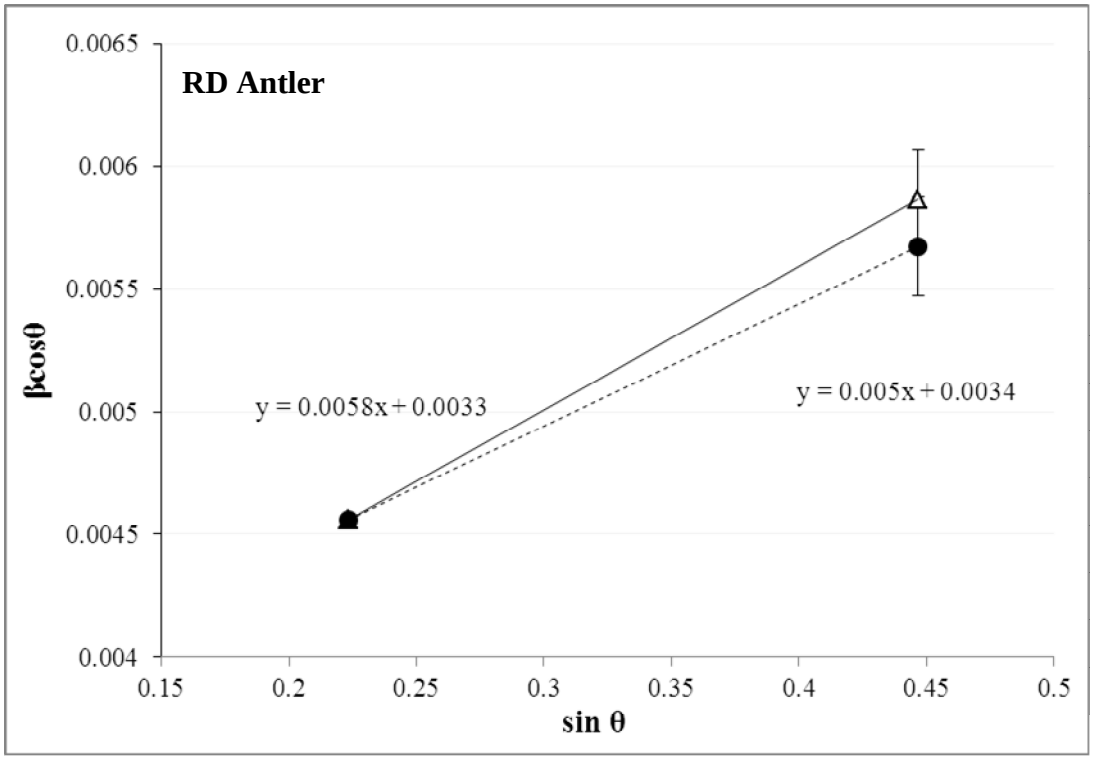

Figure 8.13 Williamson Hall plot (00ℓ reflection) for unheated red deer antler bone material. The two plots (obtained from repeat analysis of the same data) highlight the fitting errors associated with the 004 reflection.

8.3.3 Single Line Analysis

Single line size/ strain analysis (section 5.1.3) was carried using the 002 peak. As briefly mentioned in the previous section and discussed in section 9.3, this peak was deemed suitable due to reliability in the FWHM data (i.e. small errors associated with peak fitting as the 002 peak is not overlapped by other peaks and is not as broad as the other reflections). The calculated size values using single line analysis were different to those calculated using Williamson Hall analysis (Table 8.6). The errors associated with size values in Table 8.6, were greater than the errors calculated from Williamson-hall plot analysis, whilst the errors associated with strain values were significantly smaller. With regards to strain, the value for rostrum was approximately half the value calculated for the other bone types. A similar value of strain was observed for red deer antler, bovine, porcine and human specimens. A significantly

greater value of strain was observed for urinary calculi specimen A in comparison to the other urinary calculi specimens, whilst the lowest value was observed for specimen G. A range of strain values were observed for the remainder of the urinary calculi specimens, although a trend was observed where A > B ≈ C ≈D > E > F > G. A significantly lower value of strain was observed for sHAp3 and a trend was observed where sHAp1 > sHAp2 > sHAP3.

Specimen	Size (nm)	Strain
Rostrum	43 ± 2	0.012 ± 0.00001
Bovine	47 ± 5	0.028 ± 0.001
Porcine	48 ± 9	0.027 ± 0.002
Human	48 ± 4	0.024 ± 0.001
RD Antler	59 ± 7	0.028 ± 0.006
UC_A	97 ± 9	0.044 ± 0.004
UC_B	52 ± 5	0.023 ± 0.002
UC_C	66 ± 7	0.023 ± 0.003
UC_D	54 ± 5	0.024 ± 0.002
UC_E	44 ± 3	0.017 ± 0.002
UC_F	41 ± 4	0.012 ± 0.001
UC_G	42 ± 3	0.006 ± 0.0001
sHAp1	79 ± 7	0.043 ± 0.003
sHAp2	64 ± 4	0.038 ± 0.002
sHAp3	43 ± 3	0.008 ± 0.0001

Table 8.6 Crystallite strain values for bone, urinary calculi and synthetic HAp specimens calculated using single line analysis described by Langford (1992). Errors calculated from the standard deviation of three repeats.

8.3.4 Compositional Broadening

As highlighted in the previous sections, techniques used to obtain independent values for crystallite size and strain are to some extent limited in bone mineral research (discussed further in section 9.3), due to broad peaks, relatively low symmetry associated with the hexagonal space group and large lattice parameters. Consequently, a novel approach was adopted to investigate crystallographic direction dependence broadening due to compositional variations. This method was defined by Leineweber & Mittemeiher (2003); however the authors modelled broadening on strain alone and did not consider size broadening contributions (section 5.1.3). This section will firstly consider the impact of strain broadening contribution to simulated data (values obtained from Leineweber & Mittemeiher). The model is then extended to include size broadening contribution, a concept that has not previously been explored. The model is applied to synthetic HAp data (sHAp3) for comparison.

8.3.4.1 Strain/ size broadening contribution to the simulated data

Leineweber & Mittemeiher's (2003) model and data, which was based on iron nitride (FeN), was simulated (using equation 5.18 and parameters outlined in section 5.1.3), to investigate the influence of strain broadening. Increasing the strain broadening contribution value resulted in a greater magnitude of broadening across all crystallographic directions. Consequently, the $B^{f}{}_{\Delta 2\theta,hkl} / \tan \theta_{0,hkl}$ value (a function of the angle between the diffraction vector and the 00ℓ direction) increases between the (00ℓ) and (hk0) planes. Thus, data set values increase as a function of the y and x axis, illustrated in Figure 8.14. An increase in strain, increases $B_{\xi} d\alpha_3/d\xi$ and $B_{\xi} d\alpha_1/d\xi$ values. In Figure 8.14, simulated dataset A correspond to $B_{\xi} d\alpha/d\xi$ values of ~ 0.0009, for B of ~ 0.0018 and for C of ~ 0.0025.

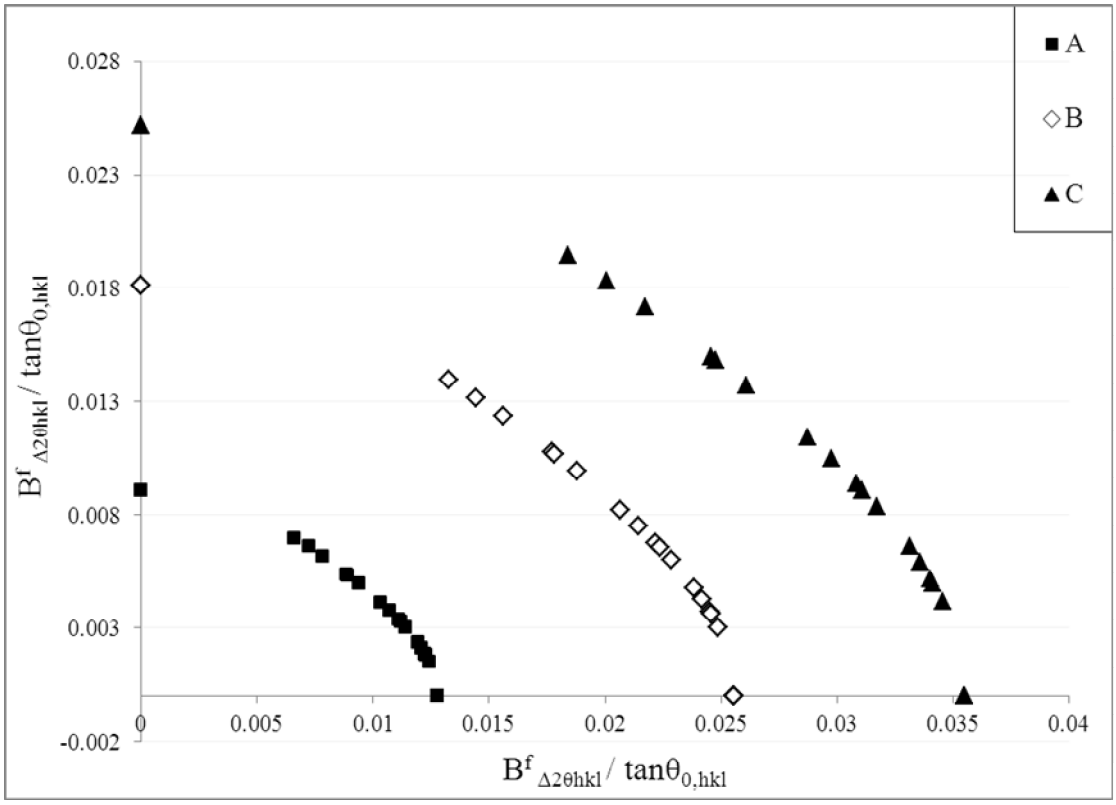

Figure 8.14 The effect of increasing the amount of strain (where B_ξ dα/ dξ values are A ~0.0009, B ~ 0.0018 and C ~ 0.0025) in equation 5.17 (section 5.1.3), on the data obtained from Leineweber and Mittemeijer (2003).

Leineweber and Mittemeijer's (2003) model (equation 5.18) was extended to include size broadening contributions as shown in equation 8.1:

$$B^f{}_{s+s} = B^f{}_{strain} + \left[a(b + c\sin\phi\right] \quad \textbf{(8.1)}$$

, where, B^f_{S+S} relates to size and strain direction dependence structural broadening, B^f_{strain} is strain direction dependence structural broadening (equation 5.18) and a, b and c fitting coefficients assigned to size broadening contributions.

As shown in Figure 8.15, rather than a continuous 'arc' of data (when only strain is considered, ♦), inclusion of size (◊) causes separation/ dispersion of the data and appears to result in several separate 'arcs' of data points. With inclusion of size contribution, $B_\xi \, d\alpha / d\xi$ values become smaller.

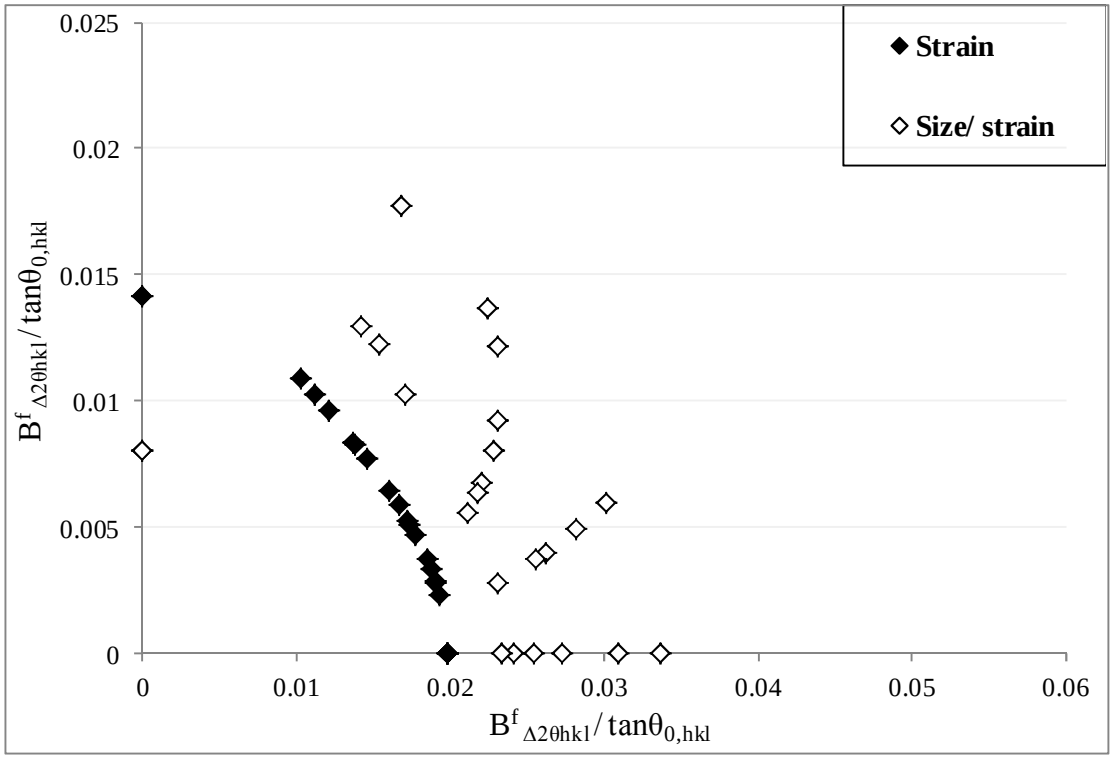

Figure 8.15 The effect of including size broadening contribution (equation 8.8, section 5.1.3), on the data obtained from Leineweber and Mittemeijer (2003).

8.3.4.3 Comparison of Simulated Data to Synthetic Hydroxyapatite Data

Comparison of the simulated data (strain contribution only) to data obtained from synthetic HAp specimen (sHAp3) highlights a significant difference (Figure 8.16). There is a poor fit between the two sets of data due to the dispersion of the sHAp3 data. This suggests additional direction dependence broadening which cannot be modelled by strain contribution alone (discussed further in section 9.3). A spread in the sHAp3 data along the y and x axes ($\Phi = 0$ and $\Phi = 90$) is also observed.

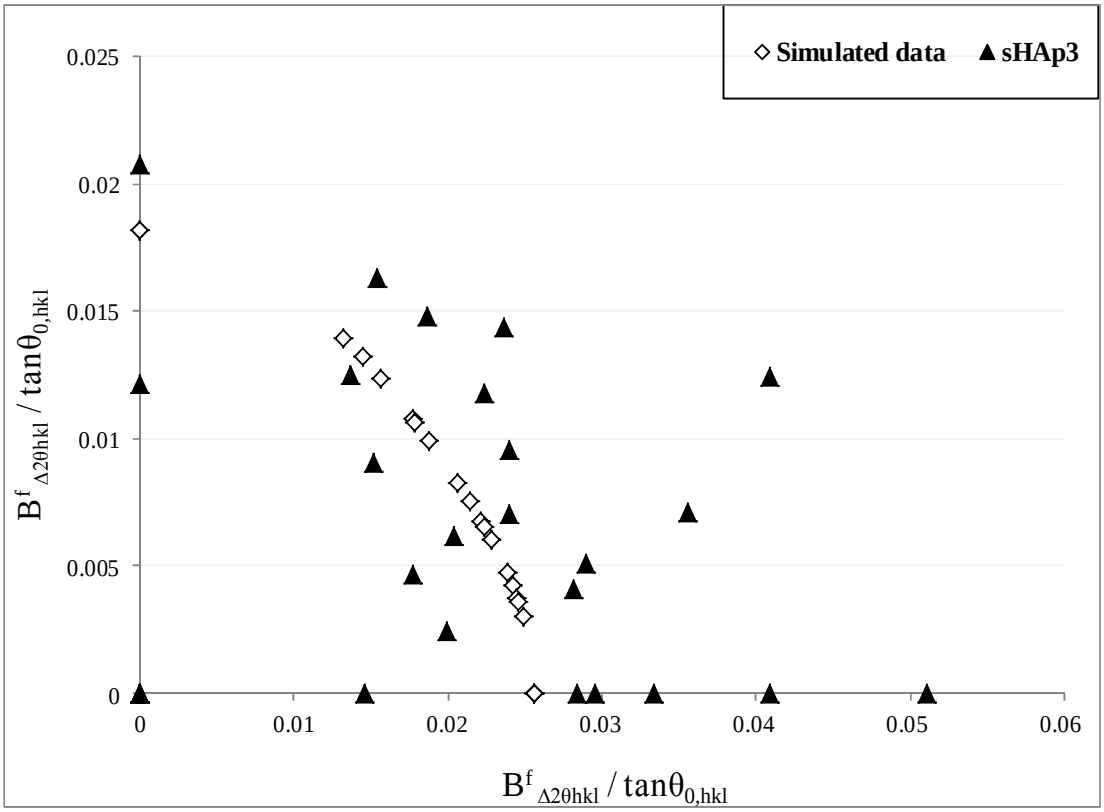

Figure 8.16 Comparison of the data obtained from Leineweber and Mittemeijer (2003). (assuming strain contribution only) to data obtained from synthetic HAp specimen (sHAp3).

As shown in Figure 8.17, when size broadening contribution is included in the simulated data model, it starts to resemble sHAp3 data. Introducing size broadening decreased $B_{\xi}d\alpha_3/d\xi$: $B\xi d\alpha 1/d\xi$ values from ~ 0.0018 to ~ 0.0008. The ratio of $B_{\xi}d\alpha_3/d\xi$: $B\xi d\alpha 1/d\xi$ = 1.

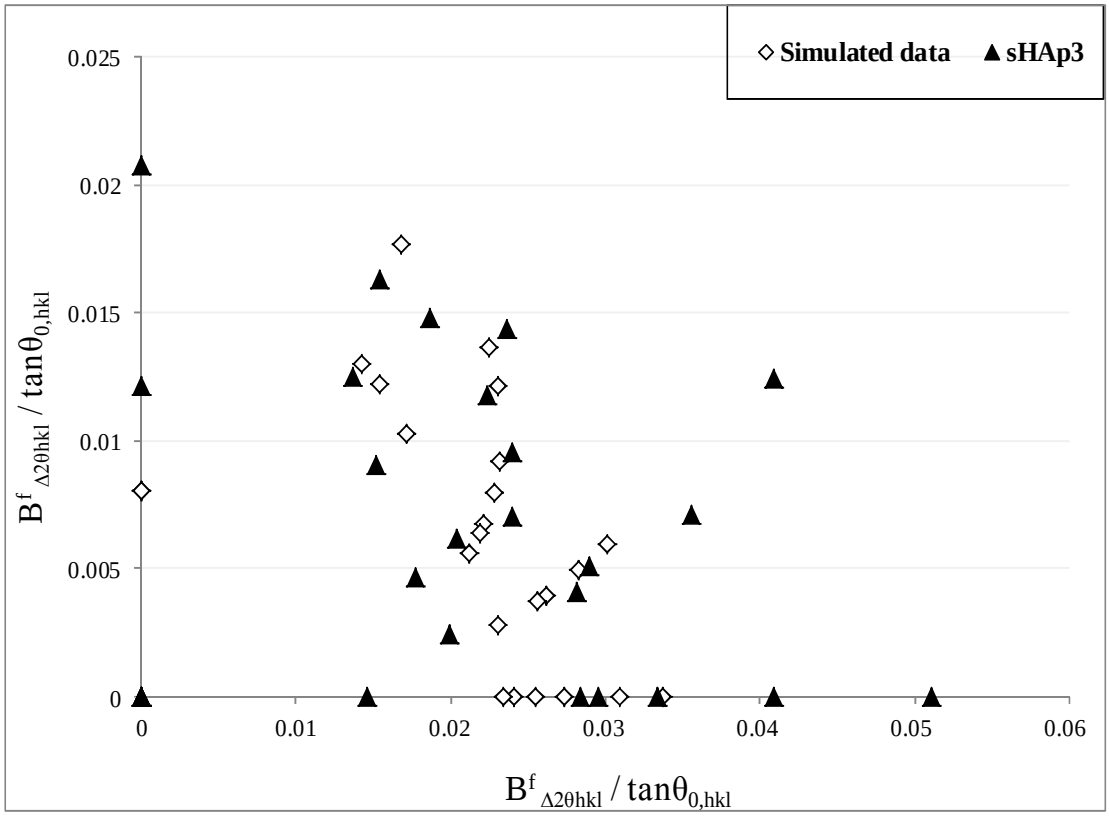

Figure 8.17 Comparison of the data obtained from Leineweber and Mittemeijer (2003), (which has been extended to include size broadening contributions) to data obtained from synthetic HAp specimen (sHAp3).

Calculation of $d\alpha_1/d\xi$ and $d\alpha_3/d\xi$ from known composition dependence of the lattice parameters of B-type carbonate substitution ('a'(y)/ Å = -0.006y + 9.4348 and 'c'(y)/Å = 0.0025y + 6.8694) using Vegards law (section 5.1.3), provided values of 3 x 10^{-5} and -2 x 10^{-5}. Thus, the ratio of $d\alpha_3/d\xi$: $d\alpha 1/d\xi$ is equal to -0.06667. This is significantly different from the fitted parameter ratio ($B_{\xi}d\alpha_3/d\xi$: $B\xi d\alpha 1/d\xi$) which was calculated as 1.

8.4 In vivo hydroxyapatite crystal size control

8.4.1 Investigating the amount of citrate: UV-VIS Analysis

Using the equations outlined in section 7.2.2.6; the concentration and consequently the amount of citric acid present within bone and urinary calculi specimens was calculated. For bone types, a trend was observed where red deer antler > porcine > bovine > rostrum with regards to the amount of citrate (Table 8.7).

Specimen	**Citric Acid (g/100g)**
Rostrum	0.030 ± 0.004
Bovine	0.038 ± 0.004
Porcine	0.088 ± 0.012
Red Deer Antler	0.663 ± 0.003
UC_A	0.055 ± 0.003
UC_B	0.028 ± 0.002
UC_C	0.244 ± 0.020
UC_D	0.070 ± 0.010
UC_F	0.097 ± 0.017
UC_G	0.035 ± 0.006

Table 8.7 The calculated amount of citric acid (g / 100g) extracted from the bone and urinary calculi specimens. Errors calculated from the standard deviation of three repeats

The amount of citrate present within red deer antler specimen was significantly greater than the other bone types. With respect to urinary calculi specimens, the amount of citrate present ranged from 0.028 – 0.097 g / 100 g for the majority of specimens, with the exception of specimen C where the amount of citrate calculated was 0.244 g / 100 g (Table 8.7). Specimen C exhibited the largest amount of citrate whilst the lowest amount of citrate was observed for specimen B. The amount of citric acid was not determined for specimen E due to insufficient amount of material.

Plotting coherence length against amount of citric acid revealed no correlation between bone types. The amount of citric acid calculated for rostrum and bovine specimens were similar even though the coherence lengths differ significantly for these specimens. Conversely, although red deer antler, porcine and bovine specimens have similar coherence lengths (25 - 29 nm), the amount of citric acid was significantly greater for red deer antler specimens (Figure 8.18).

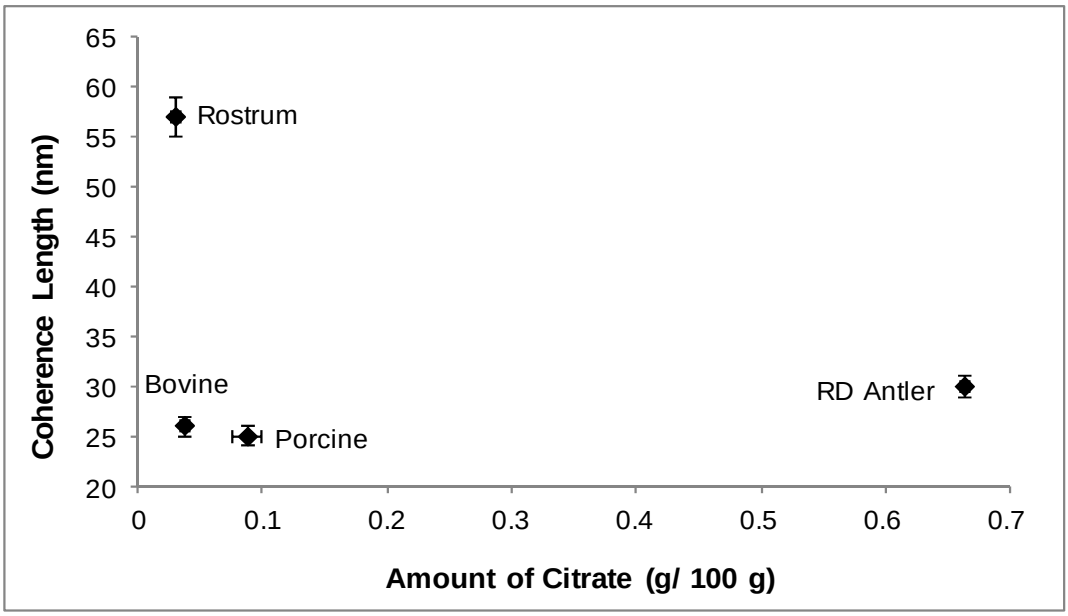

Figure 8.18 Coherence length (nm) plotted against the amount of citrate for each bone type.

No correlation between coherence length and amount of citrate was observed for urinary calculi specimens, as shown in Figure 8.19. Although the amount of citrate calculated for specimens B and G (0.027 and 0.035 g / 100 g respectively) are similar, the coherence length for these two specimens are significantly different (27 and 77 nm respectively). Conversely, although specimens D and C exhibit similar coherence lengths (32 and 31 nm respectively), the amount of citrate calculated for these two specimens was significantly different (0.07 and 0.244 g / 100g respectively).

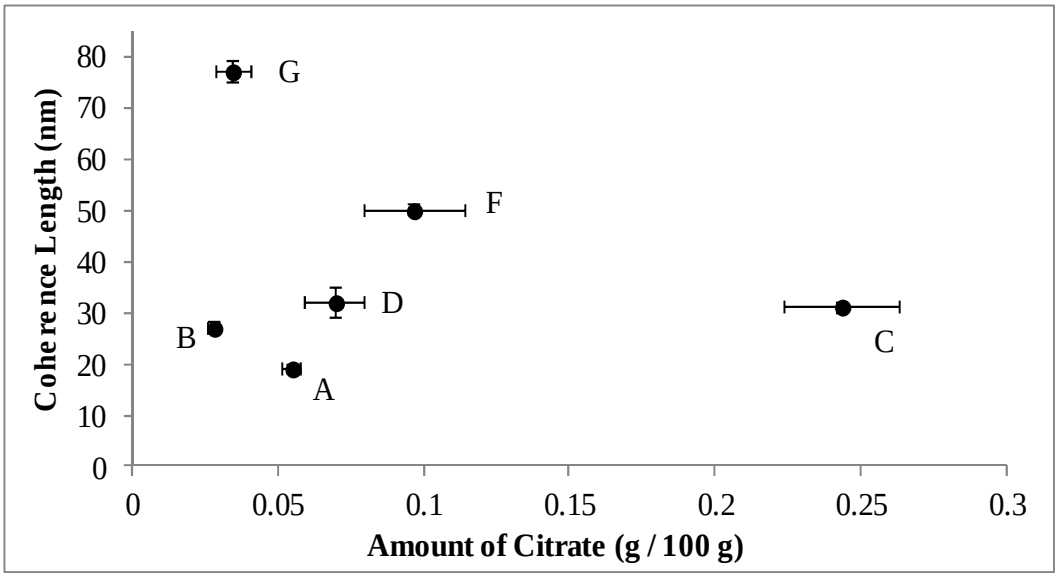

Figure 8.19 Coherence length (nm) plotted against the amount of citrate for each urinary calculi specimen. Specimen E was not analysed due to insufficient material.

As discussed in chapter 3, collagen is thought to provide a mechanical form of *in vivo* HAp crystallite size control. Consequently, this was investigated by plotting coherence length against amide I: phosphate ratio for bone and urinary calculi specimens A, D and E, as shown in Figure 8.20.

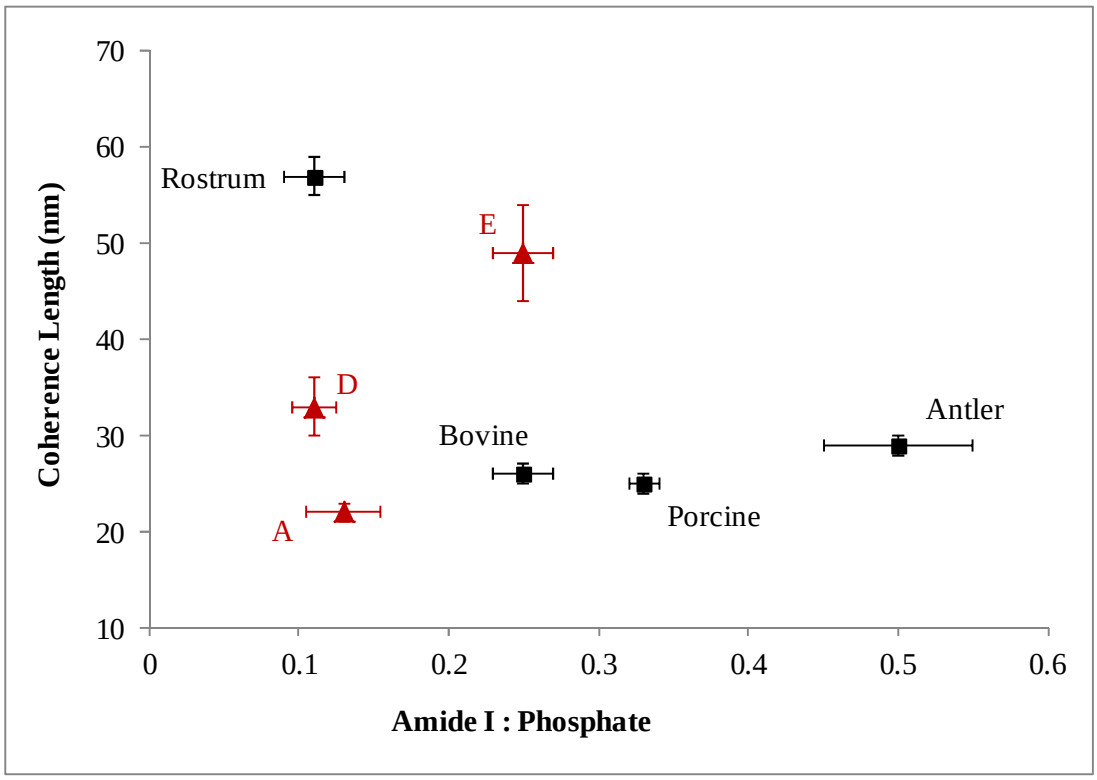

Figure 8.20 Coherence length (nm) plotted against amide I to phosphate ratio for each bone type (■) and urinary calculi specimens (▲) A, D and E.

A weak correlation is observed for bone types, with increasing amide I: phosphate ratio values, a decrease in coherence length is observed. However, red deer antler exhibited a considerably larger amide I: phosphate ratio but similar coherence length to bovine and porcine specimens. In contrast, with increasing amide I: phosphate ratio, an increase in coherence length was observed for urinary calculi specimens. The amide I: phosphate ratios for urinary calculi specimens B, C, F and G are not reported due to insufficient amount of material.

8.4.2 Carbonate Content: FTIR Analysis

In general, the carbonate to phosphate ratio was much lower for synthetic HAp specimens, whilst bone specimens exhibited the largest carbonate to phosphate ratio (Table 8.8). Carbonate to phosphate ratios are not reported for urinary calculi

specimens B, C, F and G due to insufficient amount of material required for FTIR analysis.

Specimen	Carbonate : Phosphate (Area)
Rostrum	0.02 ± 0.0007
Human	0.025 ± 0.0003
Bovine	0.026 ± 0.0010
Porcine	0.031 ± 0.0008
Red Deer Antler	0.035 ± 0.0010
UC_A	0.020 ± 0.0008
UC_D	0.010 ± 0.0001
UC_E	0.007 ± 0.0008
sHAp 1	0.004 ± 0.0003
sHAp 2	0.002 ± 0.0003
sHAp 3	0.015 ± 0.0001

Table 8.8 Carbonate to phosphate ratio for all specimen groups. Errors calculated from the standard deviation of three repeats.

Plotting coherence length against carbonate to phosphate ratios revealed a correlation for all specimen groups (Figure 8.21). With increasing coherence length, a decrease in carbonate to phosphate ratio was observed for all specimens. A difference was observed in the gradient of the correlation for the three specimen groups.

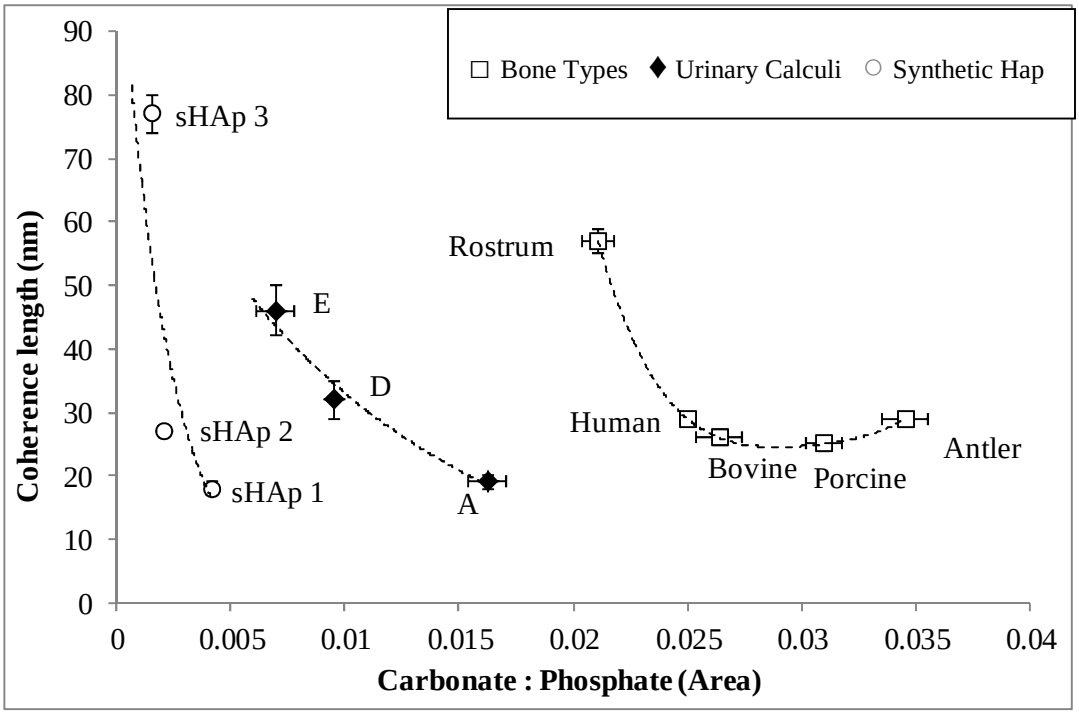

Figure 8.21 Coherence length plotted against carbonate: phosphate revealed a correlation for bone, urinary calculi and synthetic HAp specimens

8.4.3 Lattice Strain and Crystallite Size

Plotting crystallite size (obtained from Williamson Hall analysis, section 8.3.2) against strain values (obtained from single line analysis, section 8.3.3) for all specimens revealed a correlation (Figure 8.22). With increasing strain values, the corresponding crystallite sizes increased for all specimen groups.

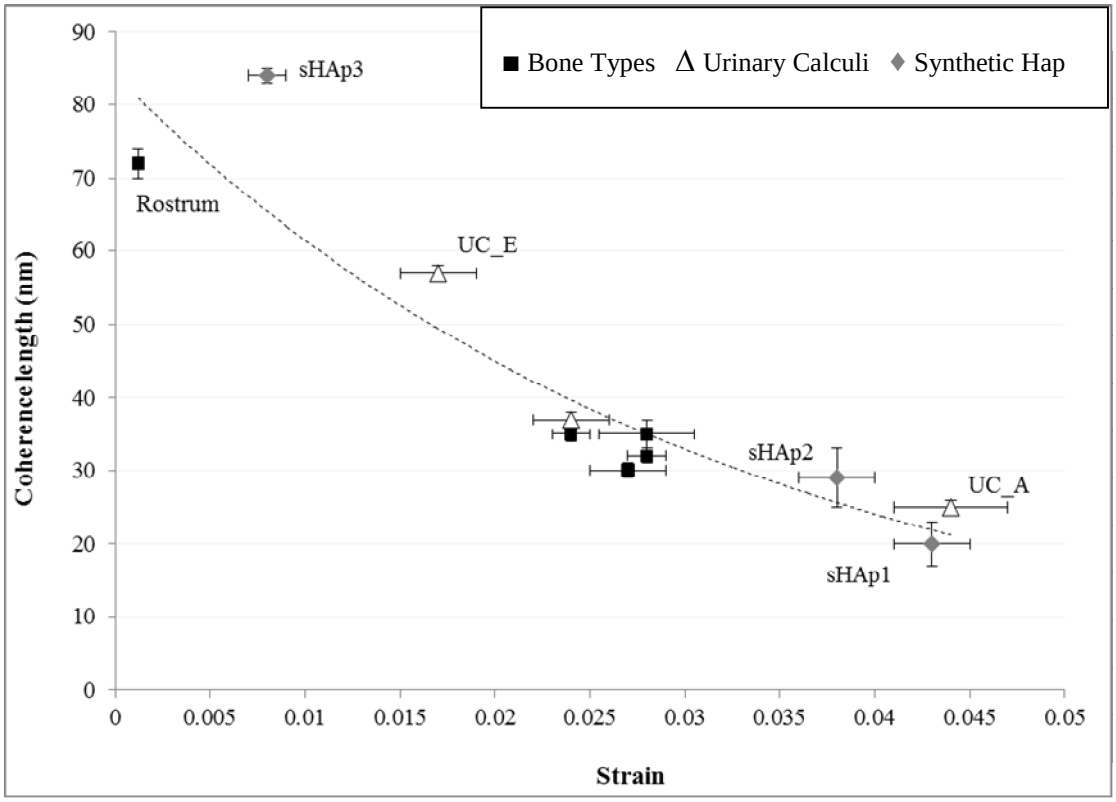

Figure 8.22 Crystallite size (nm) plotted against strain for bone (■), urinary calculi (Δ) and synthetic HAp (♦) specimens. Crystallite size values were obtained from Williamson Hall plot analysis (section 8.3.2) whilst strain values were calculated using single line analysis (section 8.3.3).

8.5 General Response to Heat Treatment

8.5.1 Mass Loss of Statically Heated Bone Specimens

A loss in mass was observed for all statically heated bone specimens. The average mass loss differed depending on bone type, with red deer antler specimens displaying the largest loss (an average of 53 %) whilst the smallest loss was observed for rostrum specimens (11 %). A slightly greater average mass loss was observed for porcine specimens (38 %) in comparison to bovine specimens (33 %). All specimens heated for longer periods of time, irrespective of temperature, showed a slightly greater mass

loss than specimens heated for shorter periods. Mass loss values recorded for bovine bone specimens heated at 600 ^{o}C and 800 ^{o}C are provided in Table 8.9. Mass loss data bovine bone heated at 650, 700 and 750 ^{o}C is provided in appendix B, along with mass loss data for heated porcine, red deer antler and rostrum specimens.

	Mass Loss (wt. %)	
	600 ^{o}C	**800 ^{o}C**
Dwell Period		
1m		21 ± 2
5m		33 ± 1
10m		35 ± 1
20m		35 ± 1
30m		35 ± 1
1hr	33 ± 2	34 ± 1
2hr	33 ± 1	34 ± 1
4hr	34 ± 1	34 ± 1
6hr	32 ± 1	
24hr	35 ± 2	
48hr	35 ± 2	
72hr	34 ± 1	

Table 8.9 Mass loss (weight percentage, wt. %) for bovine bone heated at 600 ^{o}C and 800 ^{o}C at different periods of time (dwell period). Errors calculated from the standard deviation of three repeats.

With regards to anorganic specimens, mass loss was recorded after the initial heat treatment used to remove the organic matrix and also after the second heat treatment. A significantly greater mass loss (which was comparable to mass loss observed for 'organic' analogues, within 3%) was observed after the first heating in comparison to the second heating. An average mass loss of 2% was recorded for the second heat treatment for both bovine and porcine anorganic specimens. Mass loss data for anorganic specimens (bovine and porcine) is provided in appendix B.

8.5.2 Colour Change: Visual and Colourimetric Analysis

For statically heated bone, at temperatures of 600 and 650 ^{o}C for short periods of time (30 mins – 1 hr), the bone changed from cream to light grey in colour whilst bone specimens heated for extended periods (> 2 hrs) at the same temperature were white in colour. This trend was also observed at higher temperatures (700, 750 and 800 ^{o}C), however the series of colour changes occurred at shorter heating periods. For example, a blue/grey colour was observed for bone specimens heated at 750 ^{o}C for 10 minutes in contrast to bone heated at 650 ^{o}C, where this colour was only observed for samples heated for at least 1 hr. A colour change from ivory to black was also observed for bone specimens heated for very short periods of time (< 5 mins) at temperatures higher than 650 ^{o}C. Figure 8.21 illustrates the colour changes in bone specimens heated at 650^{o}C and 750^{o}C for various time periods. The 'anorganic' bone specimens, after the first heat treatment to remove the organic matrix, were dark brown in colouration. After the second heat treatment, the change in colour appeared to follow the same trend as discussed above.

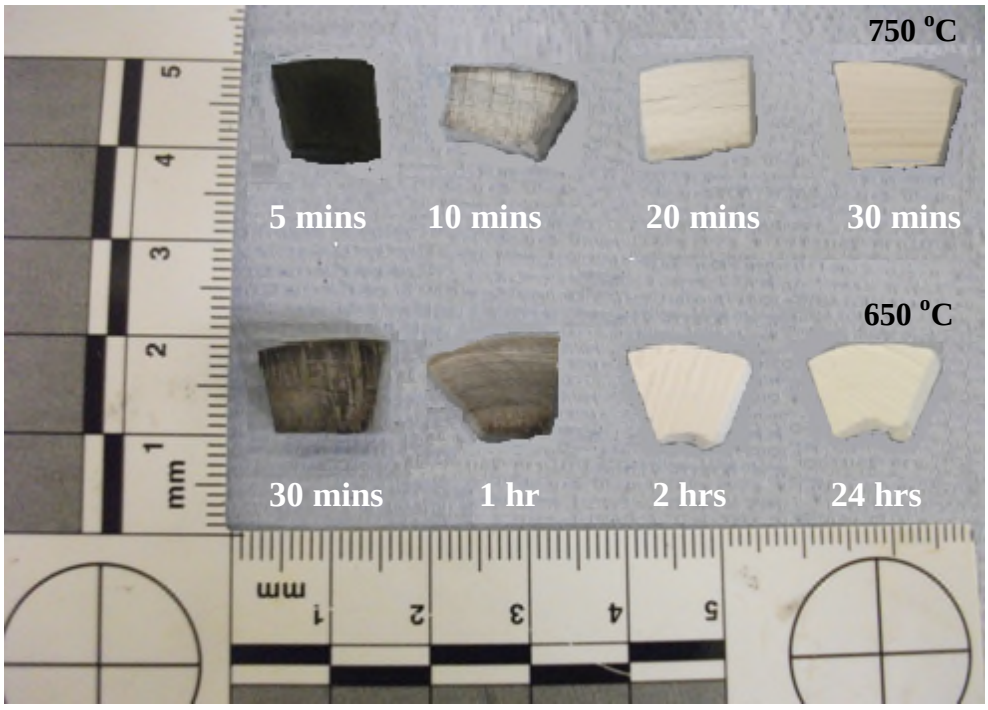

Figure 8.23 Photograph highlighting the colour change in bovine bone specimens heated at 650 ^{o}C (bottom) and 750 ^{o}C (top) for various time periods.

Colourimetric analysis numerically records the colour change of bone during heat treatment using L*a*b colour space values, as discussed in section 5.2.3. Initial observation of the colourimetry data revealed upon heating, 'L' values increased. In general, both 'a' and 'b' values decreased for all temperature and time ranges. L*a*b* values for bone heated at 600 ^{o}C and 800 ^{o}C are given in Table 8.10 for comparison. Colour values for bovine bone heated at 650, 700 and 750 ^{o}C can be found in appendix C.

	600 ^{o}C				**800 ^{o}C**		
	L*	**a***	**b***		**L***	**a***	**b***
Dwell Period							
1m					52 ± 9	3.2 ± 2.0	9.9 ± 9.0
5m					50 ± 15	-0.3 ± 0.5	0.5 ± 0.9
10m					80 ± 1	-0.3 ± 0.4	0.1 ± 0.1
20m					93 ± 1	-0.2 ± 0.4	1.1 ± 0.3
30m					94 ± 1	-0.2 ± 0.3	1.1 ± 0.2
1hr	71 ± 2	0.9 ± 0.03	3.4 ± 0.1		94 ± 1	-0.2 ± 0.2	1.3 ± 0.1
2hr	75 ± 1	0.9 ± 0.02	3.4 ± 0.1		95 ± 1	-0.4 ± 0.2	1.3 ± 0.3
4hr	86 ± 2	0.5 ± 0.02	2.6 ± 0.2		92 ± 2	-0.2 ± 0.3	1.0 ± 0.4
6hr	86 ± 3	0.3 ± 0.04	2.2 ± 0.1				
24hr	92 ± 3	-0.1 ± 0.10	0.9 ± 0.2				
48hr	94 ± 3	-0.3 ± 0.01	0.6 ± 0.4				
72hr	94 ± 4	-0.3 ± 0.02	0.7 ± 0.1				

Table 8.10 L*a*b colour scale values for bovine bone heated at 600 ^{o}C and 800 ^{o}C for different periods of time (dwell period). As discussed in section 5.2.3, figure 5.9, L* relates to the black - white (0 – 100), a* the red – green (positive to negative) and b* the yellow – blue (positive to negative) linear colour spaces. Errors calculated from the standard deviation of three repeats.

8.5.3 X-ray Diffraction Analysis

8.5.3.1 Statically Heated Bone

The primary phase and in general the only phase of all bone specimens (unheated and those heated up to 1200 ^{o}C) resembled calcium HAp. HAp peaks for unheated bone were broad, resulting in overlapping peaks, whilst in general HAp peaks of heated bone specimens were narrower. Additional peaks, which could not be attributed to HAp, were also observed in a small number of heated bone specimens. These additional mineral phases were identified as magnesium oxide (~ 37 2θ (^{o})) and/ or calcium oxide (~ 43 2θ (^{o})) and were observed in all bone specimens heated above 800^{o}C. CaO was not observed in red deer antler specimens. (The 2θ values provided correspond to the most intense peaks observed for these mineral phases). At temperatures above 1200 ^{o}C, further additional phases including tetra tricalcium phosphate (TTCP), alpha tricalcium phosphate (α –TCP) and beta tricalcium phosphate (β – TCP) were observed. The main diffraction peaks associated with these mineral phases are provided in appendix D. Quantification of these additional mineral phases, with regards to heating and cooling rates, is detailed in section 8.8.1.2.

Narrower HAp peaks were observed for bone specimens heated at the same temperature but for longer time periods in comparison to specimens heated for shorter periods of time (Figure 8.24). This trend was observed for all temperature ranges.

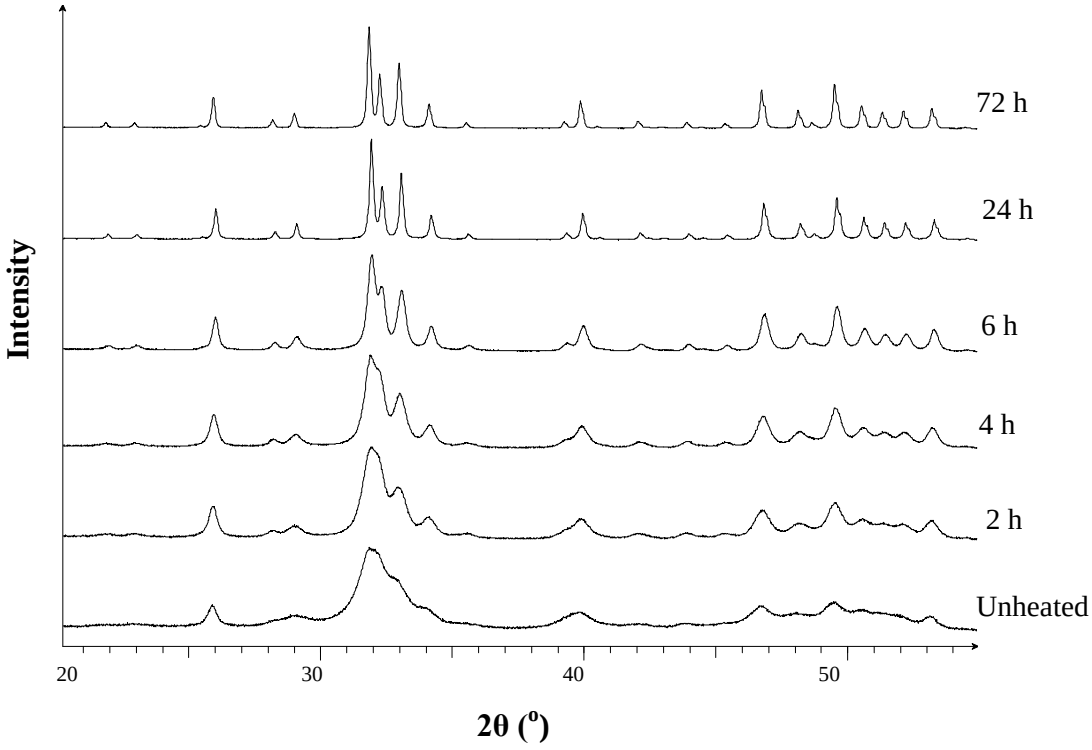

Figure 8.24 X-ray diffractograms of (from top to bottom) unheated bovine bone and bovine bone specimens heated at 600°C for 2, 4, 6, 24 and 72 hours.

When heated for the same period of time, a decrease in HAp peak broadening was observed with increasing temperature (Figure 8.25)

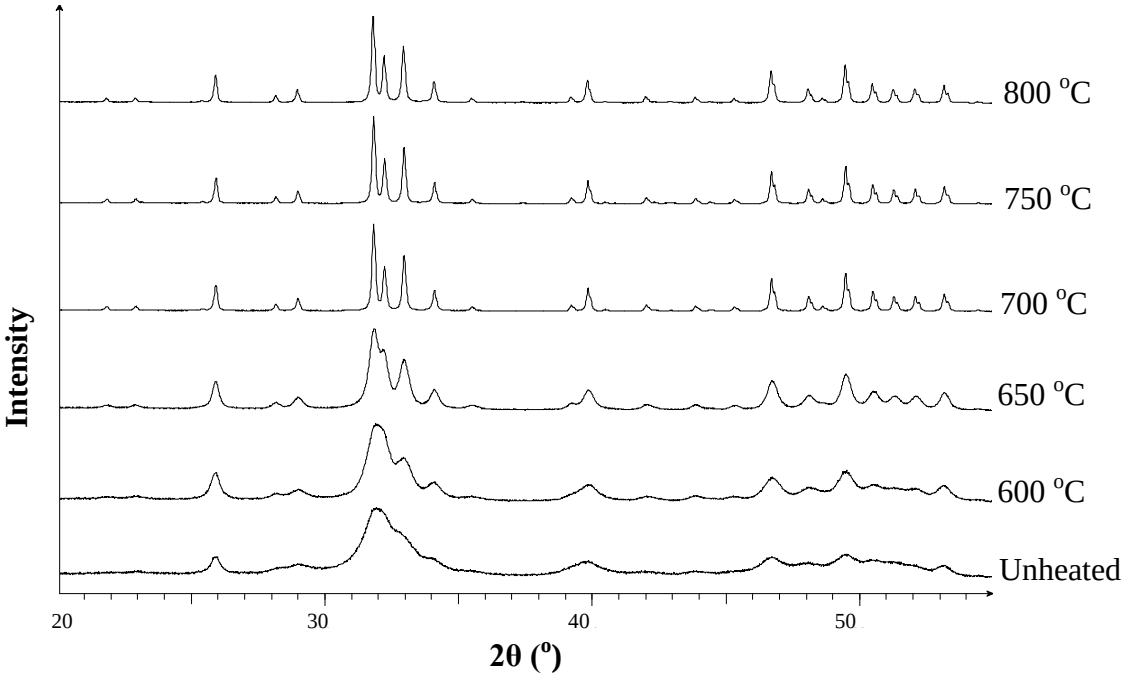

Figure 8.25 X-ray diffractograms of fresh, unheated bovine bone and bovine bone specimens heated for 1 hour at 600, 650, 700, 750 and 800 °C, which highlights the greater extent of crystallisation at higher temperatures in comparison to lower temperatures.

At temperatures > 800 °C, a rapid decrease in peak broadening was observed in the diffractograms of all bone specimens when heated for only 5 minutes whilst broad, overlapping peaks were still present for specimens heated at temperatures < 550 °C for 48 hours (Figure 8.26). After careful consideration, bone specimens heated to temperatures ranging from 600 – 800 °C were used to examine the crystallisation kinetics of statically heated bone (discussed further in section 8.6). Specimens heated to temperatures outside of this range were excluded.

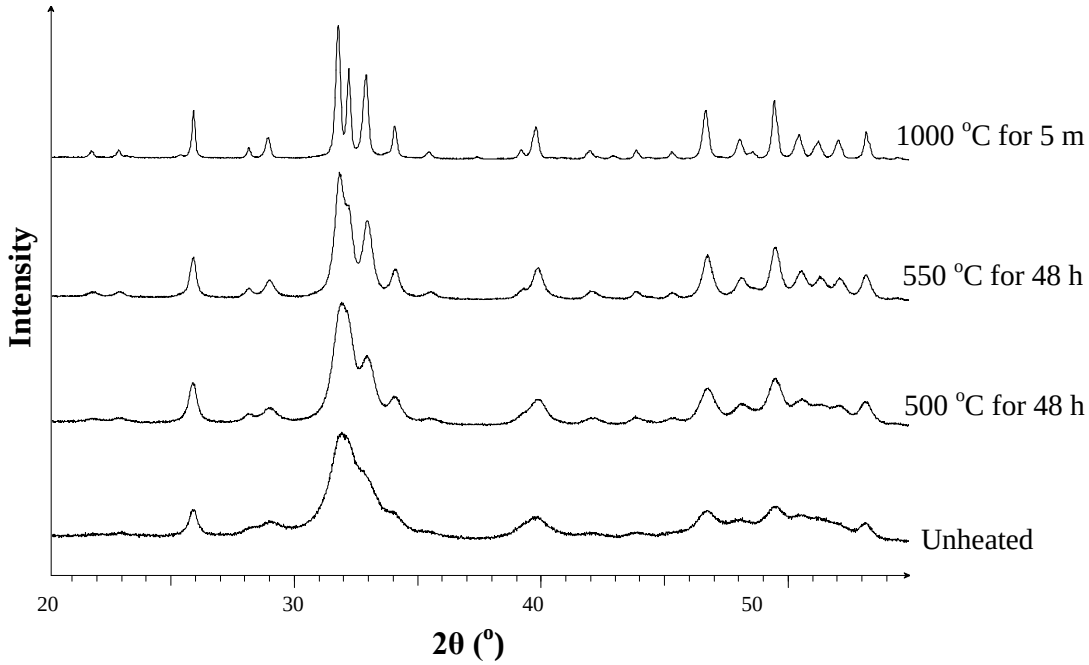

Figure 8.26 X-ray diffractograms illustrating the rapid crystallisation (within minutes) of bone specimens heated to temperatures > 800°C, whilst the broad peaks observed at temperatures < 550 °C, suggest there is not sufficient energy to initiate the crystallisation process, even after heating the bone for longer than 48 hrs.

Quantitative analysis of the diffraction data in terms of coherence length is detailed separately in section 8.6, whilst lattice parameter values, which provide an indication of lattice chemical changes (due to loss and incorporation of ions), are considered below.

During heat treatment, lattice parameter behaviour differed depending on the axial length observed. Plotting 'c' axis lattice parameter against time (Figure 8.51B, section 8.8.2), revealed a decrease in 'c' axis data for each temperature. This data was used to develop a time-temperature predictive model and is considered in more depth in section 8.8.2. When 'a' axis lattice parameter data was plotted against time, a trend was observed for each temperature (Figure 8.27). The 'a' axis values initially decrease, then increase before decreasing and seeming to plateau.

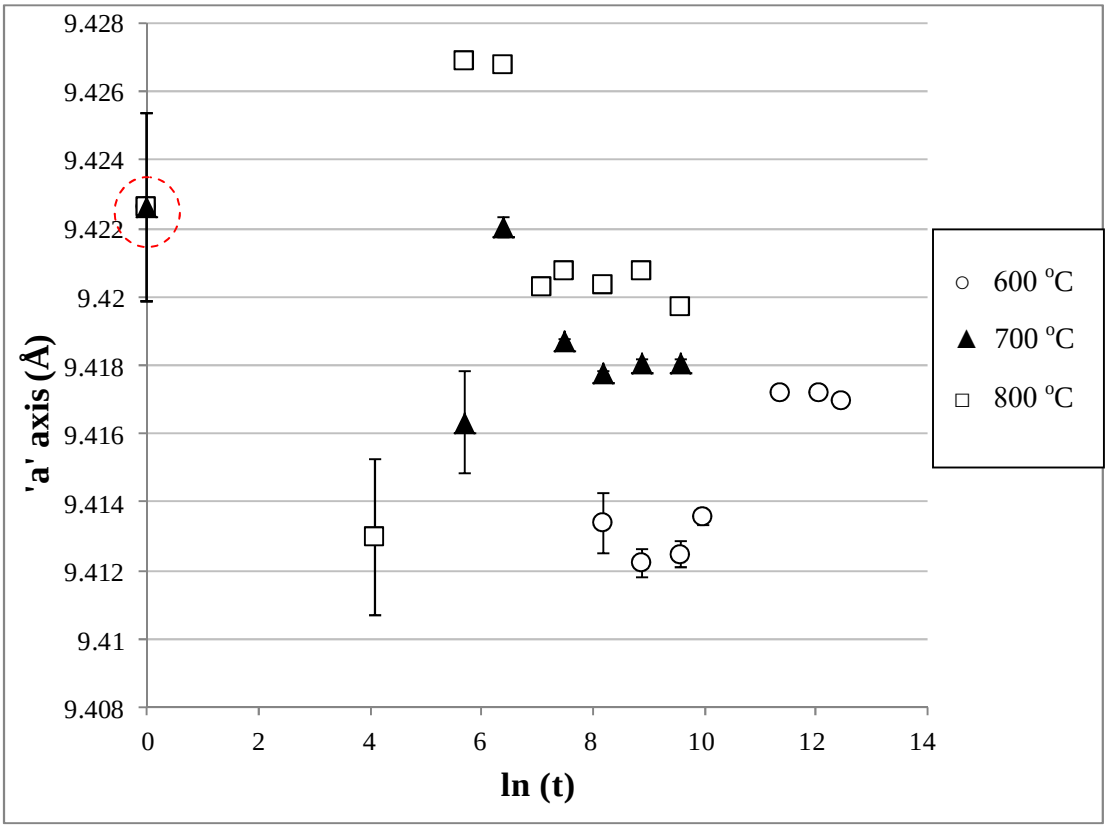

Figure 8.27 Behaviour of 'a' axis lattice parameter data when bovine bone was heated for increasing time periods at 600, 700 and 800 °C. Unheated bone lattice parameter values are included (circled in red for clarity).

8.5.4 Fourier Transform Infrared Spectroscopy Analysis

Several changes were observed in FTIR spectra of heated bone specimens (irrespective of bone type) in comparison to unheated bone material (Figure 8.28). A decrease in the intensity of amide I and II (1750 – 1500 cm^{-1}) peaks as well as the carbonate peaks (1500 - 1350 cm^{-1} and 900 – 820 cm^{-1}), was observed for heated bone specimens. The main peak corresponding to the phosphate bond (1200 – 900 cm^{-1}) was sharper and more resolved in heated bone specimens.

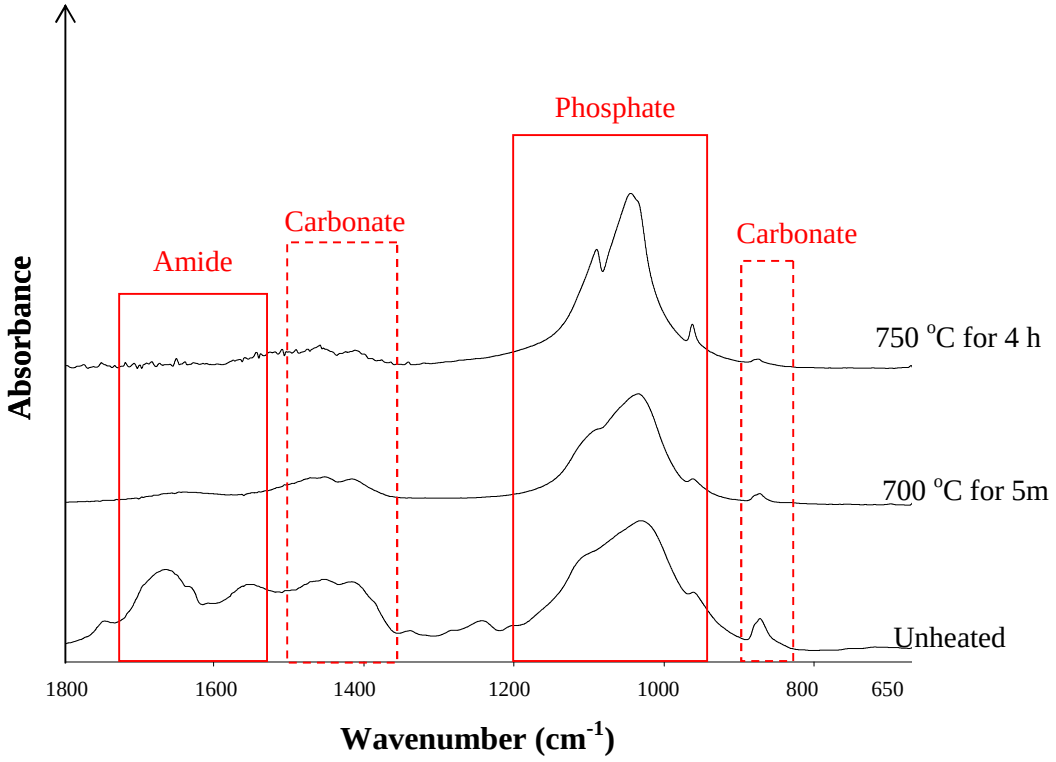

Figure 8.28 FTIR spectra of unheated bovine bone and bovine bone heated at 700 °C for 5 minutes and 750 °C for 4 hours which highlight the changes in the amide, carbonate and phosphate peaks.

8.5.5 Differential Scanning Calorimetric Analysis

Upon heating four prominent peaks were observed in the DSC spectra of all bone specimens (Figure 8.29). A broad endothermic peak, with low intensity was observed between 25 – 100 °C, with a peak maximum at approximately 75 °C (Peak 1). A sharp, low intensity endothermic peak was also observed between approximately 120 – 160 °C (Peak 2). Two overlapping exothermic peaks were also observed between approximately 275 – 500 °C. The maximum of the first and most intense peak was observed at approximately 350 °C (Peak 3). The second peak maximum, which appeared to 'shoulder' the peak at approximately 350 °C was observed at approximately 450 °C (Peak 4) and was most prominent in the red deer antler

spectrum. Although present, the aforementioned peaks were significantly less prominent in rostrum and anorganic spectra, in comparison to the spectra of the other bone types. No peaks were observed between approximately 500 ^{o}C and 600 ^{o}C for all bone types.

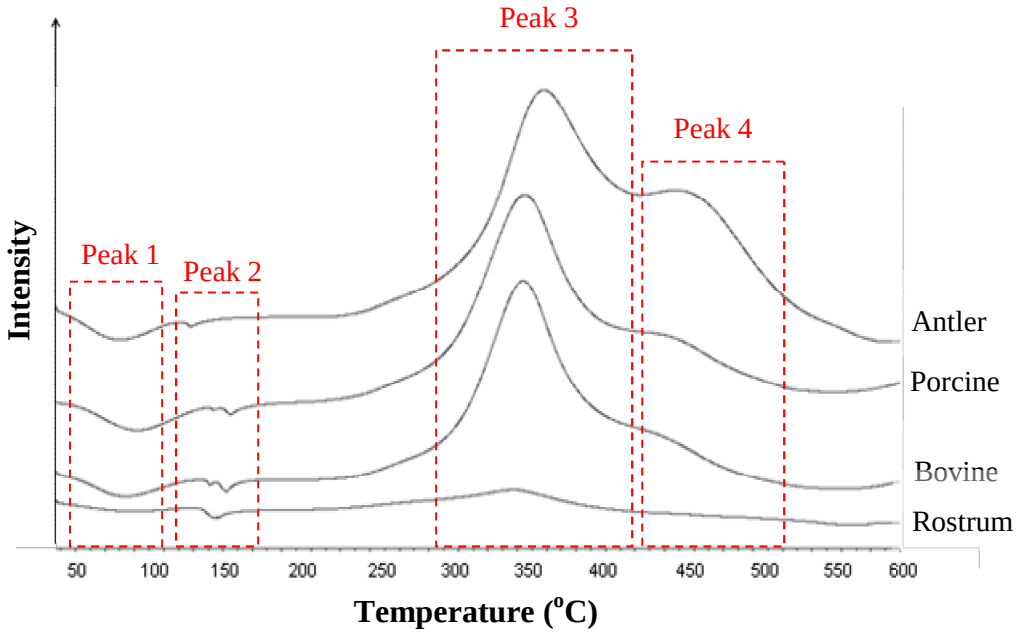

Figure 8.29 DSC spectra for red deer antler, porcine, bovine and rostrum

8.6 Bone Crystallisation Kinetics: Static Heating

Bone crystallisation kinetics was investigated using bone specimens which had been statically heated at 600, 650, 700, 750 and 800 ^{o}C for various time periods (section 7.2.1.3, Table 7.4). Coherence lengths (which give some indication of the degree of crystallisation) in three crystallographic directions <00ℓ>, <hk0> and <0k0> were calculated using the Scherrer equation (as discussed in section 5.3.1). Using coherence length data, the activation energy, the rate of crystal growth and the spontaneous nucleation were calculated, the results of which are presented in this section.

8.6.1 Activation Energy

Plotting coherence length data (normalised to the largest CL value for each bone type, essentially the instrument resolution function value) against ln (time) for each temperature, revealed a sigmoidal relationship for all three crystallographic directions and all bone types (Figure 8.30). The sigmoidal curves for porcine, anorganic bovine and anorganic porcine specimens are provided in appendix E.

.

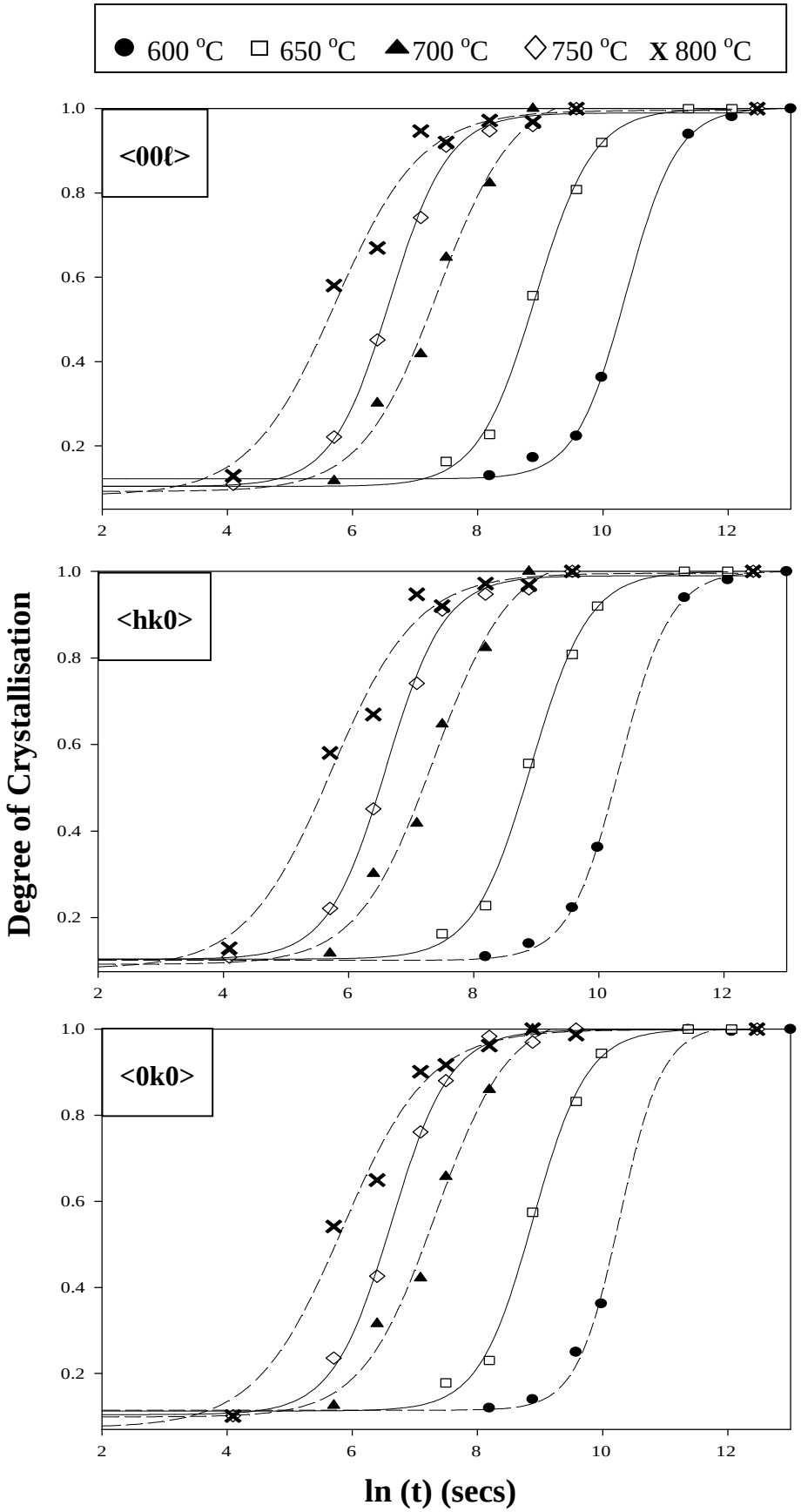

Figure 8.30 Sigmoidal curves representing the crystallisation process in three crystallographic directions, <00ℓ>, <hk0> and <0k0> for bovine bone heated at 600, 650, 700, 750 and 800 °C for various time periods. Errors are not shown for clarity.

The equations obtained from fitting sigmoidal curves were used to calculate the time at which 50% crystallisation occurred for all temperatures. This data was used to construct an Arrhenius plot (Figure 8.31) where 1/T plotted against ln (k) revealed a linear relationship (ln (k) is the negative value for ln (t) calculated from the sigmoidal curves).

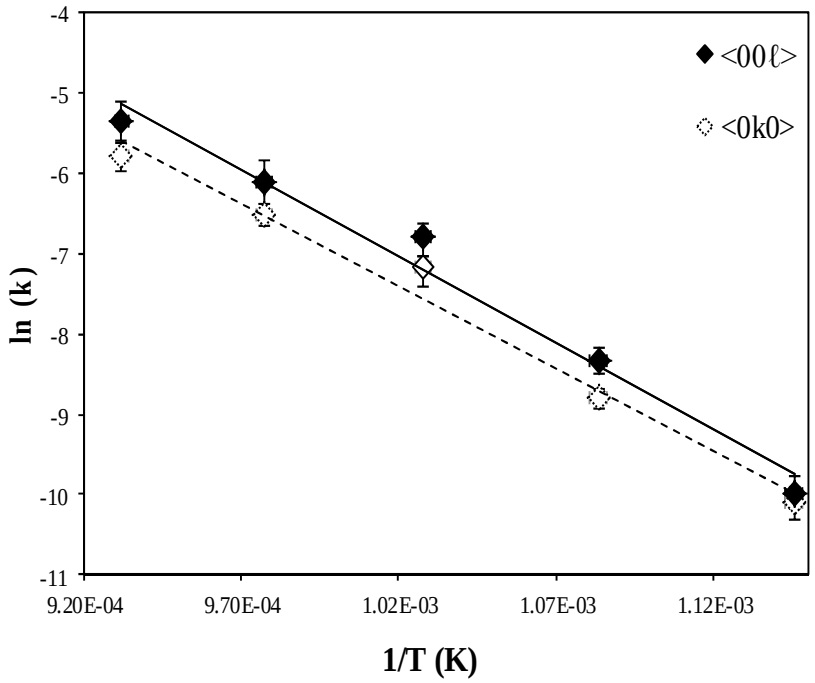

Figure 8.31 Arrhenius plots constructed from the sigmoidal plot data at 50% crystallisation for bovine bone in <00ℓ> and <0k0> crystallographic directions. Y-axis errors were calculated from errors associated with fitting the data with a sigmoidal curve (Figure 8.30).

The gradient of the linear line was used to calculate the activation energy according to the Arrhenius equation for all bone types:-

$$k = Ae^{\frac{-Ea}{RT}} \qquad \textbf{(8.2)}$$

, where A is a pre-exponential factor, Ea is the activation energy, R is the gas constant (8.31 $JK^{-1}mol^{-1}$), T is the absolute temperature and k is the rate constant.

Calculated activation energies for bovine and porcine specimens as well as their 'anorganic' analogues, in three crystallographic directions, are outlined in Table 8.11. Taking experimental errors into consideration, there was no significant difference between the four bone types or in the three crystallographic directions.

	<00ℓ>	**<0k0>**	**<hk0>**
Bovine	181 ± 4	171 ± 5	179 ± 3
Anorganic (Bovine)	195 ± 5	176 ± 3	183 ± 4
Porcine	195 ± 4	185 ± 4	183 ± 6
Anorganic (Porcine)	201 ± 6	191 ± 3	187 ± 4

Table 8.11 Calculated Activation energies (calculated in kJ mol $^{-1}$) for bovine and porcine bone as well as their anorganic analogues in three crystallographic directions.

8.6.2 Kolmogorov-Johnson-Mehl-Avrami (KJMA)Parameters

For the first time, coherence length data calculated for three crystallographic directions <00ℓ>, <hk0> and <0k0> was fitted to the Kolmogorov-Johnson-Mehl-Avrami (KJMA) model, as shown in equation 8.3:

$$Y = 1 - \exp(-kt^n) \qquad \textbf{(8.3)}$$

, where k is the rate of crystal growth and n relates to spontaneous nucleation. Y corresponds to the proportion of material transformed at a constant temperature for a given time period (t).

The KJMA model describes how solids transform from one phase to another at constant temperature The KJMA model will be referred to as the Avrami model/ equation for the remainder of this thesis. This novel approach provided directional dependent information on the spontaneous nucleation of bone mineral and the rate of crystal growth during heat treatment. Fitting the coherence length data to equation 8.3 and plotting against ln (t) revealed a linear relationship (Figure 8.32).

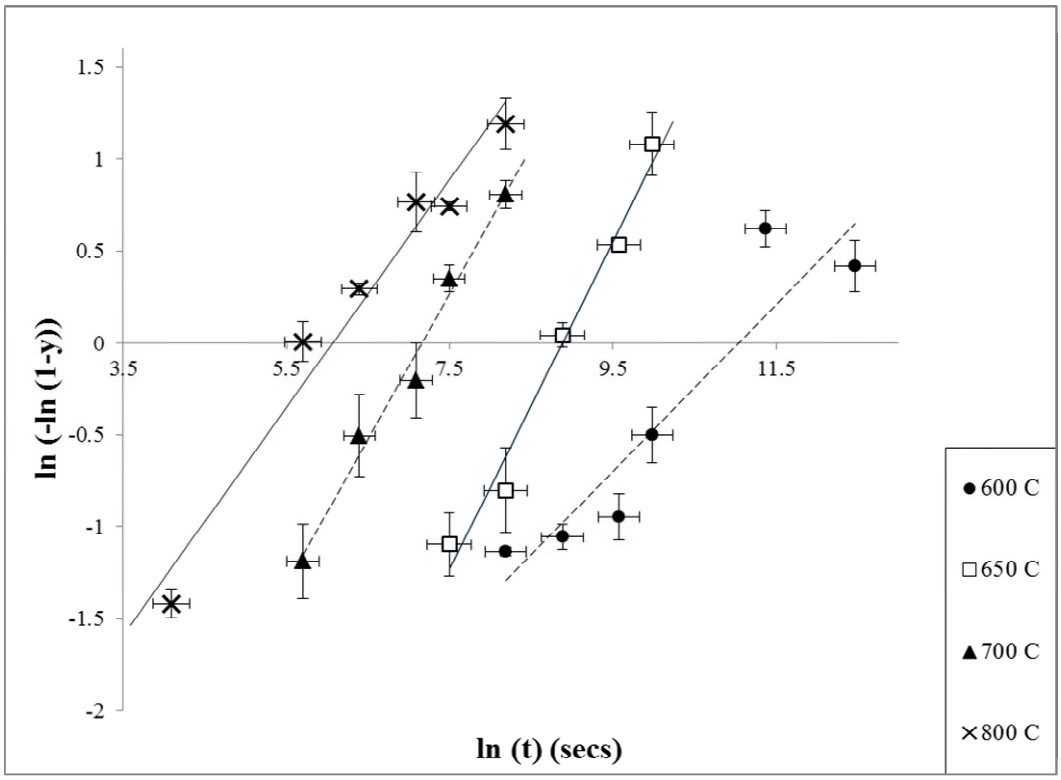

Figure 8.32 Coherence length data for bovine bone heated at 600, 650, 700 and 800 ^{o}C fitted to the Avrami equation. The slopes and intercepts yield values of 'n' and 'k' respectively. Y-axis errors were calculated from the standard deviation of three repeats whilst the x-axis errors were calculated from errors associated with fitting coherence length data with a sigmoidal curve (Figure 8.30).

Coefficients n and k were calculated according to the Avrami equation, from the gradient and y-intercept respectively. For all bone types (bovine, porcine and their anorganic analogues) and in all three crystallographic directions, the value of n was approximately 1 (within experimental errors) when heated at lower temperatures (600 – 650 ^{o}C). The value of n was found to decrease gradually to ~ 0.5 with increasing temperature. The value for k increased slightly as the temperature increased. Porcine bone specimens appeared to display a greater k value at all observed temperatures in comparison to bovine bone specimens. Both bovine and porcine were found to have a greater 'k' value than their anorganic analogues. These trends were observed in <00ℓ>, <0k0> and <hk0> crystallographic directions for all bone specimens. An example of n and k values for bovine, porcine bone and their anorganic analogues when heated to 650 ^{o}C and 800 ^{o}C are provided in Table 8.12. Further values for n and k calculated for bovine, porcine bone and their anorganic analogues heated at temperatures of 600 ^{o}C, 700 ^{o}C and 750 ^{o}C are provided in appendix F, along with n and k values calculated from hk0 reflection data.

	<00ℓ>				**<0k0>**			
	650 ^{o}C		**800 ^{o}C**		**650 ^{o}C**		**800 ^{o}C**	
	n	k	N	k	n	k	N	k
Bovine	0.99 ± 0.01	0.49 ± 0.04	0.66 ± 0.15	4.04 ± 1.03	1.14 ± 0.06	0.36 ± 0.09	0.85 ± 0.17	4.54 ± 1.03
Bovine Anorganic	0.88 ± 0.03	0.37 ± 0.08	0.53 ± 0.02	3.26 ± 0.66	1.11 ± 0.09	0.25 ± 0.08	0.71 ± 0.06	3.21 ± 0.95
Porcine	0.94 ± 0.23	1.29 ± 0.27	0.67 ± 0.03	5.77 ± 0.73	1.07 ± 0.04	0.80 ± 0.17	0.76 ± 0.05	6.00 ± 0.52
Porcine Anorganic	0.92 ± 0.12	0.42 ± 0.09	0.57 ± 0.06	2.88 ± 0.83	1.01 ± 0.07	0.32 ± 0.05	0.69 ± 0.04	2.12 ± 0.77

Table 8.12 Calculated values of 'n' and 'k' obtained by fitting coherence length data (corresponding to <00ℓ> and <0k0> reflections) to the KJMA equation. Errors calculated from the standard deviation of three repeats.

8.6.3 Further Investigation: Role of Collagen during the Crystallisation Process

As highlighted in Table 8.12, ‘k’ values calculated using the Avrami equation differed between bone types, with greater values observed for bovine and porcine specimens in comparison to their anorganic analogues. This suggests differences in the crystallisation rate for bone specimens with and without collagen. To investigate this further, the crystallisation of both rostrum and red deer antler at 700 ^{o}C (which differ significantly in mineral and organic content) was investigated for comparison with the behaviour of bovine and porcine bone.

As shown in Figure 8.33, a decrease in peak broadening for red deer antler was observed after a shorter heating period in comparison to rostrum, bovine and porcine. A decrease in peak broadening was also observed at a shorter heating period for porcine in comparison to bovine.

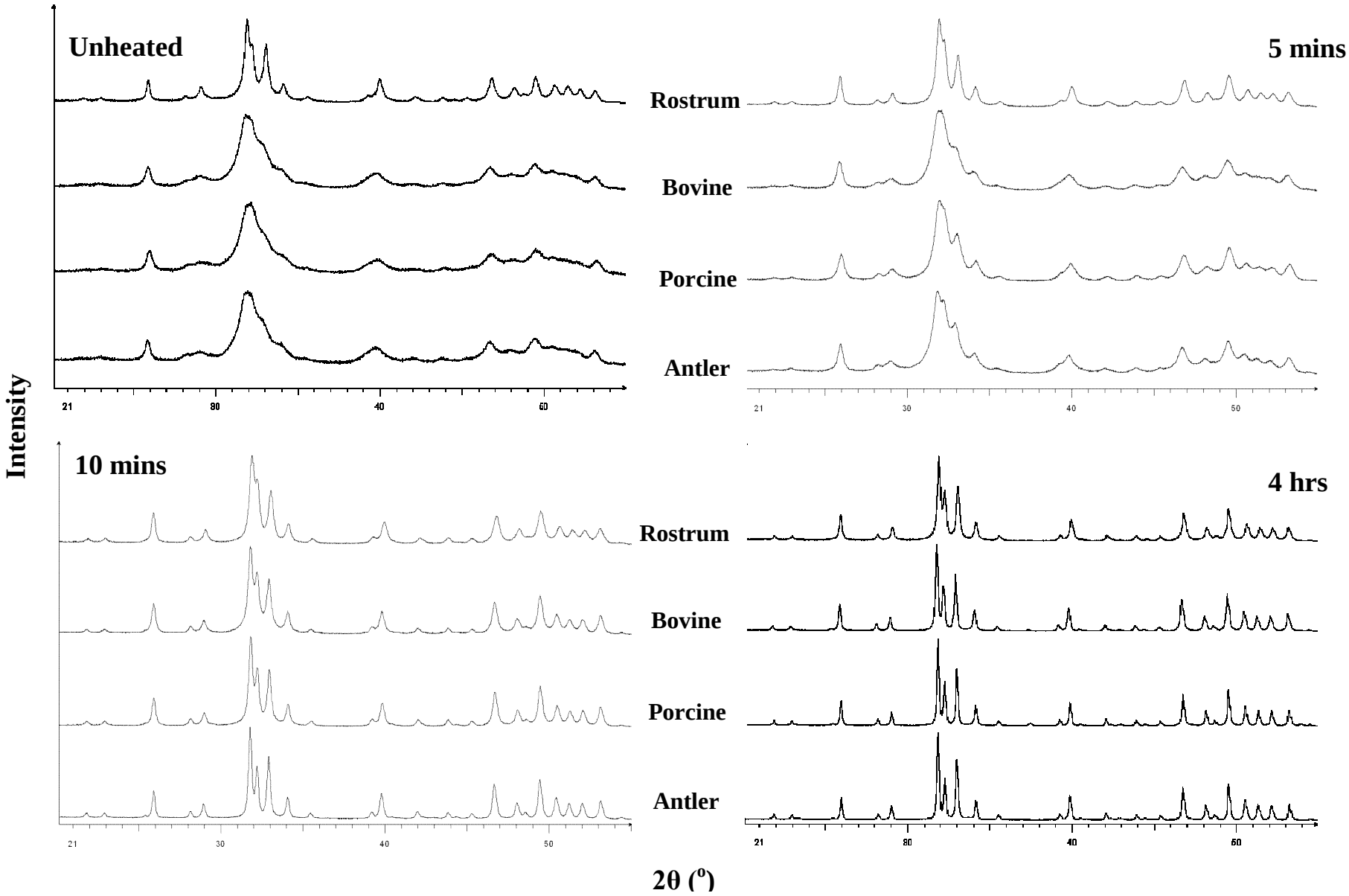

Figure 8.33 Diffractograms of unheated (top left) rostrum, bovine, porcine and red deer antler specimens and these bone types heated at 700 °C for 5 minutes (top right), 10 minutes (bottom left) and 4 hours (bottom right).

Plotting coherence length against ln (t) highlights the difference in the rate of crystallisation (rate of change in the coherence length) between the four bone types (Figure 8.34). The onset of crystallisation (in the <00ℓ> direction) occurs at approximately 1, 4 and 6 minutes for red deer antler, porcine and bovine respectively and 5.5 hours for rostrum.

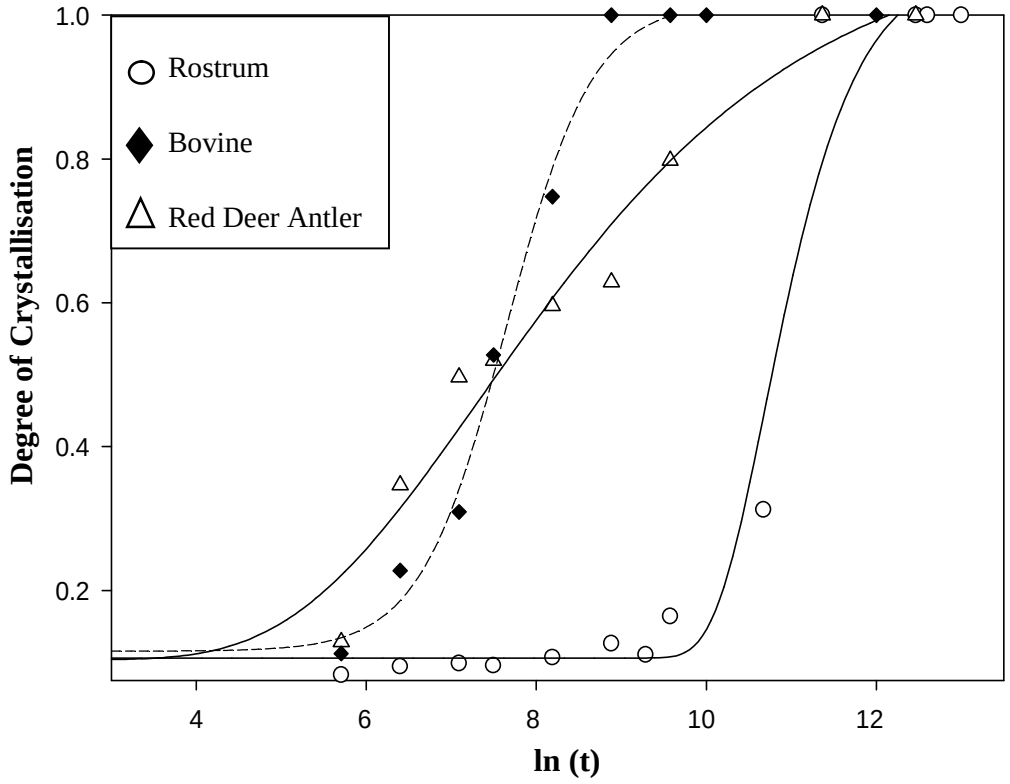

Figure 8.34 Plot of coherence length (normalised) against time revealed the onset of crystallisation of rostrum (○), bovine (♦) and red deer antler (Δ) mineral when heated at 700 ^{o}C occurred at different time periods. The difference in the gradients of the sigmoidal curves is also evident. Errors are excluded for clarity.

As red deer antler exhibits a greater organic content than rostrum (section 8.2.1), it is proposed the time at which the onset of crystallisation occurs is influenced by exothermic energy produced during the combustion of collagen, discussed further in section 9.5.2. In order to investigate this hypothesis, the exothermic energy (Jg $^{-1}$) released during the heat treatment of each bone type was calculated using DSC (Table

8.13). A trend was observed with regards to the exothermic energy values where red deer antler > porcine > bovine > rostrum> anorganic bovine

Bone Type	Exothermic Energy (Jg^{-1})
Anorganic_Bovine	144 ± 46
Rostrum	224 ± 68
Bovine	1649 ± 177
Porcine	2042 ± 194
Red Deer Antler	3961 ± 253

Table 8.13 Exothermic energies for each bone type. Calculated from the integration of the exothermic peaks between 300 – 500 ^{o}C in the DSC spectra. Errors calculated from the standard deviation of three repeats.

8.7 Observations of Dynamically Heated Bone

8.7.1 General Observations

During dynamic heating, the main mineral phase for all bone types resembled calcium HAp. There was no change in HAp diffraction peaks until approximately 590 ^{o}C for red deer antler, 600 ^{o}C for bovine, porcine and human and 630 ^{o}C for rostrum; where in each case a rapid decrease in peak broadening was observed (Figure 8.35). This rapid change is highlighted in Figure 8.36. For all bone types, during cooling from 900 ^{o}C to room temperature, no changes in HAp diffraction peaks was observed. Various additional mineral phases were observed for all bone types, detailed further in section 8.7.3.

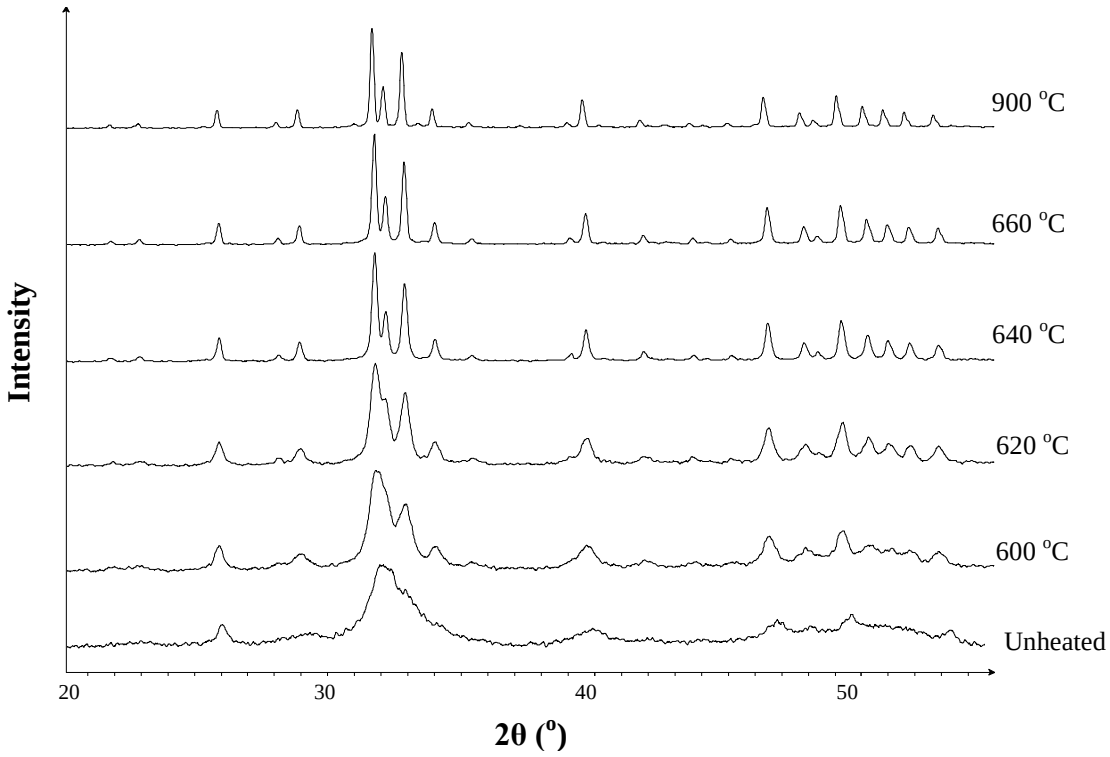

Figure 8.35 X-ray diffractograms of unheated bovine bone and bovine bone dynamically heated to 600, 620, 640, 660 and 900 °C.

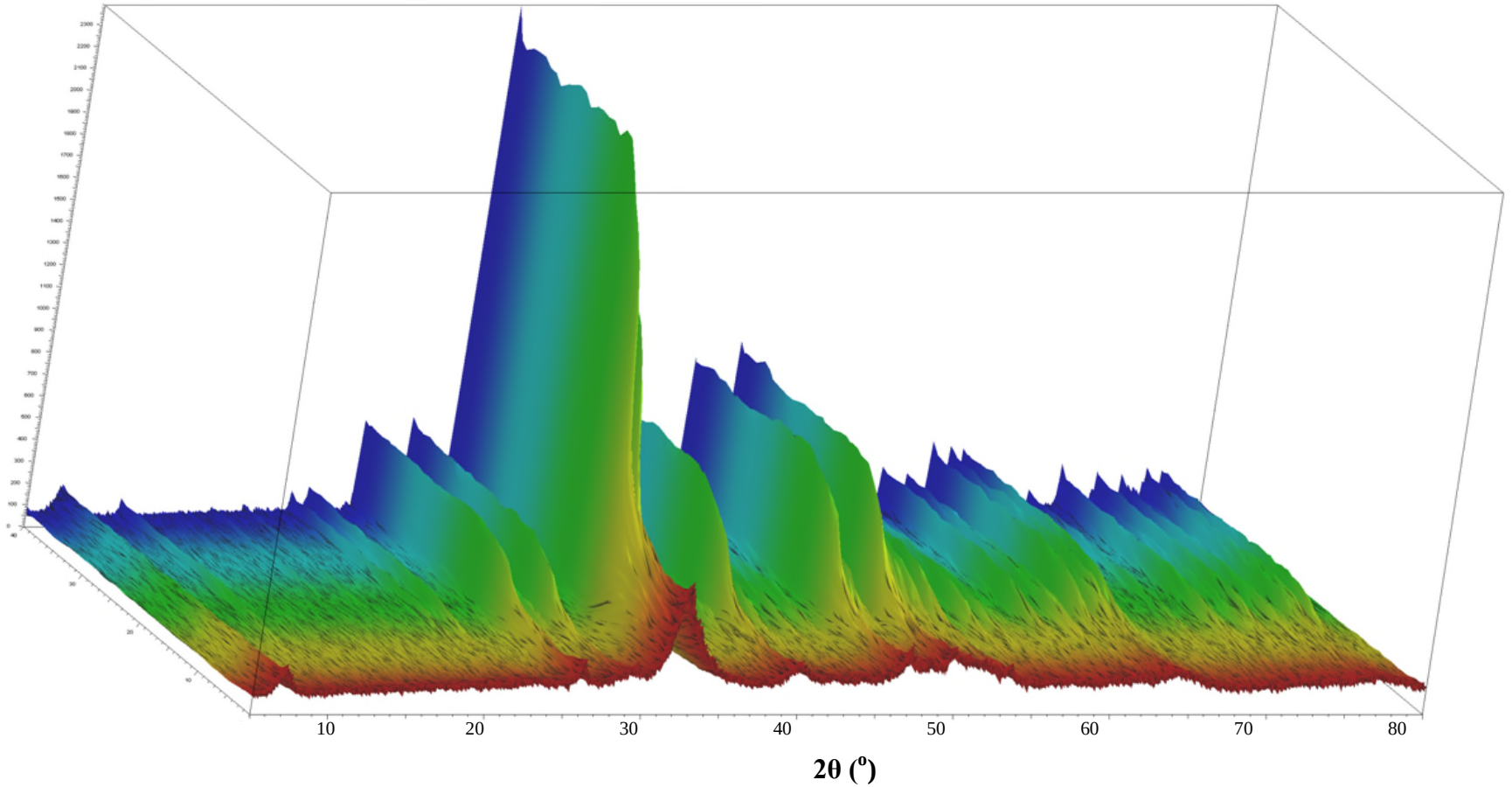

Figure 8.36 3D plot of diffractograms obtained from dynamically heated bovine bone (25 – 900 °C). This figure highlights the rapid decrease in peak broadening.

8.7.2 Crystallisation Process

8.7.2.1 Coherence Length

Plotting coherence length (which is an indication of crystallite size and lattice strain) calculated from the diffractograms of dynamically heated bone against temperature, revealed a sigmoidal relationship (Figure 8.37). The sigmoidal curves were used to determine the temperature at which the onset of crystallisation began. This was identified as the temperature at which the first significant gradient change is observed in the curve (circled red in Figure 8.37). The onset of crystallisation occurred at slightly different temperatures for each bone types: - red deer antler (~ 590 ^{o}C), bovine, porcine, anorganic (~ 600 ^{o}C) and rostrum (~ 630 ^{o}C). This was, within errors, the same for both the <00ℓ> and <0k0> crystallographic directions.

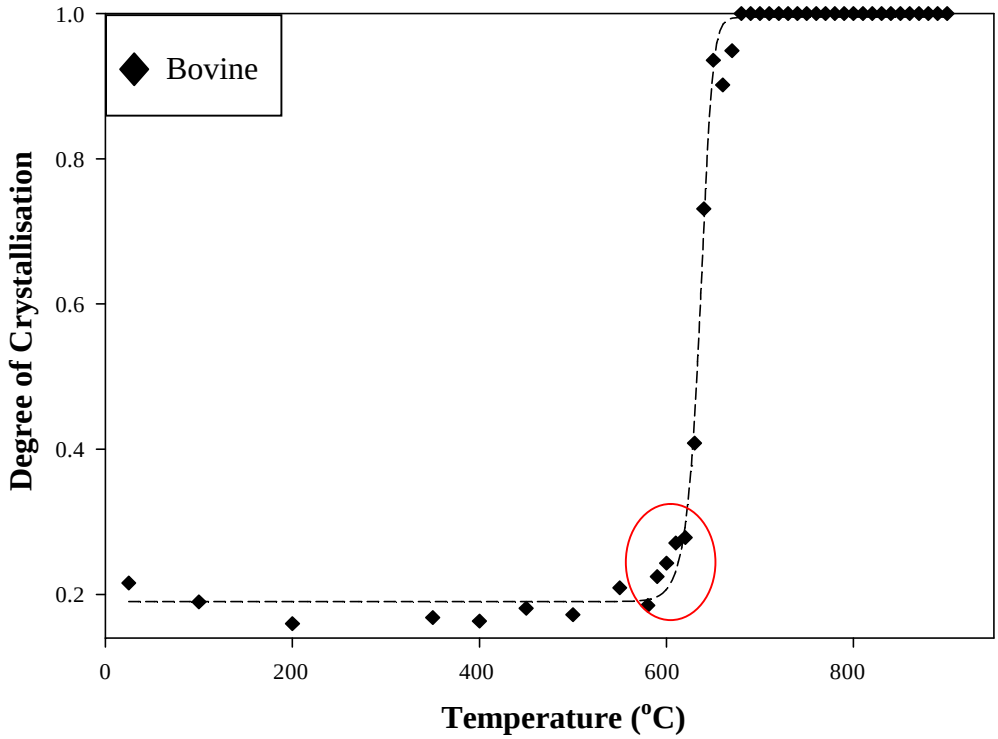

Figure 8.37 Plot depicting the sigmoidal relationship between temperature and coherence length, <00ℓ>, for dynamically heated bovine bone.

After the onset of crystallisation, continued crystal growth (as indicated by an increase in coherence length) differed between bone types. This is evident by the difference in the gradients of the 'linear' part of the sigmoidal curves for each bone type. Crystallisation of rostrum mineral occurred over a short temperature range before plateauing (due to reaching instrument resolution limits) whilst for red deer antler, this process occurred over a wider temperature range (Figure 8.38). The gradients of human, bovine and porcine curves were comparable.

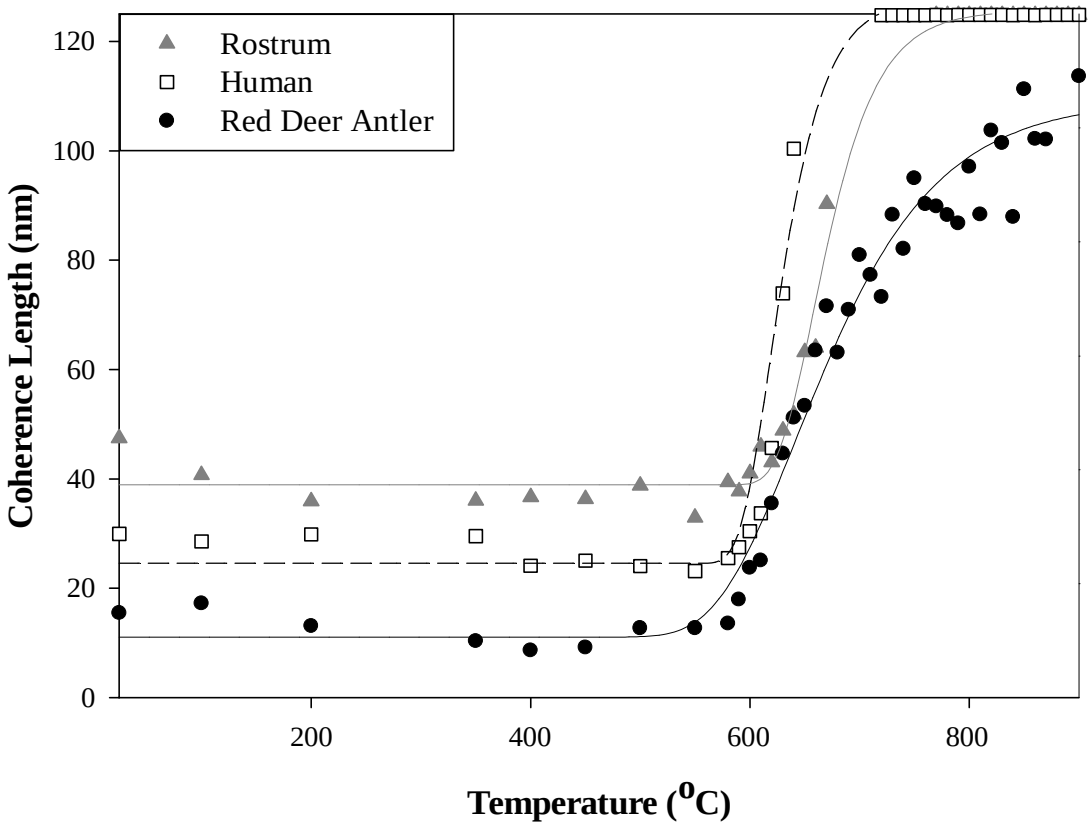

Figure 8.38 Coherence length (normalised), <00ℓ>, plotted against temperature for dynamically heated rostrum (▲), human (□) and red deer antler (●). The graph highlights the difference in the gradient of the curves for the bone types, indicating the crystallisation process is different for these bone types during heat treatment. The temperature at which the onset of crystallisation occurs is also evident. Errors calculated for clarity.

To semi - quantify this crystal growth process, the temperature at which the sigmoidal curve plateaued (due to reaching the instrument resolution limits, excluding red deer antler) for each bone type was investigated. This gives some indication of crystal

growth ‘rate’ during heat treatment. For human and porcine bone, the curve plateaued at ~ 650 ^{o}C, for bovine at ~ 680 ^{o}C and for rostrum ~ 740 ^{o}C, in both crystallographic directions. For red deer antler, the coherence length remained below the instrument resolution limits, although the data appeared to begin to plateau at > 800 ^{o}C. The observed gradients and temperature were consistent in both <00ℓ> and <0k0> crystallographic directions.

In order to quantify the change in coherence length (i.e. the crystallisation process) during heat treatment, the sigmoidal curves were used to calculate the temperature at which 50 % crystallisation occurred, as a function of crystallographic direction and bone type (Table 8.14).

50% Crystallisation (^{o}C)		
Bone Type	**<00ℓ>**	**<0k0>**
Rostrum	700 ± 3	702 ± 5
Bovine	647 ± 7	655 ± 5
Porcine	632 ± 4	630 ± 3
Human	631 ± 3	635 ± 3
Red Deer Antler	663 ± 7	658 ± 7

Table 8.14 Temperature at which 50 % crystallisation was calculated (including errors) for each bone type from the coherence length versus temperature sigmoidal curves (Figure 8.38). Errors calculated from the errors associated with fitting the sigmoidal curves.

The temperature differed according to bone type. Rostrum mineral reached 50% crystallisation at approximately 700 ^{o}C, red deer antler and bovine by approximately 650 ^{o}C and 660 ^{o}C respectively, and porcine and human by approximately 630 ^{o}C. The calculated values for <00ℓ> and <0k0> crystallographic directions were, within errors, the same for each bone type.

8.7.2.2 Lattice Parameters

Lattice parameter data was obtained from the diffractograms at each temperature in order to investigate the chemical changes occurring during *in situ* heat treatment (section 4.2.1). Plotting lattice parameter values against temperature revealed four distinct transition regions, identified by a change in the gradient for both the ‘a’ and ‘c’ axis lattice parameter data, for all bone types (Figure 8.39).

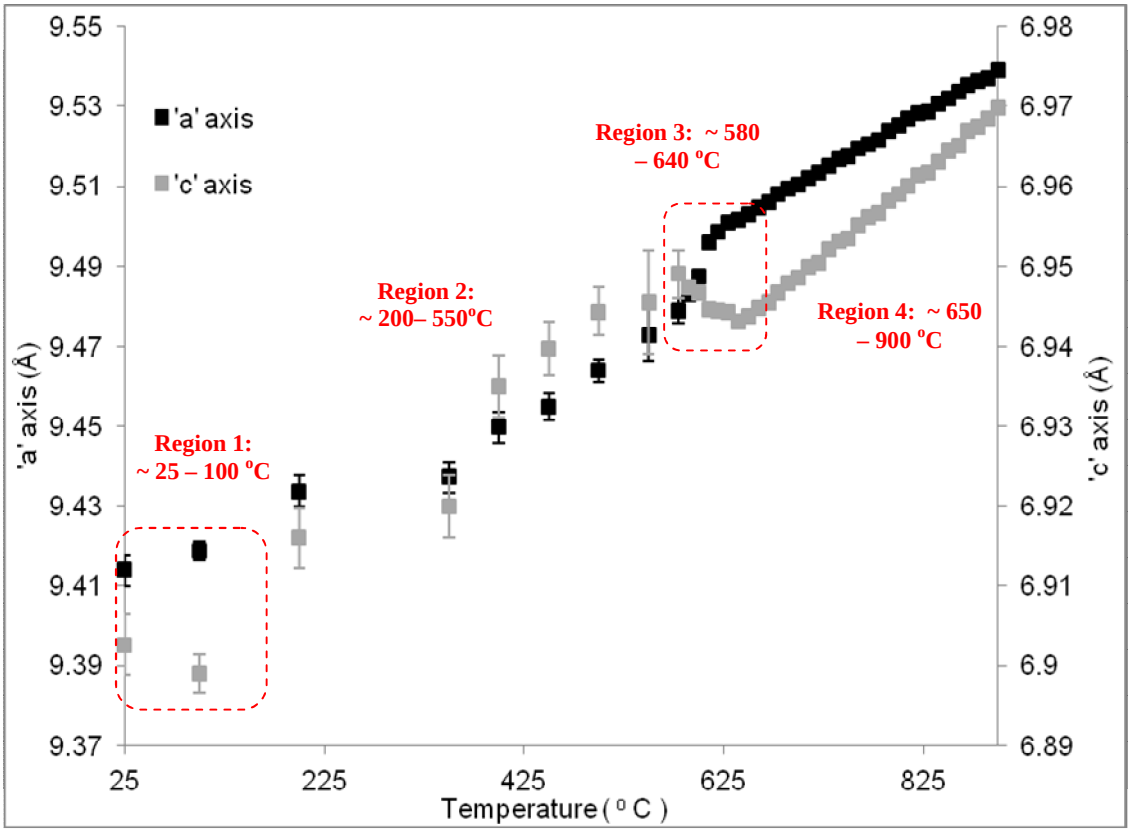

Figure 8.39 Plot highlighting the four transitional changes observed when lattice parameter data (‘a’ and ‘c’ axis) is plotted against temperature for the human bone specimen.

In general, the ‘a’ axis data increased during heat treatment, with a prominent increase observed at region 3. In contrast, the ‘c’ axis data initially decreases (region 1), then increases (region 2), a sudden decrease is then observed at the temperature of approximately 50% crystallisation (region 3) which is followed by an increase in the data (region 4). Similar lattice parameter behaviour was observed for all bone types

although the temperature ranges for each region and the gradients for region 3 differed between the bone types (Figure 8.40, appendix G). For rostrum, region 3 was observed between 650 – 700 ^{o}C, bovine approximately 580 – 650 ^{o}C and for both human and porcine the temperature range for region 3 was between 580 – 640 ^{o}C. Region 3 was less prominent for red deer antler and occurred over a shorter temperature range (640 - 660 ^{o}C), as shown in Figure 8.40.

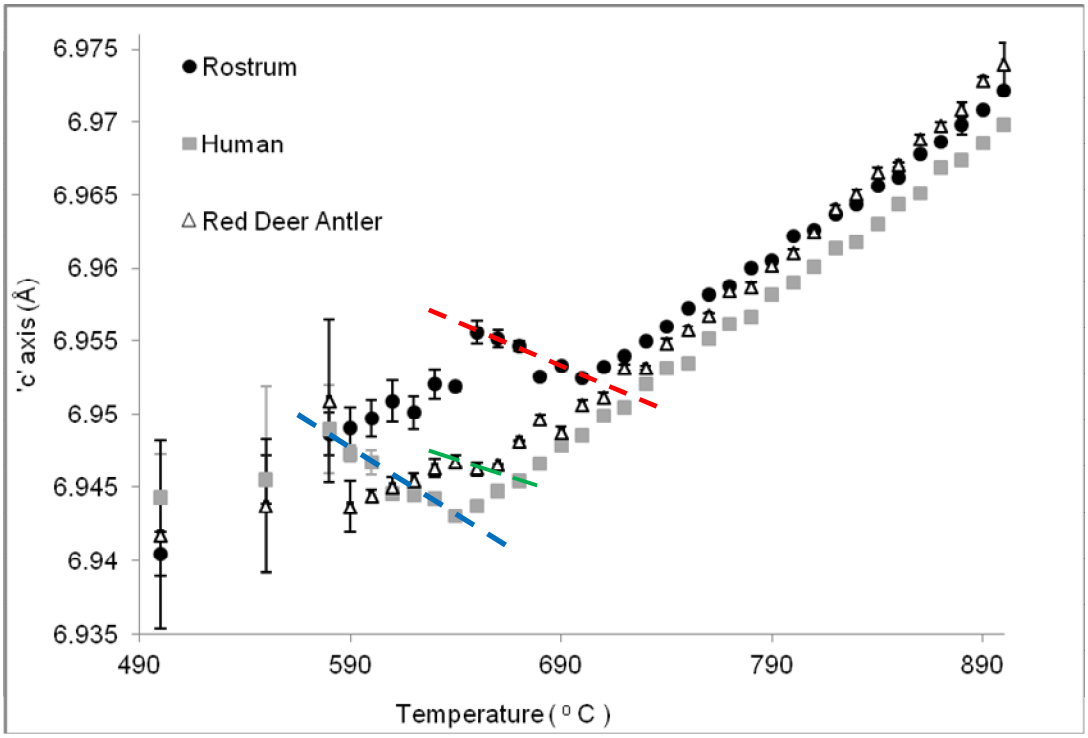

Figure 8.40 Plot of the 'c' axis lattice parameter data for rostrum, red deer antler and human. The gradient change in region 3 has been highlighted for each bone type with a negative linear line (rostrum, red deer antler and human).

As outlined in section 4.2.1, changes to lattice parameters during heat treatment can be attributed to the loss of lattice incorporated water (up to 400 ^{o}C), thermal expansion and ion exchange. Carbonate ion substitutions in particular have been

shown to have a significant effect on lattice parameters (section 2.2.2). Based on this premise, simple linear models were developed as shown in equation 8.4:

$$'a' = x + tecT + A\alpha + B\beta \qquad \text{and} \qquad 'c' = y + tecT + A\gamma + B\delta \tag{8.4}$$

, where 'a' and 'c' are calculated to give 'a' and 'c' axis lattice parameter data. These values were plotted against temperature to graphically simulate the dynamic data. 'x' refers to 'a' axis lattice parameter data whilst 'y' corresponds to 'c' axis lattice parameter data obtained from the unheated bone specimen. These values differed depending on bone type and were calculated from the dynamic X-ray diffraction data collected at 25 ^{o}C. The abbreviation 'tec' relates to the thermal expansion coefficient, which corresponds to the linear transitional regions 2 and 4 (shown in Figure 8.39) whilst T relates to the temperature. Values for α, β, γ and δ were obtained from previous work (detailed in section 2.2.2) and correspond to the gradient and intercept values obtained from incorporation of increasing amounts of A – or B – type carbonate (LeGeros, 1969). A and B relate to the relative percentage of A and B type carbonate respectively.

This theoretical model provided qualitative analysis of the amount of A- and B- type carbonate (%) required to alter the lattice parameter data observed during dynamic heat treatment. This enabled assessment of whether changes in lattice parameter values were solely due to carbonate ion exchange and thermal expansion or whether other processes were also significantly responsible for the observed changes. The model was applied to temperature regions ~ 400 ^{o}C > T < 550 ^{o}C and ~ 650 ^{o}C > T < 900 ^{o}C, (regions 2 and 4, Figure 8.39) where the gradient was consistent for all specimens, suggesting thermal expansion was predominately responsible for the change in the lattice parameters. By applying the model to these regions, it was possible to determine whether the change in gradient between approximately 580 - 640 ^{o}C (region 3, Figure 8.39), was solely due to the loss or gain of carbonate or whether other chemical exchanges were occurring. Crucially, if the only dominant chemical process occurring was the loss or gain of carbonate, the

amount of carbonate required to alter the lattice parameters would be similar for both ‘a’ and ‘c’ axial lengths.

Using the linear model, it was evident that this was not the case for the majority of bone types. The amount of carbonate required to simulate the changes in the ‘a’ and ‘c’ lattice parameters differed for porcine, human, rostrum and red deer antler (Table 8.15).

Bone Type	**B-type Carbonate Content (%)**	
	a -axis	c- axis
Bovine	3.8	3.6
Porcine	4.4	0.4
Human	2.4	1.5
Red Deer Antler	5	1
Rostrum	4	2.1

Table 8.15 The amount of B – type carbonate (%) required to simulate the dynamically heated lattice parameter data for both the ‘a’ and ‘c’ axes, calculated using the linear model in equation 8.4. In this example, A-type carbonate was kept constant at 0%. The model was also used to observe increasing amounts of A-type carbonate. The relationship remained the same as that recorded in this table.

According to the model, when A-type carbonate was kept constant at 0%, less B type carbonate was required to simulate the changes in the ‘c’ axis in comparison to the ‘a’ axis. This is highlighted by both the porcine specimen, where the difference in amount of carbonate (%), is a factor of 10 and the red deer antler specimen, where a difference of a factor of 5 is observed. In contrast, the amount of carbonate required to simulate the lattice parameter data for the bovine specimen was consistent for both ‘a’ and ‘c’ axes. The model was also used to observe increasing amounts of A-type carbonate. The relationship remained the same as that detailed above, with increasing amounts of A-type carbonate, less B-type carbonate was required to simulate the ‘c’

axis data than the 'a' axis. Again, the amount of carbonate required to simulate the bovine lattice parameters remained consistent for both 'a' and 'c' axes.

8.7.3 Thermal Decomposition

Additional mineral phases were detected in all dynamically heated bone specimens. In general, α – TCP, β –TCP, CaO and MgO were observed in all bone types when heated above 600 ^{o}C. CaO was not observed for red deer antler. The temperature at which the mineral phases first appeared differed according to bone type (Table 8.16). As detailed in section 4.2.2, during thermal decomposition of HAp, β – TCP is thought to transform into α – TCP with increasing temperature. The temperature at which this transformation first appeared to occur for each bone type is also reported in Table 8.16. This transformation was denoted by a simultaneous gradual decrease in the intensity of the main β – TCP peak and a gradual increase in in the intensity of the main α – TCP.

	Approx. temperature (^{o}C) at which each mineral phase first appeared				
	MgO	**CaO**	**β -TCP → Transformation → α - TCP**		
Bone Type					
Bovine	620	700	700	740	830
Porcine	620	640	670	710	800
Human	620	630	670	710	810
Red Deer Antler	640	-	650	700	830
Rostrum	670	670	700	720	820

Table 8.16 Temperature at which the thermal decomposition products of HAp were first observed for each dynamically heated bone type. The temperature at which β –TCP begins to transform into α – TCP is also reported.

For all bone types, MgO, CaO and β -TCP first appeared within the temperature range 620 – 700 ^{o}C, whilst the temperature range at which β – TCP appeared to start transforming into α - TCP was ~ 700 – 740 ^{o}C. The complete transformation of β – TCP to α – TCP appeared to occur within 810 – 830 ^{o}C. The first appearance of CaO and β - TCP was reported at a higher temperature for rostrum and bovine bone in comparison to the other bone types. Further, MgO was first observed at higher temperatures for rostrum in comparison to the other bone types. The temperature at which β – TCP was first observed was lower for red deer antler than the other bone types. Quantification of the mineral phases in terms of weight percentage at 900 ^{o}C and once cooled to room temperature (25^{o}C) is detailed below.

The main mineral phase for all bone types heated to 900 ^{o}C and once cooled resembled calcium HAp. At 900 ^{o}C, the weight percentage of MgO was approximately 1% for all bone types. The amount of MgO remained constant for all bone types during cooling to room temperature. Calcium oxide (CaO) was observed in all bone types except red deer antler. Unlike MgO, the amount present was dependent on bone type and temperature. At 900 ^{o}C, the percentage of CaO for rostrum and human was approximately 3%, for porcine 2 % and for bovine 1%. CaO was not observed for red deer antler. During cooling to room temperature, a decrease in the percentage of CaO was observed for all bone types. This trend was also observed for α –TCP, where this mineral phase was present at 900 ^{o}C (3 – 4 % for all bone types), but was not observed once cooled. β – TCP was not observed at 900 ^{o}C or once cooled to room temperature for all bone types. Figure 8.41 highlights the presence (or absence) of these mineral phases in bone specimens heated to 900 ^{o}C and after cooling.

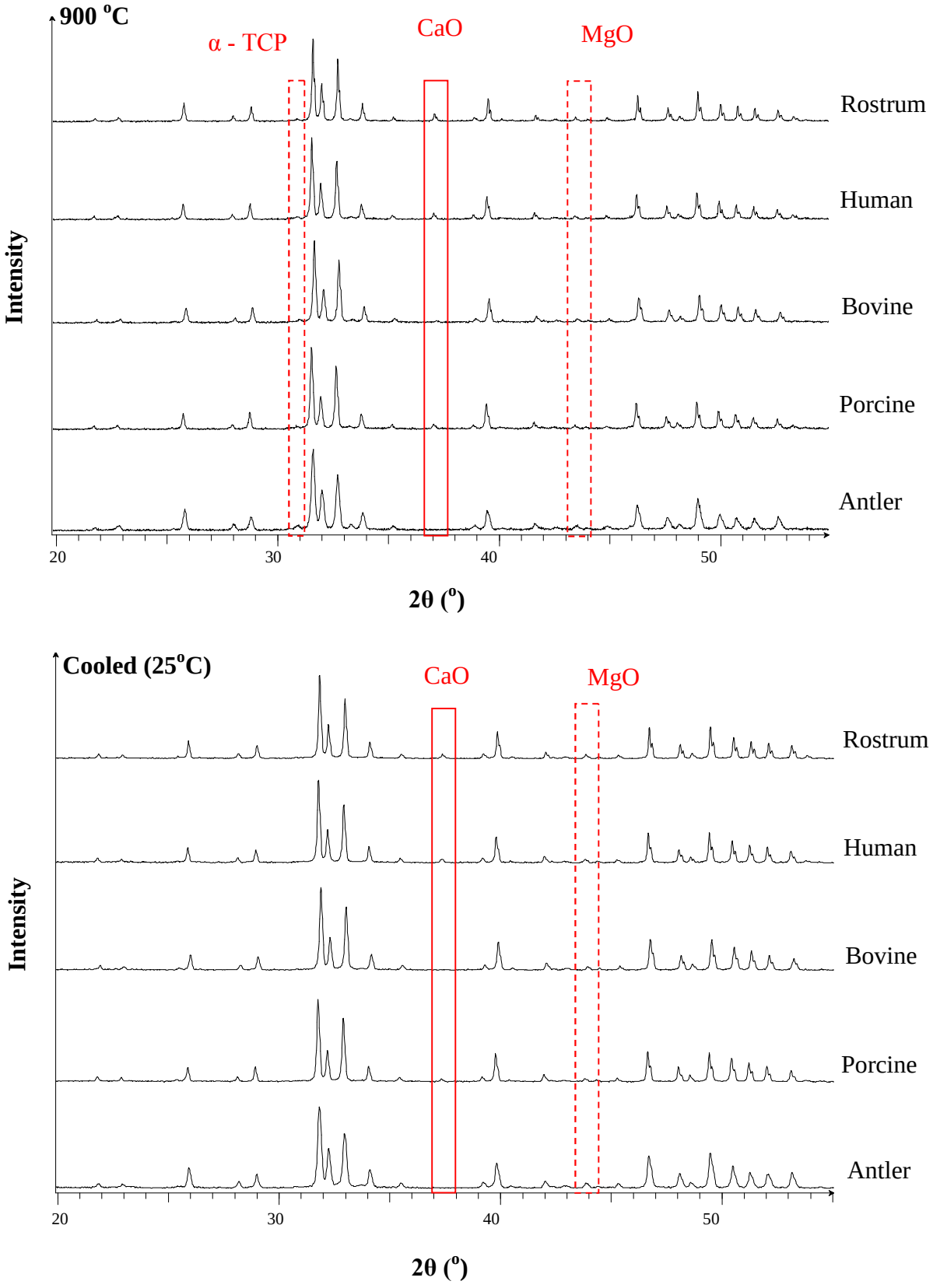

Figure 8.41 Diffractograms highlight the presence or absence of α – TCP, CaO and MgO in bone specimens dynamically heated to 900 °C (top) and after cooling to room temperature (bottom)

8.8 Further Interpretation of Results

8.8.1 Effect of Different Heating and Cooling Rates on Crystallisation and Thermal Decomposition: Can research be compared?

8.8.1.1 Crystallisation

A decrease in diffraction peak broadening was observed for all specimens irrespective of the heating and cooling regimen employed. With regards to the heating and cooling regimens employed (defined in section 7.2.1.3), the coherence lengths ranged from 32 – 38 nm and 19 – 28 nm for <00ℓ> and <0k0> crystallographic directions respectively. Coherence lengths for 'quenched'[2] and 'heated'[3] specimens were the same (within errors). Slightly larger coherence length values were observed for specimens allowed to cool[4] in comparison to specimens that were quenched immediately after the dwell period (Figure 8.42, Figure 8.43). This was observed in both crystallographic directions, although differences between quenched and cooled samples were more pronounced in the <0k0> direction.

[2] Quenched specimens are placed in the furnace at temperature and removed immediately after the dwell period. Essentially these specimens are air quenched.
[3] Heated specimens are heated from room temperature and removed immediately after the dwell period.
[4] Cooled specimens are placed into the furnace at temperature and after the dwell period are cooled to room temperature within the furnace

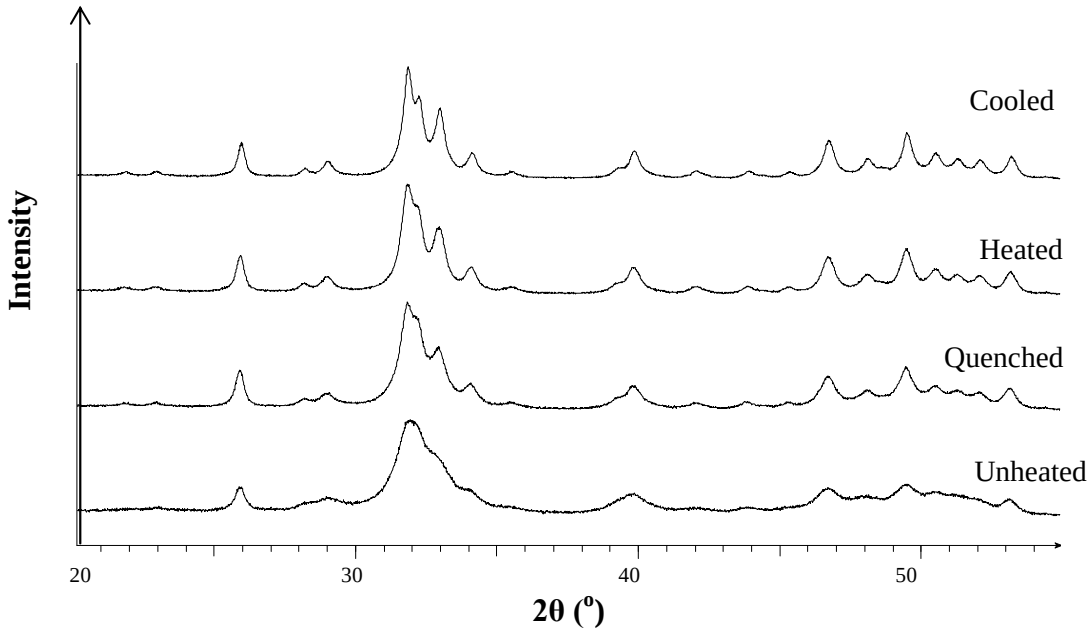

Figure 8.42 X-ray diffractograms of unheated, quenched, heated, cooled and both heated and cooled bovine bone specimens. The specimens were heated at 700 °C for 10 minutes..

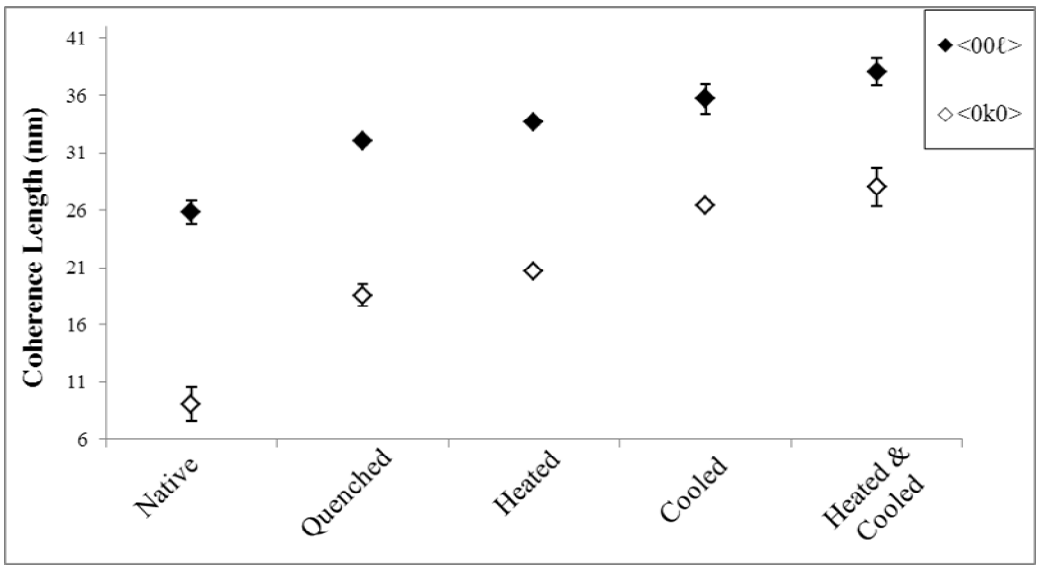

Figure 8.43 Coherence length plotted for each heating regimen in <00ℓ> and <0k0> crystallographic directions. (Bovine bone specimens heated at 700 °C for 10 mins). Errors calculated from standard error of three repeats.

The rate at which a sample is heated or cooled was also investigated. In general, the results revealed a larger coherence length for specimens which had been heated or cooled at a rate of 2 ^{o}C per minute. In relation to the heating rate, specimens heated at temperature ('quenched') and specimens heated at a rate of 25 and 10 ^{o}C per minute were similar, with coherence lengths between 32 - 34 nm (for the 00ℓ reflection). A coherence length of 46 nm was calculated for specimens heated at a rate of 2 ^{o}C, (Figure 8.44, Figure 8.45).

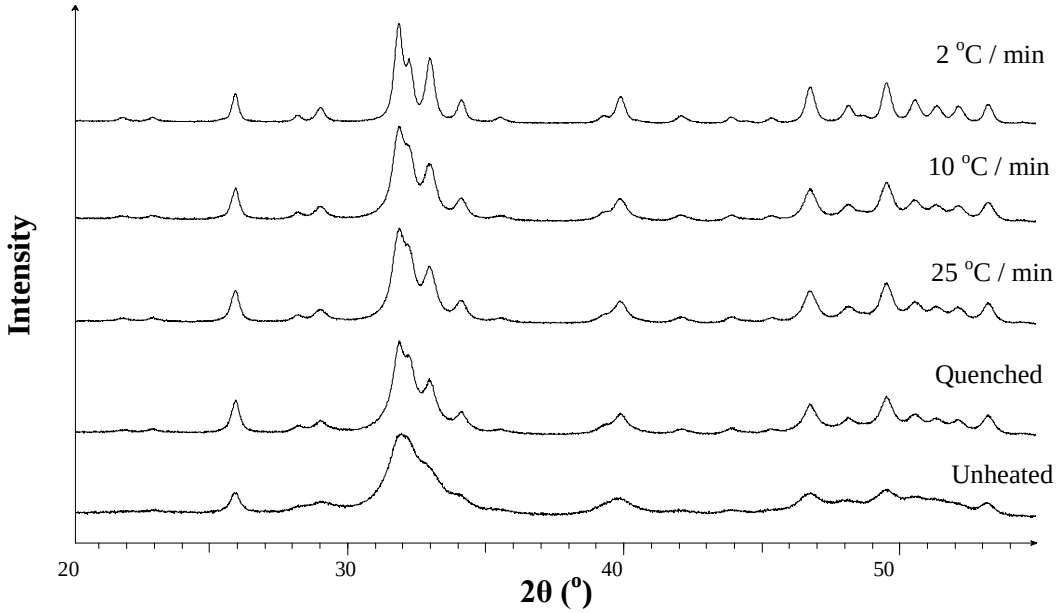

Figure 8.44 X-ray diffractograms of unheated bovine bone and bovine bone heated to 700 ^{o}C (at various rates), dwelled for 10 minutes and then quenched.

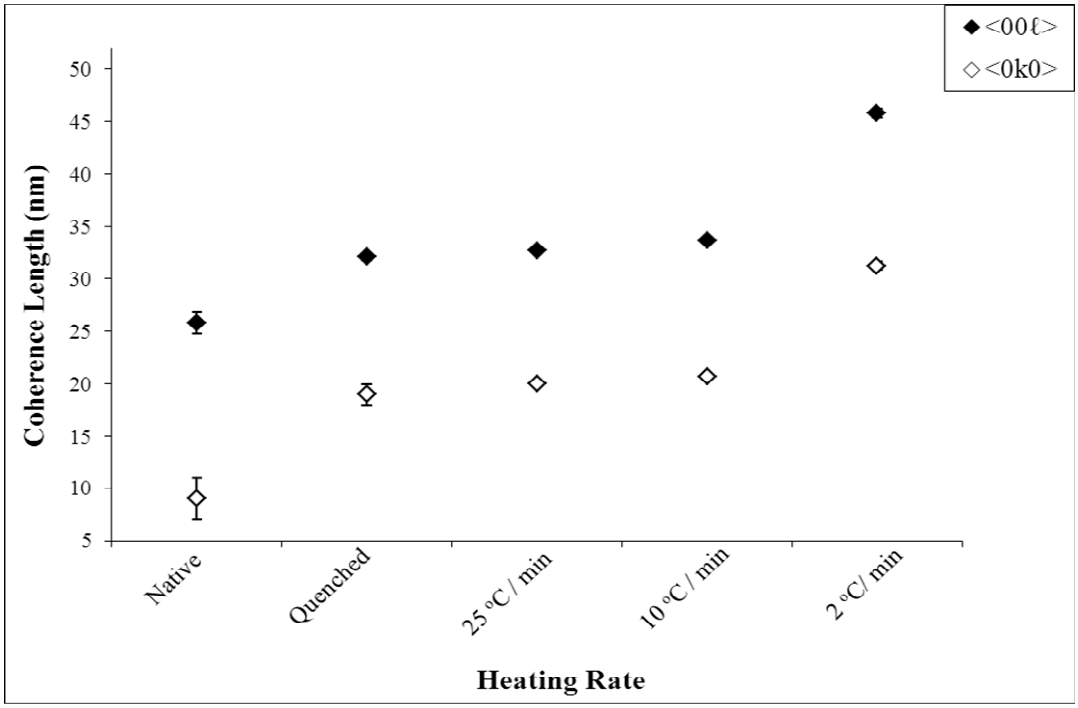

Figure 8.45 Coherence length plotted for each heating rate for bovine bone heated to 700 ^{o}C , dwelled for 10 minutes and quenched (in <00ℓ> and <0k0> crystallographic directions). Errors calculated from standard deviation of three repeats.

Taking into account specimens cooled at a ramp rate of 2, 10 and 25 ^{o}C min^{-1}, a linear relationship was observed where an increase in coherence length was observed with decreasing cooling rate. The coherence length for quenched specimens was, within errors, similar to specimens that had been cooled at a rate of 25 ^{o}C, with coherence lengths of 32 and 31 nm respectively. A coherence length of 49 nm was calculated for the specimens that had been cooled at a rate of 2 ^{o}C per minute. (Figure 8.46, Figure 8.47). With increasing dwell period, the coherence length values for all specimens were similar irrespective of heating and cooling rate employed.

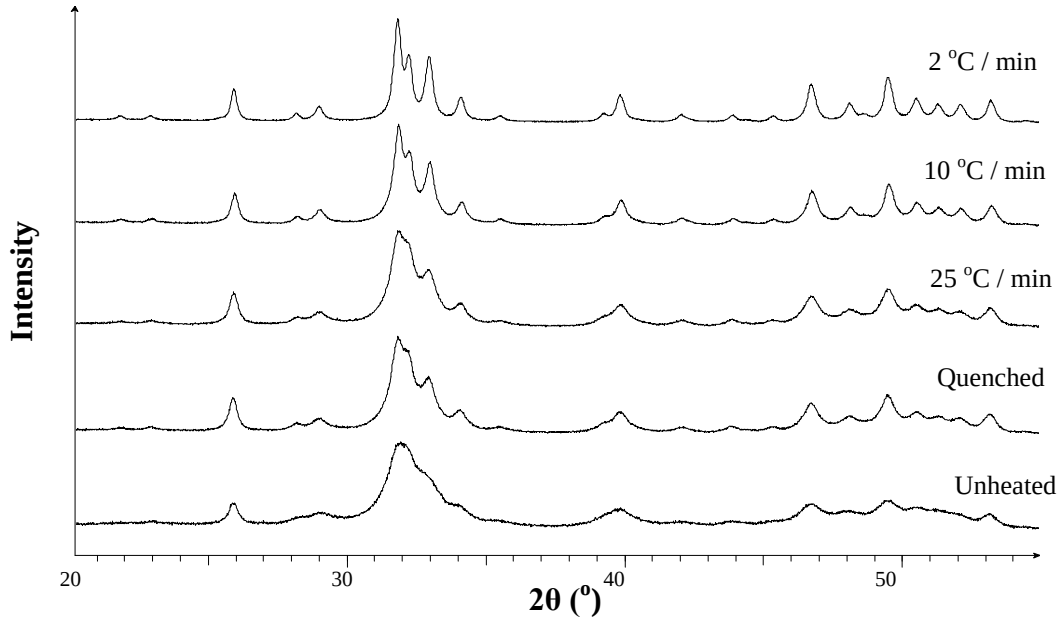

Figure 8.46 X-ray diffractograms of unheated bovine bone and bovine bone put into the furnace at temperature (700 °C), dwelled for 10 minutes and then allowed to cool at various rates

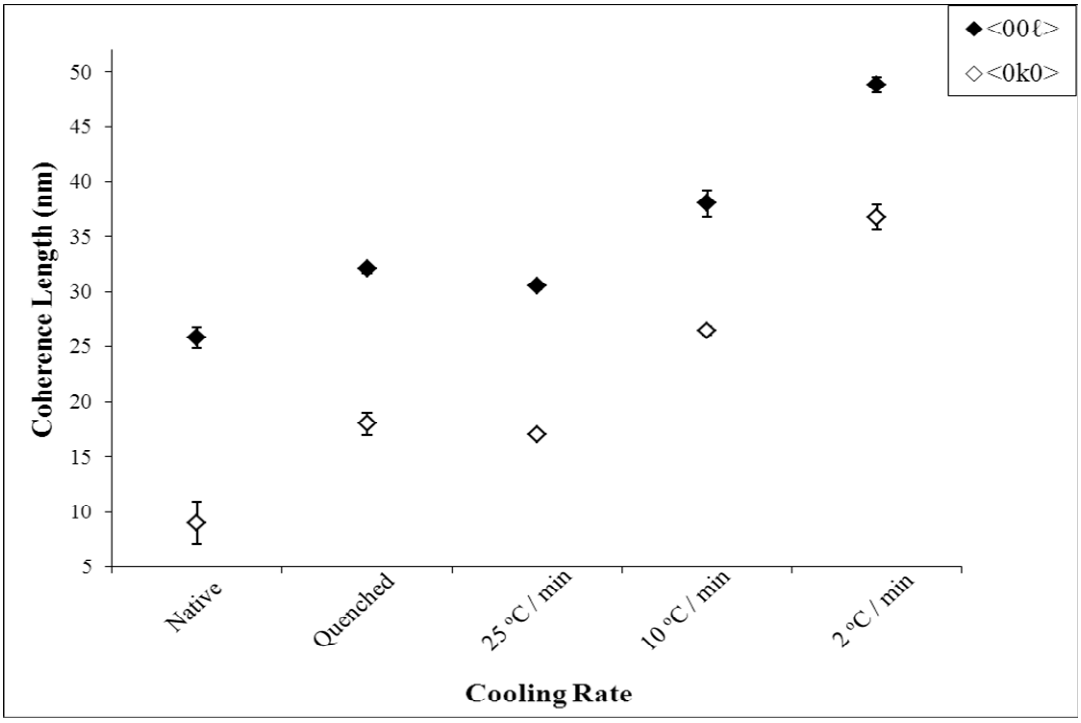

Figure 8.47 Coherence length plotted for each cooling rate for bovine bone heated at 700 °C, dwelled for 10 minutes and allowed to cool (in <00ℓ> and <0k0> crystallographic directions). Errors calculated from the standard deviation of three repeats.

8.8.1.2 Thermal Decomposition

As there appeared to be a significant difference in the crystallisation of bone mineral when 'slow' cooled (at a rate of 2 ^{o}C min^{-1}) in comparison to specimens quenched immediately after heating, the impact of these cooling regimens on the thermal decomposition of bone mineral was considered.

With a dwell temperature of 1200 ^{o}C for two hours, the two cooling regimens had little or no effect on the thermal decomposition process (Figure 8.48, Table 8.17). The main phase for all specimens resembled calcium HAp. Magnesium oxide (MgO) was observed in all specimens. Calcium oxide (CaO) was also present in porcine, bovine and rostrum specimens. For both cooling regimens, the quantity of magnesium oxide was the same for all specimens (1%) whilst calcium oxide differed slightly between bone types. A small amount of tetra tricalcium phosphate (TTCP) was observed in bovine, porcine and red deer antler specimens which were quenched immediately after the dwell period.

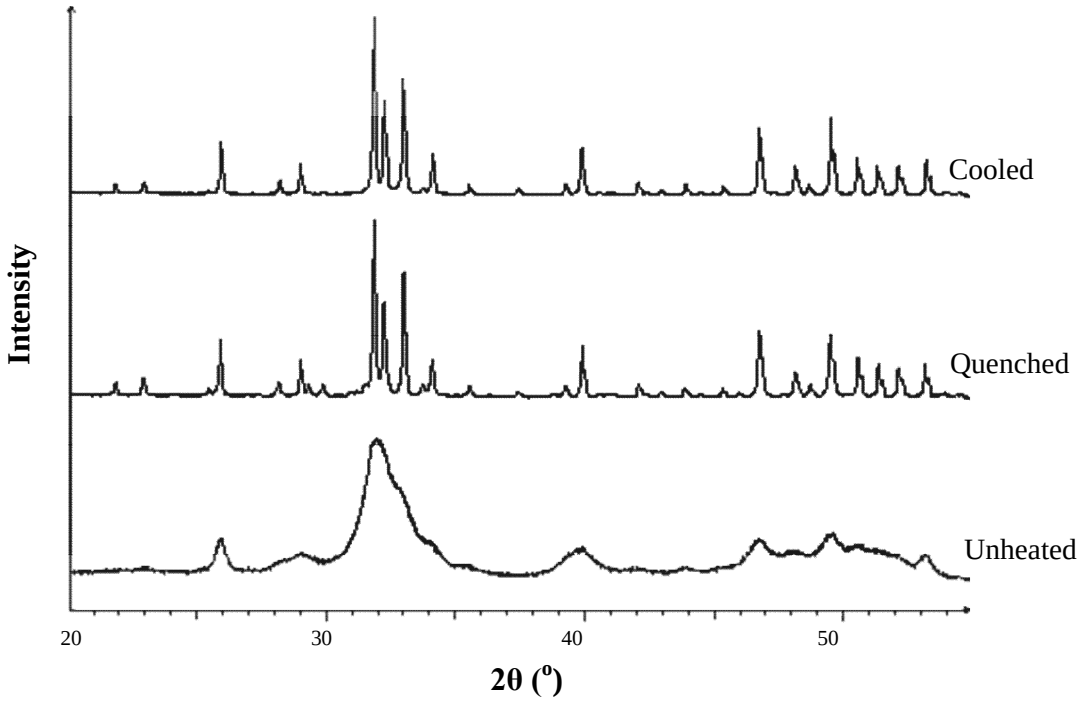

Figure 8.48 X-ray diffractograms of unheated bovine bone and bovine bone heated at 1200 ^{o}C for 2 hours and either quenched immediately after the dwell period or allowed to cool to room temperature in the furnace

	Mineral Phases (wt. %)			
	HAp	**TTCP**	**CaO**	**MgO**
Bone Type (Heated 1200 °C for 2hrs)	**Cooled**			
Rostrum	96 ± 1		4 ± 1	1 ± 0.1
Bovine	98 ± 0.2		1 ± 0.2	1 ± 0.1
Porcine	97 ± 0.3		2 ± 0.1	1 ± 0.1
Red Deer Antler	99 ± 0.2		-	1 ± 0.1
	Quenched			
Rostrum	96 ± 0.5		3 ± 0.1	1 ± 0.1
Bovine	93 ± 3	5 ± 3	1 ± 0.1	1 ± 0.1
Porcine	90 ± 5	8 ± 5	1 ± 0.1	1 ± 0.1
Red Deer Antler	97 ± 0.5	2 ± 0.5	-	1 ± 0.1

Table 8.17 The mineral phases and the percentage present in specimens heated at 1200 °C for 2 hours and either quenched immediately after the dwell period or cooled to room temperature in the furnace. Errors calculated from the standard deviation of three repeats.

At 1400 °C, the thermal decomposition products observed differed significantly between the two cooling regimens (Figure 8.49).

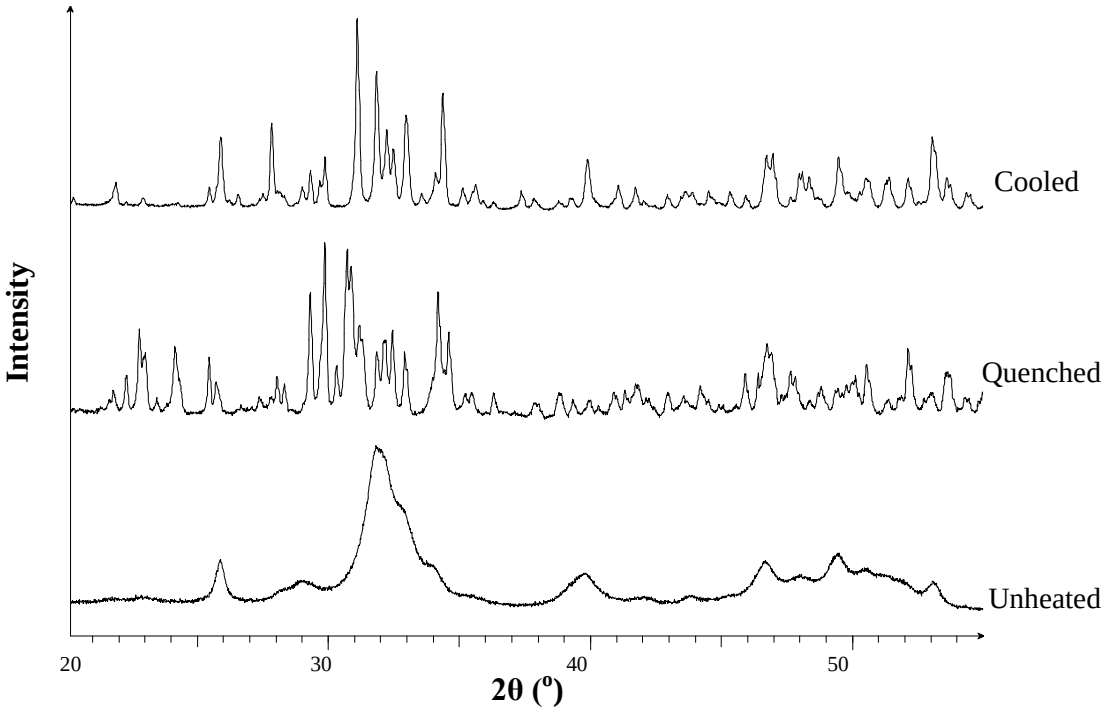

Figure 8.49 X-ray diffractograms of unheated bovine bone and bovine bone heated at 1400 °C for 2 hours and either quenched immediately after the dwell period or allowed to cool to room temperature in the furnace.

Differences in the thermal decomposition products between bone types were also observed (Table 8.18). The mineral phases observed for both cooled and quenched specimens were HAp, TTCP, α and β TCP, CaO and MgO although the quantities of these mineral phases differed. The presence and quantity of magnesium oxide (1%) was, within errors, similar for all specimens irrespective of regimen employed. Calcium oxide was present in all cooled specimens but was absent in the quenched specimens (Table 8.18).

For the cooled specimens, the main phases identified for rostrum was HAp and TTCP whilst for human, bovine, porcine and red deer antler the main phases were HAp and β – TCP. Approximately 13 – 24% of TTCP was also observed in human, bovine and porcine specimens, whilst only a small percentage (4%) of this mineral phase was observed in red deer antler specimens. In comparison to cooled specimens, a much smaller quantity of HAp was observed for quenched specimens. In the case of rostrum, the main mineral phase was TTCP (44%) although HAp was also observed (35%). Small percentages of α and β – TCP were also observed. The main phases for human, bovine porcine and red deer antler specimens (which were present in approximately equal amounts) were TTCP and α – TCP. A very small percentage of β-TCP was also observed for these bone types. HAp was observed in bovine specimens (3%) but not in porcine or human specimens.

	Mineral Phases (wt. %)					
	HAp	**TTCP**	**α -TCP**	**β - TCP**	**CaO**	**MgO**
Bone Type (Heated 1400 ^{o}C for 2hrs)	**Cooled**					
Rostrum	63 ± 1	35 ± 1		2 ± 1	0.1 ± 0.02	1 ± 0.1
Human	41 ± 0.2	24 ± 2		35 ± 2	1 ± 0.1	1 ± 0.1
Bovine	38 ± 5	13 ± 3		38 ± 1	1 ± 0.1	1 ± 0.4
Porcine	38 ± 1	21 ± 0.2		40 ± 1	1 ± 0.1	1 ± 0.1
Red Deer Antler	51 ± 1	4 ± 1	5 ± 1	38 ± 1	1 ± 0.4	1 ± 0.1
	Quenched					
Rostrum	35 ± 2	44 ± 1	15 ± 1	4 ± 0.1		1 ± 0.1
Human		51 ± 1	43 ± 2	5 ± 0.6		1 ± 0.1
Bovine	3 ± 1	43 ± 0.1	47 ± 3	6 ± 2		1 ± 0.1
Porcine		50 ± 0.3	44 ± 1	5 ± 1		1 + 0.1
Red Deer Antler		41 ± 1	54 ± 1	3 ± 1		1 + 0.1

Table 8.18 The mineral phases and the percentage present in specimens heated at 1400 ^{o}C for 2 hours and either quenched immediately after the dwell period or cooled to room temperature in the furnace. Errors calculated from the standard deviation of three repeats.

As aforementioned, the thermal decomposition products observed varied between bone types. To determine whether this was due to different ions present in the lattice as previously reported (discussed in section 4.2.2), elemental analysis of each bone type was carried out using LA-ICP-MS. A single specimen for each bone type was analysed for this preliminary investigation. Future work would include elemental analysis on more specimens. Unfortunately, only lead (Pb), strontium (Sr), zinc (Zn), iron (Fe) potassium (K) and magnesium (Mg) were selected for data analysis due to the accuracy of the measured values in comparison to the certificated values for both the bone meal and bone ash standards. The errors associated with other elements were deemed too large to be used reliably. Consequently, the absolute quantification of each element has not been reported due to the possibility of inaccuracies. A semi quantification was possible by taking the ratio of each element measured for a specimen to the quantity of phosphorus measured in the bone ash standard, as shown in Figure 8.50. The values were normalised to 100 to ensure the scale was kept constant; allowing for easier comparison.

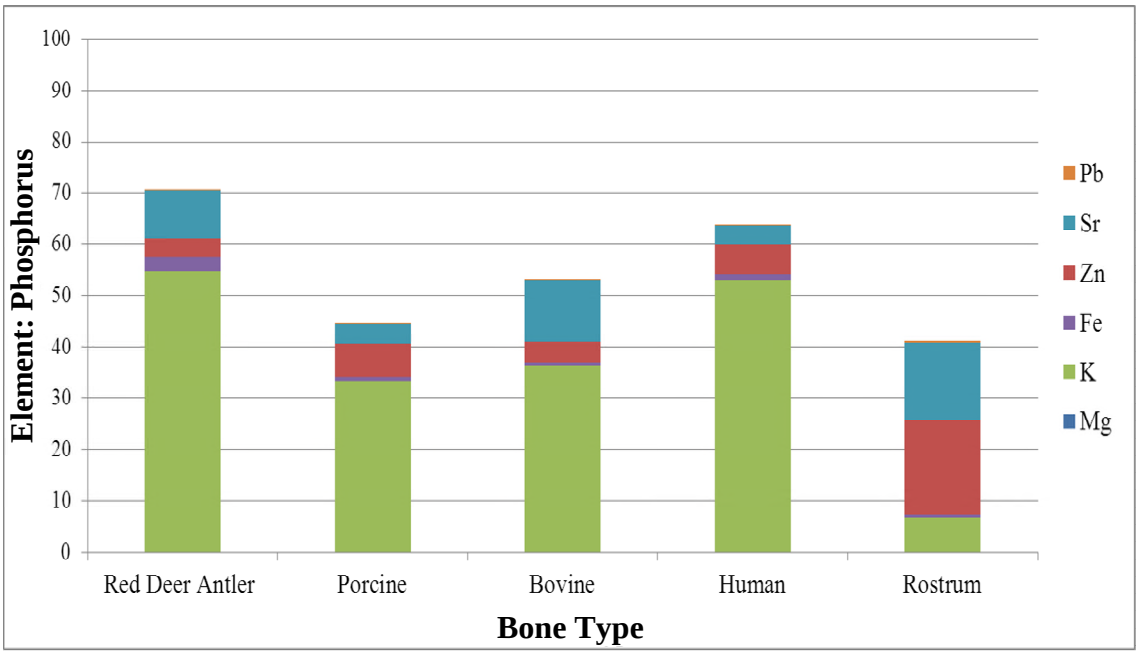

Figure 8.50 Specimen element to standard element ratio (ppm) for unheated bone types

For red deer antler, porcine, bovine and human bone specimens, a greater ratio of potassium (K) was observed in comparison to the other elements. For rostrum, this was not the case, and a greater ratio of zinc (Zn) was observed in comparison to the other bone types. The iron (Fe) ratio values were similar for all bone types, except red deer, where a slightly larger ratio value was observed. Strontium (Sr) ratio varied depending on bone type, with the largest amount of strontium observed in rostrum. The magnesium (Mg) and lead (Pb) ratios were similar for all bone types, although the values were very small in comparison to the other elements

8.8.2 Developing a Predictive Model to Determine the Time and Temperature of an Unknown

To develop a predictive model for determining the time and temperature at which an unknown bone specimen has been heated, several parameters were calculated from statically heated bovine bone data. Coherence lengths in <00ℓ> and <0k0> crystallographic directions (discussed in section 8.6, Figure 8.30), colour, lattice parameters (‘a’ and ‘c’ axes) and the amide I: phosphate ratio for statically heated bovine bone were calculated. For each temperature, data obtained for each parameter data was plotted against time and the data fitted using a variety of curves (Table 8.19, Figure 8.51). The curve fitted was dependent on the relationship between the specific parameter and the time. No correlation was observed ‘a’ axis data was plotted against time for each temperature (Figure 8.27, Section 8.5.3). Further, although plotting carbonate to phosphate ratio against time revealed a negative sigmoidal relationship, the temperature curves were within very close proximity and in some instances overlapped, making it difficult to distinguish between the various temperatures (Figure 8.51, C). Consequently, ‘a’ axis and carbonate to phosphate data were not used to develop the model.

Parameter	Curve Type
Coherence Length (00ℓ and 0k0)	Sigmoidal
Lattice Parameter: ‘a’ axis	No correlation
Lattice Parameter: ‘c’ axis	Exponential Decay (Linear for 600 ^{o}C)
Carbonate: Phosphate	Negative Sigmoidal
Colour: ‘L’ value*	Sigmoidal

Table 8.19 The parameters investigated to develop the time and temperature predictive model as well as the curve type fitted to the data when plotted against the time. (*Initial value taken from lowest ‘L’ value from the entire data set.).

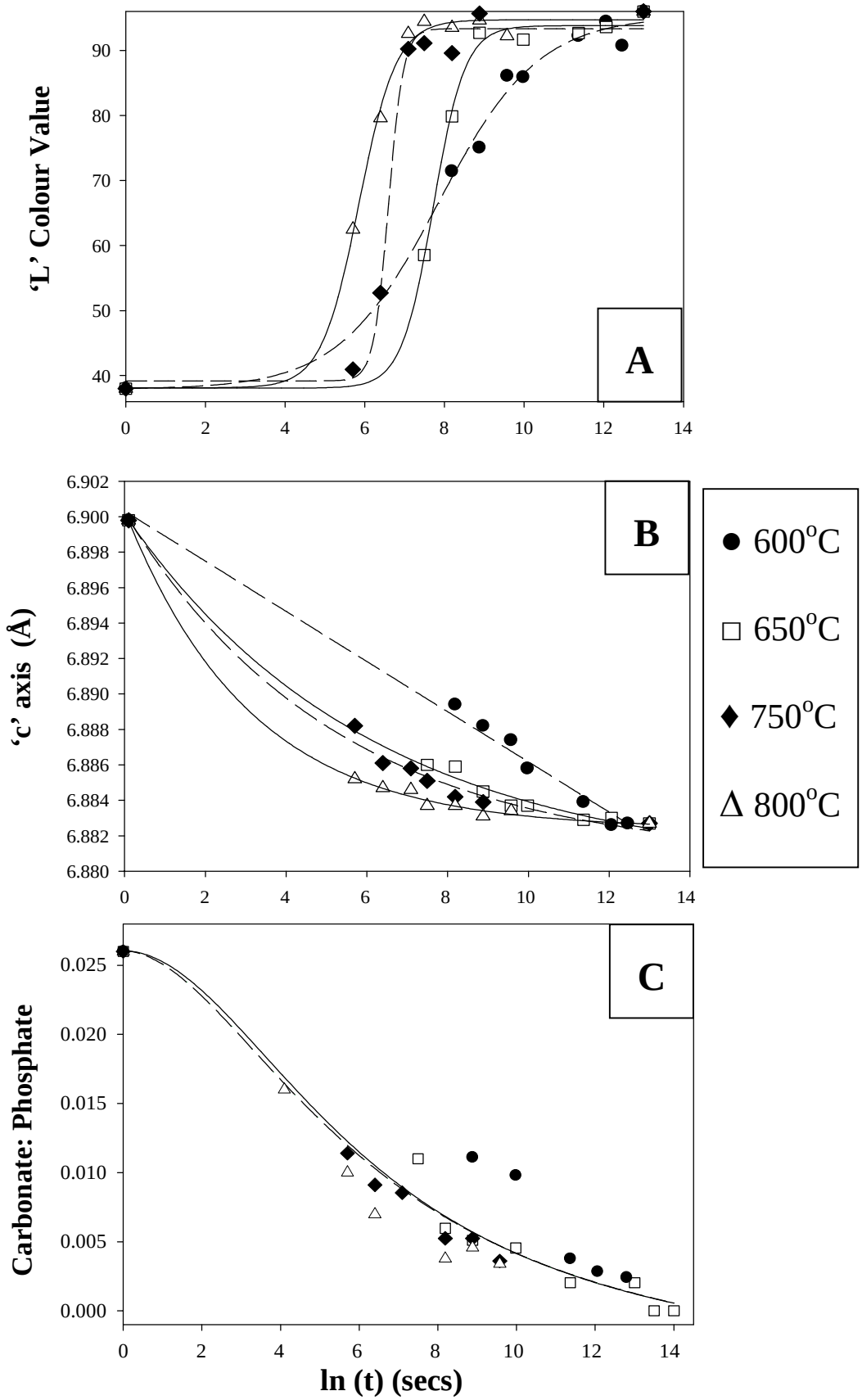

Figure 8.51 Plots of each parameter investigated: 'L' colour value (A), 'c' axis (B) and carbonate: phosphate (C) against ln (t) for each temperature. To demonstrate the close proximity and overlapping nature of the carbonate: phosphate data (C) without distracting from the data points, curves have been fitted to 650 and 750 ^{o}C only. Errors are excluded for clarity.

By rearranging the equations calculated from fitted curves and using the parameters calculated for the 'unknown' specimen[5], the time at which the parameter was possible at each temperature was calculated. This data was then used to produce a further graph where the calculated time values were plotted against the corresponding temperature for each parameter investigated. A linear relationship was observed regardless of parameter investigated. The predictive model is based on the theory that the point at which the trend lines cross reveals the time and temperature at which the unknown has been heated (Figure 8.52). To calculate the time and temperature, the linear equations were solved simultaneously.

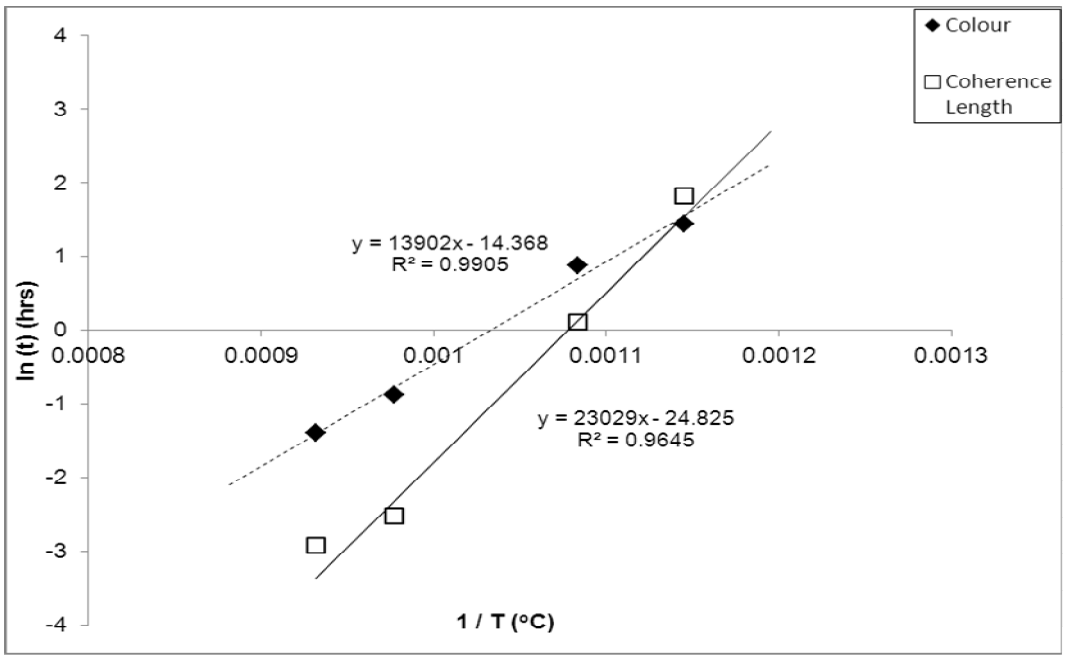

Figure 8.52 Linear plots obtained by calculating (using the equations of the curves in Figure 8.51) the time at which the parameter values of the unknown were possible for each temperature. This plot demonstrates how the linear plots for colour and coherence length cross at a particular point which corresponds to a time and temperature, calculated by solving the linear equations simultaneously.

[5] *'Unknown' specimens and consequently the calculated parameters for this analysis were selected at random from statically heated bovine bone specimen data (time and temperature known). These bone specimens were essentially utilised as reference samples to determine the accuracy of the predictive model.*

The accuracy of the predictive model varied depending on the time and temperature at which the specimen had been heated and the parameters used. In most instances, the linear trend lines for the parameters would intersect the trend line for the coherence length data, at different points resulting in several time and temperature determinations However, by repeating the analysis for several of the 'unknown' specimens it was found that the time and temperature from the linear equations of colour and coherence length data provided the most accurate results. The accuracy of the model decreased with increasing temperature and longer heating periods (Figure 8.53, Table 8.20).

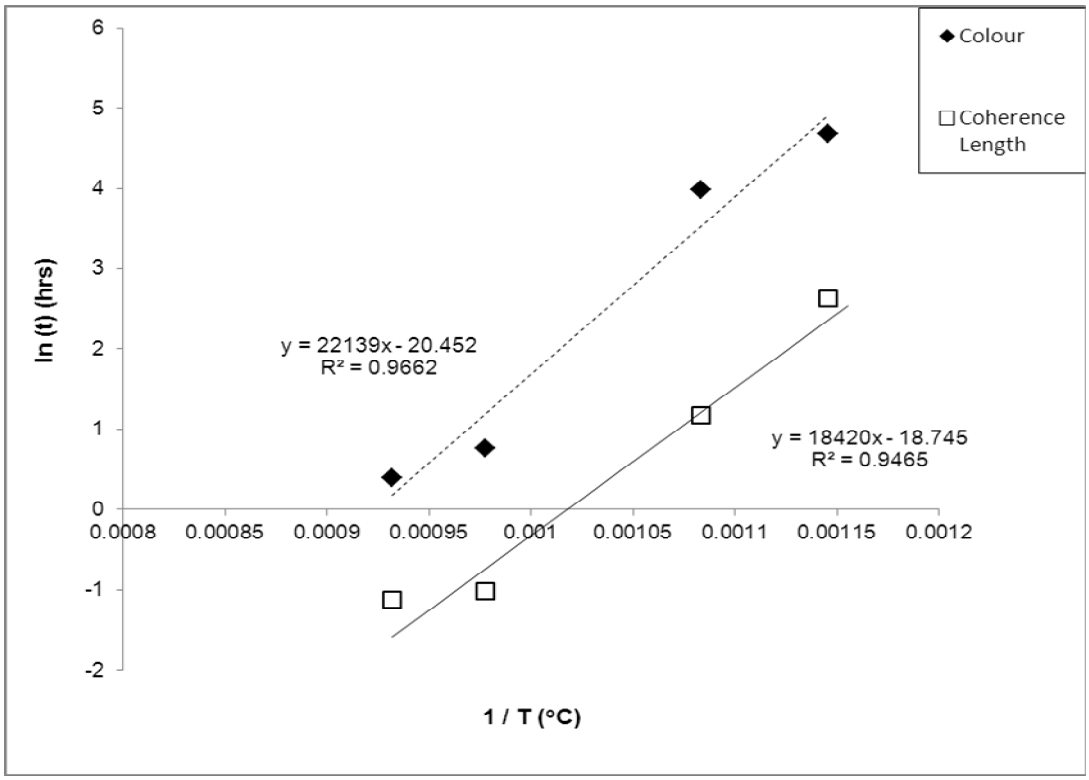

Figure 8.53 Linear plots obtained by calculating (using the equations of the curves in Figure 8.51), the time at which the parameter values of the unknown (600 ^{o}C for 48 hrs) were possible for each temperature. In this instance, the linear plots for colour and coherence length do not cross and the time and temperature for the 'unknown' cannot be calculated.

Actual			Predicated	
Temperature (^{o}C)	**Dwell Period**		**Temperature (^{o}C)**	**Dwell Period**
600	1 hr		636	55 m
600	6 hr		600	5 hr
750	5 m		742	4.6 m
750	20 m		696	1.3 hr
800	5 m		803	4.5 m
800	4 hr		704	1.6 hr

Table 8.20 Examples of times and temperatures simultaneously predicated using the model along with the actual times and temperatures at which the bovine bone had been heated.

8.8.3 Species Differentiation: Dynamic Heating

A Wilcoxon signed rank test was used to statistically compare lattice parameter data from bone types which had been dynamically heated. This test was deemed to be the most appropriate and robust statistical analysis as it is the non-parametric analogue to the paired two-sample t-test and does not assume normal distribution. A more detailed account of the Wilcoxon signed rank test is provided in appendix H.

For this analysis, lattice parameter values in the temperature range 800 – 900 ^{o}C were used. In this temperature range, it is assumed the dominant factor affecting lattice parameter behaviour was linear thermal expansion rather than ionic exchange (Figure 8.39, section 8.7.2.2). No statistical differences were observed between the bone types

using ‘c’ axis data. However, the ‘a’ axis showed a significant difference, $p < 0.05$ for the majority of the bone types (Table 8.21). Bovine and porcine specimens were not significantly different, $p > 0.05$. Furthermore, both bovine and porcine were not significantly different to that of the red deer antler. Human was significantly different from all bone types investigated, with a confidence level of at least 95 %.

	Red Deer Antler	**Rostrum**	**Human**	**Porcine**
Bovine	**p > 0.05**	**p < 0.01**	**p < 0.05**	**p > 0.05**
Red Deer Antler		**p < 0.01**	**p < 0.01**	**P > 0.05**
Rostrum			**p < 0.05**	**p < 0.01**
Human				**p < 0.05**

p< 0.01
p<0.05
Not sig

Table 8.21 ‘p’ values obtained from statistical analysis of the ‘a’ axis lattice parameter data obtained from the dynamically heated bone specimens.

Chapter 9: DISCUSSION

The results presented within this thesis have provided a new insight into control of *in vivo* HAp crystal size as well as the physicochemical modifications to bone mineral during heat treatment. More than 1000 samples have been analysed during this study. A variety of biological HAp specimens were utilised and characterised in terms of crystallite size and strain, organic content and relative amount of carbonate. Producing an 'anorganic' bone specimen without the use of chemicals was also investigated. Novel approaches were employed to report crystallisation kinetics of heated bone mineral in individual crystallographic directions. For the first time, dynamic heat treatment was employed to examine the physicochemical changes to bone *in situ* as well as the effects of cooling. This research not only questioned the current view on *in vivo* crystallite size control and the mineral and organic relationship during heat treatment, but further analysis of the data allowed investigation into contemporary issues and debates. Species differentiation and determining time and temperature of unknown heated bone specimens was investigated, as well as whether, due to the use of different heating and cooling regimens, heated bone data is comparable between research groups

This chapter will discuss the findings presented in chapter 8 and will lead the reader from material characterisation of the specimens utilised, including investigation into accurately calculating crystallite size and strain. *In vivo* crystallite size control will then be considered before discussing crystal growth and thermal decomposition of bone mineral during static and dynamic heat treatment. Applications of the research with respect to heating and cooling rates, a time and temperature predictive model and species differentiation will be discussed. A summary of the key findings is provided at the end of this chapter in Figures 9.1 and 9.2.

9.1 Production of an Anorganic Bone Analogue

In order to understand the role of the organic matrix during heat treatment, a reference specimen which had very little or no collagen, but the same nanocrystalline mineral microstructure generally observed for bone was required. Previous studies have removed the organic matrix from bone specimens using chemical methods or high temperature heat treatment (Wright & Schwarcz, 1996, Haberko *et al*., 2006, Baraket *et al*, 2009, Hu *et al*, 2010). Unfortunately, the confounding effects of these methods on the mineral microstructure were not considered. Heating bone to temperatures $\geq 600\ ^{o}C$ is known to dramatically change the mineral microstructure (Rogers & Daniels, 2012, Greenwood *et al*., 2012). Changes to the mineral microstructure caused by aqueous solutions have also been reported (Kim *et al*., 1995, Karampas *et al*., 2012, Liu *et al*., 2013).

This research has however demonstrated low temperature heat treatment can be used to remove the organic matrix from bone, without significantly altering the mineral microstructure. Heating bone specimens at temperatures $< 400\ ^{o}C$ was not sufficient to remove the organic matrix. This is confirmed by the presence of amide peaks in FTIR spectra (Figure 8.2). Heating to temperatures exceeding $400\ ^{o}C$ resulted in a change to the mineral microstructure, which is observed in both the XRD and FTIR data. The diffraction peaks become narrower, which signifies an increase in crystallite size and lattice order (Figure 8.1). This is confirmed by an increase in resolution of the phosphate peak in the FTIR data. The intensity of the carbonate peak in the FTIR data suggests a significant loss of carbonate at temperatures exceeding $500\ ^{o}C$. Consequently, this study has shown that the optimum heating regime required to remove the organic matrix from bovine and porcine bone without significantly altering the mineral microstructure, is $400\ ^{o}C$ for a period of 2 hours.

9.2 Specimen Characterisation

For this research, biologically formed and synthetic HAp specimens were required. Unheated specimens were characterised prior to experimental analysis in terms of coherence length and organic content. In general, the main mineral phase resembled calcium HAp for all specimens. Although small quantities of monetite and β-TCP were observed in urinary calculi specimens B and F respectively, the peaks associated with these mineral phases did not overlap the HAp peaks relating to the crystallographic directions investigated for this research. Thus, it was deemed acceptable to use these specimens. XRD revealed a greater coherence length in the <00ℓ> direction then the <hk0> directions for all specimens, which suggests direction dependence broadening. This direction dependence has previously been reported for unheated bone specimens (Rogers & Daniels, 2002, Beckett *et al*., 2011).

For bone types, coherence length values suggest crystallite size and lattice strain are similar for bovine, porcine, their anorganic analogues and red deer antler specimens. This was later confirmed and is discussed further in section 9.3. The coherence length calculated for rostrum suggests this material exhibits larger, more ordered crystals in comparison to the other bone types. This is confirmed by the narrower diffraction peaks for rostrum (section 8.2.1). The amide I: phosphate ratio may suggest the amount of collagen differs between bone types, with red deer antler > porcine > bovine > rostrum > anorganic analogues. The coherence lengths for anorganic bone specimens were similar to their organic counterparts, whilst a significantly lower amide I: phosphate was observed for anorganic specimens. This validates that heating bone at low temperatures is sufficient to remove the majority of the organic content without altering the mineral microstructure.

A wide variety of coherence lengths and variations in diffraction peak widths confirmed that both urinary calculi and synthetic HAp specimens differed in crystallite size and lattice disorder. Further, the amide I: phosphate ratio suggested urinary calculi specimens, A, D and E differed according to organic content.

9.3 Calculation of Crystallite Size and Strain

As discussed in section 5.1.3, refinement techniques currently used to calculate crystallite size and strain for nano HAp may be limited due to crystallographic direction broadening dependence (i.e. HAp crystallite size and lattice strain differ depending on crystallographic direction). This concept has previously been reported (Rogers *et al.*, 2010), in some instances by comparing coherence lengths only (Bloebaum *et al.*, 1997, Gashti *et al.*, 2014), however refinement techniques used to calculate size and strain of nano apatites have not previously been critically assessed.

Crystallographic direction dependence broadening for biological and synthetic HAp was highlighted in section 8.3, with more broadening associated in the <hk0> direction and the least amount of broadening in the <00ℓ> direction. The difference in the extent of broadening between crystallographic directions may suggest differences in crystallite size or in the strain, or a combination of the two. This is the same for the greater extent of broadening in red deer antler data in comparison to rostrum data. Crystallographic direction dependence broadening was confirmed by plotting the angle between the <00ℓ> and the other directions, against the FWHM of the peaks. A wide dispersion in the FWHM values in the <hk0> direction highlights the unreliability of this data, as the crystallite size and strain should be equal across all <hk0> reflections; however this is not the case. The wide range of FWHM values in this crystallographic direction may be a consequence of uncertainty associated with broad, overlapping peaks. However, it may also suggest that there is a wide range of different material compositions. Arguably, this is confounded further as wide compositional variations in bone material probably exist due to ionic substitutions. Thus, the unreliability of FWHM values from the <hk0> reflections should be considered when analysing nanocrystalline HAp diffraction data.

9.3.1 Rietveld Refinement

The limitation of Rietveld refinement for nanocrystalline materials such as bone was highlighted in Figure 8.7. Most Rietveld refinement software packages use a fixed profile function such as the Caglioti function, which assumes equal crystallite size and strain contributions across all crystallographic directions (McCusker *et al*., 1999, Gozzo *et al*., 2006). Consequently, in crystallographic direction dependent materials such as bone, Rietveld refinement results in a poor fit, particularly in the <00ℓ> directions where peak broadening is narrower (due to smaller crystallite size, less strain or a combination of both).

9.3.2 Williamson Hall Analysis

Williamson Hall analysis was employed to calculate crystallite size and strain. Larger crystallite size values were calculated for rostrum, UC_E and sHAp3 (57 – 84nm) in comparison to the other bone types, which ranged from 20 – 37 nm (Table 8.5). Taking into account strain, a trend was difficult to determine due to large errors associated with this parameter. It is proposed this was caused by errors associated with fitting a peak to the 004 reflection, which is overlapped by other reflections and is extremely broad. These errors were demonstrated by repeat analysis of the same data, changing only the limits of the 2θ range and the number of surrounding peaks fitted. Any changes to the FWHM values will affect the Williamson hall plot, and consequently the size and strain values. As reported, FWHM values obtained from the 002 peak, were within errors, consistent, however small changes were observed in FWHM values for the 004 peak. These changes had little impact on the y-intercept values (used to calculate crystallite size); however the gradient of the line (used to calculate strain) was considerably affected, as shown in Figures 8.12 and 8.13. Thus, strain values were not consistent, even when calculated from the same data. The reliability of this analysis to determine strain using 00ℓ reflections is questionable. Unfortunately, in bone mineral research this crystallographic direction is often chosen for Williamson Hall plot analysis as the other

reflections tend to be less intense and/ or overlapped by other peaks. It is proposed that although this analysis may not provide reliable strain values, it may be an accurate method to calculate crystallite size.

9.3.3 Single Line Analysis

Single line analysis was employed to calculate size and strain from the 002 reflection only (Langford, 1992). This peak was chosen as it is not significantly overlapped by other peaks, although intensity was compromised. The errors associated with the strain values were much smaller in comparison to Williamson Hall analysis, although the errors associated with crystallite size seemed to be greater for single line analysis. In general, the trend between crystallite size and strain seemed to be, that smaller crystallite size was associated with smaller strain value. This seems to contradict previous studies which report that a highly disordered HAp structure (greater values of strain) may inhibit crystal growth, as discussed in chapter 3. Due to the errors associated with crystallite size values, it is proposed that single line analysis may not be the best model to independently calculate crystallite size and strain.

9.3.4 Compositional Size and Strain Broadening

As discussed above, Rietveld refinement, Williamson Hall and single line analysis are to a certain extent limited in terms of calculation crystallite size and strain for nanocrystalline materials. Consequently Leineweber and Mittemeijer's (2003) model of direction dependence broadening due to compositional changes, was applied for the first time to bone mineral data. The model was extended to include size broadening contribution, which may possibly be used to independently calculate size and strain dependence as well as broadening due to compositional variations in bone material.

The dispersion of the data corresponding to sHAp3 in comparison to Leineweber and Mittemeijer's data (the simulated data) suggests additional direction dependence broadening not modelled by equation 5.18; which considers only strain broadening contributions. This could either be caused by other compositional broadening elements and/ or contribution from size broadening. Dispersion of the data corresponding to sHAp3 was simulated for Leineweber and Mittemeijer's data by extension of the strain equation to include size broadening. $B_{\xi}d\alpha/d\xi$ values (related to strain broadening contributions) decrease with inclusion of size, which highlights that total peak broadening encompasses both size and strain contributions.

By applying and extending Leineweber and Mittemeijer's model for HAp data, it has been possible to demonstrate that both size and strain broadening contributions are dependent on crystallographic direction. Further, applying this model to the compositional dependence of HAp lattice parameters on carbonate substitution, has shown that strain broadening contributions in HAp cannot be attributed to the composition variations caused solely by carbonate substitutions. This was evident as the fitting parameter ratio value (which was equal to 1) was significantly different to the ratio value calculated from the compositional dependence lattice parameter values (which equalled -0.06667). Thus, this suggests there must be other compositional variations in HAp which contribute to strain broadening. This may be due to the presence of other extraneous ions. Ionic substitutions or vacancies must occur during carbonate substitution in order to maintain a neutral charge balance. It is also possible that differences in the two ratio values are due to the compositional broadening contributions from A-type carbonate. Substitution of A-type carbonate has also been shown to have a compositional dependence on lattice parameter values. Further work would be required to investigate whether it is possible to simultaneously model both A- and B-type carbonate compositional dependence broadening.

9.4 Hydroxyapatite Crystal Size Control

As discussed in chapter 3, there are currently three very distinct schools of thought with regards to *in vivo* HAp crystallite size control. Firstly, a mechanical restriction in the form of collagen has previously been proposed (Boskey, 2003, Nudelman *et al.*, 2010, Wang *et al.*, 2012). This assumption is generally made due to the correlation between *in vivo* crystallite size and organic content (Curry, 1999, Zioupos, *et al.*, 2005). With low collagen content, HAp crystals tend to be larger (rostrum, enamel) whilst systems with larger amounts of collagen tend to exhibit smaller crystals (red deer antler, dentin). These observations have previously only been made with regards to bone material. This research considered both bone and urinary calculi specimens, with the results suggesting collagen restriction does not play a primary role in *in vivo* HAp crystallite size control. It is proposed that although there appears to be a correlation for bone, *in vivo* HAp crystallite size and collagen content are independent (Figure 8.20).

The second school of thought suggests an extrinsic control mechanism and assumes organic macromolecules such as citrate, bind to the surface of HAp crystals, which consequently limits crystal growth (López –Macipe, 1998, Martins *et al.*, 2008, Xie and Nancollas, 2010, Hu *et al.*, 2010 & 2011). The novel approach utilised for this thesis, which allowed quantification of citrate, suggested no correlation between the amount of citrate and *in vivo* biological HAp crystallite size (Figures 8.18 & 8.19). The role of citrate on *in vivo* HAp crystallite size has only recently been considered. It is proposed that studies within this research area are possibly flawed due to sample preparation (discussed in chapter 3). Further, one has to question whether any extrinsic source of control is required for *in vivo* HAp crystal size control, when nano-sized synthetic HAp crystals can be formed in the absence of these extrinsic molecules (as shown in this research, section 7.1.3 and section 8.2.3).

The third and more implicit school of thought may suggest an intrinsic source of control. Many studies have suggested lattice disorder causes an increase in dissolution rates and/ or a decrease in crystallite size (Bigi *et al.*, 1993, Fuierer *et al.*, 1994, Bigi *et al.*, 1995, Kanzaki et al., 2000, Van der Houwen *et al.*, 2003); however these observations have not previously been correlated with *in vivo* HAp crystallite size

control. Previous studies for example have suggested incorporation of carbonate ions (which increases lattice strain), results in smaller crystals and an increase in dissolution (Baig *et al.*, 1996, Tang *et al.*, 2003, Shellis *et al.*, 1999, Tang *et al.*, 2004, Yao *et al.*, 2009, Yao & LeGeros, 2010, Delgado-López, 2012). This was investigated by comparing the relative amount of carbonate present in bone, urinary calculi and synthetic HAp specimens. As shown in Figure 8.21, for all specimen groups, crystallite size decreased with increasing amounts of carbonate. Interestingly, the extent to which the amount of carbonate influenced crystallite size differed between specimen groups. It is proposed that this is due to the presence of other impurities and carbonate substitutions alone cannot strictly provide an *in vivo* size control model. Taking this into account, it is suggested that a smaller amount of carbonate had more of an impact on synthetic HAp crystallite size than the biological specimens, as it is assumed carbonate is the only/ most significant impurities present within synthetic HAp specimens. Conversely, a larger amount of carbonate was observed in bone specimens. Due to other ionic substitutions (which must occur during carbonate substitution in order to maintain a neutral charge balance, Wopenka & Pasteris, 2005, discussed in chapter 3), it seems plausible that a larger amount of carbonate observed in bone could correspond to a similar crystallite size observed for synthetic HAp specimens. To provide an accurate model for *in vivo* crystallite size control, the overall lattice strain associated with each specimen was considered.

As discussed above, strain calculated from Williamson Hall analysis was found to be unreliable due to fitting errors associated with the 004 reflection, whilst limitations associated with crystallite size calculations using single peak analysis were observed. Consequently, crystallite size values from Williamson Hall analysis and strain values from single peak analysis were compared to determine the relationship between lattice strain and crystallite size. Arguably, these two parameters, which are dependent on one another when only one analysis method is employed, may be more reliable when calculated from two very independent analysis methods. The results suggest that there is a correlation between lattice strain and crystallite size (Figure 8.22). Lattice strain has been reported to increase HAp dissolution. Thus; it is proposed that crystals with large amounts of strain cannot physically grow beyond a certain size due to the rate of dissolution. Further, smaller crystals exhibit larger surface areas which are thought to

accelerate the dissolution process. Lattice strain, as a form of intrinsic source of *in-vivo* HAp crystallite size control has not previously been reported.

9.5 Static Heating

9.5.1 General Response to Heat Treatment

9.5.1.1 Mass and Colour Change

The mass loss observed for all specimens irrespective of time and temperature is consistent with the common consensus that upon heating bone, combustion of the organic and evolution of gases from the mineral matrix occurs (Munro *et al*., 2007, Ubelaker, 2009) The loss of surface absorbed and lattice incorporated water may also contribute towards mass loss (LeGeros *et al*., 1978) A greater mass loss observed for red deer antler may be associated with the initial amount of organic matrix present. This is somewhat confirmed when the amide I to phosphate ratio for all unheated bone types is taken into account (section 9.2). The greater the amide I to phosphate ratio (which provides a relative indication of organic content), a larger average mass loss was observed. The mass loss associated with anorganic analogues of porcine and bovine bone after the first heat treatment (400 ^{o}C for 2 hours), is probably caused by the loss of lattice incorporated water and the combustion of the organic matrix. As discussed in section 9.1, there is no evidence to suggest a change in the mineral microstructure of the anorganic specimens. It is proposed the 2% average mass loss observed after the second heating, may be due to the loss of water incorporated into the bone specimen during the time period between the two heat treatments.

As with mass loss, the change in colour of bone specimens is consistent with previous work (Shipman *et al*., 1984, Thompson, 2004, Devlin & Herrman, 2008, Waterhouse,

2013). Change in colour, which has previously been recorded as a function of temperature only, has been associated with chemical changes such as the combustion of the organic and crystallisation of the mineral microstructure (section 4.1.1). This research has shown the colour change in bone (which gives some indication on the chemical processes occurring) is not only dependent on temperature but also the period of time the bone is heated. This was confirmed as the series of colour changes was observed at shorter time periods for higher temperatures (≥700 ^{o}C) in comparison to the lower temperatures (≤ 650 ^{o}C). Regardless of temperature, the same series of colour changes were observed (albeit at different time intervals) which highlights the fundamental problem with current methods of colour typing of burnt bone. It seems unlikely the temperature to which a bone specimen has been heated to can be estimated within an error of ± 50 ^{o}C (Shipman *et al.*, 1984, Grévin, 1998), if time is overlooked. Simultaneously predicting both time and temperature for heated bone specimens was investigated in this work and is discussed further in section 9.8.2.

9.5.1.2 X-ray Diffraction Analysis

During heat treatment a decrease in diffraction peak broadening is observed due to the crystallisation process (increase in crystallite size and structural order). This research has shown the rate of crystallisation and thermal decomposition of HAp, are dependent on both time and temperature. Discussion of XRD data in terms of coherence length (a measure of crystallite size and strain) and investigation into bone mineral crystallisation kinetics is provided in section 9.5.2.

In general, when heated, ‘a’ and ‘c’ lattice parameters of HAp structure in bone behaved differently, although they both extend beyond stoichiometric values. The behaviour of the ‘a’ axial length is consistent with previous studies (Holcomb & Young, 1980, Dowker & Elliott, 1983, Shi *et al*., 2005). It is proposed that the initial contraction in the ‘a’ axis is due to the loss of A-type carbonate, although it has been suggested this is due to the loss of lattice incorporated water (LeGeros *et al*., 1978). After the initial contraction, the continued expansion in the ‘a’ axis may be caused by the incorporation

of B-type carbonate into vacant A-site vacancies. Thus, the amount of A-type carbonate is increased. This seems plausible as synthetic A-type carbonated HAp can only be produced at high temperatures (> 900 ^{o}C) (Rey *et al*., 1989, Penel *et al*., 1998, Gibson & Bonfield, 2002, Frank-Kamenetskaya *et al*, 2011). It is suggested the third stage observed at temperatures ≥ 700 ^{o}C, is due to the loss of the recently incorporated A-type carbonate (Shi *et al*., 2005), which would cause a contraction in the 'a' axis (LeGeros *et al*., 1969). This three stage carbonate loss is not apparent in the 'c' axis data as the loss of B-type carbonate and incorporation of A-type carbonate both cause a contraction in the 'c' axial length. Thus, a contraction in the 'c' axis regardless of time and temperature is observed (Figure 8.51B).

Statically heating bone has revealed thermal decomposition of bone mineral is dependent on both temperature and dwell period. The presence of CaO has previously been reported at temperatures of ~ 600 ^{o}C (Beckett *et al*., 2011), however the influence of the dwell period on thermal decomposition of HAp has not previously been considered. MgO was not expected within the temperature range employed (600 – 800 ^{o}C). Although the presence of MgO has previously been reported in bovine and porcine bone specimens heated up to 1400 ^{o}C (Mkukuma *et al*., 2004, Beckett *et al*., 2011), this mineral phase may have been overlooked in specimens heated to lower temperatures as it is present in such small quantities. Thus, for the first time, this research suggests the formation of MgO occurs at much lower temperatures (700 – 800 ^{o}C, dependent on the dwell period) than previously reported for statically heated bovine and porcine bone. This is confirmed by the dynamic heating results, which are considered in section 9.6.4.

9.5.1.3 FTIR Analysis

A decrease in amide I and II peak intensity (1750 – 1500 cm^{-1}) is consistent with the degradation and combustion of collagen (section 9.5.1.3). During heat treatment, carbonate ions are removed from the HAp crystal lattice in the form of carbon dioxide (Barinov *et al*., 2006, Haberko *et al*., 2006). Consequently, a decrease in carbonate peak

intensity is also observed (Mkukuma *et al*., 2004). The phosphate peak becomes sharper and more resolved due to an increase in the short range order of the phosphate ions and crystallite size (Rey *et al*., 1991, Turunen *et al*., 2013).

9.5.1.4 DSC Analysis

The DSC curves obtained for this research are, in general, consistent with previous studies (Lozano *et al.*, 2003). The broad endothermic peak observed at 25 – 100 ^{o}C may be due to the loss of surface absorbed water molecules (Heredia *et al.*, 2013). It is proposed that the second endothermic peak at 125 – 150 ^{o}C is associated with the complex denaturising process of collagen (Barbani *et al*., 2011). Prior to combustion of collagen, thermal denaturation of collagen causes destruction of the triple helix structure. This occurs through disruption of structural water which bridges together the three polypeptide chains followed by disruption of the hydrogen bonds between the helices (Barbani *et al*., 2011). This process requires a source of energy, thus an endothermic peak is observed. Previous studies have reported this endothermic peak at lower temperatures (~50 – 60 ^{o}C). The higher values reported in this thesis may be due to the complex interaction between the organic and mineral within bone. Barbani *et al*. (2011) for example found with increasing synthetic HAp to collagen ratio, this endothermic peak was observed at higher temperatures. This may also explain why this endothermic peak was observed at slightly lower temperatures for red deer antler (which has a larger organic to mineral ratio as discussed section 9.2) than the other bone types.

The exothermic peaks with maxima of 350 ^{o}C and 450 ^{o}C represent the complex process of the organic (mainly collagen) combustion (Lozano *et al*., 2002). The intensity of the peaks in the DSC spectra differed for bone types. Variations in the thermograms heat flow intensity are dependent on collagen mass (*ibid*). Taking this into account, the DSC data complements the FTIR results and suggests the amount of collagen follows the trend; red deer antler > porcine > bovine > rostrum. A previous study by Etok *et al.* (2007) reported an exothermic peak between ~ 525 - 600 ^{o}C, which the authors associate with changes to the mineral microstructure of their animal by

product meat and bone meal (MBM) specimen. This peak was not observed in this research and has not been reported in other studies. It is proposed that rather than being associated with mineral microstructural changes, the exothermic peak observed by Etok *et al*. (2007) may be due to the combustion of other complex organic molecules not found in bone.

9.5.2 Bone Crystallisation Kinetics

Literature on bone mineral crystallisation kinetics is limited. Prior to this research, the activation energy for bone was not known although crystallisation of synthetic HAp from amorphous and sol gel phases had been investigated (Gross *et al.*, 1998, Milev *et al.*, 2003). The Kolmogorov-Johnson-Mehl-Avrami (KJMA) model was used to calculate the kinetics associated with the phase transformation within bone during heat treatment (i.e. the crystallisation process). This unique approach involved applying coherence length data to the KJMA model. This allowed for the first time, directional dependence calculation of activation energy, spontaneous nucleation rate and rate of crystallisation (Greenwood *et al.*, 2012).

9.5.2.1 Activation Energy

The calculated activation energies were similar for all bone types and crystallographic directions. The results provide an average bone mineral crystallisation activation energy of 183 ± 8 kJ mol^{-1}. This suggests a similar fundamental growth mechanism for all bone types in all crystallographic directions. These results are comparable to previous work which examined the crystallisation of HAp from amorphous and sol-gel phases using DSC and TGA measurements (Gross *et al.*, 1998, Milev *et al.*, 2003). These studies reported crystallisation activation energy values of 274 kJ mol^{-1} and 235 kJ mol^{-1} respectively. The lower values (183 ± 8 kJ mol^{-1}) reported in this thesis, may be due to the initial, nanocrystalline state of unheated bone mineral. It is proposed higher activation energies were reported by Gross *et al.* (1998) and Milev *et al.* (2003) as these

studies reported the energy required for HAp crystal nucleation and growth. The activation energy values reported in this thesis were associated with crystal growth only.

9.5.2.2 Application of the KJMA model to X-ray diffraction Data

The classical use of the KJMA model results in the determination of two parameters, 'n' and 'k' (Maffezzoli et al., 1995, Martin, 2010). The parameter 'k' represents the rate of crystallisation, whilst 'n' reflects the spontaneous nucleation rate and the dimensional increase in crystal volume. For a three dimensional growth with unsaturated nucleation points, n would have a value close to 4 and if the nucleation rate equalled zero, then $n \approx 3$. A three dimensional, diffusion based growth would have an n value close to 1.5. Unfortunately, the interpretation of n is ambiguous across the literature as contributions from the nucleation rate and the growth dimensions are not fully understood (Lam & Rogers, 2011).

X-ray diffraction data has previously been applied to the KJMA model to study the transformation kinetics of HAp (Najafia et al., 2008, Kasioptas et al., 2010). In all of these studies, the fraction of transformed HAp was used as the dependent variable to construct sigmoidal curves. For example, Ivankovic (2010) characterised the kinetics of an aragonite to HAp process and reported values of $n \approx 0.5$ and an activation energy of 77.8 ± 5 kJ mol^{-1}.

In contrast, for this study, the HAp coherence length was applied to the KJMA model, which allowed a single crystallographic direction to be considered. This offered a unique and advantageous way to determine crystallisation kinetics of bone mineral. This approach fixes the dimensional growth to 1 (as only one crystallographic direction is being considered), meaning a first order kinetics would have an n value of 2, if growth and nucleation were occurring simultaneously and a value of 1, if nucleation sites were saturated. For a diffusion dominated growth, this means n would have a value of ~ 0.5.The results of this study therefore suggest that for all bone groups and in all observed crystallographic directions; bone mineral crystallisation becomes a diffusion limited process at higher temperatures. This process is demonstrated more convincingly

in the <00ℓ> direction than the <0k0> direction. As the <00ℓ> direction exhibits a slightly greater reaction rate at 650 ^{o}C, it is plausible a diffusion limited growth is reached prior to that within the <0k0> direction.

With regards to rate constant (k), a typical trend was observed where the rate increased significantly with increasing temperature, for all bone groups and crystallographic directions. This is unsurprising as rate is dependent on temperature (Atkins & Jones, 2005). Increasing this variable increases the average kinetic energy of molecules and consequently there are more collisions per unit time (ibid). The rate however differed significantly between bone types, with anorganic specimens possessing the lowest rate and porcine the largest rate. This trend is consistent between both temperature and crystallographic directions; although at higher temperatures the difference becomes much smaller. This may be explained by the apparent greater organic content within porcine specimens. Crystallisation rate is influenced by factors such as catalytic action and intrinsic sources of additional energy. The relative mass loss due to heating was greatest for porcine and least for the anorganic specimens when compared at the same time-temperature points. As discussed in section 4.1.1, bone mass loss during heating arises from the evaporation of water, combustion of the organic matrix and evolution of volatiles. Potentially this may provide an additional source of ions resulting in an increased crystallisation rate. Furthermore, DSC results (section 8.5.5) suggests the combustion of the organic (calculated from exothermic reaction which peak between ~300 - 500 ^{o}C, dependent on bone type), causes an enthalpy change of 1.65 kJ g^{-1} and 2.04 kJ g^{-1} for bovine and porcine bone respectively, thus providing an intrinsic source of additional energy. Thus, it is proposed the rate of bone mineral crystallisation (for statically heated bone) is influenced by combustion of the organic.

9.5.2.3 The Role of Collagen on Crystallisation Kinetics

Collagen in bone is often reported to have a ‘shielding’ effect on bone mineral during heat treatment (Walsh, 1994, Person *et al.*, 1996, Roberts, 2002, Etok *et al.*, 2007). In this study it is proposed the energy associated with the combustion of the organic matrix

promotes HAp crystallisation. This hypothesis was validated by calculating the exothermic energy produced during static heat treatment of red deer antler, porcine, bovine and rostrum specimens as well as observing the crystallisation of these bone specimens (section 8.6.3.). Comparing the time at which the onset of crystallisation was observed to the exothermic energies calculated from DSC data reveals an interesting trend. The greater the amount of exothermic energy calculated, the earlier the onset of crystallisation was observed for the different bone types. This supports the suggestion that combustion of the organic matrix promotes bone mineral crystallisation. This is somewhat validated further by the DSC results. If collagen truly 'shielded' bone mineral during heat treatment, the physicochemical changes such as crystallisation would occur at a similar temperature as the complete combustion of the organic. This is not the case. The exothermic peak assigned to the combustion of the organic plateaus prior (~ 500 ^{o}C) to the temperature at which the onset of crystallisation occurs (~ 600 ^{o}C) (section 8.5.5).

After the onset of crystallisation, the continued growth of HAp crystallites differed between bone types (highlighted in Figure 8.34). Assuming there is little or no lattice strain after the onset of crystallisation, the continued growth of red deer antler crystals occurs at a slower rate than rostrum HAp crystals. This behaviour was also observed for dynamically heated red deer antler bone specimen and is therefore discussed further in section 9.6.2.

9.6 Dynamically Heated Bone

In recent years, an increasing number of studies have examined the behaviour of bone during static heating, which have provided indications of microstructural changes and thermal decomposition processes as discussed in chapter 4 (Ravaglioli *et al.*, 1996, Hiller *et al.*, 2003, Harbeko *et al.*, 2006, Beckett *et al.*, 2011, Castillo *et al.*, 2013). Unfortunately, these studies overlook the confounding effects of cooling and cannot strictly provide a complete model of the physicochemical changes. Therefore, for the

first time, this research employed a controlled hot stage X-ray diffraction system (HS-XRD) to provide dynamic data on the physicochemical changes within bone mineral during heat treatment (Greenwood *et al.*, 2013). The use of HS-XRD in bone mineral research is limited. Previous work documented thermal decomposition of bone using HS-XRD (Mkukuma *et al.*, 2004), but changes to crystallite size and strain and unit dimensions (lattice parameters) have not previously been reported. Changes to coherence length and lattice parameters of dynamically heated bone are discussed separately below.

9.6.1 General Observations

As expected from statically heated bone (section 9.5), a decrease in diffraction peak broadening with increasing temperature was observed, suggesting an increase in crystallite size and structural order. For the first time, dynamically heating bone has shown the crystallisation of bone mineral occurs rapidly over a very short temperature range. In comparison, previous static studies have documented the crystallisation process over a period of time at a constant temperature (Stiner *et al.*, 1995, Piga *et al.*, 2009, Beckett *et al.*, 2011, Greenwood *et al.*, 2012). During cooling, full width maximum values (corresponding to HAp) were consistent (the peaks remained unchanged). This suggests the cooling rate employed for dynamic heat treatment had little or no effect on HAp crystallisation process (after the specimen had been heated to 900 ^{o}C).

9.6.2 Coherence Length

The sigmoidal relationship between coherence length and temperature for dynamically heated bone agrees with previous static heated bone studies (Piga *et al.*, 2008 & 2009, Greenwood *et al.*, 2012). The onset of crystallisation for all bone types was observed within a temperature range of just ~40 ^{o}C. The slightly higher temperature for rostrum in comparison to the other bone types may be associated with lattice disorder and

energy. As discussed in section 9.2, unheated rostrum bone mineral exhibited the largest coherence length which suggests not only larger crystallites but also a greater microstructural order (less strain). This was confirmed by refinement of the data to establish crystallite size and strain values (section 9.3). It is proposed that the lattice energy associated with the HAp structure of rostrum is significantly less than the other bone types, which exhibit smaller crystallite sizes and larger lattice strain values (section 9.3). It is suggested that this increased lattice energy contributes to reducing the amount of energy input required to promote crystal growth during heat treatment. Therefore, the onset of crystallisation would occur at earlier temperatures for systems with greater lattice disorder. Furthermore, it is suggested that HAp crystals associated with bovine, porcine, human and red deer antler specimens exhibit a greater surface area to volume ratio due to their initial small size and consequently represent a higher energy state in comparison to rostrum crystals. Consequently, the onset of crystallisation occurs at a slightly higher temperature for rostrum in comparison to the other bone types.

Dynamically heating bone has shown the continued growth of HAp crystals differs between bone types. This is highlighted by the sigmoidal curve gradients and coherence length data at 900 ^{o}C (Figure 8.38). Assuming there is minimal or no strain associated with HAp crystals after the onset of crystallisation (Rogers & Daniels, 2002), the coherence length data suggests growth of red deer antler crystals are retarded during heat treatment. The rapid change in coherence length data for bovine, porcine, human and rostrum after the onset of crystallisation, suggests a rapid increase in crystallite size and lattice order. This rapid change is not observed for red deer antler and the coherence length data is significantly lower at 900 ^{o}C in comparison to the other bone types (which reach the instrument resolution limits). It is proposed this is because the crystallisation process is limited by the organic to mineral ratio in unheated bone. Red deer antler has a greater amount of collagen (section 9.2) than the other bone types, and therefore it is proposed that there is less mineral material and larger ‘voids’ between the crystals. Consequently, the inter-crystal connectivity is much lower due to fewer grain boundaries and less growth fronts, which limits the growth of red deer antler crystals.

Coherence length data for bovine, porcine and human bone in comparison to that of rostrum validates the previous suggestion that lattice energy contributes to crystal

growth. The change in coherence length between the onset of crystallisation and after plateauing (due to reaching the instrument resolution limit); occurs over a longer temperature period for rostrum than bovine, porcine and human bone. This suggests a slower growth mechanism for rostrum crystals. As discussed earlier, it is proposed that lattice energy associated with HAp lattice of rostrum is significantly less than the other bone types. The continued growth of rostrum crystals occurs over a longer and higher temperature range as there is less lattice energy contribution. Greater lattice energies would reduce the amount of energy input required from the heat treatment, thus the crystallisation process occurs over a shorter temperature range.

Quantification of coherence length data revealed the temperature at which 50% crystallisation occurs, is not significantly different between the observed crystallographic directions. This confirms previous static studies which suggest HAp crystals transform from a highly anisotropic morphology to a system which is more ordered with larger equi-dimensional crystallites (Rogers & Daniels, 2002, Danilchenko *et al*., 2006). As discussed in section 9.3, unheated HAp is a highly anisotropic material (direction dependence crystallite size and strain) which is reflected in the coherence lengths. The coherence length is larger in (00ℓ) planes. In order for the structurally equivalent (hk0) planes of HAp crystallites to reach 50% crystallisation at the same temperature as the (00ℓ) plane, crystal growth in the (hk0) plane must occur at a faster rate. As the coherence length of unheated bone denotes crystallite size and lattice strain, it seems plausible that a larger amount of lattice microstrain is observed along the (hk0) planes than the (00ℓ) planes. The growth of HAp crystals during heat treatment has been associated with lattice disorder, which may provide a driving source of energy for the transformation from an anisotropic state to a more ordered equi-dimensional system (Rogers & Daniels, 2002).

The temperature at which 50% crystallisation was calculated differed between bone types. It is proposed that this is due to both the organic to mineral content and associated lattice energy as discussed earlier. 50% crystallisation was recorded at similar temperatures for both red deer antler and rostrum. For red deer antler, it is proposed that the organic to mineral ratio limits crystal growth and therefore more energy is required for continued growth of the crystallites. Rostrum, which is a highly

ordered material, is assumed to have very little associated lattice energy. Without contribution from lattice energy, the continued growth of rostrum HAp crystallites as well as the onset of crystallisation occurs at higher temperatures.

9.6.3 Lattice Parameters

Changes in the lattice parameters during heat treatment are thought to be caused by loss of surface and lattice incorporated water (up to 400 ^{o}C), ion exchange (especially carbonate) and thermal expansion (LeGeros *et al*. 1978, Kim *et al*., 2003, Shi *et al*., 2005, Wang *et al*., 2010). Dynamically heating bone has revealed four distinct transition regions in the lattice parameter data for all bone types. The transition regions are delimited by a change in gradient (Figure 8.39). The first transition region (~ 25 – 100 ^{o}C), may be due to the loss of surface bound water. The linear relationship observed for the second (~ 200 – 550 ^{o}C) and fourth (~630 – 900 ^{o}C) transitional regions, where the gradient was constant for all bone types and for both axial lengths suggests there was no significant change in the material. It is proposed that the expansion in the lattice parameters within these two regions is predominately due to thermal expansion. Changes to lattice parameters due to the loss of lattice incorporated water (up to 400 ^{o}C) (LeGeros *et al*., 1978) may not have been observed due to the effects of thermal expansion. The third transition region (~ 580 – 640 ^{o}C, dependent on bone type) (where an expansion in the ‘a’ axis and a contraction in the ‘c’ axis was observed), may be due to the incorporation of B-type carbonate into vacant A-type sites (section 4.2.1). This behaviour was also observed for statically heated bone specimens, as discussed in section 9.5.1.2. The third transition region was observed in the same temperature range as the onset of crystallisation, for each bone type. It is proposed that the behaviour of the lattice parameters may also be associated with the transformation from a highly disordered material to a more ordered state with larger crystallites.

As discussed for coherence length in section 9.6.2, it is proposed the temperature range for the third transition region differs according to bone type due to the associated energy required for the transformation from one state (small crystals, more strain) to another

(larger crystals, less strain). For example, the third transitional region is observed at higher temperatures for rostrum in comparison to the other bone types. The HAp crystallites are larger and more ordered for rostrum, which results in a smaller surface area to volume ratio and represent a lower energy state. Consequently, changes to the crystal structure (which alters the lattice parameters) of ordered systems require a greater amount of energy (gained at a higher temperature) in comparison to disordered systems.

Using the single linear theoretical model described in section 8.7.2.2, the amount of A and B type carbonate required to simulate the gradient in transition regions two and four, was calculated as a percentage. The amount differed for 'a' and 'c' axial lengths of rostrum, human, porcine and red deer antler specimens. This suggests changes to the HAp structure is not solely due to the loss of carbonate, but must also be attributed to the loss or gain of extraneous ions. This may include incorporation of B-type carbonate into vacant A-type sites (section 9.5.1.2). This is to a certain extent validated by the results discussed in section 9.3.4, which suggested peak broadening from strain contributions cannot solely be attributed to B- type carbonate substitution in unheated synthetic HAp specimens. The amount of carbonate required to simulate the gradients for bovine bone was approximately equal for both axes. This suggests the dominant process causing changes to the lattice parameters is the loss of the carbonate ions. However, the loss and gain of extraneous ions from bovine mineral may not have been sufficient to be detected through changes in the lattice parameters, over and above the loss of the carbonate.

9.6.4 Thermal Decomposition Products

Thermal decomposition of dynamically heated bone has previously been investigated, however the effects of cooling were not considered. Differences in the amount of calcium oxide between bone types have previously been reported and give an indication of whether the HAp structure is calcium rich or calcium deficient (with regards to the relative proportion of calcium) (Gibson *et al.*, 2000, Mkukuma *et al.*, 2004). In this

study, the results at 900 ^{o}C suggest both rostrum and human bone are calcium rich whilst the lack of calcium oxide for the red deer antler may suggest a calcium deficient system. To confirm this, further research would be required to investigate the thermal decomposition products at temperatures exceeding 1400 ^{o}C (section 9.8.1.2).

By employing a dynamic heating regimen, the stability of CaO and MgO during cooling has for the first time been considered. A greater percentage of CaO was observed prior to cooling suggesting this mineral phase is not thermally stable once formed. It is proposed that during cooling, a number of calcium ions are incorporated back into the thermally stable HAp crystal lattice, through the suggested OAP pathway (section 4.2.2). In contrast, the percentage of MgO once cooled was similar to the value calculated at 900 ^{o}C. It is proposed that unlike calcium ions, magnesium ions are not incorporated back into the HAp crystal lattice during cooling. The capability of the crystal lattice to accommodate magnesium ions may be reduced due to competitive substitution of other ions during cooling. This research also validates previous synthetic HAp studies (Liao *et al*., 1999, Lin *et al*, 2000, Wang *et al*., 2009) which report the transformation of β –TCP to α-TCP, and that these mineral phases are not thermally stable. These mineral phases are thought to reconstitute into HAp during cooling via a proposed OAP pathway. The OAP pathway was not investigated during this research and further work would be required to confirm the presence of OAP in heated bone, possibly using FTIR (discussed in section 10.3).

For the first time, dynamically heating bone has provided the temperatures at which these mineral phases are first observed. The temperature at which CaO and MgO was observed is slightly lower than observed for statically heated bone; this is discussed further in the next section. However, this validates the static data (sections 9.5.1.2 & 9.8.1.2) with regards to MgO. The presence of this mineral phase was observed at much lower temperature than previously reported (Beckett, 2009). Further, previous static studies have suggested the formation of β – TCP and α –TCP occurs at temperatures exceeding 1200 ^{o}C, this is also validated by the static studies in this research (discussed in section 9.8.1.2). However, for dynamically heated bone this is not the case, and these mineral phases were observed at much lower temperatures (670 – 830 ^{o}C). This is discussed further in the next section.

9.7 Comparison of Static and. Dynamic Heating

Unexpectedly, the onset of crystallisation for dynamically heated bone was similar for all bone types (within a range of ~ 40 ^{o}C). This is not comparable to statically heated bone, where the onset of crystallisation seemed to be dependent on the amount of organic matrix in unheated bone specimens. As proposed in section 9.5.2.3, during static heating, combustion of the organic matrix provides an intrinsic energy source, which contributes to amount of energy input required to promote crystallisation. If this was the case for dynamically heated bone, the onset of crystallisation would occur at a much lower temperature for red deer antler, which exhibits the greatest abundance of organic matrix. However, this was not observed and the onset of crystallisation was similar for all bone types (~40 ^{o}C). It is proposed this is due to the difference in the heating regimens employed for dynamic and static experiments.

The heating rate employed for the dynamic work (ramp rate of 10 ^{o}C min^{-1}, with a dwell period at each temperature interval of 10 minutes) was significantly slower than for static heating (where the specimens were placed in the furnace at temperature). Consequently, it is proposed the intrinsic energy provided from the combustion of the organic matrix is expended at a much slower rate for dynamically heated bone. This essentially creates an 'anorganic' specimen prior to the onset of crystallisation. Thus, the energy from the combustion of the organic does not aid the crystallisation process for dynamically heated bone. In comparison, for statically heated bone specimens, due to the rapid heating rate, the energy associated with combustion of the organic is available during the crystallisation process. Therefore, the exothermic energy from the combustion of the organic contributes to the overall amount of energy required to promote crystallisation during static heating. Thus, the onset of crystallisation is observed at lower temperatures for statically heated bone mineral in comparison to dynamically heated bone.

At first instance, lattice parameter data of dynamically heated bone does not appear to be comparable to statically heated bone lattice parameter values (Figures 8.27, 8.39 and 8.51B). It is proposed this is due to the effects of thermal expansion. The fundamental premise of dynamic heat treatment is the collection of data whilst heating.

Consequently, small changes to lattice parameter values caused by the loss or gain of ions may be obscured by changes caused by thermal expansion. This is not the case for statically heated bone as specimens are cooled prior to analysis. As discussed in section 9.6.3, at approximately 600 ^{o}C, a change in the lattice parameters, which is not caused by thermal expansion, is observed in the dynamic data (Figure 8.39, region 3). This behaviour is also observed in the static data but at slightly higher temperatures (Figure 8.27). This is possibly due to the incorporation of B-type carbonate into vacant A-type sites (section 9.5.1.2). This is somewhat validated through the qualitative assessment of carbonate using the linear theoretical model discussed in section 9.6.3. The results obtained from the model suggested changes to the lattice parameters at approximately 600 ^{o}C (Figure 8.39, region 3,) cannot solely be due to the loss of carbonate, but must also be attributed to the loss or gain of other ions. This may also include incorporation of B-type carbonate into vacant A-type sites. Thus, the three stage carbonate loss proposed by Holcomb & Young (1980), Dowker & Elliott (1983) and Shi *et al.* (2005) (discussed in section 4.2.1) seems plausible, when considering lattice parameter behaviour of static and dynamic heated bone.

The temperatures at which β-TCP, α- TCP, CaO and MgO were observed also differed between static and dynamically heated bone. These thermal decomposition products were observed at lower temperatures in dynamically heated bone specimens. It is proposed this is again due to the heating rate employed. Dynamic heating provides the system with more energy due to a slower heating rate. Thus, thermal decomposition of HAp occurs at lower temperatures. Furthermore, it is proposed the quantity of the additional mineral phases may differ for statically and dynamically heated specimens due to the effects of cooling. As discussed in sections 9.6.4 and 9.8.1.2, CaO is not thermally stable and a decrease in the quantity of this mineral phase was observed during cooling. This phenomenon is not limited to CaO. The quantity of the thermal decomposition products in bone statically heated to 1400 ^{o}C and allowed to cool, differed in comparison to the quenched specimens, as discussed in section 9.8.1.2. Potentially, quenched specimens may be similar to dynamically heated bone as they offer a ‘snapshot’ of the chemical processes occurring at temperature (accepting the heating regimen would need to be kept constant and small differences may be observed due to rapid cooling). Thus, this suggests at higher temperatures, the quantity of the

thermal decomposition products would differ between dynamically and statically heated bone. Further work would be required to validate this.

Parameter	Static	Dynamic
Onset of crystallisation	Dependent on exothermic energy provided from the combustion of the organic. Difference observed between species.	No contribution from exothermic energy associated with organic combustion due to slow heating rate, essentially producing ‘anorganic’ specimens. Little difference observed between species.
Lattice Parameters	Dependent upon on ionic exchanges	Dependent on thermal expansion as well as ionic changes
Thermal decomposition products	Influenced by cooling regimen employed	Observed at lower temperatures as the system is provided with more energy due to a slower heating rate.

Table 9.1 Summary of the differences between statically and dynamically heated bone

9.8 Additional Investigation for the Applications of Research

9.8.1 Heating and Cooling Rates

9.8.1.1 Crystallisation

A decrease in diffraction peak broadening is observed for heated bone specimens, irrespective of heating and cooling regimen employed. This indicates an increase in crystallite size and order (Rogers & Daniels, 2002). Coherence length values within the <00ℓ> direction were within errors, similar for each regimen. This suggests the regimen employed had little effect on crystallite size and strain in this particular crystallographic direction. This was not the case in the <0k0> direction, where a difference in coherence length was observed between specimens which had been cooled and those which were quenched. A greater coherence length was observed for cooled specimens, signifying larger crystallite sizes and more order within the HAp structure. This suggests the additional energy provided from the cooling period had little effect on crystallite growth in the <00ℓ> direction but promoted the growth of the crystals in the <0k0> direction. This validates the results previously discussed in section 9.5.2, where it was suggested the growth of crystallites in <hk0> directions occur at a faster rate than in <00ℓ> directions, even though the energy input is the same. Thus, HAp in bone transforms from highly anisotropic material to one which is equi-dimensional and more ordered. This also highlights the confounding effect of cooling in comparison to quenched specimens, if only in the <0k0> direction.

To investigate the effect of heating regimens further, heating and cooling rates were considered. The results of this study suggested the rate at which bone specimens are cooled, has the most impact on coherence length values. This highlights the importance of the dynamic heating study. Firstly taking into account the influence of heating rates, there was very little difference in coherence length values in both crystallographic directions, between the specimen heated at temperature and the specimens heated from room temperature at rate of 25 ^{o}C and 10 ^{o}C per minute. However, coherence length

values were considerably larger for specimens heated at a rate of 2 ^{o}C per minute. This heating rate is much slower and consequently more energy is supplied during heat treatment.

The rate at which specimens were cooled seemed to have a considerable effect on coherence length. With slower cooling rates larger coherence length values were observed. Specimens cooled at a rate of 25 ^{o}C per minute were similar to quenched specimens. Coherence lengths of specimens cooled at a slower rate were considerably larger. Again this is due to the amount of energy supplied to the system during the cooling period. A slow cooling rate, such as 2 ^{o}C per minute, supplies energy over a longer period which promotes continued crystal growth during cooling.

9.8.1.2 Thermal Decomposition

The effect of cooling on the thermal decomposition of biological HAp has not previously been reported. There have however been a limited number of studies which have concentrated on thermal decomposition and reconstitution of synthetic HAp (Liao *et al*., 1999, Lin *et al*., 2000, Wang *et al*., 2009). The results of this study have highlighted the thermal stability of biological HAp when heated to 1200 ^{o}C. Only very small quantities of additional calcium phosphate mineral phases were observed at this temperature. The absence of CaO in cooled and quenched red deer antler specimens is in agreement with dynamically heated results discussed in section 9.6.4, and may suggest red deer antler mineral is deficient in calcium (i.e. the relative proportion of calcium is lower for red deer antler) (Mkukuma *et al*., 2004). The results suggest at 1200 ^{o}C, cooling has a slight influence on the thermal decomposition products observed. TTCP was present in quenched bovine, porcine and red deer antler bone specimens but was not observed in cooled specimens. The presence of TTCP in quenched specimens suggests this mineral phase is not thermally stable at 1200 ^{o}C and reconstitutes to HAp during cooling. This is supported by Liao *et al.* (1999) and will be considered in more depth below. The absence of TTCP in quenched rostrum specimens may be expected. As discussed in sections 9.2 and 9.3, it is assumed that rostrum

mineral is a much more ordered system, with less lattice strain than the other bone types. It is proposed the more ordered a system, the greater the thermal stability.

At 1400 ^{o}C, the confounding effect of cooling on thermal decomposition of HAp is substantial. As reported in previous studies (Ando *et al*., 1958., Beckett *et al*., 2011) when heated to 1400 ^{o}C, thermal decomposition of HAp results in the formation of additional mineral phases:- TTCP, TCP, CaO and MgO (Figure 4.3, section 4.2.2). However, for the first time, this research has highlighted that the quantities of these mineral phases differ depending on the cooling regimen employed. This is due to the thermal stability of these calcium phosphate mineral phases and reconstitution of HAp during cooling, as discussed in section 4.2.2. Quenched specimens essentially offer a 'snapshot' of the thermal decomposition processes occurring at dwell temperature. Thus, presence of large quantities of TTCP and α-TCP in quenched specimens is consistent with previous synthetic HAp studies (Liao *et al*., 1999, Lin *et al*., 2000, Wang *et al*., 2009). According to these studies, at ~1200 ^{o}C, a proportion of HAp transforms to β-TCP and TTCP and by 1400 ^{o}C, β-TCP undergoes a further transformation to α-TCP (*ibid*). As these transformations are reported to be reversible, the smaller percentage of TTCP and the absence of α-TCP in cooled specimens (with the exception of the red deer antler) seem plausible.

In addition to differences in the quantity of these additional mineral phases due to the cooling regimen employed, differences were also apparent between bone types, when heated at 1400 ^{o}C. For both cooled and quenched regimens, a greater percentage of HAp was observed for rostrum, which validates the previous proposition, that rostrum HAp is more thermally stable than other bone types. It has previously been proposed the percentage of TCP in heated bone specimens is dependent on Ca/ P molar ratio (Gibson *et al*., 2000). A greater proportion of α – TCP observed in red deer antler specimens suggests this material is possibly calcium deficient (Mkukuma *et al*., 2004). This is validated by the absence of CaO in dynamically heated red deer antler specimens (section 9.6.4) as well as the specimens statically heated at 1200 ^{o}C. A smaller percentage of TCP observed in rostrum specimens heated at 1400 ^{o}C and a larger percentage of CaO observed in the specimens heated at 1200 ^{o}C, suggests rostrum is a calcium rich material (i.e. a greater relative proportion of calcium) (*ibid*).

In order to determine whether the thermal decomposition products observed in heated bone are dependent on the original ionic chemistry of the specimens, elemental analysis of unheated bone specimens was carried out. Unfortunately, due to the limitations outlined in section 8.8.1.2, further work would be required to provide an in depth insight into the thermal decomposition processes. This is considered in section 10.3. The elemental results presented in this thesis have however been used to validate and possibly refute previous studies concentrating on thermal decomposition and *in vivo* HAp crystallite size control.

A greater ratio of potassium observed in red deer antler, porcine, bovine and human bone in comparison to rostrum supports the premise that TCP formation is favoured in the presence of these ions (Beckett, 2009). A small percentage of TCP was observed in unheated rostrum, whilst this was one of the major mineral phases observed in porcine, bovine and human specimens, as discussed above. A greater ratio of zinc observed for rostrum was not expected. Zinc has been reported to be a co-factor for collagen synthesis (McClain, 1973, Starcher *et al*., 1980, Kaplan *et al*., 2004). Thus, one would expect a system with a greater proportion of zinc to have a larger abundance of collagen. This is not the case for rostrum and in fact red deer antler, which exhibited the smallest ratio value for zinc, has a greater proportion of organic matrix in comparison to other bone types (section 9.2). Interestingly, zinc is also thought to have a regulatory role on the mineral matrix. As discussed in chapter 3, incorporation of zinc into the mineral lattice has also been reported to play a crucial role in *in vivo* HAp crystal size control (Fuierer *et al*., 1994, Bigi *et al*., 1995, Cuisinier *et al*., 1995, Mayer *et al*., 2000) Studies are conflicting; however the result presented in this thesis seem to validate studies which suggest incorporation of Zn reduces crystal defects, resulting in a reduction in structural disorder and larger crystallite sizes (Fuierer *et al*., 1994, Bigi *et al*., 1995). Rostrum bone mineral exhibits the largest HAp crystallite size and a greater ratio of zinc than the other bone types, which exhibit a similar crystallite size and zinc ratio. Studies have also suggested incorporation of magnesium into the HAp structure may influence *in vivo* HAp crystallite size. Again, the research is conflicting; however the results presented in this thesis suggest the incorporation of Mg reduces crystallite size (Bigi *et al*., 1993, Fuierer *et al*., 1994, Kanzaki et al., 2000), as a greater ratio of this ion was observed in porcine, bovine, human and red deer antler specimens in

comparison to rostrum. The incorporation of Mg is thought to increase lattice disorder, which increases the dissolution of HAp crystals, resulting in smaller crystals (chapter 3). The amount of strontium observed differed between bone types, with rostrum exhibiting the largest amount. This is surprising as incorporation of strontium into the HAp crystal lattice has been shown to induce lattice strain, impair *in vivo* crystal growth and increase HAp dissolution (Christoffersen *et al*., 1997, Cabrera *et al*., 1999). As mentioned, rostrum mineral exhibits larger crystals and less lattice strain than the other bone types, thus the results do not appear to validate previous studies.

Other interesting traits were observed from elemental analysis of unheated bone specimens. The ratio of iron was much greater for red deer antler in comparison to the other bone types. Red deer antler bone tissue is filled with blood, which contains various ions required for rapid calcification (Fennessy & Suttie, 1985, Rolf & Enderle, 1999, Cho *et al*., 2001). Minute traces of blood may have been present in red deer antler specimens prior to analysis, which may be the source of the iron. The greater ratio of lead observed in human specimens may be due to the age of the individual. Research has shown lead accumulates in bone and tooth mineral during an individual's life (Steenhout & Pourtois, 1981, Wittmers *et al.*, 1988, Hu *et al*., 1996, Cheng *et al.*, 1998). The amount of lead observed is also somewhat dependent on nutritional factors such as a low calcium diet and environmental factors including smoking and alcohol consumption (Hu *et al*., 1996, Cheng *et al.*, 1998). As the human bone specimen utilised in this research was obtained from the femur of a 55 year old male, a greater ratio of lead may be expected. The other bone types would not be subjected to increased lead concentrations from the environmental factors outlined above.

9.8.2 Time and Temperature Prediction

Determining the period of time and temperature at which a bone specimen has been heated has not previously been achieved. Inferences regarding temperature are often reported from the colour of an unknown heated bone specimen (Shipman et al., 1984, Grévin et al., 1998), but these studies fail to take into account dwell period. The novel

multi parameter approach undertaken in this thesis has shown predicting time and temperature of an unknown heated bone specimen may be possible, although there are some limitations. Firstly, the model is dependent on the parameter chosen. For example, the 'a' axis lattice parameter data could not be used for the model as changes to the 'a' axial length were sporadic during heat treatment (Figure 8.27, section 8.5.3). It is proposed this is due to the loss and gain of A- and B-type carbonate ions at different temperatures as discussed in section 9.5.1.2. Although a correlation was observed for carbonate to phosphate ratio data, the temperature curves (> 600 ^{o}C) overlapped making it difficult to distinguish between temperature and time and erroneous results were obtained. This suggests the amount of carbonate lost at each dwell period was similar for temperatures exceeding 600 ^{o}C. While the temperature curves for 'c' axis lattice parameter data did not overlap, the lattice parameter values became increasing similar with longer heating periods for temperatures > 600 ^{o}C. Consequently, the predicted temperature was in most instances hugely incorrect when 'c' axis lattice parameter data was employed.

The most comprehensive model in terms of simultaneously predicting accurate time and temperature (within errors) was developed using coherence length data and 'L' colour value data. The change in colour of heated bone has previously been used to successfully predict the probability of obtaining a DNA profile (Fredericks, 2011). Although the model detailed in this thesis was successful at predicting the time and temperature of bone heated for short time periods, inaccuracies arose for bone specimens heated for longer time periods. It is proposed that this is due to the rapid change in coherence length and colour during heat treatment at higher temperatures. Due to instrument resolution limits, coherence length data plateaus, which results in the sigmoidal relationship observed. This is the same for 'L' colour value data, which is used to quantify colour changes from black to white. Once carbonisation occurs, L values remained constant at approximately 90 (no associated units). Therefore, at certain times and temperatures the data overlaps due to reaching the limits of the parameter data, which is highlighted by a plateau in the data. At higher temperatures, the data plateaus at shorter time periods, as the chemical changes occur at a faster rate. Further work within this area is required to enable accurate calculation of both time and temperature (discussed further in section 10.3).

9.8.3 Species differentiation: Dynamically heated bone

Species differentiation of burnt bone using X-ray diffraction has the potential to be of significant value to the field of forensic science and archaeology. To date, studies in this area are conflicting and do not consider the confounding effects of cooling (Beckett *et al.*, 2011, Piga *et al.*, 2013). Using the X-ray diffraction data obtained from dynamically heating bone, this research suggests inter-species differences exists and validates previous work carried out by Beckett *et al.* (2011). For the first time, the results presented in this thesis suggest it may be possible to statistically differentiate human bone from other bone types using 'a' axis lattice parameter data obtained during dynamic heating. As this was a preliminary study, further work would be required to validate whether it was possible to differentiate human from a wide range of species, as discussed in section 10.3.

It is important to note that Beckett *et al.* (2011) reported no significant difference in the 'a' axis data and limited statistical difference in the 'c' axis data between species heated at 600 ^{o}C. This is perhaps due to the fact that only one temperature was considered, whereas a temperature range was selected for the work presented in this thesis. Furthermore, unlike Beckett *et al.* (2011), the temperature range considered for this analysis exceeded the temperature at which the onset of crystallisation was observed.

9.9 Summary of Discussion: Key Findings

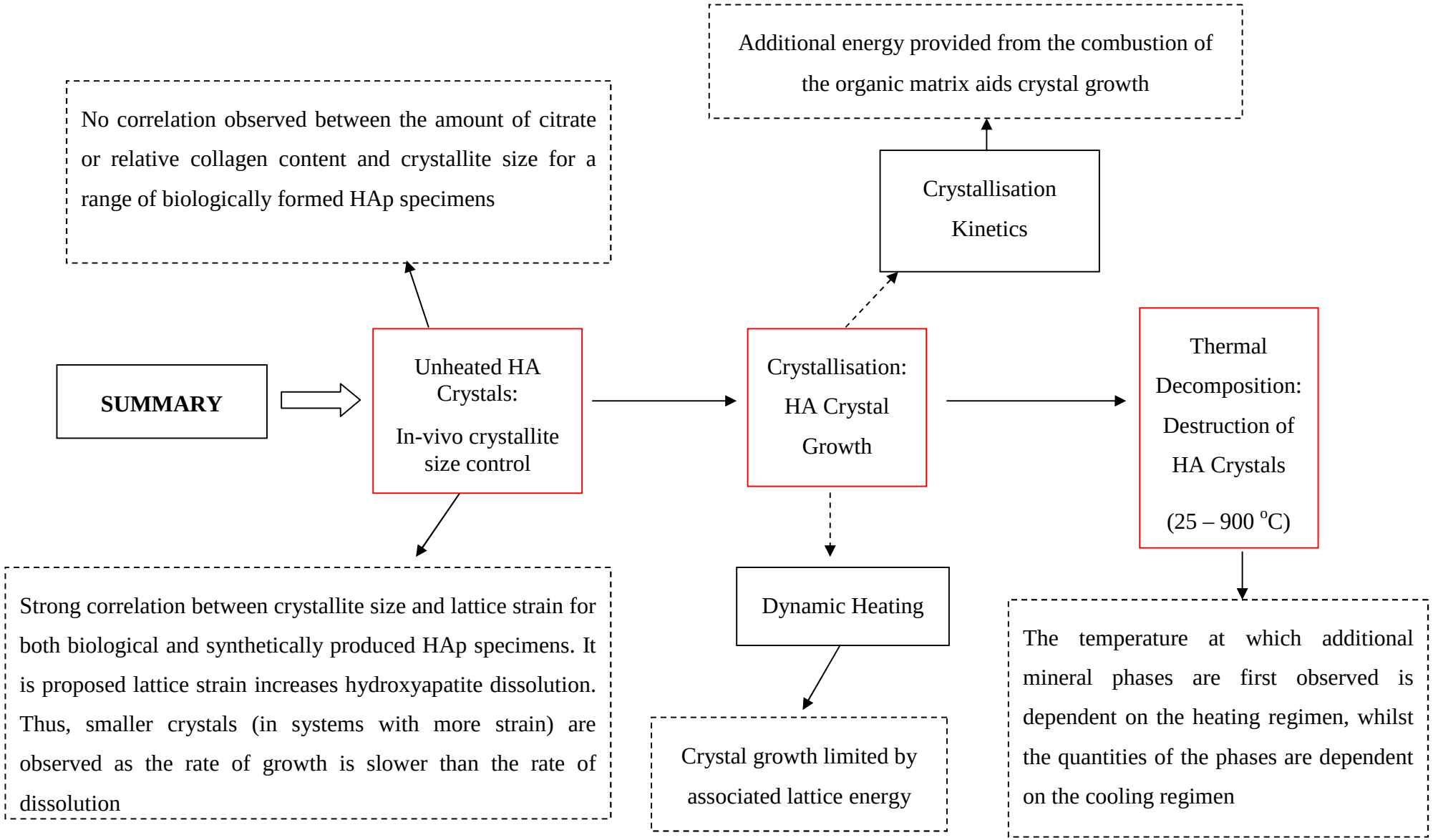

Figure 9.1 Flow diagram summarising the key findings of this research

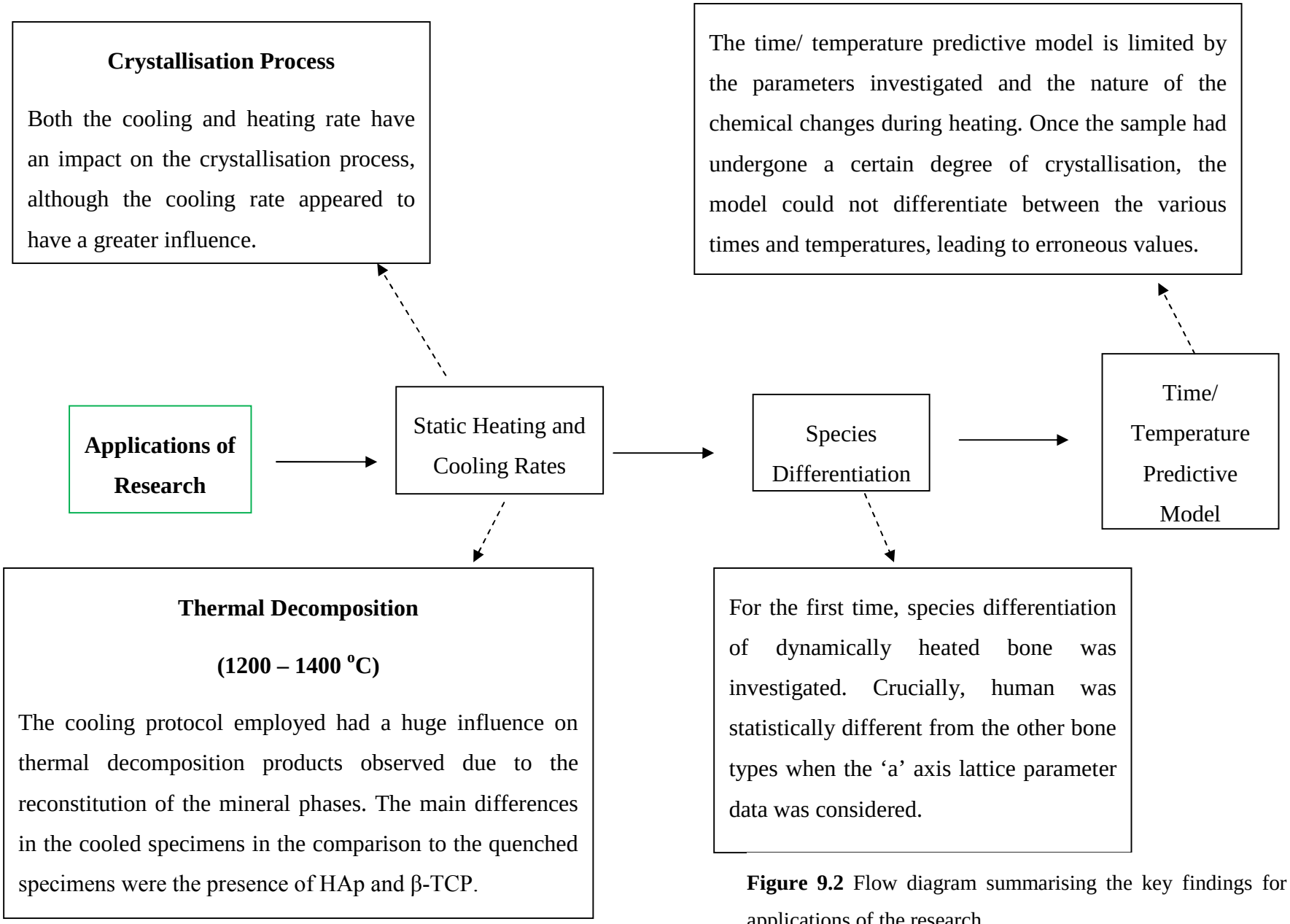

Figure 9.2 Flow diagram summarising the key findings for the applications of the research

Chapter 10: CONCLUSIONS

10.1 Research Conclusions

The main aim of the work presented in this thesis was to provide a new insight into the fundamental mechanisms and processes associated with physicochemical changes to bone during heat treatment. This was achieved by considering the growth and thermal decomposition of HAp crystals during heating. In order to fully appreciate these processes, the native state of HAp in terms of *in vivo* crystallite size was also investigated. A range of synthetic and biological HAp specimens were employed for this research. These specimens were characterised according to crystallite size, citrate and carbonate content and mineral to organic ratio. For the first time, this research has shown heat treatment can be used to produce 'anorganic' bone specimens without significantly changing the mineral microstructure. Typically chemicals are used to remove the organic matrix, although research has suggested any aqueous solution including water can chemically change the HAp structure.

Prior to heat treatment of bone, the control mechanisms associated with *in vivo* HAp crystal size were considered. For the first time, this research has provided evidence that lattice strain plays a fundamental role in *in vivo* crystal size control. It is proposed this intrinsic source of control promotes crystal dissolution. HAp structures with increased lattice strain will exhibit smaller crystals as the rate of crystal growth is slower than the dissolution rate. This contradicts studies which report extrinsic sources of control. In recent years, the role of citrate in *in vivo* HAp crystallite size control, has received a huge amount of attention in the literature. However, no correlation between the amount of citrate and *in vivo* crystallite size was observed for a range of biological HAp specimens investigated for this research. Further, mechanical restriction in the form of collagen was considered. No correlation between the relative amount of collagen and crystallite size was observed.

A number of novel approaches were employed to investigate physicochemical changes to bone during heat treatment. This research has for the first time reported the

crystallisation kinetics of bone mineral. Adopting Kolmogorov-Johnson-Mehl-Avrami (KJMA) model to investigate changes to coherence length of statically heated bone, allowed for the first time, directional dependence calculation of spontaneous nucleation rate, rate of crystallisation and activation energy associated with bone mineral crystallisation.

The activation energy was comparable for all bone types suggesting the fundamental growth mechanism is similar. The mean crystallisation activation energy for bone mineral is 183 ± 8 kJ mol^{-1}. Interestingly, a spontaneous nucleation of approximately 0.5 was calculated for all bone types, which suggests bone mineral crystallisation becomes a diffusion limited process at higher temperatures. The rate of crystallisation increased significantly with increasing temperature, although the rate values differed between bone types. This was attributed to the combustion of the organic matrix, as larger crystallisation rate values were observed for bone types with a greater organic to mineral content. It is proposed combustion of the organic matrix may potentially provide an additional source of ions as well as an intrinsic source of additional energy, which promotes crystallisation. Further analysis of red deer antler and rostrum specimens, which differ significantly in organic content, seemed to validate this hypothesis. Thus, it is proposed that rather than 'shielding' the mineral as previously reported; combustion of the organic matrix promotes crystallisation. Further analysis of statically heated bone data was applied to develop a time/ temperature predictive model. Several parameters including colour, coherence length, carbonate: phosphate ratio and lattice parameters were investigated. Unfortunately, this novel multi parameter approach is limited. After the onset of crystallisation, the material transforms rapidly and simultaneous differentiation of time and temperature becomes more difficult.

In order to fully understand physicochemical changes to bone during heat treatment, a dynamic heating approach was employed to investigate the confounding effects of cooling. For the first time, *in situ* changes to coherence length and lattice parameters were reported. The coherence length data, which is a measure of crystallite size and strain, suggests the process of crystallisation is dominated by lattice disorder and energy as well as mineral to organic content. It is proposed lattice energy contributes to the crystallisation process, whilst a larger organic content retards the growth of HAp

crystals during heating due to a lower inter-crystal connectivity. The transformation of HAp crystals from a highly anisotropic state to an equi-dimensional state was highlighted. Investigation of the lattice parameters revealed changes to the HAp structure of bone cannot solely be due to the loss of carbonate, but must also be attributed to the loss and gain of other extraneous ions. Crucially, the 'a' axis lattice parameter data for human was statistically different to the other bone types. Dynamically heating bone has also revealed calcium oxide; a thermal decomposition product of HAp, is not thermally stable during cooling.

In general, data collected from statically and dynamically heated bone is not comparable. As the heating rate is much slower, dynamically heating bone essentially produces an anorganic specimen prior to the crystallisation temperature. Unlike statically heated bone where the combustion of the organic matrix provides an additional intrinsic source of energy, the only contributing factor to the crystallisation process in dynamically heated bone is lattice energy. Due to thermal expansion, the lattice parameters did not behave in the same manner for dynamically and statically heated bone, with the exception at the temperature at which the onset of crystallisation was observed. Dynamically heating bone has revealed calcium phosphate thermal decomposition products of HAp are not thermally stable. Once cooled, the presence and quantities of additional mineral phases differ to those observed at temperature. Once formed magnesium oxide was found to be thermally stable during cooling.

Further analysis revealed that for statically heated bone, the presence and quantities of the thermal decomposition products were also dependent on the cooling regimen employed ('slow' cooled or quenched). Due to the low thermal stability of the calcium phosphate thermal decomposition products, reconstitution to HAp occurs during cooling. Conversely, quenched specimens essentially offer a 'snapshot' of thermal decomposition of HAp at temperature. Potentially, quenched specimens may offer a dynamic view of the physicochemical changes. Dependence on cooling regimen was not limited to thermal decomposition processes; the cooling regimen also had an effect on the crystallisation process. A slower cooling rate provides more energy allowing continued HAp crystal growth. This was also the case for a slower heating rate, although not as pronounced.

Finally the work presented in this thesis has challenged the use of current X-ray diffraction refinement techniques for nanocrystalline materials such as bone. Rietveld refinement, Williamson Hall and single line analysis were considered. This research has highlighted the fundamental flaws associated with these techniques when used to refine data obtained from nanocrystalline HAp specimens. Due to fixed profile functions employed during implantation of Rietveld refinement, direction dependence broadening is not accounted for, whist phenomenological Rietveld refinements (which account for direction dependence broadening) cannot provide direct quantification of crystallite size and strain. Williamson Hall plot analysis is common within bone research, however the work presented here suggests calculation of lattice strain using this technique may not be reliable. This is due to fitting errors associated the broad, overlapped 004 peak. Single line analysis, which is arguably advantageous over Williamson Hall analysis as only one peak is required, provided crystallite size and strain values. However, due to the errors associated with crystallite size values the sole use of this technique was deemed inadequate for analysis of nanocrystalline materials. Due to the fundamental flaws associated with current refinement techniques, it is proposed that crystallite size and strain should be calculated from two different refinement techniques. This provides independent values of crystallite size and strain. Direction dependence broadening due to compositional variations in the material was for the first time considered for HAp. This novel approach highlighted crystallite size and strain direction dependence broadening in HAp. Although, many studies have highlighted the compositional dependence of HAp lattice parameters during the incorporation of increasing amounts of carbonate, this research has shown compositional peak broadening cannot solely be attributed to B-type carbonate. Further extension of this work would be required in order to investigate other possible sources of compositional variations caused by other ions or even A-type carbonate substitutions.

10.2 Contribution to knowledge

By adopting several novel methods, the work presented in this thesis provides a new insight into the chemical processes and mechanisms associated with unheated and heated bone. The results provide a significant contribution to knowledge across a wide range of disciplines.

Within biomedical research, a range of synthetic HAp specimens which differ according to crystallinity, are often required for various medical applications. For this reason several studies have investigated the primary control mechanism for *in vivo* HAp crystallite size. Whilst many of these studies report an extrinsic source, the results presented in this thesis suggest an intrinsic source in the form of lattice strain. This new school of thought may potentially be considered in future studies, where the primary aim is to synthesise HAp with differing crystallinity.

High temperature processing of bone is often used for medical, biomaterial and orthopaedic applications. The crystallisation kinetics investigation presented in this thesis allows a greater understanding of mineral microstructural changes at certain temperatures and heating periods. In particular, the crystallisation activation energy value will allow a more informed decision regarding the temperature applied and the effect on bone mineral. This study is the first to demonstrate *in situ* changes to mineral microstructure during heat treatment. This has highlighted the confounding effects of cooling on bone mineral, which provides a complete model of the physicochemical changes. This fundamental research will no doubt be beneficial to future heated bone studies.

Within the field of forensic science and archaeology, the potential to determine the temperature and period of time a piece of bone has been heated would be of great value (section 1.2). This research has highlighted the potential to use a predictive model to achieve this. Although limited, with further work, this model could potentially be used to contextualise burning events which could potentially provide a vast amount of information within the field of forensic science and archaeology.

Within all these disciplines, this research has demonstrated results from different research groups may not be comparable due to differences in heating and cooling regimens employed. This may be crucial with regards to collaborations and comparisons of work.

Overall, the research has challenged some of the current views within bone mineral research including *in vivo* HAp crystallite size control mechanisms and the mineral/ organic relationship during heat treatment. The research has also validated work which is currently disputed, including whether the physicochemical modifications to bone during heat treatment can be differentiated according to species and whether heated bone results from different research groups can be compared. This provides a platform for future research and debate.

10.3 Future Recommendations

Bone has been studied within a wide range of disciplines for several decades. Along with the work presented in this thesis, further work within this area is a necessity if this complex composite material is to be fully understood in terms of formation, mineral chemistry and variations in the characteristics of bone mineral during heat treatment.

To provide a fundamental understanding of the physicochemical processes associated with heat treatment, fresh, defleshed bone specimens were utilised for this research. Such 'ideal' specimens are not necessarily comparable to 'real life' specimens as many external factors may influence bone mineral chemistry. For example, in a forensics case, if an individual has burnt a body to conceal evidence, bone chemistry may be influenced by the surrounding soft body tissue, as discussed previously in section 7.1.4. Further, archaeological bone specimens may be influenced by the process of diagenesis, where ionic exchange from the burial environment may cause changes to bone mineral chemistry. As only a few studies have taken these factors into consideration, this area of research requires further work. A greater understanding of bone chemistry in relation to bone diseases such as osteoporosis and osteoarthritis will also be beneficial within biomedical research. Currently these diseases are characterised according to bone mass

density and architecture, rather than the fundamental chemical quality of bone mineral. Further research within this area may provide better solutions for the prevention, detection and treatment of these diseases. Further, a fundamental understanding of bone chemistry with regards to paleopathology and archaeological specimens could aid in identifying diseases in archaeological skeletons. This could potentially lead to a better understanding of health and disease in past populations.

Within this thesis, the potential to construct a time/ temperature predictive model from chemical characteristics of bone heated to different times and temperatures was considered. Although the model worked in some instances, it proved difficult to differentiate bone which had been heated at high temperatures (> 700 ^{o}C) and for longer time periods (section 9.8.2). Further work could include looking at other characteristics of heated bone using techniques such as mechanical testing or the model could be applied to lower temperatures (< 500 ^{o}C). Predicting time and temperature of bone specimens heated to lower temperatures may prove beneficial within archaeological science and may for example provide further information on the cooking practices of ancient populations.

The potential to differentiate human bone from non – human specimens using dynamic heat treatment and X-ray diffraction was highlighted in this thesis. However, only a small sample set was employed and further work should be considered to investigate whether dynamically heating bone can be used to differentiate bone from a variety of species. This could potentially offer an answer as to whether species differentiation is possible using X-ray diffraction, an area of research which is currently conflicting in static heating studies. Furthermore, investigating the chemical processes of bone dynamically heated to higher temperatures than reported in this thesis could potentially validate whether quenched specimens are comparable, as proposed in section 9.7. This may also offer a new insight into the thermal stability of biological calcium phosphate mineral phases, a study which has not previously been fully investigated.

Further research into thermal decomposition of HAp is required. FTIR analysis should be considered for bone heated up to 1400 ^{o}C. This could potentially provide a greater understanding of the thermal decomposition pathway of HAp. In particular, this may provide more information on the OAP phase. Elemental analysis of bone should be

considered using thermogravimetric and mass spectrometry techniques, which could potentially provide a more in depth understanding of the role of certain elements during thermal decomposition of HAp. Thermogravimetric analysis for instance would allow investigation into the loss of surface bound and lattice incorporated water during heat treatment. Although this research has shown no significant changes to the mineral microstructure of anorganic material using XRD and FTIR, the loss of water was not considered. As with producing anorganic bone material, chemical and radiation methods are also often used to preserve and/ or sterilise bone material. For example, storage of bone in ethanol and formaldehyde and sterilisation using cobalt radiation and boiling has been reported in the literature. In most instances, the studies fail to consider the potential effects on the mineral microstructure. Thus, further work into this area of research is required and would prove beneficial within the field of biomedicine.

REFERENCES

Abrams, S., Reusse, A., Ward, A. and Lacapra, J. (2008), "A simulated arson experiment and its effect on the recovery of DNA", *Canadian Society of Forensic Science Journal,* vol. 41, no. 2, pp. 53.

Ando, J. (1958), "Tricalcium phosphate and its variation", *Bulletin of the Chemical Society of Japan,* vol. 31, no. 2, pp. 196-201.

Aoba, T. (1997), "The effect of fluoride on apatite structure and growth", *Critical Reviews in Oral Biology & Medicine,* vol. 8, no. 2, pp. 136-153.

Astala, R. and Stott, M. (2005), "First principles investigation of mineral component of bone: CO_3 substitutions in HAp", *Chemistry of Materials,* vol. 17, no. 16, pp. 4125-4133.

Atkins, P. W. and Jones, L. L (2005), *Chemical Principles: The Quest for Insight,* 3rd revised edition, New York: W.H.Freeman and Company Ltd.

Atkins, P. and Paula, D. J. (2005), "Molecular Rotations and Vibrations", *The Elements of Physical Chemistry,* 4th edition, Oxford: Oxford University Press, pp. 494.

Baig, A., Fox, J., Young, R., Wang, Z., Hsu, J., Higuchi, W., Chhettry, A., Zhuang, H. and Otsuka, M. (1999), "Relationships among carbonated apatite solubility, crystallite size, and microstrain parameters", *Calcified Tissue International,* vol. 64, no. 5, pp. 437-449.

Baig, A. A., Fox, J. L., Hsu, J., Wang, Z., Otsuka, M., Higuchi, W. I. and LeGeros, R. Z. (1996), "Effect of Carbonate Content and Crystallinity on the Metastable Equilibrium Solubility Behavior of Carbonated Apatites", *Journal of Colloid and Interface Science,* vol. 179, no. 2, pp. 608-617.

Barakat, N. A. M., Khil, M. S., Omran, A. M., Sheikh, F. A. and Kim, H. Y. (2009), "Extraction of pure natural HAp from the bovine bones bio waste by three different methods", *Journal of Materials Processing Technology,* vol. 209, no. 7, pp. 3408-3415.

Barbani, N., Rosellini, E., Cristallini, C., Guerra, G. D., Krajewski, A. and Mazzocchi, M. (2011), "HAp-collagen composites. Part I: can the decrease of the interactions between the two components be a physicochemical component of osteoporosis in aged bone?", *Journal of Materials Science: Materials in Medicine,* vol. 22, no. 3, pp. 637-646.

Barinov, S., Rau, J., Cesaro, S. N., Ďurišin, J., Fadeeva, I., Ferro, D., Medvecky, L. and Trionfetti, G. (2006), "Carbonate release from carbonated HAp in the wide temperature range", *Journal of Materials Science: Materials in Medicine,* vol. 17, no. 7, pp. 597-604.

Barralet, J., Knowles, J., Best, S. and Bonfield, W. (2002), "Thermal decomposition of synthesised carbonate hydroxyapatite", *Journal of Materials Science: Materials in Medicine,* vol. 13, no. 6, pp. 529-533.

Baxter, J. D., Biltz, R. and Pellegrino, E. (1966), "The physical state of bone carbonate. A comparative infra-red study in several mineralized tissues.", *The Yale Journal of Biology and Medicine,* vol. 38, no. 5, pp. 456.

Bazin, D., Chappard, C., Combes, C., Carpentier, X., Rouzière, S., André, G., Matzen, G., Allix, M., Thiaudière, D. and Reguer, S. (2009), "Diffraction techniques and vibrational spectroscopy opportunities to characterise bones", *Osteoporosis International,* vol. 20, no. 6, pp. 1065-1075.

BBC News (2013), *April Jones trial: Bone fragments from 'human skull'*, available at: http://www.bbc.co.uk/news/uk-wales-22596503 (Accessed 21/08/13).

Becker, J. S. and Dietze, H. (1998), "Inorganic trace analysis by mass spectrometry", *Spectrochimica Acta Part B: Atomic Spectroscopy,* vol. 53, no. 11, pp. 1475-1506.

Beckett, S. (2009), *Inter-species variation in bone mineral*. A thesis submitted in partial fulfilment of the requirements of Cranfield University for the degree of Doctor of Philosophy. Shrivenham, United Kingdom: Cranfield University,

Beckett, S., Rogers, K. D. and Clement, J. G. (2011), "Inter-Species Variation in Bone Mineral Behavior upon Heating", *Journal of Forensic Sciences,* vol. 56, no. 3, pp. 571-579.

Beniash, E., Metzler, R. A., Lam, R. S. and Gilbert, P. (2009), "Transient amorphous calcium phosphate in forming enamel", *Journal of Structural Biology,* vol. 166, no. 2, pp. 133-143.

Bennett, J. L. (1999), "Thermal Alteration of Buried Bone", *Journal of Archaeological Science,* vol. 26, no. 1, pp. 1-8.

Berketa, J. W. (2013), "Maximizing postmortem oral-facial data to assist identification following severe incineration", *Forensic Science, Medicine, and Pathology,* pp. 1-9.

Bett, J. A., Christner, L. G. and Hall, W. K. (1967), "Hydrogen held by solids. XII. Hydroxyaptite catalysts", *Journal of the American Chemical Society,* vol. 89, no. 22, pp. 5535-5541.

Bigi, A., Falini, G., Foresti, E., Ripamonti, A., Gazzano, M. and Roveri, N. (1993), "Magnesium influence on HAp crystallization", *Journal of Inorganic Biochemistry,* vol. 49, no. 1, pp. 69-78.

Bigi, A., Foresti, E., Gandolfi, M., Gazzano, M. and Roveri, N. (1995), "Inhibiting effect of zinc on hydroxylapatite crystallization", *Journal of Inorganic Biochemistry,* vol. 58, no. 1, pp. 49-58.

Biju, V., Sugathan, N., Vrinda, V. and Salini, S. (2008), "Estimation of lattice strain in nanocrystalline silver from X-ray diffraction line broadening", *Journal of Materials Science,* vol. 43, no. 4, pp. 1175-1179.

Bloebaum, R., Skedros, J., Vajda, E., Bachus, K. and Constantz, B. (1997), "Determining mineral content variations in bone using backscattered electron imaging", *Bone,* vol. 20, no. 5, pp. 485-490.

Boanini, E., Gazzano, M. and Bigi, A. (2010), "Ionic substitutions in calcium phosphates synthesized at low temperature", *Acta Biomaterialia,* vol. 6, no. 6, pp. 1882-1894.

Bohic, S., Heymann, D., Pouëzat, J. A., Gauthier, O. and Daculsi, G. (1998), "Transmission FT-IR microspectroscopy of mineral phases in calcified tissues", *Comptes Rendus de l'Académie des Sciences-Series III-Sciences de la Vie,* vol. 321, no. 10, pp. 865-876.

Bonar, L., Roufosse, A., Sabine, W., Grynpas, M. and Glimcher, M. (1983), "X-ray diffraction studies of the crystallinity of bone mineral in newly synthesized and density fractionated bone", *Calcified Tissue International,* vol. 35, no. 1, pp. 202-209.

Bonucci, E. (2000), "Basic composition and structure of bone". In: An, Y.H. and Draughn, R.A. (eds). *Mechanical testing of bone and the bone-implant interface.* Boca Raton: CRC Press, pp. 3-21.

Boskey, A. (2003), "Bone mineral crystal size", *Osteoporosis International,* vol. 14, pp. S16-S21.

Boskey, A. and Mendelsohn, R. (2005), "Infrared analysis of bone in health and disease", *Journal of Biomedical Optics,* vol. 10, no. 3, pp. 031102-1-031102-9.

Boskey, A., Gadaleta, S., Gundberg, C., Doty, S., Ducy, P. and Karsenty, G. (1998), "Fourier transform infrared microspectroscopic analysis of bones of osteocalcin-deficient mice provides insight into the function of osteocalcin", *Bone,* vol. 23, no. 3, pp. 187-196.

Boskey, A., Spevak, L., Paschalis, E., Doty, S. and McKee, M. (2002), "Osteopontin deficiency increases mineral content and mineral crystallinity in mouse bone", *Calcified Tissue International,* vol. 71, no. 2, pp. 145-154.

Brangule, A., Gross, K. A., Komarovska, L. and Viksna, A. (2014), "Exploring zinc apatites through different synthesis routes", *Key Engineering Materials,* vol. 587, pp. 171-176.

Brenner, C. H. and Weir, B. S. (2003), "Issues and strategies in the DNA identification of World Trade Center victims", *Theoretical Population Biology,* vol. 63, no. 3, pp. 173-178.

Brown, W. and Chow, L. (1976), "Chemical properties of bone mineral", *Annual Review of Materials Science,* vol. 6, no. 1, pp. 213-236.

Cabrera, W. E., Schrooten, I., De Broe, M. E. and D' Haese, P. C. (1999), "Strontium and bone", *Journal of Bone and Mineral Research,* vol. 14, no. 5, pp. 661-668.

Cáceres, I., Lozano, M. and Saladié, P. (2007), "Evidence for bronze age cannibalism in El Mirador Cave (Sierra de Atapuerca, Burgos, Spain)", *American Journal of Physical Anthropology,* vol. 133, no. 3, pp. 899-917.

Calderin, L., Stott, M. and Rubio, A. (2003), "Electronic and crystallographic structure of apatites", *Physical Review B,* vol. 67, no. 13, pp. 134106-1-134106-7.

Camacho, N., Rinnerthaler, S., Paschalis, E., Mendelsohn, R., Boskey, A. and Fratzl, P. (1999), "Complementary information on bone ultrastructure from scanning small angle X-ray scattering and Fourier-transform infrared microspectroscopy", *Bone,* vol. 25, no. 3, pp. 287-293.

Carden, A. and Morris, M. D. (2000), "Application of vibrational spectroscopy to the study of mineralized tissues (review)", *Journal of Biomedical Optics,* vol. 5, no. 3, pp. 259-268.

Castillo, R. F., Ubelaker, D. H., Acosta, J. A. L., de la Rosa, R. J. E. and Garcia, I. G. (2013), "Effect of Temperature on Bone Tissue: Histological Changes", *Journal of Forensic Sciences,* vol. 58, no. 3, pp. 578-582.

Castro, W., Hoogewerff, J., Latkoczy, C. and Almirall, J. R. (2010), "Application of laser ablation (LA-ICP-SF-MS) for the elemental analysis of bone and teeth samples for discrimination purposes", *Forensic Science International,* vol. 195, no. 1, pp. 17-27.

Cattaneo, C., DiMartino, S., Scali, S., Craig, O. E., Grandi, M. and Sokol, R. J. (1999), "Determining the human origin of fragments of burnt bone: a comparative study of histological, immunological and DNA techniques", *Forensic Science International,* vol. 102, no. 2–3, pp. 181-191.

Chang, C., Huang, J., Xia, J. and Ding, C. (1999), "Study on crystallization kinetics of plasma sprayed hydroxyapatite coating", *Ceramics International,* vol. 25, no. 5, pp. 479-483.

Chaumat, G., Müller, K. and Reiche, I. (2012), "Preliminary experiments on model artificially altered samples to consolidate degraded and wet archaeological bone with azelaic acid", *ArchéoSciences,* no. 1, pp. 213-222.

Chen, Z., Deutsch, T. G., Dinh, H. N., Domen, K., Emery, K., Forman, A. J., Gaillard, N., Garland, R., Heske, C. and Jaramillo, T. F. (2013), "UV-Vis Spectroscopy". In: Chen, Z., Dinh, H.N. and Miller, E. (eds). *Photoelectrochemical Water Splitting: Standards, Experimental Methods, and Protocols.* New York: Springer, pp. 49-62.

Chen, Z., Fu, Y., Cai, Y. and Yao, J. (2012), "Effect of amino acids on the crystal growth of hydroxyapatite", *Materials Letters,* vol. 68, pp. 361-363.

Cheng, Y., Willett, W. C., Schwartz, J., Sparrow, D., Weiss, S. and Hu, H. (1998), "Relation of nutrition to bone lead and blood lead levels in middle-aged to elderly men: The normative aging study", *American Journal of Epidemiology,* vol. 147, no. 12, pp. 1162-1174.

Cho, G., Wu, Y. and Ackerman, J. L. (2003), "Detection of hydroxyl ions in bone mineral by solid-state NMR spectroscopy", *Science,* vol. 300, no. 5622, pp. 1123-1127.

Christoffersen, J., Christoffersen, M. R., Kolthoff, N. and Bärenholdt, O. (1997), "Effects of strontium ions on growth and dissolution of hydroxyapatite and on bone mineral detection", *Bone,* vol. 20, no. 1, pp. 47-54.

Clark, B., Frost, T. and Russell, M. (eds). (1993), *UV Spectroscopy: Techniques, Instrumentation and Data Handling,* London: Chapman & Hall.

Combes, C. and Rey, C. (2010), "Amorphous calcium phosphates: synthesis, properties and uses in biomaterials", *Acta Biomaterialia,* vol. 6, no. 9, pp. 3362-3378.

Cooper, A. and Johnson, C. M. (1994), "Differential scanning calorimetry". In: Jones, C., Mulloy, B. and Thomas, A.H. (eds). *Microscopy, optical spectroscopy, and macroscopic techniques,* Totowa, New Jersey: Humana Press, pp. 125-136.

Correia, P. M. and Beattie, O. (2002), "A critical look at methods for recovering, evaluating, and interpreting cremated human remains". In: Haglund, W.D. and Sord, M.H. (eds.). *Advances in Forensic Taphonomy: Method, Theory, and Archaeological Perspectives,* Boca Raton: CRC Press, pp. 435-450.

Cuisinier, F., Steuer, P., Voegel, J., Apfelbaum, F. and Mayer, I. (1995), "Structural analyses of carbonate-containing apatite samples related to mineralized tissues", *Journal of Materials Science: Materials in Medicine,* vol. 6, no. 2, pp. 85-89.

Culity, B. (1978), *Elements of X-ray Diffraction,* 2nd ed, Reading, Massachusetts: Addison-Wesley Publishing Company, inc.

Currey, J. D. (1999), "The design of mineralised hard tissues for their mechanical functions", *Journal of Experimental Biology,* vol. 202, no. 23, pp. 3285-3294.

Currey, J. D. (2002), *Bones: structure amd mechanics,* Princeton: Princeton University Press.

Danilchenko, S., Kukharenko, O., Moseke, C., Protsenko, I. Y., Sukhodub, L. and Sulkio-Cleff, B. (2002), "Determination of the bone mineral crystallite size and lattice strain from diffraction line broadening", *Crystal Research and Technology,* vol. 37, no. 11, pp. 1234-1240.

Danilchenko, S., Pokrovskiy, V., Bogatyrov, V., Sukhodub, L. and Sulkio-Cleff, B. (2005), "Carbonate location in bone tissue mineral by X-ray diffraction and temperature-programmed desorption mass spectrometry", *Crystal Research and Technology,* vol. 40, no. 7, pp. 692-697.

De Keijser, T. H., Langford, J., Mittemeijer, E. J. and Vogels, A. (1982), "Use of the Voigt function in a single-line method for the analysis of X-ray diffraction line broadening", *Journal of Applied Crystallography,* vol. 15, no. 3, pp. 308-314.

Delgado-López, J. M., Iafisco, M., Rodríguez, I., Tampieri, A., Prat, M. and Gómez-Morales, J. (2012), "Crystallization of bioinspired citrate-functionalized nanoapatite with tailored carbonate content", *Acta Biomaterialia,* vol. 8, no. 9, pp. 3491-3499.

Devlin, J. B. and Herrmann, N. P. (2008), "Bone colour as an interpretive tool of the depositional history of archaeological cremains", *The Analysis of Burned Human Remains,* vol. 13, pp. 109-128.

Dinnebier, R. E. and Billinge, S. J. (eds). (2008), *Powder Diffraction: Theory and Practice,* Cambridge: RSC Publishing.

Dorozhkin, S. V. and Epple, M. (2002), "Biological and medical significance of calcium phosphates", *Angewandte Chemie International Edition,* vol. 41, no. 17, pp. 3130-3146.

Dowker, S. and Elliott, J. (1983), "Infrared study of trapped carbon dioxide in thermally treated apatites", *Journal of Solid State Chemistry,* vol. 47, no. 2, pp. 164-173.

Dunn, J. (2003), "Differential thermal analysis and differential scanning calorimetry", *Characterization of materials,* vol. 1, pp. 362.

Dyer, J. R. (1965), "Applications of absorption spectroscopy of organic compounds", Michigan: Prentice-Hall.

Eanes, E. and Posner, A. (1970), "A note on the crystal growth of hydroxyapatite precipitated from aqueous solutions", *Materials Research Bulletin,* vol. 5, no. 6, pp. 377-383.

Elliott, J. C., Mackie, P. and Young, R. (1973), "Monoclinic hydroxyapatite", *Science,* vol. 180, no. 4090, pp. 1055-1057.

Elliott, J. (1962), "Some observations on the crystal chemistry of carbonate-containing apatites", *Archives of Oral Biology,* vol. 7, pp. 277-282.

Elliott, J. (1969), "Recent progress in the chemistry, crystal chemistry and structure of the apatites", *Calcified Tissue Research,* vol. 3, no. 1, pp. 293-307.

Elliott, J. (1973), "The problems of the composition and structure of the mineral components of the hard tissues", *Clinical Orthopaedics and Related Research,* vol. 93, pp. 313-345.

Elliott, J., Wilson, R. and Dowker, S. (2002), "Apatite structures", *Advances in X-ray Analysis,* vol. 45, pp. 172-181.

Emadi, R., Roohani Esfahani, S. I. and Tavangarian, F. (2010), "A novel, low temperature method for the preparation of ß-TCP/HAP biphasic nanostructured ceramic scaffold from natural cancellous bone", *Materials Letters,* vol. 64, no. 8, pp. 993-996.

Emerson, W. and Fischer, E. (1962), "The infra-red absorption spectra of carbonate in calcified tissues", *Archives of Oral Biology,* vol. 7, no. 6, pp. 671-683.

Eshtiagh-Hosseini, H., Housaindokht, M. R. and Chahkandi, M. (2007), "Effects of parameters of sol–gel process on the phase evolution of sol–gel-derived hydroxyapatite", *Materials Chemistry and Physics,* vol. 106, no. 2, pp. 310-316.

Etok, S. E., Valsami-Jones, E., Wess, T. J., Hiller, J. C., Maxwell, C. A., Rogers, K. D., Manning, D. A., White, M. L., Lopez-Capel, E. and Collins, M. J. (2007), "Structural and chemical changes of thermally treated bone apatite", *Journal of Materials Science,* vol. 42, no. 23, pp. 9807-9816.

Featherstone, J. and Nelson, D. (1980), "The effect of fluoride, zinc, strontium, magnesium and iron on the crystal-structural disorder in synthetic carbonated apatites", *Australian Journal of Chemistry,* vol. 33, no. 11, pp. 2363-2368.

Feki, H. E. l., Rey, C. and Vignoles, M. (1991), "Carbonate ions in apatites: Infrared investigations in thev 4 CO3 domain", *Calcified Tissue International,* vol. 49, no. 4, pp. 269-274.

Fennessy, P. and Suttie, J. (1985), "Antler growth: nutritional and endocrine factors", *Biology of Deer Production. Royal Society of New Zealand Bulletin,* vol. 22, pp. 239-250.

Fernández-Jalvo, Y., Díez, J.C, Cáceres, I. and Rosell, J. (1999), "Human cannibalism in the Early Pleistocene of Europe (Gran Dolina, Sierra de Atapuerca, Burgos, Spain)", *Journal of Human Evolution,* vol. 37, no. 3–4, pp. 591-622.

Frank-Kamenetskaya, O., Kol'tsov, A., Kuz'mina, M., Zorina, M. and Poritskaya, L. (2011), "Ion substitutions and non-stoichiometry of carbonated apatite-(CaOH) synthesised by precipitation and hydrothermal methods", *Journal of Molecular Structure,* vol. 992, no. 1, pp. 9-18.

Fredericks, J. D. (2011), *Development of New Tools for Forensic Analysis of DNA from Compromised Bone.* A thesis submitted in partial fulfilment of the requirements of Cranfield University for the degree of Doctor of Philosophy. Shrivenham, United Kingdom: Cranfield University.

Fredericks, J. D., Bennett, P., Williams, A. and Rogers, K. D. (2012), "FTIR spectroscopy: A new diagnostic tool to aid DNA analysis from heated bone", *Forensic Science International: Genetics,* vol. 6, no. 3, pp. 375-380.

Fuierer, T. A., Lore, M., Puckett, S. A. and Nancollas, G. H. (1994), "A mineralization adsorption and mobility study of hydroxyapatite surfaces in the presence of zinc and magnesium ions", *Langmuir,* vol. 10, no. 12, pp. 4721-4725.

Ganss, B., Kim, R. H. and Sodek, J. (1999), "Bone sialoprotein", *Critical Reviews in Oral Biology & Medicine,* vol. 10, no. 1, pp. 79-98.

Garbett, N. C., Merchant, M. L., Helm, C. W., Jenson, A. B., Klein, J. B. and Chaires, J.B. (2014), "Detection of cervical cancer biomarker patterns in blood plasma and urine by differential scanning calorimetry and mass spectrometry", *PLoS One,* vol. 9, no. 1, pp. 1-12

Gashti, M. P., Hegemann, D., Stir, M. and Hulliger, J. (2014), "Thin film plasma functionalization of polyethylene terephthalate to induce bone-like hydroxyapatite nanocrystals", *Plasma Processes and Polymers,* vol. 11, no. 1, pp. 37-43.

George, A. and Veis, A. (2008), "Phosphorylated proteins and control over apatite nucleation, crystal growth, and inhibition", *Chemical Reviews,* vol. 108, no. 11, pp. 4670-4693.

George, A., Bannon, L., Sabsay, B., Dillon, J. W., Malone, J., Veis, A., Jenkins, N. A., Gilbert, D. J. and Copeland, N. G. (1996), "The carboxyl-terminal domain of phosphophoryn contains unique extended triplet amino acid repeat sequences forming ordered carboxyl-phosphate interaction ridges that may be essential in the biomineralization process", *Journal of Biological Chemistry* ,vol. 271, no. 51, pp. 32869-32873.

Gericke, A., Qin, C., Spevak, L., Fujimoto, Y., Butler, W. T., Sørensen, E. S. and Boskey, A. L. (2005), "Importance of phosphorylation for osteopontin regulation of biomineralization", *Calcified Tissue International,* vol. 77, no. 1, pp. 45-54.

Ghadimi, E., Eimar, H., Marelli, B., Nazhat, S. N., Asgharian, M., Vali, H. and Tamimi, F. (2013), "Trace elements can influence the physical properties of tooth enamel", *SpringerPlus,* vol. 2, no. 1, pp. 1-12.

Gibson, I. R. and Bonfield, W. (2002), "Novel synthesis and characterization of an AB-type carbonate-substituted hydroxyapatite", *Journal of Biomedical Materials Research,* vol. 59, no. 4, pp. 697-708.

Gibson, I., Rehman, I., Best, S. and Bonfield, W. (2000), "Characterization of the transformation from calcium-deficient apatite to β-tricalcium phosphate", *Journal of Materials Science: Materials in Medicine,* vol. 11, no. 12, pp. 799-804.

Gill, P., Moghadam, T. T. and Ranjbar, B. (2010), "Differential scanning calorimetry techniques: Applications in biology and nanoscience", *Journal of Biomolecular Techniques,* vol. 21, no. 4, pp. 167.

Goh, T., Williamson, R. and Buqué, G. (2004), *Model Answers in Additional Mathematics,* Oxford: Heinemann.

Gozzo, F., De Caro, L., Giannini, C., Guagliardi, A., Schmitt, B. and Prodi, A. (2006), "The instrumental resolution function of synchrotron radiation powder diffractometers in the presence of focusing optics", *Journal of Applied Crystallography,* vol. 39, no. 3, pp. 347-357.

Greenwald, I. (1945), "The effect of phosphate on the solubility of calcium carbonate and of bicarbonate on the solubilty of calcium and magnesium phosphates ", *Journal of Biological Chemistry,* vol. 161, no. 2, pp. 697-704.

Greenwood, C., Rogers, K., Beckett, S. and Clement, J. (2012), "Bone mineral crystallisation kinetics", *Journal of Materials Science: Materials in Medicine,* vol. 23, no. 9, pp. 2055-2060.

Greenwood, C., Rogers, K., Beckett, S. and Clement, J. (2013), "Initial observations of dynamically heated bone", *Crystal Research and Technology,* vol. 48, no. 12, pp. 1073-1082.

Grévin, G., Bailet, P., Quatrehomme, G. and Ollier, A. (1998), "Anatomical reconstruction of fragments of burned human bones: A necessary means for forensic identification", *Forensic science international,* vol. 96, no. 2–3, pp. 129-134.

Griffiths, P. R. and Pariente, G. L. (1986), "Introduction to spectral deconvolution", *Trends in Analytical Chemistry,* vol. 5, no. 8, pp. 209-215.

Gross, J. H. (2004), *Mass Spectrometry,* Germany: Springer

Gross, K. A. and Berndt, C. C. (2002), "Biomedical application of apatites", *Reviews in Mineralogy and Geochemistry,* vol. 48, no. 1, pp. 631-672.

Gross, K. A., Gross, V. and Berndt, C. C. (1998), "Thermal analysis of amorphous phases in hydroxyapatite coatings", *Journal of the American Ceramic Society,* vol. 81, no. 1, pp. 106-112.

Grupe, G. and Hummel, S. (1991), "Trace element studies on experimentally cremated bone. I. Alteration of the chemical composition at high temperatures", *Journal of Archaeological Science,* vol. 18, no. 2, pp. 177-186.

Haberko, K., Bućko, M. M., Brzezińska-Miecznik, J., Haberko, M., Mozgawa, W., Panz, T., Pyda, A. and Zarębski, J. (2006), "Natural hydroxyapatite—its behaviour during heat treatment", *Journal of the European Ceramic Society,* vol. 26, no. 4, pp. 537-542.

Handschin, R. and Stern, W. (1992), "Crystallographic lattice refinement of human bone", *Calcified Tissue International,* vol. 51, no. 2, pp. 111-120.

Handschin, R. and Stern, W. (1995), "X-ray diffraction studies on the lattice perfection of human bone apatite (Crista iliaca)", *Bone,* vol. 16, no. 4, pp. S355-S363.

Haverty, D., Tofail, S. A., Stanton, K. T. and McMonagle, J. B. (2005), "Structure and stability of hydroxyapatite: Density functional calculation and Rietveld analysis", *Physical Review B,* vol. 71, no. 9, pp. 094103.

Hedges, R. E. (2002), "Bone diagenesis: An overview of processes", *Archaeometry,* vol. 44, no. 3, pp. 319-328.

Heinrich, A., Schwark, T., Simeoni, E. and von Wurmb-Schwark, N. (2009), "Genetic identification of fire deaths", *Forensic Science International: Genetics Supplement Series,* vol. 2, no. 1, pp. 253-254.

Hempel, U., Reinstorf, A., Poppe, M., Fischer, U., Gelinsky, M., Pompe, W. and Wenzel, K. (2004), "Proliferation and differentiation of osteoblasts on biocement D modified with collagen type I and citric acid", *Journal of Biomedical Materials Research Part B: Applied Biomaterials,* vol. 71, no. 1, pp. 130-143.

Heredia, A., Colin-Garcia, M., Peña-Rico, M. A., Beltrán, L. F. A., Grácio, J., Contreras-Torres, F. F., Rodríguez-Galván, A., Bucio, L. and Basiuk, V. A. (2013), "Thermal, infrared spectroscopy and molecular modeling characterization of bone: An insight in the apatite-collagen type I interaction", *Advances in Biological Chemistry,* vol. 3, no. 2, pp. 215-223

Herrmann, N.P. and Bennett, J.L., (1999), "The differentiation of traumatic and heat-related fractures in burned bone", *Journal of Forensic Sciences,* vol. 44, no. 3, pp. 461-469.

Hiller, J., Thompson, T., Evison, M., Chamberlain, A. and Wess, T. (2003), "Bone mineral change during experimental heating: An X-ray scattering investigation", *Biomaterials,* vol. 24, no. 28, pp. 5091-5097.

Hillery, M. T. and Shuaib, I. (1999), "Temperature effects in the drilling of human and bovine bone", *Journal of Materials Processing Technology,* vol. 92–93, pp. 302-308.

Höhne, G., Hemminger, W. F. and Flammersheim, H. (2003), *Differential Scanning Calorimetry*, Germany: Springer.

Holcomb, D. and Young, R. (1980), "Thermal decomposition of human tooth enamel", *Calcified Tissue International,* vol. 31, no. 1, pp. 189-201.

Holden, J. L., Clement, J. G. and Phakey, P. P. (1995), "Age and temperature related changes to the ultrastructure and composition of human bone mineral", *Journal of Bone and Mineral Research,* vol. 10, no. 9, pp. 1400-1409.

Holden, J. L., Phakey, P. P. and Clement, J. G. (1995), "Scanning electron microscope observations of heat-treated human bone", *Forensic Science International,* vol. 74, no. 1–2, pp. 29-45.

Hu, H., Payton, M., Kornc, S., Aro, A., Sparrow, D., Weiss, S. T. and Rotnitzky, A. (1996), "Determinants of bone and blood lead levels among community-exposed middle-aged to elderly men: The normative aging study", *American Journal of Epidemiology,* vol. 144, no. 8, pp. 749-759.

Hu, Y., Liu, X. P., Ma, X., Rawal, A., Prozorov, T., Akinc, M., Mallapragada, S. K. and Schmidt-Rohr, K. (2011), "Biomimetic self-assembling copolymer-hydroxyapatite nanocomposites with the nanocrystal size controlled by citrate", *Chemistry of Materials,* vol. 23, no. 9, pp. 2481-2490.

Hu, Y., Rawal, A. and Schmidt-Rohr, K. (2010), "Strongly bound citrate stabilizes the apatite nanocrystals in bone", *Proceedings of the National Academy of Sciences,* vol. 107, no. 52, pp. 22425-22429.

Hull, A. W. (1919), "A new method of chemical analysis", *Journal of the American Chemical Society,* vol. 41, no. 8, pp. 1168-1175.

Hunter, G. K. and Goldberg, H. A. (1993), "Nucleation of hydroxyapatite by bone sialoprotein", *Proceedings of the National Academy of Sciences,* vol. 90, no. 18, pp. 8562-8565.

Ivankovic, H., Orlic, S., Tkalcec, E. and Ferrer, G. G. (2007), "Kinetics of hydroxyapatite formation from cuttlefish bones", *Proc. 10th ECerS Conf., Göller Verlag, Baden-Baden,* pp. 942-947.

Ivankovic, H., Gallego Ferrer, G., Tkalcec, E., Orlic, S. and Ivankovic, M. (2009), "Preparation of highly porous hydroxyapatite from cuttlefish bone", *Journal of Materials Science: Materials in Medicine,* vol. 20, no. 5, pp. 1039-1046.

Jackson, A. R. and Jackson, J. M. (2008), *Forensic science,* England: Pearson Education Ltd.

Jenkins, R. and Snyder, R. (1996), *Introduction to X-ray Powder Diffractometry,* New York: John Wiley & Sons.

Johnsson, M. S. and Nancollas, G. H. (1992), "The role of brushite and octacalcium phosphate in apatite formation", *Critical Reviews in Oral Biology & Medicine,* vol. 3, no. 1, pp. 61-82.

Judiciary England and Wales (2013), *Sentencing Remarks of Mr. Justice Griffith Williams: R v Mark Bridger,* available at:-

http://www.judiciary.gov.uk/Resources/JCO/Documents/Judgments/mark-bridger-sentencing-remarks-30052013.pdf (accessed 08/21).

Kaflak, A., Ślósarczyk, A. and Kolodziejski, W. (2011), "A comparative study of carbonate bands from nanocrystalline carbonated hydroxyapatites using FT-IR spectroscopy in the transmission and photoacoustic modes", *Journal of Molecular Structure,* vol. 997, no. 1, pp. 7-14.

Kang, D., Amarasiriwardena, D. and Goodman, A. H. (2004), "Application of laser ablation–inductively coupled plasma-mass spectrometry (LA–ICP–MS) to investigate trace metal spatial distributions in human tooth enamel and dentine growth layers and pulp", *Analytical and Bioanalytical Chemistry,* vol. 378, no. 6, pp. 1608-1615.

Kanzaki, N., Onuma, K., Treboux, G., Tsutsumi, S. and Ito, A. (2000), "Inhibitory effect of magnesium and zinc on crystallization kinetics of hydroxyapatite (0001) face", *The Journal of Physical Chemistry B,* vol. 104, no. 17, pp. 4189-4194.

Kaplan, B., Gönül, B., Dinçer, S., Kaya, F. N. D. and Babül, A. (2004), "Relationships between tensile strength, ascorbic acid, hydroxyproline, and zinc levels of rabbit full-thickness incision wound healing", *Surgery Today,* vol. 34, no. 9, pp. 747-751.

Karampas, I., Orkoula, M. and Kontoyannis, C. (2012), "Effect of hydrazine based deproteination protocol on bone mineral crystal structure", *Journal of Materials Science: Materials in Medicine,* vol. 23, no. 5, pp. 1139-1148.

Kasioptas, A., Geisler, T., Putnis, C. V., Perdikouri, C. and Putnis, A. (2010), "Crystal growth of apatite by replacement of an aragonite precursor", *Journal of Crystal Growth,* vol. 312, no. 16, pp. 2431-2440.

Kauppinen, J. K., Moffatt, D. J., Mantsch, H. H. and Cameron, D. G. (1981), "Fourier transforms in the computation of self-deconvoluted and first-order derivative spectra of overlapped band contours", *Analytical Chemistry,* vol. 53, no. 9, pp. 1454-1457.

Kay, M., Young, R. and Posner, A. (1964), "Crystal structure of hydroxyapatite", *Nature,* vol. 204, pp. 1050-1052.

Kim, H., Rey, C. and Glimcher, M. J. (1995), "Isolation of calcium-phosphate crystals of bone by non-aqueous methods at low temperature", *Journal of Bone and Mineral Research,* vol. 10, no. 10, pp. 1589-1601.

Koch, P. L., Tuross, N. and Fogel, M. L. (1997), "The effects of sample treatment and diagenesis on the isotopic integrity of carbonate in biogenic hydroxylapatite", *Journal of Archaeological Science,* vol. 24, no. 5, pp. 417-429.

KonicaMinolta (2014), ***Precise Colour Communication***, available at: http://www.konicaminolta.eu/en/measuring-instruments/learning-centre/colour-measurement/precise-colour-communication.html (accessed October, 2013).

Koon, H. E. C., Nicholson, R. A. and Collins, M. J. (2003), "A practical approach to the identification of low temperature heated bone using TEM", *Journal of Archaeological Science,* vol. 30, no. 11, pp. 1393-1399.

Kowal-Linka, M., Jochum, K. P. and Surmik, D. (2014), "LA-ICP-MS analysis of rare earth elements in marine reptile bones from the Middle Triassic bonebed (Upper Silesia, S Poland): Impact of long-lasting diagenesis, and factors controlling the uptake", *Chemical Geology*, vol. 363, pp. 213-228.

Lam, R. S. H. and Rogers, M. A. (2011), "Activation energy of crystallization for trihydroxystearin, stearic acid, and 12-hydroxystearic acid under nonisothermal cooling conditions", *Crystal Growth & Design,* vol. 11, no. 8, pp. 3593-3599.

Landi, E., Celotti, G., Logroscino, G. and Tampieri, A. (2003), "Carbonated hydroxyapatite as bone substitute", *Journal of the European Ceramic Society,* vol. 23, no. 15, pp. 2931-2937.

Landis, W. J., Hodgens, J. A., Arena, J., Song, M. J. and McEwen, B. F. (1996), "Structural relations between bone as determined by high microscopic tomography", *Microscopy Research and Technique,* vol. 33, pp. 192-202.

Langford, A., Dean, J., Reed, R., Holmes, D., Weyers, J. and Jones, A. (2005), *Practical Skills in Forensic Science,* Harlow, England: Prentice-Hall.

Langford, I. (1992), "The use of the pseudo-voigt function in determining microstructural properties from diffraction data by means of pattern decomposition", *NIST sp.pub,* vol. 846.

Lau, M., Lau, K., Ku, H., Cardona, F. and Lee, J. (2013), "Analysis of heat-treated bovine cortical bone by thermal gravimetric and nanoindentation", *Composites Part B: Engineering,* vol. 55, pp. 447-452.

Laye, P. (2002), "Differential thermal analysis and differential scanning calorimetry". In: Haines, P.J. (ed). *Principles of Thermal Analysis and Calorimetry,* pp. 55-93. Cornwall: RSC Publishing.

LeGeros, R. Z., Bonel, G. and Legros, R. (1978), "Types of "H_2O" in human enamel and in precipitated apatites", *Calcified Tissue Research,* vol. 26, no. 1, pp. 111-118.

LeGeros, R. Z., LeGeros, J. P., Trautz, O. R. and Shirra, W. P. (1971), "Conversion of monetite, $CaHPO_4$, to apatites: effect of carbonate on the crystallinity and the morphology of the apatite crystallites", *Advances in X-ray Analysis,* vol. 14, pp. 57-66.

LeGeros, R. Z., Trautz, O. R., Legeros, J. P., Klein, E. and Shirra, W. P. (1967), "Apatite crystallites: effects of carbonate on morphology", *Science,* vol. 155, no. 3768, pp. 1409-1411.

LeGeros, R. Z. (1965), "Effect of carbonate on the lattice parameters of apatite", *Nature*, vol. 206, pp. 403-404.

LeGeros, R. Z. (1981), "Apatites in biological systems", *Progress in Crystal Growth and Characterization,* vol. 4, no. 1, pp. 1-45.

LeGeros, R., Trautz, O., Klein, E. and LeGeros, J. (1969), "Two types of carbonate substitution in the apatite structure", *Experientia,* vol. 25, no. 1, pp. 5-7.

LeGeros, R. and Tung, M. (1983), "Chemical stability of carbonate-and fluoride-containing apatites", *Caries Research,* vol. 17, no. 5, pp. 419-429.

Leineweber, A. and Mittemeijer, E. (2003), "Anisotropic strain-like line broadening due to composition variations", *Advances in X-ray Analysis,* vol. 46, pp. 43-49.

Li, Z. Y., Lam, W. M., Yang, C., Xu, B., Ni, G. X., Abbah, S. A., Cheung, K. M. C., Luk, K. D. K. and Lu, W. W. (2007), "Chemical composition, crystal size and lattice structural changes after incorporation of strontium into biomimetic apatite", *Biomaterials,* vol. 28, no. 7, pp. 1452-1460.

Liao, C., Lin, F., Chen, K. and Sun, J. (1999), "Thermal decomposition and reconstitution of hydroxyapatite in air atmosphere", *Biomaterials,* vol. 20, no. 19, pp. 1807-1813.

Lin, F., Chun-Jen, L., Ko-Shao, C. and Jui-Sheng, S. (2000), "Thermal reconstruction behavior of the quenched hydroxyapatite powder during reheating in air", *Materials Science and Engineering: C,* vol. 13, no. 1, pp. 97-104.

Lin, X., Li, X., Fan, H., Wen, X., Lu, J. and Zhang, X. (2004), "In situ synthesis of bone-like apatite/collagen nano-composite at low temperature", *Materials Letters,* vol. 58, no. 27, pp. 3569-3572.

Liu, Q., Huang, S., Matinlinna, J. P., Chen, Z. and Pan, H. (2013), "Insight into biological apatite: physiochemical properties and preparation approaches", *BioMed Research International,* pp. 1-13.

Locardi, B., Pazzaglia, U., Gabbi, C. and Profilo, B. (1993), "Thermal behaviour of hydroxyapatite intended for medical applications", *Biomaterials,* vol. 14, no. 6, pp. 437-441.

Loong, C., Rey, C., Kuhn, L., Combes, C., Wu, Y., Chen, S. and Glimcher, M. (2000), "Evidence of hydroxyl-ion deficiency in bone apatites: An inelastic neutron-scattering study", *Bone,* vol. 26, no. 6, pp. 599-602.

López-Macipe, A., Gómez-Morales, J. and Rodríguez-Clemente, R. (1998), "Nanosized hydroxyapatite precipitation from homogeneous calcium/citrate/phosphate solutions using microwave and conventional heating", *Advanced Materials,* vol. 10, no. 1, pp. 49-53.

Lozano, L., Pena-Rico, M., Heredia, A., Ocotlan-Flores, J., Gomez-Cortes, A., Velazquez, R., Belio, I. and Bucio, L. (2003), "Thermal analysis study of human bone", *Journal of Materials Science,* vol. 38, no. 23, pp. 4777-4782.

Lutterotti, L. and Scardi, P. (1990), "Simultaneous structure and size-strain refinement by the Rietveld method", *Journal of Applied Crystallography,* vol. 23, no. 4, pp. 246-252.

Ma, G. and Liu, X. Y. (2009), "Hydroxyapatite: Hexagonal or monoclinic?", *Crystal Growth and Design,* vol. 9, no. 7, pp. 2991-2994.

Maffezzoli, A., Kenny, J. and Torre, L. (1995), "On the physical dimensions of the Avrami constant", *Thermochimica Acta,* vol. 269, pp. 185-190.

Mahamid, J., Sharir, A., Addadi, L. and Weiner, S. (2008), "Amorphous calcium phosphate is a major component of the forming fin bones of zebrafish: Indications for an amorphous precursor phase", *Proceedings of the National Academy of Sciences,* vol. 105, no. 35, pp. 12748-12753.

Malacara, D. (2002), *Color Vision and Colorimetry: Theory and Applications,* Bellingham, WA : SPIE press.

Mann, S., Heywood, B., Rajam, S. and Birchall, J. (1989), "Interfacial control of nucleation of calcium carbonate under organized stearic acid monolayers", *Proceedings of the Royal Society of London A. Mathematical, Physical and Engineering Sciences,* vol. 423, no. 1865, pp. 457-471.

Mantsch, H. H., Moffatt, D. J. and Casal, H. L. (1988), "Fourier transform methods for spectral resolution enhancement", *Journal of Molecular Structure,* vol. 173, pp. 285-298.

Marinkovic, B., de Avillez, R., Saavedra, A. and Assunção, F. C. R. (2001), "Comparison between the Warren-Averbach method and alternative methods for X-ray diffraction microstructure analysis of polycrystalline specimens", *Materials Research,* vol. 4, no. 2, pp. 71-76.

Marino, A. A. and Becker, R. (1967), "Evidence for direct physical bonding between the collagen fibres and apatite crystals in bone", *Nature* vol. 213, pp. 697-698.

Martin, D. (2010), "Application of Kolmogorov–Johnson–Mehl–Avrami equations to non-isothermal conditions", *Computational Materials Science,* vol. 47, no. 3, pp. 796-800.

Martin, R. B. and Burr, D. B. (1989), *Structure, Function, and Adaptation of Compact Bone,* New York: Raven Press.

Martins, M. A., Santos, C., Almeida, M. M. and Costa, M. E. V. (2008), "Hydroxyapatite micro- and nanoparticles: Nucleation and growth mechanisms in the presence of citrate species", *Journal of Colloid and Interface Science,* vol. 318, no. 2, pp. 210-216.

Mavropoulos, E., Rossi, A. M., Costa, A. M., Perez, C. A. C., Moreira, J. C. and Saldanha, M. (2002), "Studies on the mechanisms of lead immobilization by hydroxyapatite", *Environmental Science & Technology,* vol. 36, no. 7, pp. 1625-1629.

Mayer, I. and Featherstone, J. D. B. (2000), "Dissolution studies of Zn-containing carbonated hydroxyapatites", *Journal of Crystal Growth,* vol. 219, no. 1–2, pp. 98-101.

Mayer, I., Schlam, R. and Featherstone, J. D. B. (1997), "Magnesium-containing carbonate apatites", *Journal of Inorganic Biochemistry,* vol. 66, no. 1, pp. 1-6.

McClain, P., Wiley, E., Beecher, G., Anthony, W. and Hsu, J. (1973), "Influence of zinc deficiency on synthesis and cross-linking of rat skin collagen", *Biochimica et Biophysica Acta-General Subjects,* vol. 304, no. 2, pp. 457-465.

McCusker, L., Von Dreele, R., Cox, D., Louer, D. and Scardi, P. (1999), "Rietveld refinement guidelines", *Journal of Applied Crystallography,* vol. 32, no. 1, pp. 36-50.

Megazyme (2013), *Citric Acid (Citrate) Assay Procedure,* available at: http://secure.megazyme.com/files/BOOKLET/KCITR_1212_DATA.pdf (accessed May 2013).

Mendenhall, W., Beaver, R. J. and Beaver, B. M. (2012), *Introduction to Probability and Statistics,* 14th Edition, Boston: Cengage Learning

Meneghini, C., Dalconi, M. C., Nuzzo, S., Mobilio, S. and Wenk, R. H. (2003), "Rietveld refinement on X-ray diffraction patterns of bioapatite in human fetal bones", *Biophysical Journal,* vol. 84, no. 3, pp. 2021-2029.

Meyer, H. J. (2003), "The Kaprun cable car fire disaster—aspects of forensic organisation following a mass fatality with 155 victims", *Forensic Science International,* vol. 138, no. 1–3, pp. 1-7.

Miles, C. A., Burjanadze, T. V. and Bailey, A. J. (1995), "The kinetics of the thermal denaturation of collagen in unrestrained rat tail tendon determined by differential scanning calorimetry", *Journal of Molecular Biology,* vol. 245, no. 4, pp. 437-446.

Milev, A., Kannangara, G. and Ben-Nissan, B. (2003), "Morphological stability of hydroxyapatite precursor", *Materials Letters,* vol. 57, no. 13, pp. 1960-1965.

Miller, L. M., Vairavamurthy, V., Chance, M. R., Mendelsohn, R., Paschalis, E. P., Betts, F. and Boskey, A. L. (2001), "In situ analysis of mineral content and crystallinity in bone using infrared micro-spectroscopy of the $v_4PO_4^{3-}$ vibration", *Biochimica et Biophysica Acta-General Subjects,* vol. 1527, no.1, pp. 11-19.

Mkukuma, L. D., Skakle, J. M. S., Gibson, I. R., Imrie, C. T., Aspden, R. M. and Hukins, D. W. L. (2004), "Effect of the proportion of organic material in bone on thermal decomposition of bone mineral: An investigation of a variety of bones from different species using thermogravimetric analysis coupled to mass spectrometry, high-temperature X-ray diffraction, and fourier transform infrared spectroscopy", *Calcified Tissue International,* vol. 75, no. 4, pp. 321-328.

Moore, J., Heywood, B. and Mann, S. (1991), "The effect of monosaccharides on the nucleation and growth of hydroxyapatite", *Journal of Inorganic Biochemistry,* vol. 43, no. 2, pp. 670.

Munro, L. E., Longstaffe, F. J. and White, C. D. (2007), "Burning and boiling of modern deer bone: Effects on crystallinity and oxygen isotope composition of bioapatite phosphate", *Palaeogeography, Palaeoclimatology, Palaeoecology,* vol. 249, no. 1–2, pp. 90-102.

Munro, L. E., Longstaffe, F. J. and White, C. D. (2008), "Effects of heating on the carbon and oxygen-isotope compositions of structural carbonate in bioapatite from modern deer bone", *Palaeogeography, Palaeoclimatology, Palaeoecology*, vol. 266, no. 3–4, pp. 142-150.

Murugan, R., Rao, K. P. and Kumar, T. S. S. (2003), "Heat-deproteinated xenogeneic bone from slaughterhouse waste: Physico-chemical properties", *Bulletin of Materials Science,* vol. 26, no. 5, pp. 523-528.

Muyonga, J., Cole, C. and Duodu, K. (2004), "Fourier transform infrared (FTIR) spectroscopic study of acid soluble collagen and gelatin from skins and bones of young and adult Nile perch (*Lates niloticus*)", *Food Chemistry,* vol. 86, no. 3, pp. 325-332.

Nagata, T., Bellows, C. G., Kasugai, S., Butler, W. T. and Sodek, J. (1991), "Biosynthesis of bone proteins [SPP-1 (secreted phosphoprotein-1, osteopontin), BSP (bone sialoprotein) and SPARC (osteonectin)] in association with mineralized-tissue formation by fetal-rat calvarial cells in culture", *Biochemical Journal,* vol. 274, pp. 513-520.

Najafia, H., Nematia, Z. A., Sadeghianb, Z. and Sohrabia, N. (2008), "Crystallisation kinetics of hydroxyapatite nano-films on stainless steel through a sol–gel process", *Iranian Journal of Pharmaceutical Sciences,* vol. 4, pp. 135-140.

Nelson, D. and Featherstone, J. (1981), "Preparation, analysis, and characterization of carbonated apatites", *Calcified Tissue International,* vol. 34, pp. S69-S81.

Nelson, K. and Melton, T. (2007), "Forensic mitochondrial DNA analysis of 116 casework skeletal samples", *Journal of Forensic Sciences,* vol. 52, no. 3, pp. 557-561.

Neuman, W. and Weikel, J. (1955), "Recrystallization in bone mineral", *Annals of the New York Academy of Sciences,* vol. 60, no. 5, pp. 685-695.

Nielsen-Marsh, C. M., Hedges, R. E., Mann, T. and Collins, M. J. (2000), "A preliminary investigation of the application of differential scanning calorimetry to the study of collagen degradation in archaeological bone", *Thermochimica Acta,* vol. 365, no. 1, pp. 129-139.

Nudelman, F., Pieterse, K., George, A., Bomans, P. H., Friedrich, H., Brylka, L. J., Hilbers, P. A. and Sommerdijk, N. A. (2010), "The role of collagen in bone apatite formation in the presence of hydroxyapatite nucleation inhibitors", *Nature Materials,* vol. 9, no. 12, pp. 1004-1009.

O'Donnell, M. D., Fredholm, Y., de Rouffignac, A. and Hill, R. G. (2008), "Structural analysis of a series of strontium-substituted apatites", *Acta Biomaterialia,* vol. 4, no. 5, pp. 1455-1464.

Ohodnicki, P. R. (2008), *Crystallization and magnetic field processing of cobalt-rich cobalt, iron-based nanocrystalline and amorphous soft magnetic alloys.* A thesis submitted for the degree of Doctor of Philosophy, Accessed through ProQuest.

Ohta, N. and Robertson, A. (2006), *Colorimetry: Fundamentals and Applications,* Padstow, Cornwall: John Wiley & Sons.

Olaisen, B., Stenersen, M. and Mevåg, B. (1997), "Identification by DNA analysis of the victims of the August 1996 Spitsbergen civil aircraft disaster", *Nature Genetics,* vol. 15, no. 4, pp. 402-405.

Olszta, M. J., Cheng, X., Jee, S. S., Kumar, R., Kim, Y., Kaufman, M. J., Douglas, E. P. and Gower, L. B. (2007), "Bone structure and formation: A new perspective", *Materials Science and Engineering: R: Reports,* vol. 58, no. 3–5, pp. 77-116.

Ooi, C., Hamdi, M. and Ramesh, S. (2007), "Properties of hydroxyapatite produced by annealing of bovine bone", *Ceramics International,* vol. 33, no. 7, pp. 1171-1177.

Palmer, L. C., Newcomb, C. J., Kaltz, S. R., Spoerke, E. D. and Stupp, S. I. (2008), "Biomimetic systems for hydroxyapatite mineralization inspired by bone and enamel", *Chemical Reviews,* vol. 108, no. 11, pp. 4754-4783.

Pan, H. and Darvell, B. W. (2010), "Effect of carbonate on hydroxyapatite solubility", *Crystal Growth & Design,* vol. 10, no. 2, pp. 845-850.

Panda, R., Hsieh, M., Chung, R. and Chin, T. (2003), "FTIR, XRD, SEM and solid state NMR investigations of carbonate-containing hydroxyapatite nano-particles synthesized by hydroxide-gel technique", *Journal of Physics and Chemistry of Solids,* vol. 64, no. 2, pp. 193-199.

Parker, S. (2007), *The Human Body,* London: DK Publishing.

Paschalis, E., Betts, F., DiCarlo, E., Mendelsohn, R. and Boskey, A. (1997), "FTIR microspectroscopic analysis of normal human cortical and trabecular bone", *Calcified Tissue International,* vol. 61, no. 6, pp. 480-486.

Paschalis, E., DiCarlo, E., Betts, F., Sherman, P., Mendelsohn, R. and Boskey, A. (1996), "FTIR microspectroscopic analysis of human osteonal bone", *Calcified Tissue International,* vol. 59, no. 6, pp. 480-487.

Paschalis, E., Verdelis, K., Doty, S., Boskey, A., Mendelsohn, R. and Yamauchi, M. (2001), "Spectroscopic characterization of collagen cross-links in bone", *Journal of Bone and Mineral Research,* vol. 16, no. 10, pp. 1821-1828.

Pasteris, J. D., Wopenka, B., Freeman, J. J., Rogers, K., Valsami-Jones, E., van der Houwen, J. A. M., and Silva, M. J. (2004), "Lack of OH in nanocrystalline apatite as a function of degree of atomic order: Implications for bone and biomaterials", *Biomaterials,* vol. 25, no. 2, pp. 229-238.

Pasteris, J. D., Yoder, C. H., Rogers, K. D., Sternlieb, M. and Mann, S. (2007), "Bone apatite: The secret is in the carbonate", *GSA Denver Annual Meeting,* Paper No. 109-5

Penel, G., Leroy, G., Rey, C. and Bres, E. (1998), "MicroRaman spectral study of the PO_4 and CO_3 vibrational modes in synthetic and biological apatites", *Calcified Tissue International,* vol. 63, no. 6, pp. 475-481.

Person, A., Bocherens, H., Mariotti, A. and Renard, M. (1996), "Diagenetic evolution and experimental heating of bone phosphate", *Palaeogeography, Palaeoclimatology, Palaeoecology,* vol. 126, no. 1, pp. 135-149.

Pestle, W. J., Ahmad, F., Vesper, B. J., Cordell, G. A. and Colvard, M. D. (2014), "Ancient bone collagen assessment by hand-held vibrational spectroscopy", *Journal of Archaeological Science,* vol. 42, pp. 381-389.

Peters, F., Schwarz, K. and Epple, M. (2000), "The structure of bone studied with synchrotron X-ray diffraction, X-ray absorption spectroscopy and thermal analysis", *Thermochimica Acta,* vol. 361, no. 1, pp. 131-138.

Pienkowski, D., Doers, T. M., Monier-Faugere, M.-C., Geng, Z., Camacho, N. P., Boskey, A. L. and Malluche, H. H. (1997), "Calcitonin alters bone quality in beagle dogs", *Journal of Bone Mineral Research,* vol. 12, no. 11, pp. 1936–1943

Piga, G., Guirguis, M., Bartoloni, P., Malgosa, A. and Enzo, S. (2010), "A funerary rite study of the Phoenician–Punic necropolis of Mount Sirai (Sardinia, Italy)", *International Journal of Osteoarchaeology,* vol. 20, no. 2, pp. 144-157.

Piga, G., Malgosa, A., Thompson, T. and Enzo, S. (2008), "A new calibration of the XRD technique for the study of archaeological burned human remains", *Journal of Archaeological Science,* vol. 35, no. 8, pp. 2171-2178.

Piga, G., Solinas, G., Thompson, T. J. U., Brunetti, A., Malgosa, A. and Enzo, S. (2013), "Is X-ray diffraction able to distinguish between animal and human bones?", *Journal of Archaeological Science,* vol. 40, no. 1, pp. 778-785.

Piga, G., Thompson, T. J. U., Malgosa, A. and Enzo, S. (2009), "The potential of X-ray diffraction in the analysis of burned remains from forensic contexts", *Journal of Forensic Sciences,* vol. 54, no. 3, pp. 534-539.

Pijoan, C., Mansilla, J. and Leboreiro, I. (2007), "Thermal alterations in archaeological bones", *Archaeometry,* vol. 49, no. 4, pp. 713-727.

Posner, A., Perloff, A. and Diorio, A. (1958), "Refinement of the hydroxyapatite structure", *Acta Crystallographica,* vol. 11, no. 4, pp. 308-309.

Prahlow, J. (2010), *Forensic Pathology for Police, Death Investigators, and Forensic Scientists,* New York: Humana Press.

Pramanik, S., Hanif, A. S. M., Pingguan-Murphy, B. and Osman, N. A. A. (2012), "Morphological change of heat treated bovine bone: A comparative study", *Materials,* vol. 6, no. 1, pp. 65-75.

Pratisto, H., Frenz, M., Ith, M., Romano, V., Felix, D., Grossenbacher, R., Altermatt, H. J. and Weber, H. P. (1996), "Temperature and pressure effects during erbium laser stapedotomy", *Lasers in Surgery and Medicine,* vol. 18, no. 1, pp. 100-108.

Pretty, I. A. (2007), "Forensic dentistry: 1. Identification of human remains", *Dental Update,* vol. 34, no. 10, pp. 621-2, 624-6, 629-30 passim.

Prohaska, T., Latkoczy, C., Schultheis, G., Teschler-Nicola, M. and Stingeder, G. (2002), "Investigation of Sr isotope ratios in prehistoric human bones and teeth using laser ablation ICP-MS and ICP-MS after Rb/Sr separation", *Journal of Analytical Atomic Spectrometry,* vol. 17, no. 8, pp. 887-891.

Rainio, J., Hedman, M., Karkola, K., Lalu, K., Peltola, P., Ranta, H., Sajantila, A., Söderholm, N. and Penttilä, A. (2001), "Forensic osteological investigations in Kosovo", *Forensic Science International,* vol. 121, no. 3, pp. 166-173.

Ravaglioli, A., Krajewski, A., Celotti, G. C., Piancastelli, A., Bacchini, B., Montanari, L., Zama, G. and Piombi, L. (1996), "Mineral evolution of bone", *Biomaterials,* vol. 17, no. 6, pp. 617-622.

Reiche, I. and Chadefaux, C. (2009), "Archaeological bone from macro-to nanoscale: Heat-induced modifications at low temperatures", *Journal of Nano Research,* vol. 8, pp. 157-172.

Resano, M., García-Ruiz, E. and Vanhaecke, F. (2010), "Laser ablation-inductively coupled plasma mass spectrometry in archaeometric research", *Mass Spectrometry Reviews,* vol. 29, no. 1, pp. 55-78.

Rey, C., Renugopalakrishman, V., Collins, B. and Glimcher, M. J. (1991), "Fourier transform infrared spectroscopic study of the carbonate ions in bone mineral during aging", *Calcified Tissue International,* vol. 49, no. 4, pp. 251-258.

Rey, C., Collins, B., Goehl, T., Dickson, I. and Glimcher, M. (1989), "The carbonate environment in bone mineral: A resolution-enhanced Fourier transform infrared spectroscopy study", *Calcified Tissue International,* vol. 45, no. 3, pp. 157-164.

Rey, C., Miquel, J., Facchini, L., Legrand, A. and Glimcher, M. (1995), "Hydroxyl groups in bone mineral", *Bone,* vol. 16, no. 5, pp. 583-586.

Rey, C., Combes, C., Drouet, C., Sfihi, H. and Barroug, A. (2007), "Physico-chemical properties of nanocrystalline apatites: implications for biominerals and biomaterials", *Materials Science and Engineering: C,* vol. 27, no. 2, pp. 198-205.

Rey, C., Shimizu, M., Collins, B. and Glimcher, M. J. (1990), "Resolution-enhanced fourier transform infrared spectroscopy study of the environment of phosphate ions in the early deposits of a solid phase of calcium-phosphate in bone and enamel, and their evolution with age. I: Investigations in the v_4PO_4 domain", *Calcified Tissue International,* vol. 46, no. 6, pp. 384-394.

Rey, C., Combes, C., Drouet, C. and Glimcher, M. J. (2009), "Bone mineral: Update on chemical composition and structure", *Osteoporosis International,* vol. 20, no. 6, pp. 1013-1021.

Reyes-Gasga, J., Garcia-Garcia, R., Arellano-Jimenez, M., Sanchez-Pastenes, E., Tiznado-Orozco, G., Gil-Chavarria, I. and Gómez-Gasga, G. (2008), "Structural and thermal behaviour of human tooth and three synthetic hydroxyapatites from 20 to 600 ^{o}C", *Journal of Physics D: Applied Physics,* vol. 41, no. 22, pp. 1-11.

Reyes-Gasga, J., Martínez-Piñeiro, E. and Bres, E. (2012), "Crystallographic structure of human tooth enamel by electron microscopy and x-ray diffraction: hexagonal or monoclinic?", *Journal of Microscopy*, vol. 248, no. 1, pp. 102-109.

Rhee, S. and Tanaka, J. (1999), "Effect of citric acid on the nucleation of hydroxyapatite in a simulated body fluid", *Biomaterials*, vol. 20, no. 22, pp. 2155-2160.

Rho, J., Kuhn-Spearing, L. and Zioupos, P. (1998), "Mechanical properties and the hierarchical structure of bone", *Medical Engineering & Physics*, vol. 20, no. 2, pp. 92-102.

Rios, P. R., Siciliano Jr, F., Sandim, H. R. Z., Plaut, R. L. and Padilha, A. F. (2005), "Nucleation and growth during recrystallization", *Materials Research*, vol. 8, no. 3, pp. 225-238.

Roach, H. (1994), "Why does bone matrix contain non-collagenous proteins? The possible roles of osteocalcin, osteonectin, osteopontin and bone sialoprotein in bone mineralisation and resorption", *Cell Biology International*, vol. 18, pp. 617-628.

Roberts, S. J., Smith, C. I., Millard, A. and Collins, M. J. (2002), "The taphonomy of cooked bone: characterizing boiling and its physico–chemical effects", *Archaeometry*, vol. 44, no. 3, pp. 485-494.

Rodríguez-Lorenzo, L. M., Hart, J. N. and Gross, K. A. (2003), "Influence of fluorine in the synthesis of apatites. Synthesis of solid solutions of hydroxy-fluorapatite", *Biomaterials*, vol. 24, no. 21, pp. 3777-3785.

Rogers, K. and Zioupos, P. (1999), "The bone tissue of the rostrum of a Mesoplodon densirostris whale: A mammalian biomineral demonstrating extreme texture", *Journal of Materials Science Letters*, vol. 18, no. 8, pp. 651-654.

Rogers, K. D. and Daniels, P. (2002), "An X-ray diffraction study of the effects of heat treatment on bone mineral microstructure", *Biomaterials*, vol. 23, no. 12, pp. 2577-2585.

Rogers, K., Beckett, S., Kuhn, S., Chamberlain, A. and Clement, J. (2010), "Contrasting the crystallinity indicators of heated and diagenetically altered bone mineral", *Palaeogeography, Palaeoclimatology, Palaeoecology*, vol. 296, no. 1–2, pp. 125-129.

Rolf, H. J. and Enderle, A. (1999), "Hard fallow deer antler: A living bone till antler casting?", *The Anatomical Record*, vol. 255, no. 1, pp. 69-77.

Romberg, R. W., Werness, P. G., Riggs, B. L. and Mann, K. G. (1986), "Inhibition of hydroxyapatite - Crystal growth by bone-specific and other calcium-binding proteins", *Biochemistry*, vol. 25, no. 5, pp. 1176-1180.

Rousseau, J. J. (1998), *Basic crystallography,* New York: John Wiley & Sons, Ltd.

Schanda, J. (ed) (2007), *Colorimetry: Understanding the CIE system,* New Jersey: John Wiley & Sons, Ltd.

Schiegl, S., Goldberg, P., Pfretzschner, H. and Conard, N. J. (2003), "Paleolithic burnt bone horizons from the Swabian Jura: Distinguishing between in situ fireplaces and dumping areas", *Geoarchaeology,* vol. 18, no. 5, pp. 541-565.

Schurr, M. R., Hayes, R. G. and Cook, D. C. (2011), "Thermally induced changes in the stable carbon and nitrogen isotope ratios of charred bones", In: Schmidt, C.W. and Symes, S.A. (eds.) *The Analysis of Burned Human Remains,* pp. 95-108.

Schwark, T., Heinrich, A., Preuße-Prange, A. and von Wurmb-Schwark, N. (2011), "Reliable genetic identification of burnt human remains", *Forensic Science International: Genetics,* vol. 5, no. 5, pp. 393-399.

Senn, D. R. and Weems, R. A. (eds.) (2013), *Manual of Forensic Odontology,* 5th Edition, Boca Raton: CRC Press.

Shahack-Gross, R., Bar-Yosef, O. and Weiner, S. (1997), "Black-coloured bones in Hayonim Cave, Israel: Differentiating between burning and oxide staining", *Journal of Archaeological Science,* vol. 24, no. 5, pp. 439-446.

Shea, J. E. and Miller, S. C. (2005), "Skeletal function and structure: Implications for tissue-targeted therapeutics", *Advanced Drug Delivery Reviews,* vol. 57, no. 7, pp. 945-957.

Shellis, R. P., Lee, A. R. and Wilson, R. M. (1999), "Observations on the apparent solubility of carbonate–apatites", *Journal of Colloid and Interface Science,* vol. 218, no. 2, pp. 351-358.

Sheskin, D. J. (2003), *Handbook of Parametric and Nonparametric Statistical Procedures,* 3rd Edition, Boca Raton: CRC Press.

Shi, J., Arndt, K., Ming, Z. and Ulrich, B. (2005), "Thermally-induced structural modification of dental enamel apatite: Decomposition and transformation of carbonate groups", *European Journal of Mineralogy,* vol. 17, no. 5, pp. 769-775.

Shipman, P., Foster, G. and Schoeninger, M. (1984), "Burnt bones and teeth: An experimental study of color, morphology, crystal structure and shrinkage", *Journal of Archaeological Science,* vol. 11, no. 4, pp. 307-325.

Ślósarczyk, A., Szymura-Oleksiak, J. and Mycek, B. (2000), "The kinetics of pentoxifylline release from drug-loaded hydroxyaptite implants", *Biomaterials,* vol. 21, no. 12, pp. 1215-1221.

Smith, B. C. (2003), *Quantitative Spectroscopy: Theory and Practice: Theory and Practice,* Bodmin, Cornwall: Academic Press.

Smith, B. C. (2011), *Fundamentals of Fourier Transform Infrared Spectroscopy,* 2nd Edition, Boca Raton: CRC Press.

Smith, E. L., Hill, R. L., Lehman, I. R., Lefkowitz, R. J., Handler, P. and White, A. (1983), *Principles of Biochemistry: Mammalian Biochemistry,* New York: McGraw-Hill.

Solari, A., Olivera, D., Gordillo, I., Bosch, P., Fetter, G., Lara, V. H. and Novelo, O. (2013), "Cooked bones? Method and practice for identifying bones treated at low temperature", *International Journal of Osteoarchaeology,* doi: 10.1002/oa.2311.

Spevak, L., Flach, C. R., Hunter, T., Mendelsohn, R. and Boskey, A. (2013), "Fourier transform infrared spectroscopic imaging parameters describing acid phosphate substitution in biologic hydroxyapatite", *Calcified Tissue International,* pp. 1-11.

Squires, K. E., Thompson, T. J. U., Islam, M. and Chamberlain, A. (2011), "The application of histomorphometry and fourier transform infrared spectroscopy to the analysis of early Anglo-Saxon burned bone", *Journal of Archaeological Science,* vol. 38, no. 9, pp. 2399-2409.

Starcher, B. C., Hill, C. H. and Madaras, J. G. (1980), "Effect of zinc deficiency on bone collagenase and collagen turnover.", *The Journal of Nutrition,* vol. 110, no. 10, pp. 2095-2102.

Stauffer, E., Dolan, J. A. and Newman, R. (2007), *Fire Debris Analysis,* Amsterdam: Acadeic Press. Accessed Online via Sciencedirect: http://www.sciencedirect.com/science/book/9780126639711.

Steenhout, A. and Pourtois, M. (1981), "Lead accumulation in teeth as a function of age with different exposures.", *British Journal of Industrial Medicine,* vol. 38, no. 3, pp. 297-303.

Stephens, P. W. (1999), "Phenomenological model of anisotropic peak broadening in powder diffraction", *Journal of Applied Crystallography,* vol. 32, no. 2, pp. 281-289.

Stiner, M. C., Kuhn, S. L., Weiner, S. and Bar-Yosef, O. (1995), "Differential burning, recrystallization, and fragmentation of archaeological bone", *Journal of Archaeological Science,* vol. 22, no. 2, pp. 223-237.

Stockman, A. (2003), "Colorimetry". In: Brown, T.G., Creath, K., Kogelnik, H., Kriss, M.A., Schmit and Weber, M.J. (eds.), *The Optics Encyclopedia: Basic Foundations and Practical Applications*. Berlin: Wiley –VCH, pp. 207-226.

Sturtevant, J. M. (1987), "Biochemical applications of differential scanning calorimetry", *Annual Review of Physical Chemistry*, vol. 38, no. 1, pp. 463-488.

Surovell, T. A. and Stiner, M. C. (2001), "Standardizing infra-red measures of bone mineral crystallinity: an experimental approach", *Journal of Archaeological Science*, vol. 28, no. 6, pp. 633-642.

Symes, S., Rainwater, C. W., Chapman, E., Gipson, D. and Piper, A. (2008), "Patterned thermal destruction of human remains in a forensic setting". In: Schmidt, C.W. and Symes, S.A. (eds.), *The Analysis of Burned Human Remains*, London: Academic Press, pp. 15-54.

Tadano, S. and Giri, B. (2011), "X-ray diffraction as a promising tool to characterize bone nanocomposites", *Science and Technology of Advanced Materials*, vol. 12, no. 6, pp. 1-11.

Tampieri, A., Celotti, G., Landi, E., Sandri, M., Roveri, N. and Falini, G. (2003), "Biologically inspired synthesis of bone-like composite: Self-assembled collagen fibers/hydroxyapatite nanocrystals", *Journal of Biomedical Materials Research Part A*, vol. 67, no. 2, pp. 618-625.

Tang, R., Henneman, Z. J. and Nancollas, G. H. (2003), "Constant composition kinetics study of carbonated apatite dissolution", *Journal of Crystal Growth*, vol. 249, no. 3–4, pp. 614-624.

Tang, R., Wang, L. and Nancollas, G. H. (2004), "Size-effects in the dissolution of hydroxyapatite: An understanding of biological demineralization", *Journal of Materials Chemistry*, vol. 14, no. 14, pp. 2341-2346.

Thompson, T. (2005), "Heat-induced dimensional changes in bone and their consequences for forensic anthropology", *Journal of Forensic Sciences*, vol. 50, no.5, pp. 1008-1015.

Thompson, T., Islam, M. and Bonniere, M. (2012), "A new statistical approach for determining the crystallinity of heat-altered bone mineral from FTIR spectra", *Journal of Archaeological Science*, vol.40, no.1, pp. 416-422.

Thompson, T. J. U. (2004), "Recent advances in the study of burned bone and their implications for forensic anthropology", *Forensic Science International*, vol. 146, Supplement, pp. S203-S205.

Tilley, R. J. (2006), *Crystals and Crystal Structures*, Chippenham, Wiltshire: Wiley & Sons.

Tooke, P. (1988), "Fourier self-deconvolution in IR spectroscopy", *Trends in Analytical Chemistry*, vol. 7, no. 4, pp. 130-136.

Trautz, O. R. (1955), "X-ray diffraction of biological and synthetic apatites ", *Annals of the New York Academy of Sciences,* vol. 60, no. 5, pp. 696-712.

Trueman, C. N. G., Behrensmeyer, A. K., Tuross, N. and Weiner, S. (2004), "Mineralogical and compositional changes in bones exposed on soil surfaces in Amboseli National Park, Kenya: Diagenetic mechanisms and the role of sediment pore fluids", *Journal of Archaeological Science,* vol. 31, no. 6, pp. 721-739.

Turney, L. (2010), "The failure of DNA forensic testing: A case study of the 2009 Australian bushfire disaster", *New Genetics and Society,* vol. 29, no. 3, pp. 225-240.

Turunen, M. J., Prantner, V., Jurvelin, J. S., Kröger, H. and Isaksson, H. (2013), "Composition and microarchitecture of human trabecular bone change with age and differ between anatomical locations", *Bone,* vol. 54, no. 1, pp. 118-125.

Turunen, M., de Keijser, T., Delhez, R. and Pers, N. v. d. (1983), "A method for the interpretation of the Warren-Averbach mean-squared strains and its application to recovery in aluminium", *Journal of Applied Crystallography,* vol. 16, no. 2, pp. 176-182.

Ubelaker, D. H. (2009), "The forensic evaluation of burned skeletal remains: A synthesis", *Forensic Science International,* vol. 183, no. 1–3, pp. 1-5.

Van der Houwen, Jacqueline AM, Cressey, G., Cressey, B. A. and Valsami-Jones, E. (2003), "The effect of organic ligands on the crystallinity of calcium phosphate", *Journal of Crystal Growth,* vol. 249, no. 3, pp. 572-583.

Venkateswarlu, K., Chandra Bose, A. and Rameshbabu, N. (2010), "X-ray peak broadening studies of nanocrystalline hydroxyapatite by Williamson–Hall analysis", *Physica B: Condensed Matter,* vol. 405, no. 20, pp. 4256-4261.

Viguet-Carrin, S., Garnero, P. and Delmas, P. (2006), "The role of collagen in bone strength", *Osteoporosis International,* vol. 17, no. 3, pp. 319-336.

Volkmer, D., Sichlau, M. and Rapp, T. B. (2009), "The use of radiofrequency ablation in the treatment of musculoskeletal tumors", *Journal of the American Academy of Orthopaedic Surgeons,* vol. 17, no. 12, pp. 737-743.

Von Dreele, R. (2008), "Rietveld Refinement". In: Dinnebier, R. E. and Billinge, S. J. (eds.) *Powder diffraction: Theory and Practice,* Cambridge: RSC Publishing, pp. 266-281.

Von Wurmb-Schwark, N., Simeoni, E., Ringleb, A. and Oehmichen, M. (2004), "Genetic investigation of modern burned corpses", *International Congress Series,* vol. 1261, pp. 50-52.

Wahab, M. A. (2009), *Essentials of crystallography*, Oxford: Alpha Science International.

Walker, P. L., Miller, K. P. and Richman, R. (2005), "Time, temperature, and oxygen availability: an experimental study of the effects of environmental conditions on the color and organic content of cremated bone", *American Journal of Physical Anthropology*, vol. 40, Supplement, pp. 222.

Walsh, W., Ohno, M. and Guzelsu, N. (1994), "Bone composite behaviour: Effects of mineral-organic bonding", *Journal of Materials Science: Materials in Medicine*, vol. 5, no. 2, pp. 72-79.

Wang, C., Quan, R., Wang, H., Wei, X. and Zhao, Z. (2009), "Investigation on High-temperature decomposition characteristic of hydroxyapatite", *Nano/Molecular Medicine and Engineering, IEEE International Conference*, pp. 65-70.

Wang, X., Zuo, Y., Huang, D., Hou, X. and Li, Y. (2010), "Comparative study on inorganic composition and crystallographic properties of cortical and cancellous bone", *Biomedical and Environmental Sciences*, vol. 23, no. 6, pp. 473-480.

Wang, Y., Azaïs, T., Robin, M., Vallée, A., Catania, C., Legriel, P., Pehau-Arnaudet, G., Babonneau, F., Giraud-Guille, M. and Nassif, N. (2012), "The predominant role of collagen in the nucleation, growth, structure and orientation of bone apatite", *Nature Materials*, vol. 11, no. 8, pp. 724-733.

Warren, B. (1941), "X-Ray Diffraction Methods", *Journal of Applied Physics*, vol. 12, no. 5, pp. 375-384.

Waterhouse, K. (2013), "The effect of victim age on burnt bone fragmentation: Implications for remains recovery", *Forensic Science International*, vol. 231, no. 1–3, pp. 409.e1-409.e7.

Watson, E., O'neill, M., Justin, J. and Brenner, N. (1964), "A differential scanning calorimeter for quantitative differential thermal analysis.", *Analytical Chemistry*, vol. 36, no. 7, pp. 1233-1238.

Weiner, S. and Bar-Yosef, O. (1990), "States of preservation of bones from prehistoric sites in the Near East: A survey", *Journal of Archaeological Science*, vol. 17, no. 2, pp. 187-196.

Weiner, S. (2006), "Transient precursor strategy in mineral formation of bone", *Bone*, vol. 39, no. 3, pp. 431-433.

Wittmers Jr, L. E., Wallgren, J., Alich, A., Aufderheide, A. C. and Rapp Jr, G. (1988), "Lead in bone. IV. Distribution of lead in the human skeleton", *Archives of Environmental Health: An International Journal*, vol. 43, no. 6, pp. 381-391.

Wojnar, R. (2010), "Bone and cartilage – Its structure and physical properties". In: Öchsner, A. and Ahmed, W. (eds), *Biomechanics of Hard Tissues: Modeling, Testing and Materials,* Weinham: Wiley-VCH, pp. 1-75.

Woodhead-Galloway, J. (1980), *Collagen: The Anatomy of a Protein*, Southampton: The Camelot Press Ltd, pp. 1-59.

Wopenka, B. and Pasteris, J. D. (2005), "A mineralogical perspective on the apatite in bone", *Materials Science and Engineering: C,* vol. 25, no. 2, pp. 131-143.

Wright, L. E. and Schwarcz, H. P. (1996), "Infrared and isotopic evidence for diagenesis of bone apatite at Dos Pilas, Guatemala: Palaeodietary implications", *Journal of Archaeological Science,* vol. 23, no. 6, pp. 933-944.

Xie, B. and Nancollas, G. H. (2010), "How to control the size and morphology of apatite nanocrystals in bone", *Proceedings of the National Academy of Sciences,* vol. 107, no. 52, pp. 22369-22370.

Yan, J., Daga, A., Kumar, R. and Mecholsky, J. J. (2008), "Fracture toughness and work of fracture of hydrated, dehydrated, and ashed bovine bone", *Journal of Biomechanics,* vol. 41, no. 9, pp. 1929-1936.

Yang, Y., Cui, Q. and Sahai, N. (2010), "How does bone sialoprotein promote the nucleation of hydroxyapatite? A molecular dynamics study using model peptides of different conformations", *Langmuir,* vol. 26, no. 12, pp. 9848-9859.

Yao, F., LeGeros, J. P. and LeGeros, R. Z. (2009), "Simultaneous incorporation of carbonate and fluoride in synthetic apatites: Effect on crystallographic and physico-chemical properties", *Acta Biomaterialia,* vol. 5, no. 6, pp. 2169-2177.

Yao, F. and LeGeros, R. Z. (2010), "Carbonate and fluoride incorporation in synthetic apatites: Comparative effect on physico-chemical properties and *in vitro* bioactivity in fetal bovine serum", *Materials Science and Engineering: C,* vol. 30, no. 3, pp. 423-430.

Yilbas, B., Yilbas, Z. and Sami, M. (1996), "Thermal processes taking place in the bone during CO_2 laser irradiation", *Optics & Laser Technology,* vol. 28, no. 7, pp. 513-519.

Young, R. (1975), "Biological apatite vs hydroxyapatite at the atomic level", *Clinical Orthopaedics and Related Research,* vol. 113, pp. 249-262.

Yravedra, J. and Uzquiano, P. (2013), "Burnt bone assemblages from El Esquilleu cave (Cantabria, Northern Spain): Deliberate use for fuel or systematic disposal of organic waste?", *Quaternary Science Reviews,* vol. 68, pp. 175-190.

Zhang, Q., Chen, J., Feng, J., Cao, Y., Deng, C. and Zhang, X. (2003), "Dissolution and mineralization behaviors of HA coatings", *Biomaterials*, vol. 24, no. 26, pp. 4741-4748.

Zhao, J., Zhao, J., Chen, J., Wang, X., Han, Z. and Li, Y. (2014), "Rietveld refinement of hydroxyapatite, tricalcium phosphate and biphasic materials prepared by solution combustion method", *Ceramics International*, vol. 40, no. 2, pp. 3379-3388.

Zioupos, P. (2005), "In vivo fatigue microcracks in human bone: Material properties of the surrounding bone matrix", *European Journal of Morphology*, vol. 42, no. 1-2, pp. 31-42.

Zucca, N., Erriu, G., Onnis, S. and Longoni, A. (2004), "An analytical expression of the output of a power-compensated DSC in a wide temperature range", *Thermochimica Acta*, vol. 413, no. 1, pp. 117-125.

Appendix A: Wt. % of carbonate and lattice parameter values corresponding to Figure 2.6, Section 2.2.2

	A- type	
Wt. % CO_3	**a-axis (Å)**	**c-axis (Å)**
0.00	9.42	6.88
1.77	9.45	6.878
2.31	9.469	6.874
3.49	9.518	6.851
3.67	9.492	6.867
4.39	9.544	6.859

Table A.1 Weight percentage (wt. %) of A-type carbonate incorporated into synthetic HAp and corresponding lattice parameter values. Taken from LeGeros *et al.* (1969).

	B- type	
Wt. % CO3	**a-axis (Å)**	**c-axis (Å)**
0.5	9.43	6.87
2.5	9.42	6.88
4.28	9.41	6.88
8.96	9.38	6.89
15.1	9.35	6.9
20.53	9.31	6.92
22.22	9.3	6.93

Table A.2 Weight percentage (wt. %) of B-type carbonate incorporated into synthetic HAp and corresponding lattice parameter values. Taken from LeGeros *et al.* (1969).

Appendix B: Mass loss values for heated bone types

:	**Porcine Mass Loss (wt. %)**				
	600 °C	**650 °C**	**700 °C**	**750 °C**	**800 °C**
Dwell Period					
1m				29 ± 4	31 ± 3
5m			35 ± 2	37 ± 2	39 ± 2
10m			37 ± 1	40 ± 1	41 ± 1
20m			38 ± 2	40 ± 2	38 ± 2
30m		34 ± 1	36 ± 1	40 ± 1	38 ± 1
1hr	35 ± 2	38 ± 2	39 ± 1	37 ± 2	37 ± 1
2hr	38 ± 3	39 ± 2	37 ± 2	38 ± 1	41 ± 1
4hr	34 ± 1	39 ± 2	37 ± 1	40 ± 1	41 ± 2
6hr	40 ± 2	39 ± 1			
24hr	36 ± 2	36 ± 3			
48hr	41 ± 1	40 ± 1			
72hr	41 ± 1				

Table B.1 Mass loss (weight percentage, wt. %) for porcine bone heated at 600, 650, 700, 750 and 800 °C for different periods of time (dwell period). Errors calculated from the standard deviation of three repeats.

	Bovine Mass Loss (wt. %)				
	600 °C	**650 °C**	**700 °C**	**750 °C**	**800 °C**
Dwell Period					
1m				20 ± 5	21 ± 2
5m			29 ± 2	30 ± 3	33 ± 1
10m			35 ± 1	32 ± 1	35 ± 1
20m			33 ± 1	36 ± 2	35 ± 1
30m		32 ± 2	33 ± 1	35 ± 2	35 ± 1
1hr	33 ± 2	33± 2	34 ± 2	34 ± 1	34 ± 1
2hr	33 ± 1	34 ± 1	35 ± 1	34 ± 2	34 ± 1
4hr	34 ± 1	33 ± 1	34 ± 1	36 ± 1	34 ± 1
6hr	32 ± 1	36 ± 3			
24hr	35 ± 2	34 ± 2			
48hr	35 ± 2	35 ± 1			
72hr	34 ± 1				

Table B.2 Mass loss (weight percentage, wt. %) for bovine bone heated at 600, 650, 700, 750 and 800 °C for different periods of time (dwell period). Errors calculated from the standard deviation of three repeats.

	Anorganic Bovine Mass Loss (wt. %)				
	Initial Heat Treatment (400 °C for 2 hrs)				
	600 °C	650 °C	700 °C	750 °C	800 °C
Dwell Period					
1m				30 ± 3	31 ± 4
5m			32 ± 3	28 ± 3	32 ± 2
10m			30 ± 2	29 ± 2	28± 1
20m			30 ± 1	29 ± 1	31 ± 2
30m		29 ± 1	30 ± 1	28 ± 2	28 ± 1
1hr	30 ± 1	30 ± 2	31 ± 1	32 ± 3	29 ± 1
2hr	30 ± 2	30 ± 1	30 ± 2	28 ± 1	28 ± 2
4hr	31± 2	27 ± 2	29 ± 2	28 ± 1	28 ± 1
6hr	33 ± 3	32 ± 1			
24hr	30 ± 1	31 ± 2			
48hr	30 ± 1	29 ± 1			
72hr	30 ± 2				

Table B.3 Mass loss (weight percentage, wt. %) for bovine bone heated at 400 °C for 2 hrs to produce an 'anorganic' bone specimen. The mass losses are correlated with the second heat treatment (temperature and dwell period) each anorganic specimen was subsequently subjected to.

	Anorganic Bovine Mass Loss (wt. %)				
	Second Heat Treatment				
	600 °C	650 °C	700 °C	750 °C	800 °C
Dwell Period					
1m				1 ± 0.3	2 ± 0.5
5m			2 ± 0.3	1 ± 0.2	2 ± 0.3
10m			1 ± 0.2	2 ± 0.1	1 ± 0.2
20m			1 ± 0.2	1 ± 0.1	2 ± 0.1
30m		1 ± 0.2	1 ± 0.1	2 ± 0.1	1 ± 0.2
1hr	1 ± 0.2	1 ± 0.1	1 ± 0.1	2 ± 0.1	1 ± 0.1
2hr	1 ± 0.1	1 ± 0.1	2 ± 0.1	2 ± 0.1	1 ± 0.2
4hr	1± 0.2	1 ± 0.2	1 ± 0.1	1 ± 0.1	1 ± 0.1
6hr	1 ± 0.2	1 ± 0.1			
24hr	2± 0.1	2 ± 0.1			
48hr	1 ± 0.2	1 ± 0.1			
72hr	1 ± 0.1				

Table B.4 Mass loss (weight percentage, wt. %) for anorganic bovine bone heated at 600, 650, 700, 750 and 800 °C (after the initial heat treatment at 400 °C for 2 hrs) for different periods of time (dwell period). Errors calculated from the standard deviation of three repeats.

	Anorganic Porcine Mass Loss (wt. %)				
	Initial Heat Treatment (400 °C for 2 hrs)				
	600 °C	650 °C	700 °C	750 °C	800 °C
Dwell Period					
1m				35 ± 2	36 ± 4
5m			36 ± 1	37 ± 3	35± 2
10m			36± 3	34 ± 2	36± 1
20m			36 ± 1	35 ± 1	36± 1
30m		35 ± 1	36± 2	36 ± 2	37 ± 2
1hr	33 ± 1	35 ± 1	37 ± 2	36 ±1	35± 1
2hr	28 ± 3	33 ± 2	35 ± 2	34 ± 2	36 ± 2
4hr	33± 1	32 ± 2	36± 2	37 ± 2	35 ± 1
6hr	33 ± 1	34 ± 2			
24hr	33 ± 2	35 ± 1			
48hr	32 ± 1	35 ± 2			
72hr	34 ± 1				

Table B.5 Mass loss (weight percentage, wt. %) for porcine bone heated at 400 °C for 2 hrs to produce an 'anorganic' bone specimen. The mass losses are correlated with the second heat treatment (temperature and dwell period) each anorganic specimen was subsequently subjected to.

	Anorganic Porcine Mass Loss (wt. %)				
	Second Heat Treatment				
	600 °C	650 °C	700 °C	750 °C	800 °C
Dwell Period					
1m				1 ± 0.2	2 ± 0.4
5m			1 ± 0.1	3 ± 0.2	2 ± 0.2
10m			3 ± 0.3	2 ± 0.2	3 ± 0.1
20m			2 ± 0.6	3 ± 0.4	2 ± 0.2
30m		1 ± 0.2	3 ± 0.1	3 ± 0.1	3 ± 0.2
1hr	2 ± 0.2	1 ± 0.1	3 ± 0.6	2 ± 0.2	2 ± 0.3
2hr	2 ± 0.1	2 ± 0.2	4 ± 0.1	2 ± 0.3	3 ± 0.2
4hr	3 ± 0.3	3 ± 0.2	2 ± 0.3	4 ± 0.3	3 ± 0.1
6hr	4 ± 1	3 ± 0.1			
24hr	2 ± 0.2	2 ± 0.1			
48hr	3 ± 0.4	2 ± 0.1			
72hr	2 ± 0.2				

Table B.6 Mass loss (weight percentage, wt. %) for anorganic porcine bone heated at 600, 650, 700, 750 and 800 °C (after the initial heat treatment at 400 °C for 2 hrs) for different periods of time (dwell period). Errors calculated from the standard deviation of three repeats.

	Mass Loss (wt. %), Heated at 700 °C	
	Rostrum	**Red Deer Antler**
Dwell Period		
5m	10 ± 1	51 ± 4
10m	10 ± 1	51 ± 3
20m	10 ± 1	55 ± 2
30m	10 ± 1	55 ± 1
1hr	11 ± 2	52 ± 1
2hr	10 ± 1	54 ± 2
3hr	11 ± 2	-
4hr	12 ± 1	54 ± 1
12hr	13 ± 2	-
24hr	14 ± 1	52 ± 2
72hr	14 ± 1	56 ± 2

Table B.7 Mass loss (weight percentage, wt. %) for red deer antler and rostrum specimens heated at 700 °C for different periods of time (dwell period). Errors calculated from the standard deviation of three repeats.

Appendix C: L*a*b colour values for heated bovine bone

	650 ^{o}C		
	L*	**a***	**b***
Dwell Period			
30m	58 ± 1	0.6 ± 0.08	2.0 ± 0.3
1hr	80 ± 3	0.4 ± 0.04	2.2 ± 0.1
2hr	93 ± 1	-0.1 ± 0.3	0.9 ± 0.3
4hr	92 ± 2	-0.1 ± 0.2	0.7 ± 0.1
6hr	92 ± 3	-0.1 ± 0.1	0.6 ± 0.1
24hr	93 ± 4	-0.2 ± 0.2	0.7 ± 0.2
48hr	94 ± 1	-0.2 ± 0.1	0.5 ± 0.1

Table C.1 L*a*b colour scale values for bovine bone heated at 650 ^{o}C for different periods of time (dwell period). Errors calculated from the standard deviation of three repeats.

	700 ^{o}C		
	L*	**a***	**b***
Dwell Period			
5m	40 ± 1	0.5 ± 0.02	2 ± 0.1
10m	49 ± 2	-0.2 ± 0.03	1 ± 0.5
20m	78 ± 4	-0.2 ± 0.09	0.5 ± 0.4
30m	91 ± 2	- 0.1± 0.06	0.9 ± 0.3
1hr	95 ± 3	-0.2 ± 0.04	0.7 ± 0.1
2hr	93 ± 2	-0.3 ± 0.02	0.6 ± 0.3
4hr	93 ± 1	-0.1 ± 0.03	0.2 ± 0.3

Table C.2 L*a*b colour scale values for bovine bone heated at 650 ^{o}C for different periods of time (dwell period). Errors calculated from the standard deviation of three repeats.

	750 °C		
	L*	**a***	**b***
Dwell Period			
1m	50 ± 5	3 ± 0.50	6 ± 3
5m	49± 1	0.1 ± 0.06	0.5 ± 0.1
10m	53 ± 2	-0.6 ± 0.08	2.0± 0.1
20m	90 ± 1	-0.1 ± 0.04	1.0 ± 0.3
30m	91 ± 1	-0.1 ± 0.03	0.8 ± 0.1
1hr	90 ± 4	-0.2 ± 0.04	1.0 ±0.2
2hr	96 ± 2	-0.3 ± 0.01	1.0 ± 0.3
4hr	91 ± 3	-0.2 ± 0.3	0.6 ± 0.2

Table C.3 L*a*b colour scale values for bovine bone heated at 750°C for different periods of time (dwell period). Errors calculated from the standard deviation of three repeats.

Appendix D: Reference diffractograms of mineral phases

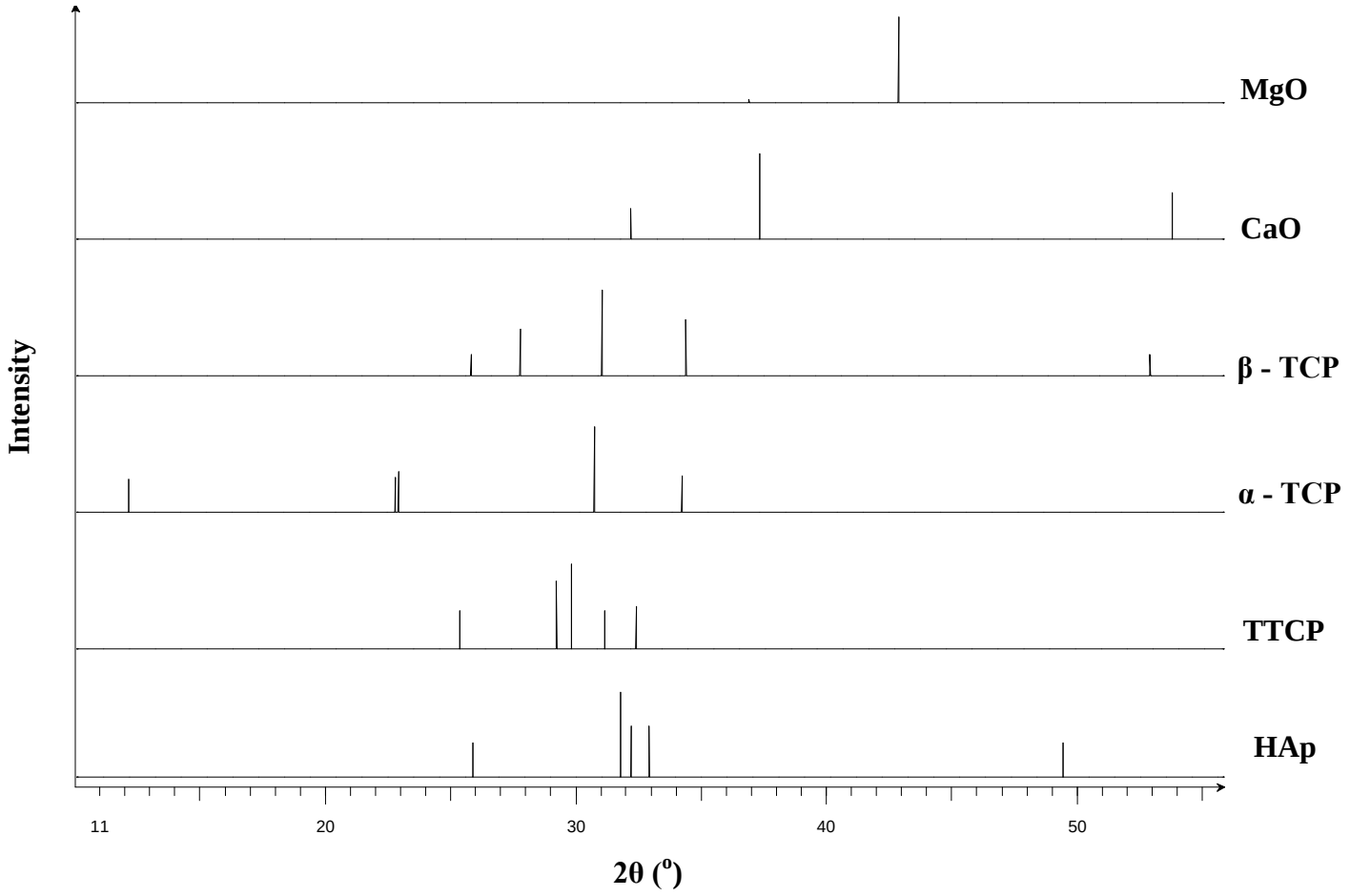

Figure D.1 Stick representations of typical diffractograms observed for the mineral phases discussed in this thesis. Up to five of the highest intensity peaks are included for each phase.

Appendix E: Static Heating-Sigmoidal Curves

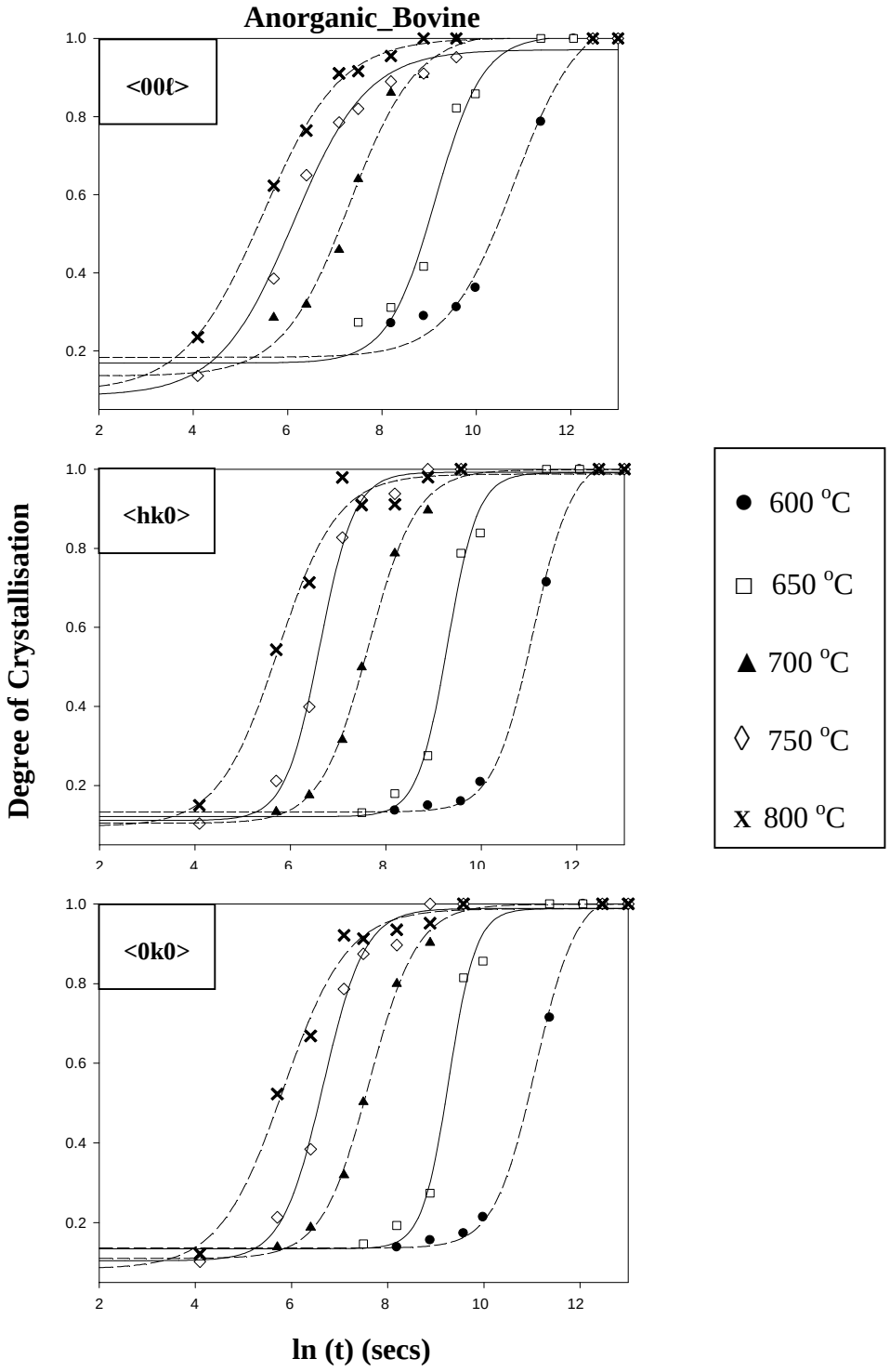

Figure E.1 Sigmoidal curves representing the crystallisation process in three crystallographic directions, <00ℓ>, <hk0> and <0k0> for anorganic bovine bone heated at 600, 650, 700, 750 and 800 °C for various time periods. Errors are not shown for clarity.

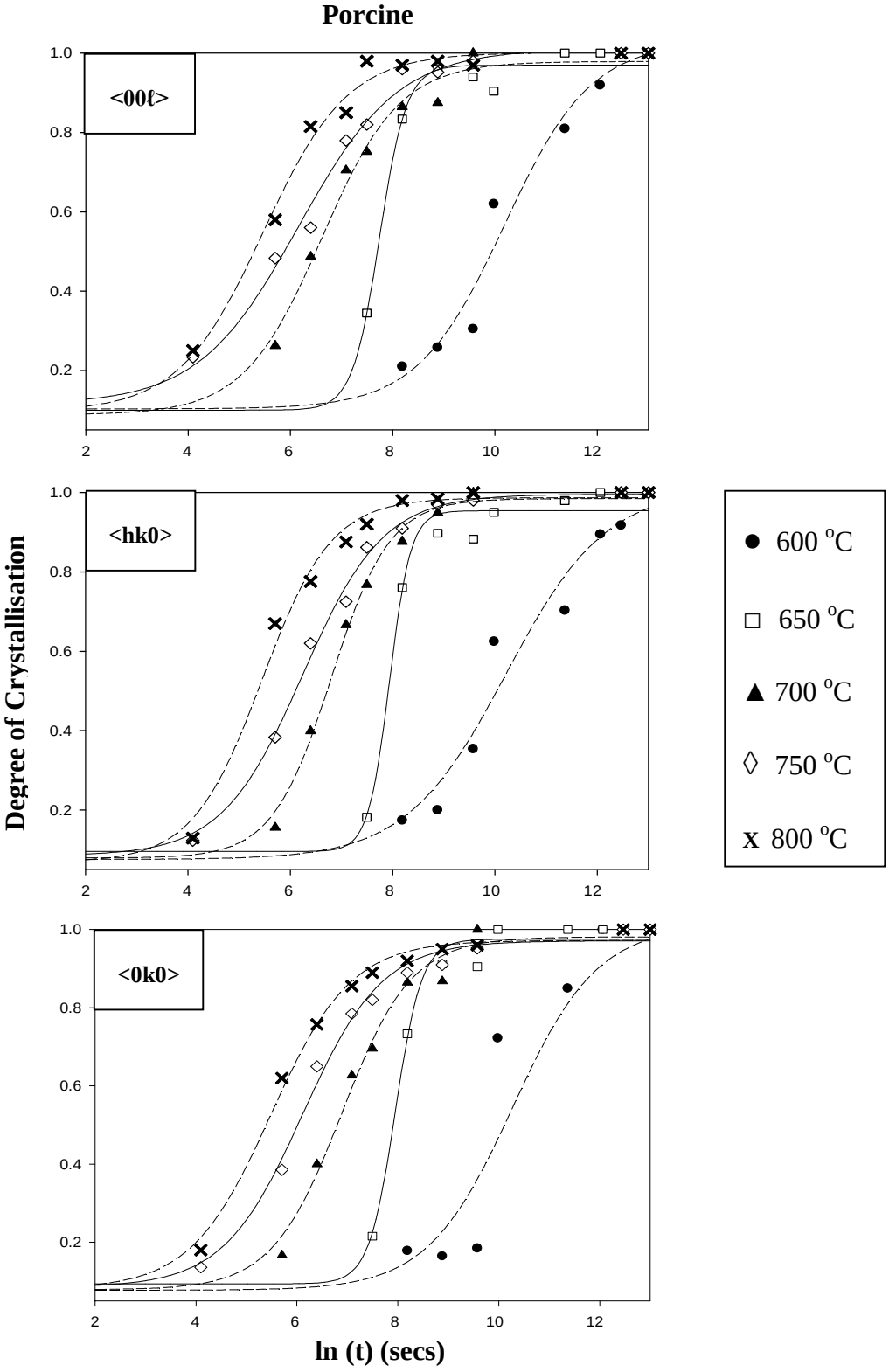

Figure E.2 Sigmoidal curves representing the crystallisation process in three crystallographic directions, <00ℓ>, <hk0> and <0k0> for porcine bone heated at 600, 650, 700, 750 and 800 °C for various time periods. Errors are not shown for clarity.

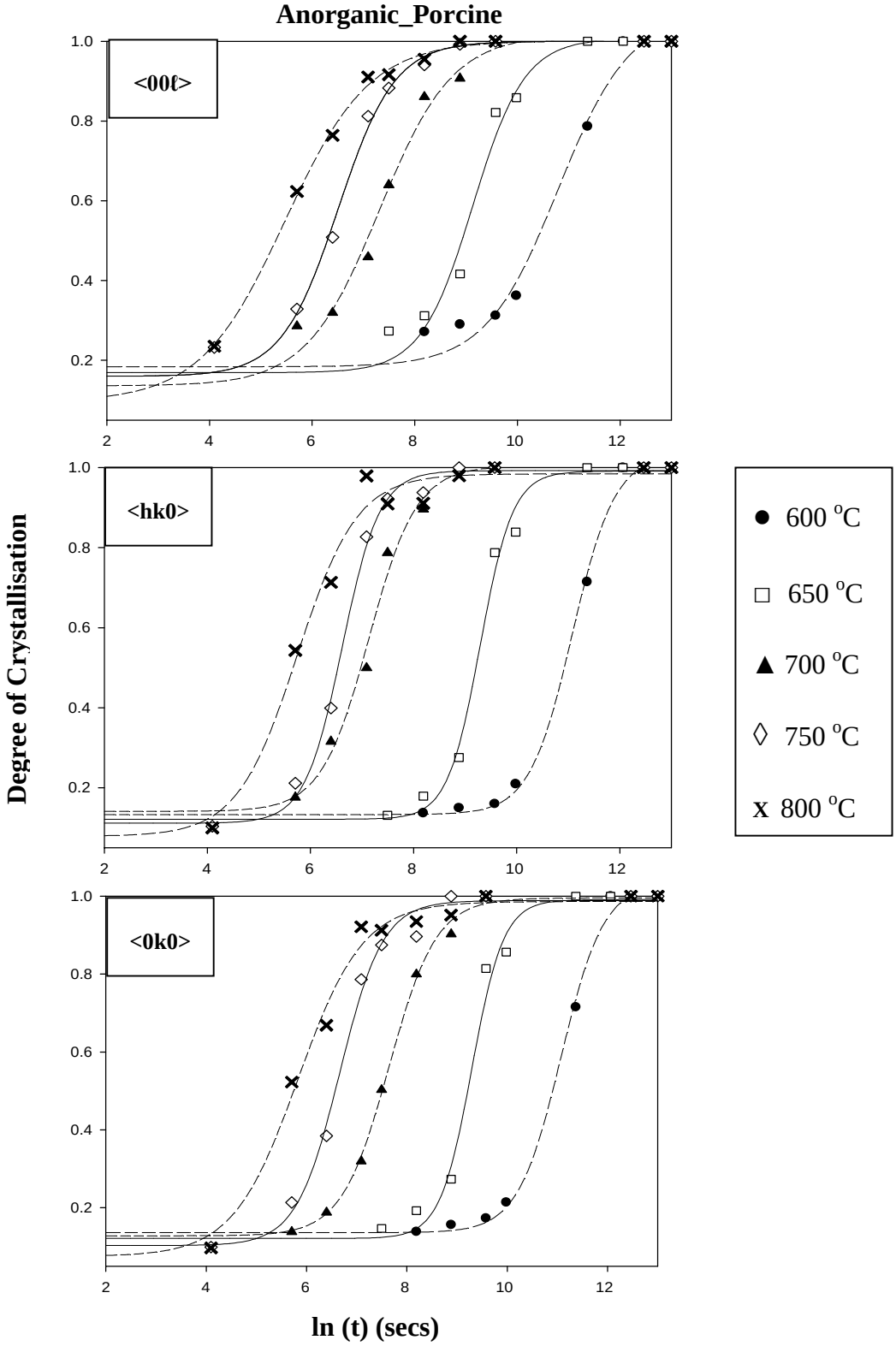

Figure E.3 Sigmoidal curves representing the crystallisation process in three crystallographic directions, <00ℓ>, <hk0> and <0k0> for anorganic porcine bone heated at 600, 650, 700, 750 and 800 °C for various time periods. Errors are not shown for clarity.

Appendix F: ‘n’ and ‘k’ values calculated from the Avrami model for bovine and porcine bone and their anorganic analogues

	<00ℓ>					
	600 °C		700 °C		750 °C	
	n	k	n	k	n	k
Porcine	0.97 ± 0.14	0.79 ± 0.17	0.64 ± 0.03	3.16 ± 0.45	0.60 ± 0.02	4.82 ± 0.11
Bovine	0.91 ± 0.06	0.40 ± 0.02	0.81 ± 0.17	2.27 ± 0.98	0.68 ± 0.03	3.54 ± 0.08
Bovine Anorganic	0.85 ± 0.06	0.22 ± 0.07	0.69 ± 0.02	1.59 ± 0.42	0.65 ± 0.07	2.92 ± 0.07
Porcine Anorganic	0.87 ± 0.09	0.22 ± 0.04	0.69 ± 0.06	1.59 ± 0.36	0.65 ± 0.05	2.92 ± 0.07

Table F.1 Calculated values of ‘n’ and ‘k’ obtained by fitting coherence length data (corresponding to the <00ℓ> reflection) to the Avrami equation, for bone specimens heated at 600, 700 and 750 °C.

	<0k0>					
	600 °C		700 °C		750 °C	
	n	k	n	k	n	k
Porcine	0.75 ± 0.13	0.76 ± 0.33	0.76 ± 0.15	2.72 ± 0.35	0.42 ± 0.09	4.67 ± 0.21
Bovine	0.81 ± 0.16	0.34 ± 0.17	1.05 ± 0.06	2.03 ± 1.09	0.73± 0.11	2.93 ± 0.09
Bovine Anorganic	0.77 ± 0.19	0.20 ± 0.18	0.94 ± 0.03	1.30 ± 0.52	0.79 ± 0.08	2.47 ± 0.15
Porcine Anorganic	0.77 ± 0.16	0.20 ± 0.17	0.94 ± 0.07	1.03 ± 0.43	0.79 ± 0.06	2.59 ± 0.08

Table F.2 Calculated values of ‘n’ and ‘k’ obtained by fitting coherence length data (corresponding to the <0k0> reflection) to the Avrami equation, for bone specimens heated at 600, 700 and 750 °C.

	<hk0>									
	600 °C		**650 °C**		**700 °C**		**750 °C**		**800 °C**	
	n	k	n	k	n	k	n	k	n	k
Porcine	0.77 ± 0.16	0.55 ± 0.13	0.86 ± 0.09	0.74 ± 0.13	0.69 ± 0.10	3.19 ± 0.19	0.42 ± 0.09	4.59 ± 0.23	0.37 ± 0.08	4.80 ± 0.16
Bovine	0.90 ± 0.11	0.32 ± 0.07	1.15 ± 0.13	0.44 ± 0.21	0.75 ± 0.19	2.89 ± 0.12	0.79 ± 0.13	2.65 ± 0.28	0.69 ± 0.12	3.62 ± 0.12
Bovine Anorganic	0.75 ± 0.09	0.09 ± 0.12	0.68 ± 0.08	0.28 ± 0.14	0.86 ± 0.17	1.27 ± 0.09	0.73 ± 0.12	2.33 ± 0.32	0.73 ± 0.11	3.66 ± 0.14
Porcine Anorganic	0.75 ± 0.08	0.09 ± 0.11	0.68 ± 0.12	0.28 ± 0.09	0.85 ± 0.14	1.27 ± 0.13	0.73 ± 0.08	2.33 ± 0.19	0.73 ± 0.12	3.66 ± 0.11

Table F.3 Calculated values of ‘n’ and ‘k’ obtained by fitting coherence length data (corresponding to the <hk0> reflection) to the Avrami equation, for bone specimens heated at 600, 650, 700, 750 and 800 °C.

Appendix G: Lattice parameters of dynamically heated bone

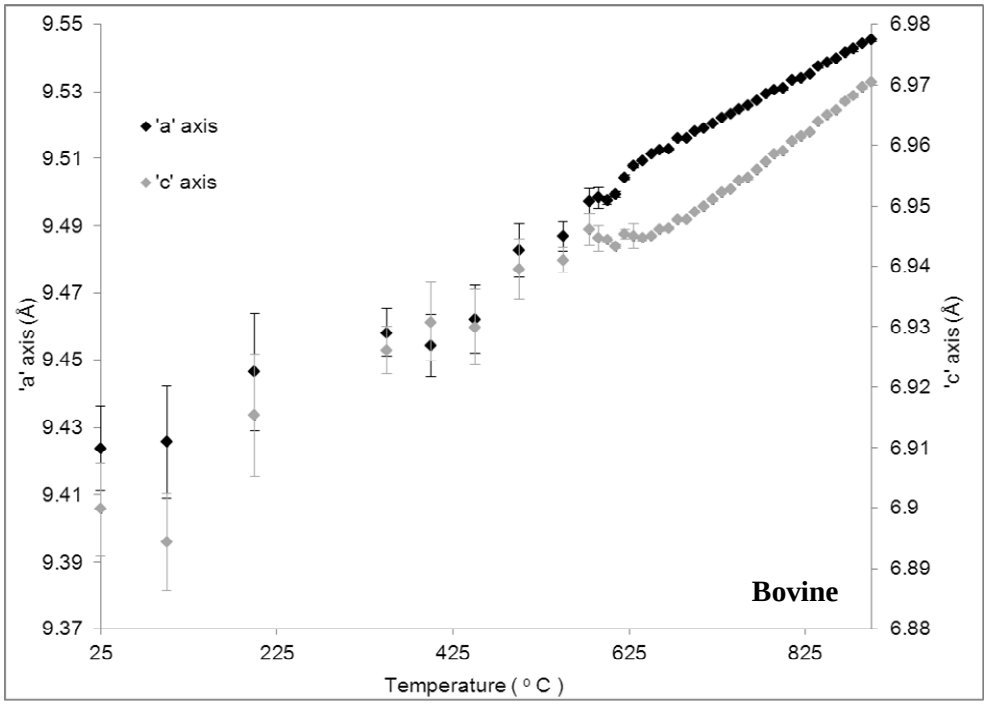

Figure G.1 Lattice parameter data ('a' and 'c' axis) plotted against temperature for dynamically heated bovine bone.

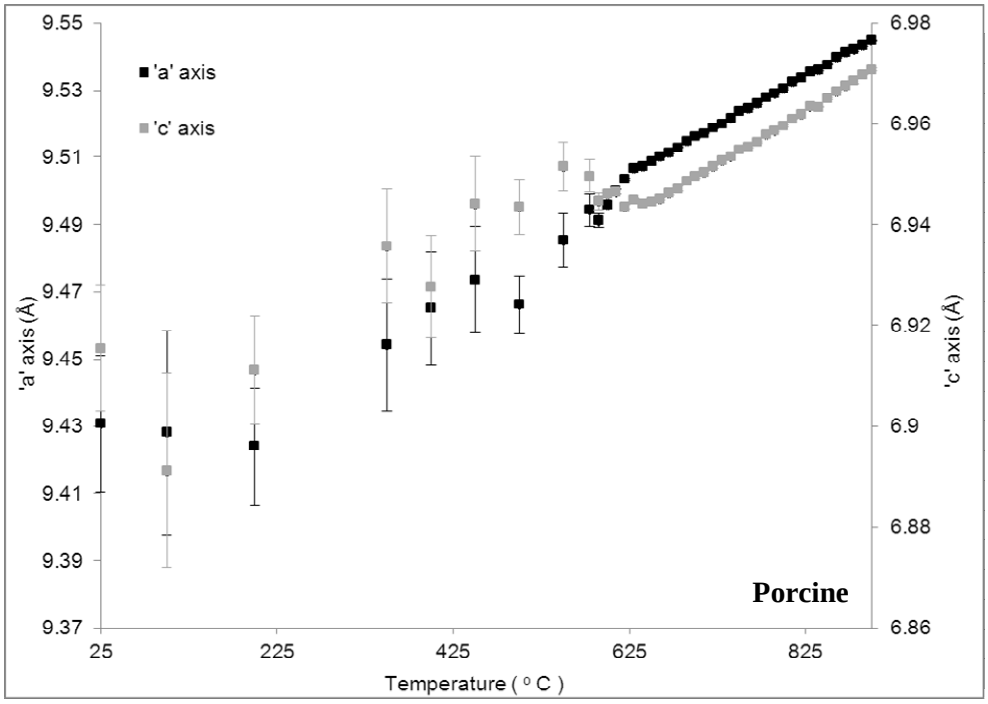

Figure G.2 Lattice parameter data ('a' and 'c' axis) plotted against temperature for dynamically heated porcine bone.

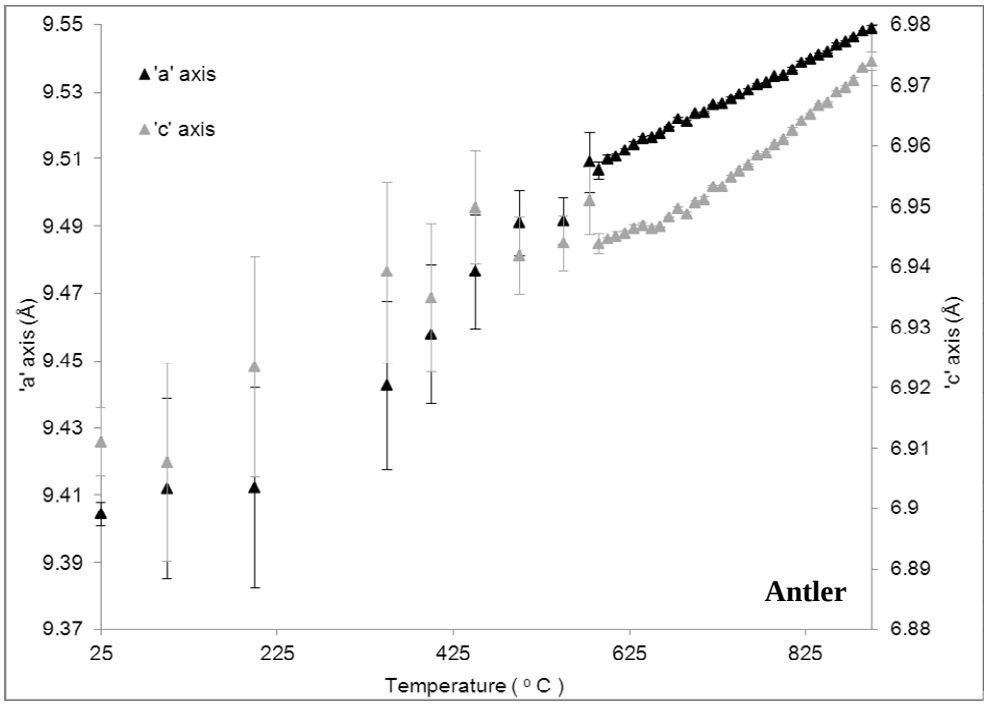

Figure G.3 Lattice parameter data (‘a’ and ‘c’ axis) plotted against temperature for dynamically heated red deer antler bone mineral.

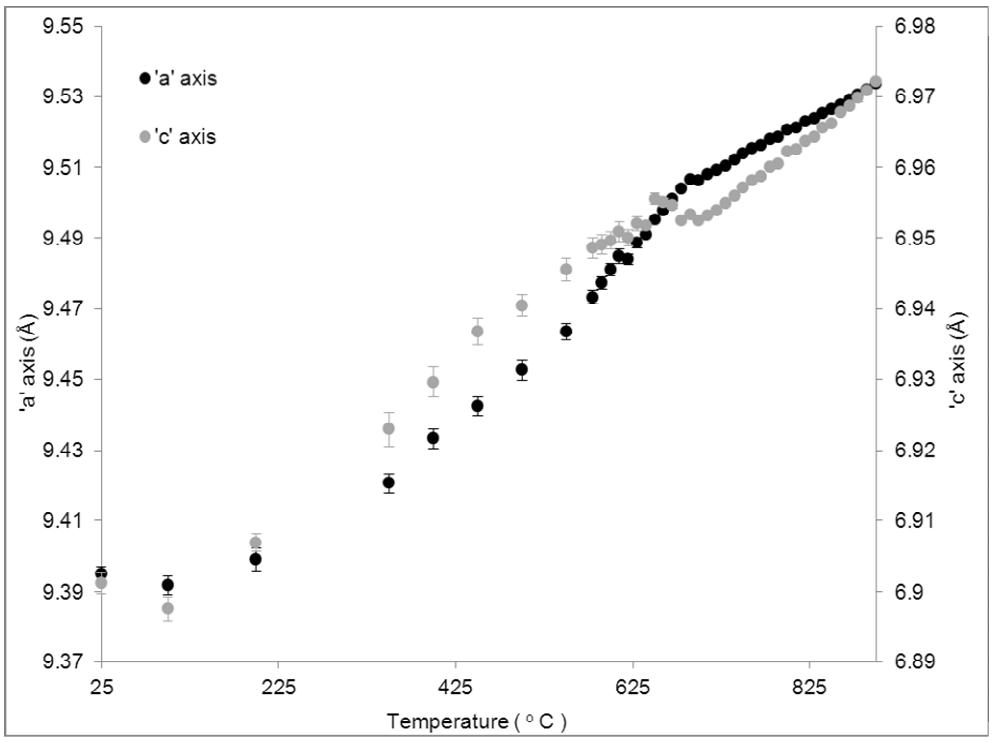

Figure G.4 Lattice parameter data (‘a’ and ‘c’ axis) plotted against temperature for dynamically heated red deer antler bone mineral.

Appendix H: Wilcoxon Signed Rank Test

As aforementioned (section 8.8.3) the Wilcoxon signed rank test is a non-parametric analogue to the paired two-sample t-test (Mendenhall *et al.*, 2012). Wilcoxon analysis does not assume normal Gaussian distribution. This statistical analysis compares two paired groups of data where there are two nominal variables and one measurement variable (Goh *et al.*, 2004). In this study, the two nominal variables are bone type and temperature whilst the measurement variable relates to 'a' axis lattice parameter data obtained from dynamically heated bone specimens. The null hypothesis for the Wilcoxon signed rank test is that if the distribution of difference scores between paired datasets are symmetric about zero, they are not statistically different (Sheskin, 2003). In Wilcoxon analysis, the difference in scores is based on the median of the differences.

To calculate the test statistic using Wilcoxon signed rank test, the difference between each of the *n* pairs is calculated ($x_1 - x_2$). In this case the difference between the lattice parameter values for each bone type is calculated at each temperature The absolute difference values (positive and negative assignments are negated at this point) are then assigned ranks, with the smallest value assigned 1 , 2 to the second smallest , and so on. Absolute difference values of 0 are eliminated from the analysis. The rank value is averaged for absolute difference values which are the same. The rank sum of the negative absolute differences (T^-) and the positive differences (T^+) are then individually calculated. The smaller of these values is the test statistic, T for a two tailed test. This value is then compared to a $T_{critical}$ value obtained from Wilcoxon signed rank test critical value tables. $T_{critical}$ is dependent on the number of pairs used in the analysis (n), whether a two tailed test or a one tailed test is employed and the significance level chosen. If $T \leq T_{critical,}$ the null hypothesis is rejected and the paired datasets are statistically different. An example of this process is provided in Table E.1, with $T_{critical}$ obtained from Mendenhall *et al.* (2012), assuming a two tailed test and a significance confidence of 0.05.

	Rostrum	Human		Wilcoxon Signed Rank Test Analysis		
Temperature (^{o}C)	**a' axis (Å)**			**Difference (x_1- $x_{2)}$**	**Absolute Difference**	**Ranked Values**
800	9.52071	9.52518		-0.0045	0.0045	1
810	9.521192	9.5268		-0.0056	0.0056	7
820	9.523059	9.5284		-0.0053	0.0053	3
830	9.523797	9.52868		-0.0049	0.0049	2
840	9.525321	9.5306		-0.0053	0.0053	3
850	9.526289	9.53213		-0.0058	0.0058	8
860	9.527712	9.53364		-0.0059	0.0059	9
870	9.529104	9.53534		-0.0062	0.0062	11
880	9.530459	9.53634		-0.0059	0.0059	9
890	9.531883	9.53718		-0.0053	0.0053	3
900	9.533623	9.53907		-0.0054	0.0054	6

$\mathbf{T^-}$	62
$\mathbf{T^+}$	0
T	0
$\mathbf{T_{critical}}$	11
$\mathbf{T \leq T_{critical}}$	Reject H_o, significantly different

Table H.1 Wilcoxon signed rank test analysis used to determine whether 'a' axis lattice parameter values obtained from rostrum and human bone (dynamically heated between 800 – 900 ^{o}C) are statically different. $T_{critical}$ obtained from Mendenhall *et al* (2012) assuming a two tailed test and a significance confidence of 0.05.

Appendix I: Publications

Title	Bone mineral crystallisation kinetics
Journal	Journal of Materials Science: Materials in Medicine
Received	7th October 2011
Accepted	11th May 2012

Title	Initial observations of dynamically heated bone
Journal	Crystal Research and Technology
Received	12th August 2013
Revised	16th October 2013
Accepted	22nd October 2013

J Mater Sci: Mater Med (2012) 23:2055–2060
DOI 10.1007/s10856-012-4679-2

Bone mineral crystallisation kinetics

C. Greenwood · K. Rogers · S. Beckett · J. Clement

Received: 7 October 2011 / Accepted: 11 May 2012 / Published online: 29 June 2012

Abstract The kinetics of bone apatite crystallisation are examined using a novel approach to obtain quantitative, direction dependence features such as growth rate and activation energy. X-ray diffraction was employed for analysis of bovine, porcine and 'anorganic' bone specimens. Apatite coherence length was utilised as the independent variable within a Johnson–Mehl–Avrami (JMA) model. A direction averaged crystallisation activation energy of 183 ± 8 kJ mol^{-1} was observed for the three bone groups. The Johnson–Mehl–Avrami 'n' exponent decreased with increasing temperature for all bone groups, indicating that apatite crystallisation changes to a diffusion limited process at higher temperatures. The results revealed little evidence to support any organic component 'protective' effect, and, on the contrary indicated that the organic matrix promotes apatite crystallisation.

1 Introduction

The thermal behaviour of bone has relevance within many fields including biomaterials and orthopaedics. Critically, the microstructure of bone mineral, which is central to its mechanical, ion storage and osteoconductive function, is particularly sensitive to temperature. High-temperature processing of bone to produce hydroxyapatite bioceramics is frequently employed for use in medical applications such as allograft and xenograft replacement [1, 2] and in biomaterial applications such as scaffold development [3, 4]. Orthopaedic surgery may utilise methods that result in significant temperature increases in bone. During drilling, temperatures may reach 300 °C causing osteonecrosis and thermal denaturing of tissues by lasers can result in temperatures of up to 800 °C. Further, a recent option for treatment of single bone metastases is radiofrequency ablation [5], and this also thermally influences bone.

Over the last 10 years or so, there have been an increasing number of studies examining the behaviour of bone when heated to its mineral melting point. In general, at temperatures below about 500 °C organic components are denatured and subsequently combusted. The evolution of water and carbon dioxide is also observed [6]. A substantial and rapid change in the mineral microstructure is observed between 600 and 700 °C when apatite lattice order and crystallite size increase significantly. At temperatures greater than 800 °C thermal decomposition of the apatite that occurs is dependent to some extent upon the original crystal chemistry [7].

Our focus has been on the rapid crystallisation process occurring at around 650 °C. The detailed response of bone at these temperatures is dependent upon composition and structure of the pre-heated material and the thermal regime. However, in general, during this process, there is rapid anisotropic change in crystallite morphology with a change from the thin plates of native mineral to a more equidimensional habit [8]. The crystallite size as measured by X-ray diffraction has been previously reported to follow a sigmoidal growth type with increasing temperature [9]. There is also a significant increase in crystallite volume and

C. Greenwood (✉) · K. Rogers · S. Beckett
Department of Engineering and Applied Science,
Cranfield University, Shrivenham, Wiltshire SN6 8LA, UK
e-mail: c.greenwood@cranfield.ac.uk

K. Rogers
e-mail: k.rogers@cranfield.ac.uk

J. Clement
Faculty of Medicine, Dentistry and Health Science,
Melbourne Dental School, The University of Melbourne,
720 Swanston Street, Melbourne, VIC 3010, Australia

a concomitant change in mechanical properties such as increased elastic modulus. There is release of lattice bound carbon dioxide and water although there is also some evidence of extraneous ion apatite substitution [7, 10].

There has been considerable speculation regarding an apparent organic–apatite relationship that influences this apatite crystallisation behaviour. The organic matter has been described as possessing a 'protective' function that mechanically shields apatite crystallisation until the organic material degrades [11–13]. However, this relationship is almost entirely based on the simple observation that crystallisation always follows organic degradation.

The work presented here adopts a materials science approach to characterise the kinetics of the apatite crystallisation. This then, for the first time, enables quantitative determination of features such as activation energy and also direction dependent considerations. Further, it explores the organic–apatite relationship with respect to any modification of the transformation kinetics afforded through any organic shielding effects.

2 Materials and methods

Bovine and porcine femoral bone were employed to determine any significant inter-species variation in thermal behaviour. The bovine femoral bone was sourced from a local abattoir whilst the pig bone was obtained from the Veterinary Laboratories Agency. All the tissue was collected from animals of similar age (~3 years old) with no known disease. Bone samples were mechanically cut (limited heating) from the cortical bone of each femur and individual specimens of approximately equal size produced. The mass of each specimen was recorded prior to and following heat treatment.

Production methods for anorganic bone material that could be used to contrast the behaviour of native bone were carefully considered. Chemical methods (especially aqueous) were found not to be suitable due to concomitant modification of the bone mineral; we measured significant changes to coherence length and/or carbonate content. Thus specimens of anorganic bone were produced by heating bovine bone to 400 °C for 2 hours. X-ray diffraction indicated no significant change to the mineral microstructure. FTIR showed that the organic content was below the minimum detectable limit and that carbonate content was not significantly changed (see Fig. 1).These 'collagen free' bone specimens were then subjected to the same range of time and heat regimes as the other bone groups as described in Table 1. Bone specimens, were subject to a range of heat and time regimes in order to observe the kinetics of crystallisation. Heating temperatures ranged from 600 to 800 °C, over time periods of 5 minutes to 96 hours. Details of the heat and time regimes are presented in Table 1. A monometer furnace was heated to the required temperature before the bone specimens were placed into the chamber centre (within individual alumina crucibles). After each set time, specimens were removed from the furnace and left to cool naturally in air. Each specimen was subsequently pulverised using a Retsch–Mixer mill (MM2000) and individually sieved through a stainless steel mesh (106 μm) to produce a homogenous sample. X-ray diffraction was employed as the primary analysis tool. This has several advantages including being able to discriminate particular phases and crystallographic directions. Diffraction data peaks were parameterised by fitting independent analytical profiles (pseudo-Voigt) to each maxima. A careful inspection of the fitting was required to ensure confidence in the derived parameter values especially at the lower temperatures; significant peak overlap resulted in fitting ambiguity and where this occurred data was excluded from further analysis. Parameters fitted were the full widths at half maximum (fwhm), maxima positions and a shape variable. The fwhm's were corrected for instrumental broadening and employed to calculate coherence lengths using the Scherrer equation. Crystallographically, the change in apatite microstructure was semi-quantitatively mapped using Williamson–Hall plots. Although not presented here, these provided a direction dependent indication of lattice microstrain (gradients) and crystallite dimensions (intercepts) from diffraction peak broadening. These were consistent with those previously observed for bone.

To examine the crystallisation kinetics the Johnson–Mehl–Avrami (JMA) model was used to characterise apatite crystallisation. This model, using isothermal transformations of a material phase, has been applied in the form,

$$Y = 1 - \exp(-kt^n)$$

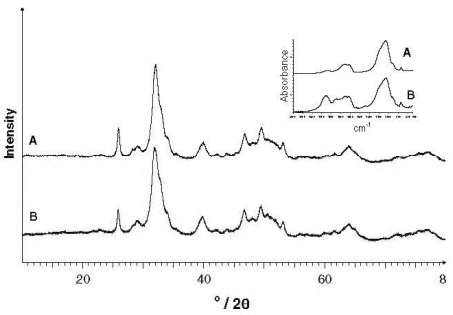

Fig. 1 X-ray diffractograms and FTIR spectra (*inset*) of anorganic bone material derived from heating at 400 °C for 2 h (*a*) and native unheated bovine bone (*b*)

Table 1 The range of heat and time regimes employed

Temperature (°C)	Time
500	48 & 96 h
550	48 h
575	24 h, 48 h
600	1 h, 2 h, 4 h, 6 h, 24 h, 48 h & 72 h
650	30 min, 1 h, 2 h, 4 h, 6 h, 24 h & 48 h
700	5 min, 10 min, 20 min, 30 min, 1 h, 2 h & 4 h
750	1 min, 5 min, 10 min, 20 min, 30 min, 1 h, 2 h & 4 h
800	1 min, 5 min, 10 min, 20 min, 30 min, 1 h, 2 h & 4 h
1000	5 & 10 min

where Y, as applied here, is the crystallisation fraction and k & n are empirically related to nucleation and growth rates (see Discussion). In this form, the Avrami constant k, may be used to describe any kth order process. Other forms of this model have been previously used but have been shown to be inappropriate for non first order kinetics [14] and the approach has also been shown to fail when applied to high levels of anisotropy [15]. The model describes sigmoidal transformations which are most frequently measured by differential scanning calorimetry or by a mass change determined from X-ray diffraction [16, 17]. We have adopted an approach, not previously reported, that employs apatite coherence length as the independent variable as this also appears to be isothermally sigmoidal in its transformation. The advantage of this novel approach is that the model may be applied independently to any crystallographic direction thus enhancing characterisation of the kinetics within morphologically anisotropic systems such as bone mineral. The diffraction maxima used for this analysis were the 002 and 030 as a compromise between overlap, intensity and differing lattice direction.

3 Results

Reproducibility was assessed by repeated heating, data collection and parameterisation of 4 independent samples from each group examined (bovine, porcine & anorganic). For each group the repeatability of the diffraction parameter values was better than 3 %. A qualitative assessment of diffraction data quality may be obtained from inspection of Fig. 2 where a typical data series for bovine tissue is presented. The change from a poorly crystalline native phase to a highly ordered mineral after 72 h at 600 °C is readily apparent. Peak parameterisation of such series through a range of temperatures enabled production of the characteristic sigmoidal curves illustrated for the bovine

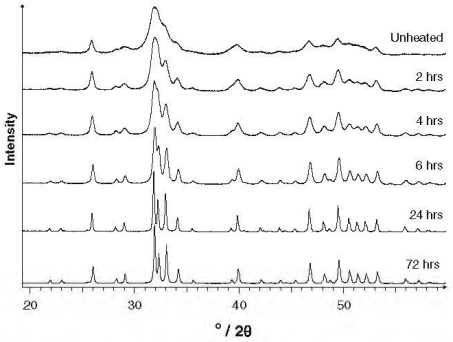

Fig. 2 X-ray diffractograms of (from *top* to *bottom*) unheated bovine bone and bovine bone specimens heated at 600 °C for 2, 4, 6, 24 and 72 h. For comparison, diffractograms have been stacked

tissue within Fig. 3. Similar curves were obtained for each bone group and each crystallographic direction. Crystallinity values were used to construct plots (Fig. 4) to derive the Avrami parameter values. These were produced from the conventional linearisation of the JMA model equation (above) where the terms are defined previously and where:

$$\ln(-\ln(1-y)) = \ln k + n \ln t$$

Limitations of the JMA model arising from crystal anisotropy are not apparent within the data presented here; the plots shown in Fig. 4 are linear, within experimental errors. Values for the Avrami constants are presented in Table 2 for each bone group at two temperatures and two crystallographic directions. At the lower temperature, n was not significantly different from unity for all bone groups and both directions. At 800 °C, n was, in all cases <1 and approached 0.5 especially along $\langle 00\ell \rangle$. The Avrami rate constant, k was significantly different when comparing bone groups at 650 °C and when comparing between temperatures.

The crystallisation activation energy was derived from regular Arrhenius analyses using the 50 % crystallinity points and plotting (Fig. 5),

$$\ln k = \ln A - E_a / RT$$

where E_a is the activation energy, R is the gas constant, T is the absolute temperature and k is the rate constant. The activation energies are presented within Table 3 for each bone group and crystallographic direction. There are no significant differences between bone groups or crystallographic directions. Errors associated with the Avrami parameter values and the activation energies were derived by propagating experimental errors from the crystallisation points employed.

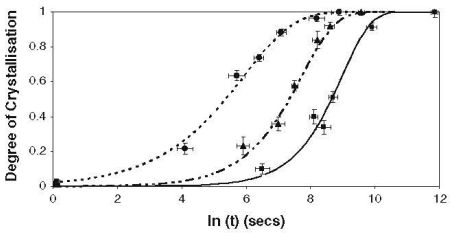

Fig. 3 Sigmodial curves (fitted using the Avrami equation) representing the crystallisation process for bovine bone specimens heated to 600 °C (*black square*), 700 °C (*black triangle*) and 800 °C (*black.circle*)

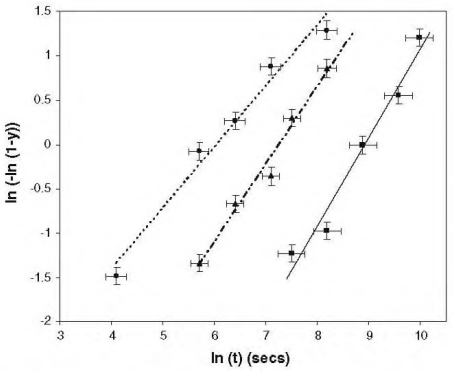

Fig. 4 The coherence length data fitted to the Avrami model. The slopes and intercepts yield values of n and k respectively for bovine bone heated at 600 °C (*black square*), 700 °C (*black triangle*) and 800 °C (*black circle*)

4 Discussion

The JMA model and X-ray diffraction have previously been used to study hydroxyapatite transformation kinetics [18, 19]. In all such studies the dependent variable used to derive the sigmoidal curves was the fraction of transformed HA. For example, the kinetics of an aragonite to hydroxyapatite process has recently been characterized and values for n (0.5) and the activation energy (77.8 ± 5 kJ mol^{-1}) reported [20].

In contrast to these previous studies, the application of the JMA model to apatite coherence length is unique and has some advantages. For classical crystal growth the parameter *'n'* reflects the spontaneous nucleation rate and the dimensional increase in crystal volume. Thus, for 3 dimensional growth with unsaturated nucleation points, n would have ideally a value close to 4 and if the nucleation rate were zero, then $n \approx 3$. When applying the JMA model to 3 dimensional, diffusion based growth, n would be expected to have a value close to 1.5. Unfortunately, in many cases the interpretation of n is ambiguous because, if $n < 4$, contributions from nucleation rate and growth dimension are confounding [21]. In contrast, our approach using a single crystallographic direction fixes the dimensionality to unity. Thus for first order kinetics n would have a value of 2 if growth and nucleation were occurring simultaneously and a value of 1 if the nucleation sites were saturated. In this case, for diffusion dominated growth, n would have a value of 0.5.

Table 2 Calculated values of n and k obtained by fitting the coherence length in the ⟨00ℓ⟩ and ⟨0k0⟩ crystallographic directions, to the Avrami model

	Porcine	Bovine	Anorganic
⟨00ℓ⟩			
650 °C			
n	0.94 ± 0.23	0.99 ± 0.01	0.88 ± 0.03
k	1.29 ± 0.27	0.49 ± 0.04	0.37 ± 0.08
800 °C			
n	0.67 ± 0.03	0.66 ± 0.15	0.53 ± 0.02
k	5.77 ± 0.73	4.04 ± 1.03	3.26 ± 0.66
⟨0k0⟩			
650 °C			
n	1.07 ± 0.04	1.14 ± 0.06	1.11 ± 0.09
k	0.80 ± 0.17	0.36 ± 0.09	0.25 ± 0.08
800 °C			
n	0.76 ± 0.05	0.85 ± 0.17	0.71 ± 0.06
k	6.00 ± 0.52	4.54 ± 1.03	3.21 ± 0.95

The results presented here thus suggest that for all groups the apatite crystallisation changes to a diffusion limited process at higher temperatures. This is unsurprising and typical of many such thermally driven crystallisation

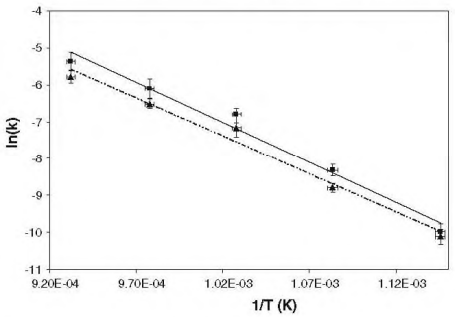

Fig. 5 Arrhenius plots for bovine bone in ⟨00ℓ⟩ (*black square*) and ⟨0k0⟩ (*black Triangle*) crystallographic directions. The gradient of the linear plots are used to calculate the Ea using the Arrhenius equation

Table 3 Calculated activation energies for all three bone groups in the ⟨00ℓ⟩ and ⟨0k0⟩ crystallographic directions

	⟨00ℓ⟩ (kJ mol ^{1})	⟨0k0⟩ (kJ mol ^{1})
Porcine	195 ± 4	185 ± 4
Bovine	181 ± 4	171 ± 5
Anorganic	195 ± 5	176 ± 3

processes. It is demonstrated convincingly in the ⟨00ℓ⟩ direction where the greater reaction rate at 650 °C leads perhaps to a diffusion limited growth prior to that within the ⟨0k0⟩ direction. A similar but converse change was apparently observed previously in an aragonite–hydroxyapatite transformation [20] although the Avrami exponent was fixed to a first order rate equation. The crystallisation rates, as expected, increase significantly for all bone groups as the temperature is increased. However, there are significant differences between the bone groups with the anorganic material possessing the lowest rate. Species differences in thermal behaviour have been observed previously [22]. This trend is consistent between temperature and crystallographic direction although at higher temperatures the difference becomes smaller (a direct comparison between temperature groups is not appropriate as the units of 'k' are s^{-n}). The crystallisation rate is, in general, influenced by factors such as catalytic action and intrinsic sources of additional energy. The relative mass loss on heating was greatest for the porcine tissue and least for the anorganic material when compared at the same time–temperature points (e.g. 40.3 % compared to 30.0 % after 2 h at 650 °C). This mass loss arises from evolution of water and volatiles, and combustion of organic materials [7]. In the case of collagen, an exothermic reaction at ~350 °C causes an enthalpy change of −8.4 kJ g^{-1} [23]. This coupled with the slightly greater lattice strain energy observed within the porcine tissue, contribute to its greater reaction rate.

The results also provide a mean crystallisation activation energy of 183 ± 8 kJ mol^{-1}. There are no statistical differences between bone groups or crystallographic directions suggesting that the fundamental growth and recovery mechanisms are similar in all cases. These values compare well to previous work examining the crystallisation of hydroxyapatite from amorphous or sol–gel phases [24, 25]. Respective values of 274 and 235 kJ mol^{-1} were determined from DSC and TGA measurements. The lower value from our work may be attributed to initial, nanocrystalline state of our material.

5 Conclusions

An aim of this work was to examine the previously described phenomenon of the organic matter in some manner protecting the mineral from crystallisation [26, 27]. A diffusion barrier mechanism had been suggested to support this hypothesis [28]. Assuming that any residual organic material remaining with our anorganic samples did not have a disproportionate effect upon the crystallisation process, then our study reveals little evidence to support any such 'shielding' action. The principal kinetic characteristics associated with the anorganic tissue were not significantly different to those of the fully organic native bone tissues, with the exception of the crystallisation rate. As the rate was least for the anorganic material it could be concluded that, rather than a protecting effect, the organic component promotes the crystallisation.

Acknowledgments Staff at Cranfield University are thanked for their assistance during this study. The authors also thank M. Kirby and staff from the Veterinary Laboratories Agency. Pascaline Grandjean and Alison Nicholson are thanked for their research project work which has supported this study.

References

1. Murugan R, Panduranga-Rao K, Sampath-Kumar TS. Heat-deproteinated xenogeneic bone from slaughterhouse waste: physico-chemical properties. Bull Mater Sci. 2003;26:523–8.
2. Yan J, Daga a, Kumar R, Mecholsky JJ. Fracture toughness and work of fracture of hydrated, dehydrated, and ashed bovine bone. J Biomech. 2008;41:1929–36.
3. Ivankovic H, Gallego Ferrer G, Tkalcec E, Orlic S, Ivankovic M. Preparation of highly porous hydroxyapatite from cuttlefish bone. J Mater Sci Mater Med. 2009; 20:1039-46.
4. Emadia R, Roohani Esfahania SI, Tavangarian F. A novel, low temperature method for the preparation of β-TCP/HAP biphasic nanostructured ceramic scaffold from natural cancellous bone. J Mater Lett. 2010;64:993–6.
5. Volkmer D, Sichlau M, Rapp TB. The use of radiofrequency ablation in the treatment of musculoskeletal tumors. J Am Acad Orthop Surg. 2009;17:737–43.
6. Peters F, Schwarz K, Epple M. The structure of bone studied with synchrotron X-ray diffraction. Thermochim Acta. 2000;361: 131–8.
7. Mkukuma LD, Skakle JMS, Gibson R, Imrie T, Aspden RM, Hukins DWL. Effect of the proportion of organic material in bone on thermal decomposition of bone Mineral: an investigation of a variety of bones from different species using thermogravimetric analysis coupled to mass spectrometry, high-Temperature X-ray diffraction, and fourier transform infrared spectroscopy. Calcif Tissue Int. 2004;75:321–8.
8. Rogers KD, Daniels P. An X-ray diffraction study of the effects of heat treatment on bone mineral microstructure. Biomaterials. 2002;23:2577–85.
9. Piga G, Malgosa A, Thompson TJU, Enzo S. A new calibration of the XRD technique for the study of archaeological burned human remains. J Archaeol Sci. 2008;35:2171–8.
10. Neuman WF, Weikel JR. Recrystallization in bone mineral. Ann N Y Acad Sci. 1955;60:685–95.
11. Roberts S, Smith C, Millard A, Collins M. The taphonomy of cooked bone:characterizing boiling and its physico-chemical effects. Archa. 2002;44:485–94.
12. Trueman CNG, Behrensmeyer AK, Tuross N, Weiner S. Mineralogical and compositional changes in bones exposed on soil

surfaces in Amboseli National Park, Kenya: diagenetic mechanisms and the role of sediment pore fluids. J Archaeol Sci. 2004;31:721–39.
13. Wang XY, Zuo Y, Huang D, Hou XD, Li YB. Comparative study on inorganic composition and crystallographic properties of cortical and cancellous bone. Biomed Environ Sci. 2010;23:473–80.
14. Marangoni AG. On the use and misuse of the Avrami equation in characterization of the kinetics of fat crystallisation. J Am Oil Chem Soc. 1998;75(1465):7.
15. Shepilov MP, Batick DS. Computer simulation of crystallisation kinetics for the model with simultaneous nucleation of randomly-oriented ellipsoidal crystals. J Non-Cryst Solids. 1994;171:141–56.
16. Sze Ho Lam R, Rogers MA Experimental validation of the modified Avrami model for non-isothermal crystallisation conditions. Cryst Eng Commun. 2011;13:866-75.
17. Supaphol P. Application of the Avrami, Malkin, and Urbanovici-Segal macrokinetic models to isothermal crystallisation of syndiotactic polypropylene. Thermochim Acta. 2001;370:37–48.
18. Kasioptas A, Geisler T, Putnis CV, Perdikouri C, Putnis A. Crystal growth of apatite by replacement of an aragonite precursor. J Cryst Growth. 2010;312:2431–40.
19. Najafia H, Nematia ZA, Sadeghianb Z, Sohrabia N. Crystallisation kinetics of hydroxyapatite nano-films on stainless steel through a sol–gel Process. Iran J Pharm Sci. 2008;4:135–40.
20. Ivankovic H, Tkalec E, Orlic S, Gallego Ferrer G, Schauperl Z. Hydroxyapatite formation from cuttlefish bones: kinetics. J Mater Sci: Mater Med. 2010;21:2711-22.
21. Sze Ho Lam R, Rogers MA. Activation energy of crystallisation for trihydroxystearin, stearic acid, and 12-hydroxystearic acid under non-isothermal cooling conditions. Cryst Growth Des. 2011;11:3593-9.
22. Beckett S, Rogers KD, Clement JG. Inter–Species variation in bone mineral behaviour upon heating. J Forensic Sci. 2011;56:571–9.
23. Lozano LF, Pena-Rico MA, Jang-Cho H, Heredia A, Villarreal E, Ocotldn-Flores AL, et al. Thermal properties of mineralized and non mineralized type I collagen in bone. Mater Res Soc Symp Proc. 2002;724:123–8.
24. Gross KA, Gross V, Berndt C. Thermal analysis of amorphous phases in hydroxyapatite coatings. J Am Ceram Soc. 1998;81:106–12.
25. Milev A, Kannangara GSK, Ben-Nissan B. Morphological stability of hydroxyapatite precursor. J Mater Lett. 2003;57:1960–5.
26. Person A, Bocherens H, Mariotti A, Renard M. Diagenetic evolution and experimental heating of bone phosphate. Palaeogeogr Palaeocl. 1996;126:135–49.
27. Etok SE, Valsami-Jones E, Wess TJ, Hiller JC, Maxwell CA, Rogers KD, et al. Structural and chemical changes of thermally treated bone apatite. J Mater Sci. 2007;42:9807–16.
28. Walsh WR, Ohno M, Guzelsu N. Bone composite behaviour—effects of mineral organic bonding. J Mater Sci Mater Med. 1994;5:72–9.

Cryst. Res. Technol. **48**, No. 12, 1073–1082 (2013) / **DOI** 10.1002/crat.201300254

Initial observations of dynamically heated bone

C. Greenwood*[1], K. Rogers[1], S. Beckett[1], and J. Clement[2]

[1] Department of Engineering and Applied Science, Cranfield University, Shrivenham, Wiltshire SN6 8LA, UK
[2] Faculty of Medicine, Dentistry and Health Science, Melbourne Dental School, The University of Melbourne, 720 Swanston Street, Melbourne 3010, Vic., Australia

Received 12 August 2013, revised 16 October 2013, accepted 22 October 2013
Published online 15 November 2013

Key words Hot Stage X-ray Diffraction (HS-XRD), crystal structure, crystallinity, hydroxyapatite, dynamically heated bone, lattice parameters.

Understanding the chemical changes within bone during heat treatment has become essential within many fields including biomaterials, archaeology and forensic science. All current approaches report the systematic heating and cooling of bone specimens (a 'static' approach). These provide information on modifications to mineral structure and chemistry including recrystallisation and thermal decomposition from bone specimens cooled to room temperature. In order to understand these fundamental processes further, we adopted, for the first time, a dynamic heating protocol coupled to an X-ray diffraction probe, which provides in situ analysis at temperature. This approach allows physico-chemical processes to be observed at elevated temperatures for five different bone types: bovine, porcine, human, rostrum and red deer antler. The results, when compared to static heating studies, illustrate individually the effects of heating and cooling upon bone mineral. On heating, the onset of recrystallisation occurs rapidly over a short temperature range for all bone types. It is proposed the continued growth of the hydroxyapatite crystals is limited by the mineral to organic ratio. Investigation of the lattice parameters has also indicated significant differences between the bone types, suggesting species differentiation is possible using X-ray diffraction analysis. Statistical analysis of the 'a' axis lattice parameter data revealed human bone is distinguishable from the other bone types.

1 Introduction

In recent years, an increasing number of studies have examined the behaviour of bone during static heat treatment. In general, the evolution of absorbed (up to 200 °C) and lattice incorporated water (up to 400 °C) is observed [1] whilst denaturing and combustion of the organic matrix is observed at temperatures up to 550 °C [2]. Between 600 and 700 °C, a rapid change in the mineral microstructure (termed the '*onset of recrystallisation*' in this paper), as demonstrated by an increase in both crystallite size and lattice order is well documented [3,4]. With increasing temperature, the crystals continue to grow which is commonly referred to as the recrystallisation process. At temperatures above 800 °C, additional phases such as magnesium oxide, calcium oxide and tetra-calcium phosphates are observed due to the thermal decomposition of the apatite. The decomposition products are thought, to a certain extent, to be dependent upon the original apatite chemistry. Melting of bone occurs at temperatures exceeding 1600 °C [5].

The loss of carbonate ions (CO_3^{2-}) from the mineral matrix has also been of significant interest in heated bone studies. In native bone mineral, carbonate ions are incorporated into the apatite lattice through the substitution of hydroxide ions (OH^-) which is termed A-type substitution as well as for the phosphate ions (PO_4^{3-}) which is known as B-type substitution [6]. Labile carbonate ions, located on the apatite surface, are also present in bone. B-type carbonate substitution is dominant in native bone specimens [7]. During heat treatment, the loss of both A and B type carbonate cause changes in the lattice parameters. The loss of A type carbonate causes expansion in the 'a' axis and a contraction in the 'c' axis. Conversely, the loss of B-type carbonate results in a contraction in the 'a' axis whilst an expansion in the 'c' axis is observed [8]. During heating, it has also been suggested

*Corresponding author: e-mail: c.greenwood@cranfield.ac.uk

carbonate ions from the B type sites (PO_4^{3-} vacancies) are incorporated into the A type site (OH^- vacancies) [9]. This is thought to occur in the temperature range 300 – 700 °C. Differential thermal analysis studies have also shown that the weight percentage of carbonate has an impact on the temperature response of synthetic carbonated hydroxyapatites [10].

Understanding the effect of heat treatment on bone mineral has a significant place within biomedical research, forensic science and archaeology. In biomedical research, heating bone specimens is essential for producing sterilised hydroxyapatite bioceramics which are frequently employed for medical applications such as allograft and xenograft replacement [11,12]. Consequently, many researchers have investigated the effect of heat treatment on bone across a wide temperature range (60 – 900 °C) [11,13]. At higher temperatures (>700 °C), microstructural changes to the mineral may modify the bio-performance of these materials, potentially to the detriment of the patient.

Bone that has been exposed to elevated temperatures is also of relevance to forensic science. Investigations of cases where an individual has burnt a body to conceal criminal evidence, benefited from studies of the microstructural and phase changes within heated bone specimens [14–18]. Most recently, the problem of identifying the species of a small fragment of burnt bone using X–ray diffraction has been of particular interest. Analytical solutions to this challenge could prove invaluable for legal cases [5,19]. However, study results within this area are conflicting and further research into the fundamental causes for differences in X-ray diffraction parameters of bone between species is required.

Archaeological bone that is found after cremation or cooking often shows indications of being burnt. This has resulted in an increasing number of studies concentrating on the effect of heat treatment on bone mineral, allowing cooking practices [20] and funeral practices of our ancestors to be further understood [21]. Burnt bone is often rejected as suitable material for isotope and DNA analysis due to the changes in composition during heating [22–24]. The potential for obtaining an isotopic or DNA profile from burnt bone material has also recently been investigated.

As highlighted, static heating studies, in which bone is heated to temperature, kept at temperature and allowed to cool prior to analysis, have provided indications of microstructural changes and thermal decomposition processes. Unfortunately, they cannot strictly provide a complete model of the physico-chemical changes as the confounding effects of cooling are not fully known. For the first time, the work presented here exploits a controlled hot stage X-ray diffraction system (HS-XRD) to provide dynamic data (in situ analysis at temperature) on the physico-chemical changes within bone mineral during heat treatment. The approach of dynamically heating bone is expected to be immensely beneficial across a wide range of disciplines and also validate the many observations that have been made from static studies.

2 Materials and methods

To investigate possible species differentiation through heated bone, porcine, bovine and human specimens were obtained. These samples were taken from the diaphysis of the femoral bone. The bovine and porcine specimens were obtained from the Animal Health Veterinary Laboratories Agency (AHVLA) and were collected from animals of similar age (~3 years old) with no known disease. Human bone was collected from a 55 year old, male donor, with full ethical approval and relatives' permission. Previous research suggested that the rate of recrystallisation upon heating can differ between species due to differences in the mineral to organic ratio [25]. Thus, two contrasting bone types were also examined, whale rostrum (from *Mesoplodon densirostris*) and red deer antler. They differ with respect to the relative amount of organic matrix and the size of the mineral crystals. Rostrum exhibits very little collagen but has significantly larger, more ordered mineral crystals than red deer antler, which exhibits smaller crystals with a large quantity of collagen [26–29]. Human, porcine and bovine bone lie within the parameters of these two extremes in terms of average crystallite size [5,25].

In order to homogenise the samples and reduce preferred orientation effects, each bone specimen was pulverised using a Retsch Mixer Mill (MM2000) and individually sieved through a stainless steel mesh (106 μm). X-ray diffraction was employed as the primary analysis tool due to its capabilities to measure crystallinity along different crystallographic directions as well as being able to differentiate between mineral phases. A comprehensive definition of 'crystallinity' can be found in [30] which states crystallinity refers to the 'amount of long range structural order within a material that can be moderated by features such as grain boundaries and point/linear/planar defects.' In this paper, 'crystallinity' is a measure of coherent domain size.

Approximately 0.5 g of bone powder from each specimen was individually packed into an alumina heating stage holder and loaded into an Anton Paar HTK-1200 high temperature X-ray diffraction chamber. A dynamic heating rate significantly lower than a typical static heating rate was employed and a temperature range from 25 – 900 °C was investigated with diffraction data collected at 25, 100, 200, 350, 400, 450, 500, 550 and 580 °C. From 580 °C, data was collected at intervals of 10 °C, up to and including the final temperature of 900 °C due to the nature of the recrystallisation process. Based on previous work, the onset of recrystallisation was expected to occur over a small temperature range, beginning at approximately 600 °C [5,25]. The heating rate was equivalent to 10 °C per minute. A 10 minute dwell period was employed at each temperature to allow collection of the diffraction data. The same regimen was employed during the cooling down period.

XRD data collection was carried out with a Panalytical X-pert diffractometer and Cu Kα radiation. A strip detector was used to collect data with stepped scans across an angular range of 15 – 80 °/2θ (4.43 – 0.78 Å d-spacing). The count time at each step was equivalent to five seconds. The structural parameters derived from the X-ray diffractograms included lattice parameters and coherence lengths. Lattice parameters were examined in order to observe chemical modification of the mineral due to ionic exchanges. To obtain the lattice parameters, Bruker Topas software (Version 4.1, 2008) was used for whole pattern fitting refinement of the diffraction profiles. Sample displacement was also refined and data corrected according to conventional X-ray diffraction analysis [31]

Coherence lengths (CL) were calculated to evaluate the change in structural order (size and strain) of the hydroxyapatite crystals. Two different crystallographic directions, <00ℓ> and <0k0>,were chosen to investigate the non-isotropic growth of crystals. Asymmetrical pseudo-voigt peaks were fitted to the 002 and 030 diffraction peaks for all diffraction profiles. Using these peaks was deemed a good compromise as although not the most intense, they are not overlapped by other diffraction peaks and offer differing lattice direction. The Scherrer equation was used to calculate the coherence length in the aforementioned crystallographic directions;

$$CL = \frac{k\lambda}{(\beta - \beta_{IRF})\cos\theta} \tag{1}$$

where k is Scherrer's constant (0.89), λ is the wavelength used (1.54 Å), β is the full width half maximum of the diffraction peak for the sample, β_{IRF} refers to full width half maximum of the NIST SRM64C silicon standard diffraction peaks and θ is the angle of diffraction. The silicon standard is used in this equation to correct for instrumental broadening.

A Wilcoxon Signed Rank test was used to statistically compare the lattice parameters obtained during this study. This test was deemed to be the most appropriate and robust statistical analysis as it is the non-parametric analogue to the paired two-sample t-test and does not assume normal distribution. The data presented in this paper revealed a non-normal distribution.

3 Results

3.1 General observations During heating, there was no change in the diffraction peaks for each bone type until approximately 580 °C for red deer antler, 600 °C for bovine, porcine and human bone and 650 °C for rostrum; where in each case a rapid change in the diffraction peaks was observed. The broad, overlapping peaks rapidly became sharper and more resolved within a temperature range of approximately 40 °C (figure 1). This rapid sharpening of the diffraction peaks, which denotes a significant increase in the size of the crystals as well as in the structural order of the mineral, will be referred to as the 'onset of recrystallisation' within this paper. The continued growth of the crystals after this point will be referred to as 'recrystallisation' for the remainder for this paper. For all bone types, during cooling from 900 °C to room temperature, no changes in the diffraction peaks were observed. Small amounts of calcium oxide (CaO) and magnesium oxide (MgO) were observed at temperatures >800 °C for bovine, porcine, human and rostrum specimens. MgO was the only additional phase observed in the data for the red deer antler specimen.

3.2 Coherence length A sigmoidal relationship between the recrystallisation process and temperature is demonstrated when coherence length (in both crystallographic directions), is plotted against the temperature (figure 2). The temperature at which the onset of recrystallisation began differed according to bone type, with the onset of recrystallisation of the red deer antler mineral (~590 °C) occurring at a much lower temperature than rostrum (~650 °C). The onset of recrystallisation of bovine, porcine and human bone mineral occurred at similar temperatures of approximately 600 °C. These temperatures were measured from the point at which the steepest gradient change was observed in the first differential of the coherence length data.

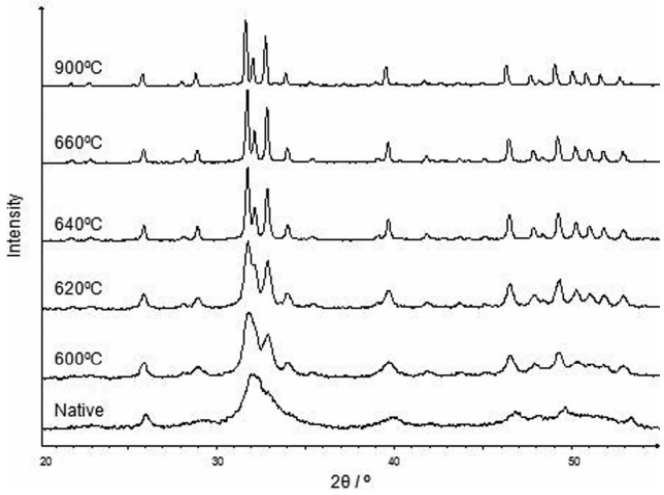

Fig. 1 X-ray diffractograms (in ascending order) of the bovine bone specimen prior to heating (native) and dynamically heated to 600, 620, 640, 660 and 900 °C depicting the short temperature range in which the onset of recrystallisation occurred. A similar pattern was observed for all bone types.

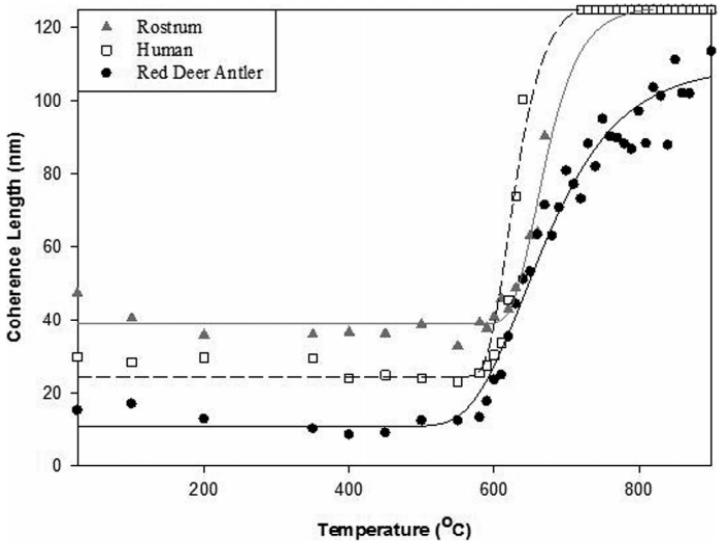

Fig. 2 Coherence length data for rostrum, human and red deer antler in the <00ℓ> direction plotted against temperature reveals a sigmoidal relationship. The same relationship was observed in the <0k0> direction for all bone types.

Table 1 Temperature (°C) at which 50% recrystallisation was calculated (including errors), for each bone type calculated from the sigmoidal curves of coherence length verses temperature.

	<00ℓ>	<0k0>
Rostrum	700 ± 3	702 ± 5
Bovine	667 ± 7	665 ± 5
Red Deer Antler	663 ± 7	658 ± 7
Porcine	632 ± 4	630 ± 3
Human	631 ± 3	635 ± 3

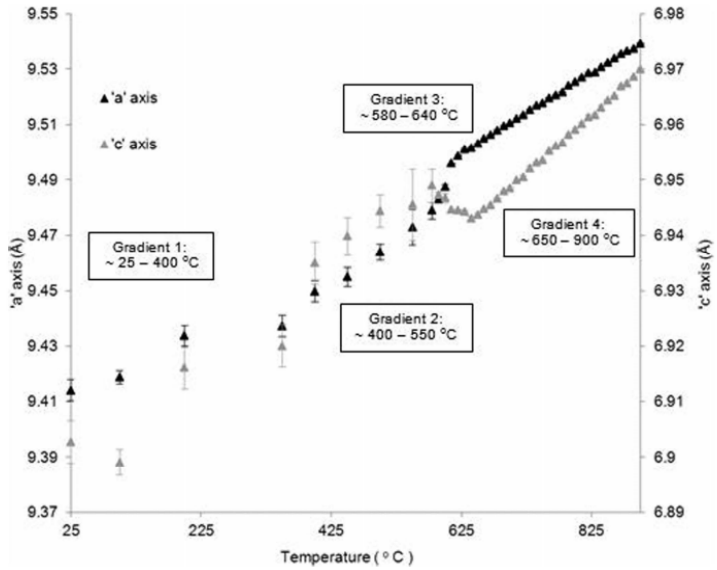

Fig. 3 Plot highlighting the four gradient changes when lattice parameter data ('a' and 'c' axes) are plotted against temperature for the human bone specimen.

Interestingly, once the onset of recrystallisation had occurred, the continued growth of the crystals, as indicated by an increase in the coherence length, differed between the bone types. This is evident by the difference in the gradients of the 'linear' section of the sigmoidal curves for each bone type (figure 2). Recrystallisation of the rostrum apatite occurred over a short temperature range whilst for red deer antler, this process occurred over a wider temperature range. At the end of the heating regimen, the coherence length data for rostrum was significantly larger than the coherence length data calculated for the red deer antler (figure 2).

In order to semi-quantify the aforementioned coherence length data, the sigmoidal curves were used to calculate the temperature at which 50% recrystallisation occurred as a function of crystallographic direction for each bone type (Table 1). The calculated values for the two crystallographic directions were, within errors, the same for each bone type. Differences between the values according to bone type are evident. Rostrum mineral reached 50% crystallisation at approximately 700 °C, bovine and red deer antler by approximately 665 °C and porcine and human by approximately 630 °C.

3.3 Lattice parameters Figure 3 shows the 'a' and 'c' lattice parameter values for human bone plotted against temperature. Four distinct transitional regions, demonstrated by a change in gradient, were observed in both the 'a' and 'c' lattice parameter data. The 'a' axis value increased throughout heat treatment. In contrast,

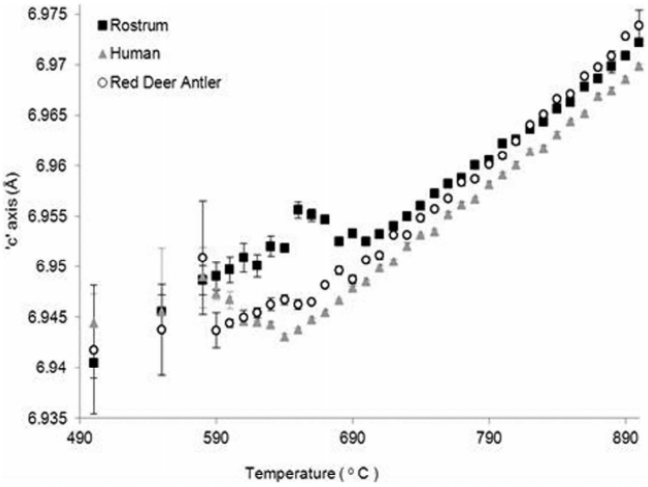

Fig. 4 Plot of the 'c' axis lattice parameter data for rostrum, red deer antler and human which highlights the difference in the gradient change within the temperature range at which 50% recrystallisation was calculated for each specimen temperature.

the 'c' axis value initially decreased (Gradient 1), then increased up to the temperature of approximately 50% recrystallisation (Gradient 2), where upon a sudden decrease (Gradient 3) followed by an increase in gradient (Gradient 4) occurred (figure 3). Similar lattice parameter behaviour was observed for all bone types although changes in the 'c' axis were less prominent in the red deer antler specimen as shown in figure 4.

During heat treatment, the change in lattice parameters can be attributed to three processes; the loss of lattice incorporated water (up to 400 °C), thermal expansion and ion exchange [1,32,33]. Carbonate ion substitutions in particular have been shown to have a significant effect on the lattice parameters of biological and synthetic apatite, depending on whether A – or B – type carbonate is lost or gained during heat treatment [8,9]. To maintain a charge balance in the apatite structure during the loss of carbonate in the form of carbon dioxide (CO_2), other chemical exchanges must occur during heat treatment [34]. Consequently, we developed a simple linear model, shown in Eq. (2), which allowed qualitative analysis of the amount of A – and B – type carbonate required to alter the lattice parameter data that observed. This calculation enabled assessment of whether the change in lattice parameter values could be explained through simple carbonate ion exchange and thermal expansion only or whether other processes are also significantly responsible for the observed changes. The linear models used (shown in Eq. (2)) are based on previous work [8]. The study observed the individual change in the gradients of the lattice parameter data (for the 'a' and 'c' axes) during the incorporation of increasing amounts of pure A – and B – type carbonate during the synthesis of calcium hydroxyapatite [8].

$$\text{'}a\text{'} = x + tecT + \mathrm{A}\alpha + \mathrm{B}\beta \quad \text{and} \quad \text{'}c\text{'} = y + tecT + \mathrm{A}\gamma + \mathrm{B}\delta \tag{2}$$

In Eq. (2), 'a' and 'c' are calculated to give 'a' and 'c' axis lattice parameter data which were plotted against temperature to graphically simulate our data. 'x' refers to the 'a' axis lattice parameter data whilst 'y' corresponds to the 'c' axis lattice parameter data of native, unheated bone. These values differed depending on bone type and were calculated from the X-ray diffraction data collected at 25 °C. 'tec' relates to the thermal expansion coefficient, which corresponds to the linear transitional regions 2 and 4 (shown in figure 4) and T relates to the temperature. Values for α, β, γ and δ were obtained from previous work (described above) and correspond to the gradient values obtained from incorporation of increasing amounts of A – or B – type carbonate [8]. A and B relate to the relative percentage of A and B type carbonate respectively.

Table 2 The amount of B – type carbonate (%) required to simulate our data for both the 'a' and 'c' axes, calculated using our aforementioned model. In this example, A-type carbonate was kept constant at 0%. Although not recorded here, the model was also used to observe increasing amounts of A-type carbonate. The relationship remained the same as that recorded below.

	a -axis	c- axis
Bovine	3.8	3.6
Porcine	4.4	0.4
Human	2.4	1.5
Red Deer Antler	5	1
Rostrum	4	2.1

The model was applied to the regions $\sim 400 > T < 550$ °C and ~ 650 °C $> T < 900$ °C, where the gradient was constant for all specimens, suggesting that thermal expansion was predominately responsible for the change in the lattice parameters. By applying the model to these regions, it was possible to determine whether the change in gradient between approximately 580 and 640 °C is solely due to the loss or gain of carbonate or whether additional and/ or other chemical exchanges must have occurred. Crucially, if the only dominant chemical process occurring was the loss or gain of carbonate ions, the amount of carbonate required to alter the lattice parameters would be similar for both the 'a' and 'c' axes.

Based on our model, this was not the case for the majority of bone types. The amount of carbonate required to simulate the changes in the 'a' and 'c' lattice parameters differed significantly for porcine, human, rostrum and red deer antler (Table 2). According our model, less B-type carbonate was required to simulate the changes in the 'c' axis in comparison to the 'a' axis. This is highlighted by both the porcine specimen, where the difference in amount of carbonate (%), is a factor of 10 and the red deer antler specimen, where a difference of a factor of 5 is observed. The amount of carbonate required to simulate the lattice parameter data for the bovine specimen was consistent for both 'a' and 'c' axes.

3.4 Species differentiation: statistical analysis For this analysis, the 'a' axis lattice parameter data in the temperature range 800 – 900 °C was used. The lattice parameters are assumed to be affected only by linear thermal expansion rather than ionic exchange for all specimens in this region. Bovine and porcine specimens were not significantly different, $p > 0.05$. Furthermore, these specimens were not significantly different to that of the red deer antler. Human was significantly different from all the bone types investigated with a confidence level of 95%.

4 Discussion

4.1 General observations As expected from previous static studies [5,16–18,25], the results outlined in this paper have shown that for all bone types, the onset of recrystallisation of bioapatite crystals occurs at temperatures $\geq$590 °C. However, dynamically heating bone has, for the first time, revealed that the onset of recrystallisation occurs rapidly over a short temperature range. This is substantiated by the change from broad diffraction peaks to highly resolved, sharp peaks in the diffractogram. In comparison, previous static studies have documented the recrystallisation process over a period of time at a constant temperature [5,16–18,25]. During cooling in our experiments, the full width maximum values of the diffraction peaks were consistent (the peaks remained unchanged), suggesting cooling has little or no effect on the recrystallisation process. The presence of CaO and MgO in all bone types except red deer antler (only MgO was observed for this specimen) has been observed in previous static studies [5,35]. Although the absence of CaO in the red deer antler data may suggest the apatite in this system is calcium deficient [35], this requires further investigation.

4.2 Coherence length Quantifying the temperature at which 50% recrystallisation occurs for two different crystallographic directions, has shown the transformation from highly anisotropic to more ordered, larger, equidimensional crystallites (See Table 1). This confirms what has also been observed in previous static heating studies [5,36]. The structurally equivalent 'a' and 'b' axes of the hydroxyapatite crystallites must grow at a faster rate in order to reach 50% recrystallisation at the same temperature as the 'c' axis. The growth of the crystals in this manner has been associated with lattice microstrain, which may be a source of energy driving the transformation from an anisotropic state to a more ordered equidimensional habit [5].

The temperature at which recrystallisation of bone mineral occurs is greater for rostrum in comparison to the other bone types. It is proposed that this is associated with the lattice energy and disorder within the bone mineral of the different specimens. The crystals associated with rostrum have the largest coherence length and therefore a greater microstructural order than the other bone types. Consequently, the rostrum mineral will have significantly less lattice energy than the apatite structure associated with the other bone types were the coherence length was much smaller. The increased lattice energy contributes to reducing the amount of energy input required to promote crystal growth during heat treatment. Furthermore, due to their initially smaller size, the crystals associated with bovine, porcine, human and red deer antler exhibit a greater surface area to volume ratio than rostrum crystals which represents a higher energy state. Consequently, the onset of recrystallisation of rostrum mineral occurs at a higher temperature than the other bone types.

This research has also shown that the coherence length at 900 °C differs between the bone types which are highlighted by the rostrum and red deer antler data (figure 2). Assuming there is little strain associated with the crystals after the onset of recrystallisation [3], the coherence length data suggests the growth of the red deer antler crystals is retarded during heat treatment. One possible explanation may be that the recrystallisation process is limited by the organic to mineral ratio within a specimen. Red deer antler has a greater ratio of collagen to mineral and therefore less mineral material and larger 'voids' between the crystals present than rostrum. Consequently, it is proposed that the inter-crystal connectivity is much lower due to fewer grain boundaries and less growth fronts, limiting the growth of the crystals within red deer antler compared to rostrum.

4.3 Lattice parameters Through dynamic heating, four distinct gradients have been observed in the 'a' and 'c' axis lattice parameters for all specimens. The first gradient (25 to 400 °C), which represents an increase for the 'a' axis is possibly a result of the loss of lattice incorporated water. The linear relationship observed for the second (400 to 550 °C) and fourth gradient (~700 to 900 °C) regions, where the gradient was constant for all specimens and for both axes, suggests the material is remaining constant and the increase observed is due to thermal expansion. It is suggested that the third region of interest (580 to 690 °C), where an increased gradient is observed in the 'a' axis whilst a decrease is observed in the 'c' axis, is due to a transformation from a highly disordered state to is more ordered state with larger crystallites. The temperature range in which this occurs corresponds to the onset of recrystallisation temperature observed for all bone types.

Changes in the lattice parameters during heat treatment are thought to be a consequence of the loss of lattice incorporated water (up to 400 °C), ion exchange (in particular the loss of carbonate) and thermal expansion [8,9,32,33]. The amount of A and B type carbonate required to simulate the gradients differed for the 'a' and 'c' axes for the porcine, human, rostrum and red deer antler bone specimens. This suggests the change in the material between the second and fourth gradients is not only due to the loss of carbonate but must also be attributed to the loss or gain of extraneous ions during heat treatment. As shown in Table 2, the calculated change in the carbonate content between the 'a' and 'c' axes differed significantly between the bone types. This is possibly due to the relative amount and/ or variability of the extraneous ions present in the apatite structures of these bone types. The calculated change in carbonate content was for the bovine specimen was approximately equal for both 'a' and 'c' axes, suggesting that carbonate loss alone could explain the changes to the lattice parameters. This may not be the case, however, because the loss and gain of extraneous ions within the bovine specimen may not have been sufficient to be detected over and above the loss of the carbonate.

The change in gradient due to a transformation in the material occurs at a higher temperature for rostrum than the other bone types. This may be due to the fact that the hydroxyapatite crystals are more ordered and much larger in native rostrum in comparison to the other bone types investigated. This results in a smaller surface area to volume ratio and represents a lower energy state. Consequently, changes to the crystal structure (which alters the lattice parameters) of ordered systems require a greater amount of energy (gained at a higher temperature) in comparison to disordered systems.

4.4 Static and dynamic heating Previous work has demonstrated that the recrystallisation of statically heated bone mineral is greatly influenced by the collagen in the specimen [25,37]. Although the role of the collagen during heat treatment is debated, recent work has suggested that the combustion of collagen provides an intrinsic energy source that contributes to the energy required for growth of the bone mineral crystallites [25]. Accordingly, the recrystallisation of red deer antler mineral would be expected to occur at a significantly lower temperature than the other bone types investigated due to the fact that antler exhibits a greater abundance of collagen.

However, this proposed relationship between collagen and bone mineral is not observed for the dynamically heated bone of the current work. Recrystallisation occurred at a similar temperature (~600 °C) for all bone types except rostrum, as previously discussed. We believe that this is due to the difference in heating regimens (static

vs. dynamic). The heating rate of the dynamic experiments was significantly less than that used in static studies. Thus, collagen combustion energy is expended slowly and prior to the onset of recrystallisation, essentially creating an 'anorganic' specimen at temperatures >450 °C. For statically heated samples, however, the rate of combustion energy release associated with the loss of the collagen is much greater and the energy made available over a shorter period of time. Consequently, exothermic energy from the combustion of collagen contributes to the overall amount of energy required to promote recrystallisation during heating. This results in recrystallisation at lower temperatures for statically heated bone mineral in comparison to dynamically heated bone.

4.5 Species differentiation In contrast to a recent study [19] but consistent with other previous work [5], the data presented here has shown that lattice parameters derived from X-ray diffraction can be used for species differentiation. Analysis of the 'a' axis lattice parameter data has shown significant differences between the majority of the bone types investigated. Although, there was no significant difference between the porcine, bovine and red deer antler specimens, our study has revealed human bone can be significantly differentiated from all the other bone types considered in this study.

5 Conclusion

The dynamic heating of bone has allowed us to postulate why XRD parameters differ depending on the heating regimen employed. For the first time, it has been shown that the recrystallisation of bone apatite during heat treatment occurs rapidly within a short temperature range. Our data has validated previous research which suggested that, during heating, biologically formed hydroxyapatite transforms from a highly anisotropic state to a system where more ordered, larger, equidimensional crystals are present. This research also suggests that bone apatite crystal growth during heat treatment may be limited by the mineral to organic ratio. Investigation of the lattice parameters indicates that the loss of carbonate is not the only chemical process that has an effect on the lattice parameters during heat treatment. Other ionic exchanges may be important. Above the onset of recrystallisation temperature, the lattice shows classical linear expansion. Analysis of the lattice parameters has revealed species differentiation is possible using 'a' axis data. Crucially, human bone was found to be significantly different in the 'a' axis dimension from that of four other species investigated in this study.

Acknowledgements The authors thank the families who kindly donated tissues through the North London Tissue Bank of the National Blood Service. The AHVLA are also thanked for the donation of the animal tissue. The provision of the rostrum bone material was gratefully received from Dr. A. Casinos of the Department of Biology, University of Barcelona, Spain, and Dr Vivian de Buffrénil of the Muséum National d'Histoire Naturelle, Paris. Many thanks are given to Dr Tim Comyn, Leeds University, UK for enabling the use of the Hot Stage X-ray Diffraction equipment and for his advice throughout the project.

References

[1] R. Z. LeGeros, G. Bonel, and R. Legros, Calc. Tiss. Res. **26**, 111 (1978).
[2] L. F. Lozano, M. A. Peña-Rico, A. Heredia, J. Ocotlán-Flores, A. Gómez-Cortés, R. Velázquez, I. A. Belío, and L. Bucio, J. Mater. Sci. **38**, 4777 (2003).
[3] K. D. Rogers and P. Daniels, Biomaterials **23**, 2577 (2002).
[4] J. C. Hiller, T. J. U. Thompson, M. P. Evison, A. T. Chamberlain, and T. J. Wess, Biomaterials **24**, 5091 (2003).
[5] S. Beckett, K. D. Rogers, and J. G. Clement, J. Forensic. Sci. **56**, 571 (2011).
[6] C. Rey, C. Combes, C. Drouet, and M. J. Glimcher, Osteoporosis Int. **20**, 1013 (2009).
[7] J. C. Elliott, Rev. Mineral Geochem. **48**, 427 (2002).
[8] R. Z. LeGeros, O. R. Trautz, E. Klein, and J. P. LeGeros, Experientia **25**, 5 (1969).
[9] J. Shi, A. Klocke, M. Zhang, and U. Bismayer, Eur. J. Mineral **17**, 769 (2005).
[10] A. Krajewski, M. Mazzocchi, P. L. Buldini, A. Ravaglioli, A, Tinti, P. Taddei, and C. Fagnano, J. Mol. Struct. **744**, 221 (2005).
[11] R. Murugan, K. Panduranga-Rao, and T. S. Sampath-Kumar, Bull. Mater. Sci. **26**, 523 (2003).
[12] J. Yan, A. Daga, R. Kumar, and J. J. Mecholsky, J. Biomech. **41**, 1929 (2008).
[13] S. Rakmae, C. Lorprayoon, S. Ekgasit,, and N. Suppakarn, Polym-Plast Technology **52**, 1043 (2013).
[14] P. Shipman, G. Foster, and M. Schoeninger, J. Archaeol. Sci. **11**, 307 (1984).
[15] J. L. Holden, P. P Phakey, and J. G. Clement, Forensic Sci. Int. **74**, 29 (1995).
[16] M. C. Stiner, S. L. Kuhn, S. Weiner, and O. Bar-Yosef, J. Archaeol. Sci. **22**, 223 (1995).

[17] G. Piga, T. J. Thompson, A. Malgosa, and S. Enzo, J. Forensic. Sci. **54**, 534 (2009).
[18] D. H. Ubelaker, Forensic. Sci. Int. **183**, 1 (2009).
[19] G. Piga, G. Solinas, T. J. U. Thompson, and A. Brunetti, J. Archaeol Sci. **40**, 778 (2013).
[20] H. E. C. Koon, R. A. Nicholson, and M. J. Collins, J. Archaeol. Sci. **30**, 1393 (2003).
[21] G. Grupe and S. Hummel, J. Archaeol. Sci. **18**:177 (1991).
[22] L. E. Munro, F. J. Longstaffe, and C. D. White, Palaeogeogr. Palaeocl. **249**, 90 (2007).
[23] M. R. Schurr, R. G. Hayes, and D. C. Cook, in: The analysis of Burned Human Remains, Eds. C. W. Schmidt and S. A. Symes, Elsevier, Amsterdam 2008, chap.5, p.95.
[24] T. Schwark, A. Heinrich, A. Preuße-Prange, and N. von Wurmb-Schwark, Forensic Sci. Int.-Genetics **5**, 393 (2011).
[25] C. Greenwood, K. Rogers, S. Beckett, and J. Clement, J. Mater Sci. Mater Med. **23**, 2055 (2012).
[26] K. D. Rogers and P. Zioupos, J. Mater Sci. Lett. **18**, 651 (1999).
[27] J. D. Currey, J. Exp. Biol. **202**, 3285 (1999).
[28] J. D. Currey, P. Zioupos, P. Davies, and A. Casino, Proc. Biol. Sci. **268**, 107 (2001).
[29] P. Y. Chena, A. G. Stokes, and J. McKittricka, Acta Biomater. **5**, 693 (2009).
[30] K. Rogers, S. Beckett, S. Kuhn, A. Chamerlain, and J. Clement, Palaeogeogr. Palaeocl. **296**, 125 (2010).
[31] B. E. Warren, Phys. Rev. **59**, 693 (1941).
[32] X. Y. Wang, Y. Zuo, D. Huang, X. D. Hou, and Y. B. Li, Biomed. Environ. Sci. **23**, 473 (2010).
[33] S. R. Kim, J. H Lee, Y. T. Kim, D. H. Riu, S. J. Jung, Y. J. Lee, S. C. Chung, and Y. H. Kim, Biomaterials **24**, 1393 (2003).
[34] B. Wopenka and J. D. Padteris, Mat. Sci. Eng. C-Bio. S. **24**, 131 (2005).
[35] I. R. Gibson, I. Rehman, S. M. Best, and W. Bonfield, J. Mater. Sci. Mater. Med. **12**, 799 (2000).
[36] S. N. Danilchenko, A. V. Koropov, I. Yu. Protsenko, S. Sulkio-Cleff, and L. F. Sukhodub, Cryst. Res. Technol. **41**, 268 (2006).
[37] S. Roberts, C. Smith, A. Millard, and M. Collins, Archa. **44**, 485 (2002).

